Current Drivers and Control Electronics for the Laser Spectroscopy of Highly Charged Ions

Stromtreiber und Steuerelektronik für die Laserspektroskopie von hochgeladenen Ionen
Vom Fachbereich Physik der Technischen Universität Darmstadt zur Erlangung des Grades eines Doktors der Naturwissenschaften (Dr. rer. nat.) genehmigte Dissertation
von Patrick Baus aus Mannheim
Tag der Einreichung: 20.06.2023, Tag der Prüfung: 17.07.2023

1. Gutachten: Prof. Dr. Gerhard Birkl
2. Gutachten: Prof. Dr. Thomas Walther
Darmstadt, Technische Universität Darmstadt

Current Drivers and Control Electronics for the Laser Spectroscopy of Highly Charged Ions
Stromtreiber und Steuerelektronik für die Laserspektroskopie von hochgeladenen Ionen

Accepted doctoral thesis
by Patrick Baus

1st reviewer: Prof. Dr. Gerhard Birkl
2nd reviewer: Prof. Dr. Thomas Walther

Date of submission: 20.06.2023
Date of thesis defense: 17.07.2023

Darmstadt, Technische Universität Darmstadt

Bitte zitieren Sie dieses Dokument als:
URN: urn:nbn:de:tuda-tuprints-276077
URL: https://tuprints.ulb.tu-darmstadt.de/27607
Jahr der Veröffentlichung auf TUprints: 2024

Dieses Dokument wird bereitgestellt von tuprints,
E-Publishing-Service der TU Darmstadt
https://tuprints.ulb.tu-darmstadt.de
tuprints@ulb.tu-darmstadt.de

Cover art: Digital laser current driver DgDrive in the foreground with a blue $488\,\mathrm{nm}$ laser in the background. Canon EOS R6, RF24-105mm F4 L IS USM, aperture F4, exposure time $\frac{1}{25}$ s.

Abstract

Recent years have seen an ever increasing range of laser diodes covering the spectral range from ultraviolet to infrared. The classic 780 nm and 830 nm NIR laser diodes have been well established and many laser designs were developed with design parameters for such diodes. Over the years the disparity in development efforts between laser diodes and supporting electronic systems has led to a subpar performance of such systems compared to NIR diode lasers.

The desire for high resolution spectroscopy of highly charged ions having optically accessible transitions in the ultraviolet and blue regime sparked an interest in high precision and compact diode lasers systems addressing these needs. At the same time, other applications like quantum computing, using arrays of neutral atoms, have seen an increasing demand for customized, compact diode laser systems for the addressing and coherent manipulation of hundreds of individual quantum systems on the way to even larger systems scaling to thousands of qubits. All of these use cases require state of the art diode laser systems designed for modern laser diodes with unprecedented stability and noise performance surpassing many of the solutions currently available.

This work compares several commercial products and devices developed in academia used as building blocks for diode laser system like laser drivers and temperature controllers. The laser current driver performance is tested in terms of compliance voltage, output noise, stability with respect to both temperature and time and their output impedance, which is a measure for their noise suppression capability. The limitations found with the tested devices are identified and their causes are explained analytically and with simulations. The laser temperature controllers which are inherently closed-loop instruments whose performance is determined by their front end were tested in terms of noise and stability using reference resistors against a reference thermometer.

These results led to the development of a novel fully digital laser diode driver and temperature controller surpassing other solutions in terms of performance by at least one order of magnitude while being open-source and highly customisable to allow adapting to the needs of both high-resolution spectroscopy and coherent control of quantum systems. The laser current driver implements a unique architecture that isolates the current source from the load to combine the high compliance voltage, demanded by modern high performance laser diode, with ultra-low current noise and stability, providing sub-shot noise performance between 20 mA and 500 mA, delivering a performance close to the limits allowed by physics. This is combined with an outstanding noise immunity allowing the use of compact switch-mode supplies to power those laser drivers without impacting their performance.

The digital temperature controller, again an open-source design, provides definitive sub-mK performance with µK resolution. The stability of this system is defined by the performance of the thermistor used, shifting the focus towards the mechanical resonator design as the ultimate performance limit.

Finally, a data logging system is presented that accompanies these high precision instruments to monitor the environment of the laboratory, the experiment and instrument parameters to give the experimenter real-time information on the state of the systems along with user-definable alerts to protect those assets.

All of these developments are in extensive use at several state of the art experiments and are considered essential for their progress.

Zusammenfassung

Die Entwicklung von Laserdioden ist in den letzten Jahren immer weiter voran geschritten. Mittlerweile wird nahezu der gesamte Wellenlängenbereich von Ultraviolett bis Nahinfrarot abgedeckt, wodurch eine Vielzahl von Lasersystemen zu Verfügung steht. Dabei hat sich eine Kluft aufgetan zwischen der Entwicklung von Laserdioden und der zugehörigen Steuerelektronik. Dies hat unweigerlich zu einer eingeschränkten Leistungsfähigkeit von Lasersystemen mit diesen modernen Dioden geführt.

Das Interesse an hochauflösender Laserspektroskopie von hochgeladenen Ionen, welche optisch zugängliche Übergänge im ultravioletten und blauen Wellenlängenbereich aufweisen führte zu einem gesteigerten Bedarf an kompakten und hoch performanten Lasersystemen. Zeitgleich ergeben sich aus der sprunghaften Entwicklung von Quantensystemen, z.B. bestehend aus Registern aus einzeln kohärent adressierbaren neutralen Atomen, welche Quantencomputer mit tausenden von Qubits in greifbaren Nähe rücken lassen, neue Anforderungen an die Stabilität, Steuerbarkeit und Integration der Lasersysteme. All diese Anwendungsfälle benötigen Systeme auf dem neusten Stand der Technik, welche die Leistung aktuell verfügbarer Lösungen hinsichtlich Stabilität und Rauschverhalten bei weitem übertrifft.

Geleitet durch diese Anforderungen beschäftigt sich diese Arbeit sich mit dem Aufbau entsprechender Lasersysteme. Es werden hierzu zunächst kommerziell verfügbare und aus wissenschaftlichen Arbeiten abgeleitete Geräte, wie Laserstromtreiber und Temperaturregler, für diese Anwendungen getestet. Die Stromtreiber werden bezüglich ihrer Konformitätsspannung, dem Ausgangsrauschen, der Stabilität, in Bezug auf Temperatur und Zeit, und der Ausgangsimpedanz untersucht. Die Grenzen der getesteten Geräte werden aufgezeigt und die Ursachen analytisch und durch Simulationen illustriert. Die Temperaturregler werden hinsichtlich ihres Messrauschens und der Stabilität gegen einen Referenzwiderstand vermessen.

Diese Erkenntnisse führten zu der Notwendigkeit einer Eigenentwicklung eines neuartigen digital Laserstromtreibers, welcher die Leistung bestehender Lösungen um mindestens eine Größenordnung übertrifft. Die dabei entstandene Open-Source Lösung ist modular und kann einfach an die Bedürfnisse der hochauflösenden Spektroskopie und der kohärenten Manipulation von Quantensystemen angepasst werden. Der Laserstromtreiber baut hierzu auf einer einzigartigen Architektur auf, welche die Stromquelle von der getriebenen Last trennt, um so die Anforderungen einer hohen Konformitätsspannung durch blaue Laserdioden mit dem Bedürfnis nach niedrigstem Stromrauschen, welches das Schottky-Rauschen bereits oberhalb von $20\,\mathrm{mA}$ unterbietet, und höchster Stabilität nahe an der Grenze des physikalisch Machbaren ermöglicht. Dies wird mit einer außergewöhnlichen Eingangsrauschunterdrückung gepaart, welche den Betrieb mit modernen und kompakten Schaltnetzteilen ermöglicht, ohne Einbußen in der Leistung befürchten zu müssen.

Der digitale Temperaturregler, welcher ebenso als Open-Source Entwicklung vorangetrieben wird, ermöglicht eine Regelstabilität von weniger als $1\,\mathrm{mK}$ mit einer µK-Auflösung. Zusammen mit dem Stromtreiber verschiebt er hierdurch die Grenzen der Laserstabilität klar in Richtung der mechanischen Stabilität des externen Laserresonators.

Zuletzt wird noch ein Datenerfassungssystem vorgestellt, welches im Zusammenspiel mit den vorgestellten Geräten sowohl die Laborumgebung, wie auch Experiment- und Geräteparameter erfassen kann, um dem Experimentator eine Echtzeitüberwachung des Experiments über mehrere Endgeräte hinweg zu ermöglichen.

Diese Neuentwicklungen werden aktuell bereits intensiv von mehreren wegweisenden Experimenten genutzt und sind mittlerweile unabdingbar für deren Erfolg geworden.

Contents

1. Changelog

> *"What I like about photographs is that they capture a moment that's gone forever, impossible to reproduce."*
>
> – Karl Lagerfeld

This work is only a momentary snapshot in time and subject to change. Future revisions will be updated as errors are found and lab-gremmlins have been evicted. If an error is found in this work, the reader is encouraged to either send an email to patrick.baus@physik.tu-darmstadt.de or file a bug report over at Github. Do note, the author has mischievously hidden some errors and typos in this work for the observant reader to find. The latest version (and all others) can always be found by navigating to https://github.com/PatrickBaus/phd_thesis or using the QR code below.

Current version: v.1.1.0

Version	Date	Comment
0.9.0	2023-06-20	Initial release submitted as the doctoral thesis.
0.10.0	2024-07-09	Updated plot colours to match the Seaborn 0.9.0+ style.
0.11.0	2024-07-09	Changed downsampling algorithm from decimation to LTTB. Affected files: dgDrive_supply_filter_bode.pgf, dgTemp_longterm.pgf, dgTemp_testmass.pgf, output_impedance_libbrecht_hall.pgf. Increased number of points in the leakage plots. Use $3-\sigma$ for the uncertainty of the temperature coefficient.
0.12.0	2024-07-09	Regenerated all plots to unify their dimensions.
0.13.0	2024-07.09	Fixed typos and other errors found so far.
0.14.0	2024-07-09	Updated APQ-Latex design template to a version based on tuda-ci 3.38.
0.15.0	2024-07-11	Changed the y-axis of the flicker noise amplitude plot to make it looker bigger. Decimate the noise psd plots to improve the uncertainty towards higher frequencies. Fixed LNA background noise data. There was an incorrect gain setting applied. Fixed dgDrive_output_impedance_comparison plot, because the sense resistor was not subtracted from the plotted results. This affected all devices but the DgDrive.

0.16.0	2024-07-12	Fixed simulated LNA noise floor. Fixed typos. Fixed the siunitx preamble for all plots.
0.17.0	2024-07-13	Updated Numpy and AllanTools to 2.0.0 and 2024.6.
0.18.0	2024-07-14	Fixed citations. Added Matplotlib and ReactiveX. Cleaned up URLs.
0.19.0	2024-07-15	Reduced font size of the DVI connector labels.
0.20.0	2024-07-15	Bump TeX Live to 2023.
1.0.0	2024-07-16	Changed compilation options to 'drfinal' for publication.
1.1.0	2024-07-16	Fixed missing printid.

2. Introduction

Highly charged ions offer a unique insight into the very fine details of the world described by quantum electrodynamics (QED). The predictions of the electron's magnetic moment (g-factor) can easily be regarded as the most accurate prediction in all science, matching the experimental value to 10 significant figures [23].

For free electrons, experimental measurements of the g-factor have most recently pushed the boundaries as far as an uncertainty of 1.3×10^{-13}. The comparison of experimental values of the g-factor with theory therefore represents the most stringent test of the QED theory [200]. Extending the application of QED to bound states requires new tests of these calculations. Computing of the g-factor in complex systems such as neutral atoms with many electrons is extremely difficult and currently impossible with decent uncertainty [22]. Using heavy highly charged ions helps both theory and experiment because it reduces the complexity and at the same times scales the QED contribution with the nuclear charge number as $Z\alpha$, reducing the required accuracy [217]. While research has primarily relied on non-optical measurement in Penning traps in the past, laser spectroscopy opens new opportunities [246] as the strong scaling of the fine- and hyperfine-structures with Z^4 and Z^3 brings those transitions into the region of visible and ultraviolet (UV) laser spectroscopy.

Highly charged ions are therefore an interesting field of research with the GSI Helmholtz Center for Heavy Ion Research at the forefront and capable of providing up to bare uranium. The AsymmetRic Trap for the measurement of Electron Magnetic moments in IonS (ARTEMIS) experiment at GSI as part of the Highly charged Ions Trap (HITRAP) platform and Facility for Antiproton and Ion Research (FAIR) aims to perform high-precision measurements of the bound electron's g-factor using a combination of laser- and microwave spectroscopy referred to as laser-microwave double-resonance spectroscopy [179]. The ARTEMIS experiment provides a unique optically accessible Penning trap design [132, 243] with the aim of measurements on hydrogen-like bismuth, $^{209}Bi^{82+}$. Currently the experiment is in its commissioning phase using boron-like Argon, $^{40}Ar^{13+}$, targeting a g-factor measurement at the 10^{-9} level [130].

Both the commissioning and the measurement on hydrogen-like bismuth require a precision laser system consisting of multiple lasers for the targeted closed transition driven by lasers and microwaves. The accessible wavelength of $^{40}Ar^{13+}$ is $441\,$nm [147], while $^{209}Bi^{82+}$ requires laser radiation at $243.8\,$nm [229]. Recent years have seen the development of new laser diodes giving diode lasers access to an increasing part of the spectrum and for both targeted ion species the fundamental wavelengths are now covered by diode lasers. $244\,$nm can be reached via a quadrupled $976\,$nm diode laser source and $441\,$nm is directly accessible due the invention of blue laser diodes. Blue laser diodes were first presented in 1994 by Nakamura et al. [166]. This was followed by the first pulsed UV laser diode developed by Akasaki et al. [17] in 1995 and 1996 the first continuous wave UV laser diode [16]. These developments then warranted the 2014 Nobel Prize in physics. This progress created the opportunity to build a compact and economic laser systems for the spectroscopy of highly charged ions based entirely on diode lasers.

For both applications, laser systems were proposed and preliminary tests conducted [18,

31, 150, 176]. These tests have shown severe limitations in the current state of the art in diode laser technology. Most laser diode drivers commercially available are based on the work of Libbrecht et al. presented in 1993 [128] which was designed for near-infrared laser diodes and the characteristics of blue laser diodes could not be foreseen at that time. The rapid development of blue light emitting diodes and laser diodes outpaced the development of the electronics to drive them which led to subpar performance of blue and UV diode lasers in comparison to their near-infrared brethren. Several groups have reported issues with the existing designs [196] without offering solutions while others attempted to improve the front end situation by including modern digital controls [77].

Such digital control is critical to stay ahead of the ever increasing complexity introduced by modern experiments. Such experiments can, for example, be found in the field of quantum computing. A promising approach is the use of large arrays of individual neutral atoms, captured using optical traps to solve the scaling problem [49]. Having hundreds to thousands of quantum systems that need addressing and manipulation requires dozens of compact laser sources that need to be orchestrated. Such orchestration is no longer feasible by hand. This level of automation requires a high degree of stability over time and temperature from the laser electronics to ensure the repeatability and reliability of the system. These qualities must be paired with an outstanding noise performance to produce the high fidelity of quantum-state manipulation necessary for quantum computers. A combination of these digital features with the performance level is currently not available on the market.

This work has has now closed the gap and provides state of the art open-source laser electronics incorporating novel approaches to the design of laser current drivers and temperature controllers for the application in high precision spectroscopy and quantum computing experiments. These solutions include modern remote-controllable digital interfaces for controlling large scale setups.

This work is split into three parts.

The **Preparation** develops the theoretical background by giving a quick introduction into control theory, noise types and current sources. It also presents the requirements for the laser system designed for ARTEMIS.

The **Results** give a detailed comparison of several laser drivers, both commercial and academic to outline the problems discovered during the testing of a blue laser systems. A laser driver design outperforming all solutions currently available is presented along with a high stability temperature controller specifically designed for the stringent needs of high precision laser spectroscopy. Additionally a compact PID controller system for lab application is presented in the context of lab temperature control together with a data monitoring system capable of logging the manifold data accumulated in a modern experiment and environmental monitoring systems. This data can then be accessed in real-time using a graphical web front end.

The **Outlook** summarizes the results developed and, with the sources of electronic noise in diode lasers suppressed, exposes the final barrier imposed by the mechanical design of laser resonators.

3. Preparation

"Begin at the beginning," the King said gravely, "and go on till you come to the end: then stop."

– Lewis Carroll, *Alice in Wonderland*

3.1. Laser System

The ARTEMIS experiment is currently in the process of commissioning. Due to the relative abundance of Argon, the ability to create highly charged ion species using an electron beam along with a scientifically relevant transition at $\lambda = (441.255\,75 \pm 0.000\,17)$ nm [147] with a lifetime of (9.573 ± 0.006) ms [119] makes Ar^{13+} an ideal candidate for this purpose. Figure 3.1 (a) shows the simplified electronic configuration of the boron-like Ar^{13+} investigated.

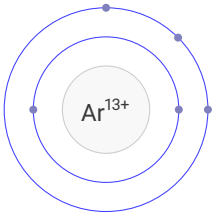

(a) Shell model of boron-like Ar^{13+}.

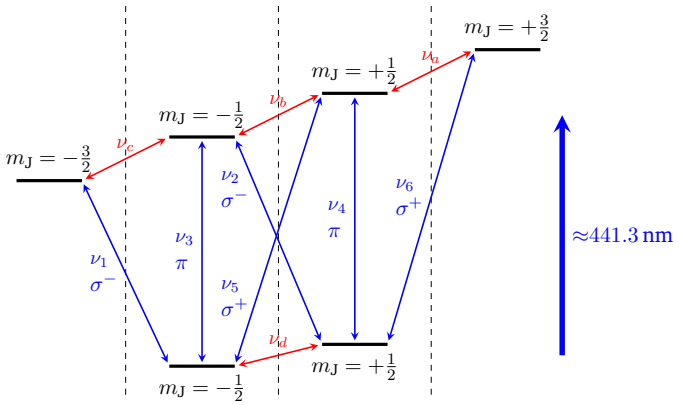

(b) Level diagram of the Ar^{13+} transitions accessible at 441 nm. Frequencies with numbers denote optical transitions, letters denote microwave transitions.

Figure 3.1.: Electronic configuration and optically accessible transitions of Ar^{13+}.

The optical transitions of highly charged Ar^{13+} around 441 nm shown in figure 3.1 (b) can be used for laser spectroscopy. The transition of interest for commissioning is the transition from the ground state $[(1s)^2(2s)^22p]^2\,P_{1/2}$ to the first exited state $[(1s)^2(2s)^22p]^2\,P_{3/2}$ [131]. The Zeeman splitting introduced by the 7 T magnet of the ARTEMIS Penning trap results in a frequency splitting of the $^2P_{1/2}$ ground state by $\nu_d = 65$ GHz and the exited $^2P_{3/2}$ state of $\nu_a = 130$ GHz. The natural linewidth of these transitions is $\Gamma \approx 2\pi \times (16.63 \pm 0.01)$ Hz which is fairly small, but there is substantial Doppler broadening of

$$\Delta\nu(\lambda = 441\,\text{nm}, T = 4\,\text{K}, m = 39.948\,\text{u}) = \frac{2}{\lambda}\sqrt{2\ln 2\frac{k_B T}{m}} \approx 2\pi \times 150\,\text{MHz}\,, \tag{3.1}$$

seen in the trap which is kept at a temperature of 4 K.

The simplified laser setup shown in figure 3.2 as a schematic was characterised by Martin [150] and its transfer accuracy of the the wavelength was calculated to be 1.2 MHz. Considering the additional long-term drift of the system led to an upper limit of the absolute wavelength uncertainty of 2.2 MHz. This can be considered more than adequate given the Doppler broadening of 150 MHz calculated in equation 3.1. While being sufficiently accurate, the system has the significant drawback of being fairly complicated to manage if not maintained on a daily basis. Its performance and uncertainty relies on the exact knowledge of the tellurium spectrum surrounding both wavelengths of the lasers.

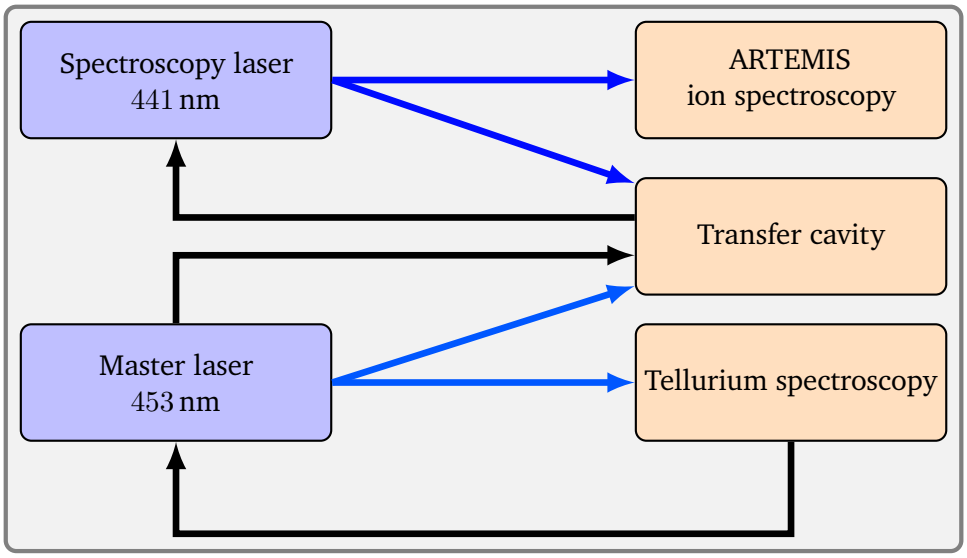

Figure 3.2.: Simplified setup of the laser system in use at ARTEMIS prior to this work. Blue lines are laser beams, black lines are electronic signals delivering feedback.

To operate the system, the master laser must first be locked to a tellurium reference transition which has to be searched manually using the tellurium spectrum charted by [150]. While not complicated, it requires a trained user nonetheless. The transfer cavity is then locked to the master laser, a straight forward process. The spectroscopy laser now has to be locked to the correct fringe of the transfer cavity. This is done by observing the tellurium background again to adjust the diode laser mode to a frequency close to the desired cavity fringe. This is by no means an automated process and requires a competent operator. Although this locking procedure requires training it does work reliably, but there are more issues that are not readily apparent.

One potential problem lies with the master laser. The whole calibration is geared towards a reference transition at 452.756 nm catalogued by Scholl et al. [194]. Replacing the master laser in case of a failure is challenging. Blue laser diodes are less flexible when tuning in comparison to their NIR cousins as discussed in [31, 150]. The diode used in the current laser was handpicked for this wavelength. This limits the availability of replacement parts and increases their replacement value. Using another diode and wavelength along with a different tellurium transition would require creating a new tellurium map which is a laborious process.

Another challenge is created by the locking scheme which becomes more complicated when introducing a third laser to complete the closed transition for the laser-microwave double-resonance spectroscopy. The setup in its present condition was already prepared for the second

spectroscopy laser which must also be locked to the transfer cavity. Currently both lasers are sent into the transfer cavity with perpendicular polarisations to separate the beams using a polarizing beam splitter. Since the reference laser is running at $453\,\mathrm{nm}$ while the spectroscopy laser is using $441\,\mathrm{nm}$, it is also possible to separate those two via a dichroic mirror. While possible, this scheme requires the close overlap of three beams along with their reflection as required for saturation. Such a setup strongly couples the three beam paths and further complicates future adjustments.

The final issue regarding the transfer cavity concerns the required high voltage for the piezoelectric actuator to adjust its length. This piezo requires up to $1.25\,\mathrm{kV}$ to reach the necessary translation required for scanning the tellurium spectrum. Not only does this pose a risk to an untrained operator, but it was also discovered during the commissioning of the current system that high frequency noise from the voltage supply is radiated and can enter the experiment. These issues were minimized by testing several power supplies, choosing the lowest noise device and keeping the supply well separated from the rest of the experiment increasing space required for the whole system.

During the commissioning and testing of the laser system it was also found that the laser drivers had issues with blue laser diodes. Those drivers used a modified in-house current source normally used for NIR diodes based on the design of Libbrecht et al. [128]. With these drivers an increasing instability was observed when adjusting the current up to the operating point. The origin of this problem lies in the larger operating voltage of the blue laser diode of up to $7\,\mathrm{V}$ compared to the more moderate $2.5\,\mathrm{V}$ of NIR diodes. The details are discussed in section 3.8.5. Other commercial drivers tested either had the same problem or were far noisier and therefore harder to work with, due to the modification made by the manufacturers to increase the compliance voltage.

To conclude, the commissioning of the laser system has brought up two issues with the current system that impact its availability and performance. The transfer cavity can be considered the Achilles' heel of the system and replacing it with a more flexible alternative like a high performance wavemeter can greatly improve the usability and flexibility of the whole laser system as it breaks up the tight dependency on the tellurium reference laser. Additionally this opens up alternative wavelengths for the spectroscopy of other highly charges ion species. The second issue was found with the laser driver and the apparent lack of commercial solutions sparked the development of a novel laser driver for the next generation of laser diodes to gain direct access to more wavelengths. This is discussed in the next section.

3.2. Laser Current Driver

Laser diodes are current driven devices, because

$$P_{out} \propto I$$

and the diode current I approximately follows the Shockley equation [203]

$$I = I_0 \left(e^{\frac{qV_d}{k_B T}} - 1 \right) . \tag{3.2}$$

where k_B is Boltzmann constant, T the temperature, q the electron charge and V_d the diode voltage. The exponential dependence of the current on the supply voltage calls for a current source to drive a laser diode safely without risking thermal damage due to excessive injection currents.

The primary function of a laser driver is therefore to provide a stable, but user adjustable, current. This current can typically be modulated at frequencies up to several MHz to shape the frequency and amplitude of the laser output light. Additional features, like current and voltage limits, aid in protecting the expensive laser diodes and it is not uncommon to have additional safeguards inside the laser head that are under control of the laser driver like a shorting relay to ensure the laser diode is shorted when the driver is disconnected or disabled.

The focus of this work lies on two types of laser diodes, indium gallium nitride (InGaN) and aluminium gallium arsenide (AlGaAs), but is not limited to those two types. The former material is, for example, used for blue laser diodes at around $450\,\text{nm}$, discussed in the previous section, and laser diodes up to green wavelengths, the latter is used for near-infrared (NIR) laser diodes such as $780\,\text{nm}$ laser diodes. Both wavelengths are used for experiments in the Atoms-Photons-Quanta group (in future referred to as *the group*). The former type is used in the ARTEMIS experiment for the spectroscopy of highly charged ions, the latter is extensively used to manipulate and control the rubidium atoms used by the quantum computing experiments. This section deals with the design challenges of such a device used for high precision laser spectroscopy. First the design requirements are established and, from those conditions, technical specifications are developed.

The design requirements are split into three parts which need to be discussed: The environment includes effects like temperature, humidity and time. That section mostly focuses on the ambient temperature though because its effects are the most pronounced. The current source electrical requirements, like drift, noise, output impedance, and modulation bandwidth are discussed as these have a profound impact on the intended application in experiments. Finally, the user interface including the external communication interfaces are defined.

3.2.1. Design Goals: Ambient Environment

The lasers and its accompanying driver is to be mostly used in a clean laboratory environment. In this particular use case the air is filtered using H14 HEPA filters, but less rigorously controlled environments must be considered as well, because not all fields of application are in optical labs. A mostly dust free industrial environment is considered acceptable as well. Typical lab temperatures are in the range of $20\,^\circ\text{C}$ to $30\,^\circ\text{C}$. This temperature range was also encountered in the labs discussed in this work before improvements were implemented as part of this work. The upper end of the range must be considered when operating the devices inside a rack where the temperatures are even higher and the device should therefore be tested for its upper limit.

A temperature of 35 °C is a typical value measured inside the racks used in the lab. Humidity is only controlled with dehumidifiers, limiting only the upper bound, resulting in a range of 15 %rH to 60 %rH.

Figure 3.3 shows a typical one day span of the lab temperature as it was found at the start of this project, plotted using Matplotlib [100].

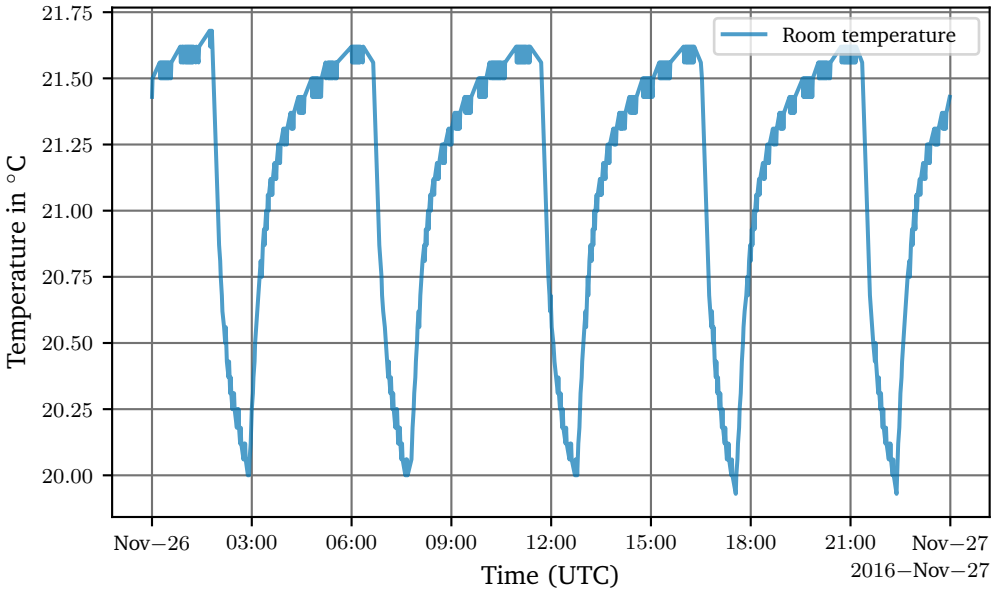

Figure 3.3.: Temperature in lab 011 of the APQ group on 2016-11-26. Recorded by the LabKraken monitor. See section 4.2 for details.

As it can be seen there are strong oscillations of the temperature around the setpoint of 21 °C as a result of the on–off air conditioning temperature controller. The commercial controller initially installed was using an IMI Heimeier `EMO T` thermoelectric actuator [76], which is a two-step valve. Although this solution was later replaced by a custom design described in section 4.3, these type of controllers are found in many other labs and temperature swings of 2 K must therefore be expected.

These environmental parameters can now be used to estimate the design requirements for the laser driver. In comparison to the other laser system used in this group, the 450 nm system [31] required for the spectroscopy of highly charged ions [150] at GSI is the more demanding system. This system was found to be more susceptible to changes of the drive current since the wavelength selective filter element was far broader in comparison to a 780 nm system [151]. This laser is stable over regions of tens of µA and requires a maximum drive current of 145 mA [174].

From these considerations, the requirements for the driver can be inferred. It should be able to supply at least 150 mA and stay well within 10 µA over the whole environmental range. Given a worst-case scenario a tolerance of 3σ (99.7 %) must be met [212].

The environmental parameters that mostly affect current sources are temperature and humidity. Air pressure is typically a matter of concern for high voltage systems [103] and secondary in consideration for this design as it is a low voltage system ($\leq$48 V). Air pressure effects are also the most expensive to test for, as a pressure chamber is required. Humidity affects electronics both directly though corrosion and also indirectly because the epoxy resin

used in the FR-4 PCBs and component moulding is hygroscopic and the absorbed humidity leads to swelling and mechanical stress. This effect is very slow at ambient temperature and can easily take days to show [105]. This parameter is therefore handled via the long-term stability and not specified separately.

Given environmental conditions, the relative coefficients can be calculated. This estimation assumes a minimum setpoint resolution of 2 steps within the mode-hop-free region of the laser and calculates the $99.7\,\%$ confidence interval. The steps are given in table 3.1:

Property	Value	Result
Stable range	$10\,\mu A$	$10\,\mu A$
2 steps of resolution	$\div 2$	$5\,\mu A$
1σ	$\div 2$	$2.5\,\mu A$
Maximum output	$150\,mA$	$17\,\mu A/A$
Temperature range	$5\,K$	$3\,\mu A/(A\,K)$
Worst case (3σ)	$\div 3$	$1\,\mu A/(A\,K)$

Table 3.1.: Estimated requirement for the temperature coefficient of the laser driver.

While the requirements look moderate at first sight, tuning a quick estimation shown in table 3.1 leads to a temperature coefficient of $1\,\mu A/(A\,K)$ or even tighter when using a higher output driver – a rather formidable specification for a current source.

Regarding the long-term stability, a $30\,d$ number can be estimated. One may be inclined to call for a drift which is smaller than the stable range, but this would be short-sighted, as there are other factors to consider. The laser including the external resonator has its own figure of merit regarding the spectral drift rate. Talvitie et al. [220] reported a drift of $2.9\,MHz/h$, which was attributed either to the external resonator itself, the piezo or the collimation lens. It is most likely that this drift was caused by mechanical changes of the external resonator as it defines the output mode of the laser. The mechanical drift limits the required stability of the current source considerably, as a typical frequency change of the internal resonator with the current of $3\,MHz/\mu A$ [242] can be assumed. The (linear) ageing drift of the external resonator over $30\,d$ is equivalent to a $720\,\mu A$ drift over the same period. For the electronics, the drift is assumed to follow an Arrhenius-like equation resulting from stress, caused during manufacturing. This may eventually change to a slow linear drift after several months of relaxation. The coefficient can either be a positive or negative and leads to

Property	Value	Result
Ageing drift limit	$720\,\mu A$	$720\,\mu A$
1σ	$\div 2$	$360\,\mu A$
Maximum output	$500\,mA$	$720\,\mu A/A$
Worst case (3σ)	$\div 3$	$240\,\mu A/A$

Table 3.2.: Estimated requirement for the long-term stability over $30\,d$ of the laser driver.

Based on these numbers, it is straightforward to see that the long-term stability of a laser driver is less important than the short-term temperature coefficient since the limiting factor is the mechanical construction of the laser. This necessitates an atomic reference for long-term stability and to compensate for acoustic resonances of the external resonator. Regarding the

choice of suitable devices, the tight specification of the temperature coefficient most likely leads to a choice of components that will pass these long-term criteria as well, alleviating a bit the burden of proof as long-term drift specifications are hard to come by since they need a lot of time to validate and cannot be extrapolated from high temperature burn-in tests [247].

All of this leads to the following design specifications regarding the stability of the current driver:

Design requirements 3.1: Current source, environmental

- Temperature range 20 °C to 35 °C
- **Temperature coefficient $\leq$1 µA/(A K)**
- Humidity (non-condensing) $\leq$75 %rH
- Humidity coefficient not specified, but included in the long-term drift
- Maximum altitude not specified
- Long-term drift over 30 d $\leq$240 µA/A

3.2.2. Design Goals: Current Source

The change in output current caused by load impedance should be an order of magnitude less than the drift specification to ensure a negligible effect compared to the drift over time. The load resistance presented by the laser diodes most commonly used in our experiments ranges from 50 Ω [174] to 30 Ω [14] and 10 Ω–15 Ω for 780 nm laser diode [87, 118]. The output impedance requirement can therefore be estimated as

$$\begin{aligned} \frac{R_{load}}{R_{out}} &= \frac{I_{set}}{I_{out}} - 1 \leq 6.7\,\mu\text{A/A} \\ R_{out} &\geq \frac{50\,\Omega}{6.7\,\mu\text{A/A}} = 7.5\,\text{M}\Omega \end{aligned} \tag{3.3}$$

An output impedance of more than 7.5 MΩ for slowly changing loads is a tough requirement, depending on the type of current source, which requires carefully selected components. A high output impedance is, for example, of importance to suppress radiated noise coming from external sources. Especially low frequency components from the mains supply can magnetically couple into the cables, because they are long enough. This noise can be substantial and a high output impedance at low frequencies is therefore important. Other applications will be discussed throughout this work. While a subpar output impedance is more of a limiting factor, the compliance voltage discussed next is a key requirement.

The compliance voltage is the maximum voltage the current source can apply to the load and is another non-ideal component of a real current source. The required voltage strongly depends on the type of laser diode used. The near-infrared laser diodes discussed above have an operating voltage of 1.5 V–3 V, while the Osram PL 450B blue laser diode is specified for 5.5 V–7 V. The 7 V required by the Osram laser diode is fairly high for a Fabry–Pérot laser diode and has proven difficult in the past [31] as most laser current drivers available are designed for the much lower forward voltage of the near infrared laser diodes. Even higher voltages of

around 12 V–15 V are required for quantum cascade lasers, but these are currently neither used nor is their use planned in any experiment in the group.

The maximum output current of the laser driver currently required for laser diodes used in the group is 250 mA for the Thorlabs `L785H1` [118]. Therefore a maximum output current of 300 mA is considered sufficient.

The current noise of the laser driver can be estimated from the laser linewidth sought after as the laser frequency is sensitive to the injection current. At low frequencies, about $-3\,\mathrm{MHz/\mu A}$ can be attributed to the thermal expansion of the internal resonator of the diode due to resistive heating [242]. Above 1 MHz this effect starts declining and exposes the change of the refractive index due to the presence of charge carriers. This high frequency effect is an order of magnitude weaker. Since the frequency sensitivity to current variations of the laser diode drops with higher frequencies, the most important range is from DC to 100 kHz.

To estimate the linewidth requirement, it is important to look at the experimental setup. While the spectroscopy of Ar^{13+} at 4 K is limited to around 150 MHz as shown on page 13, the quantum computing experiments in this group have more stringent needs. It was shown in [54, 189, 220] that with reasonable expense a passive linewidth of less than 100 kHz can be achieved. Using the relationship of the frequency sensitivity to a current modulation of laser diodes, 100 kHz translates to a current noise of $30\,\mathrm{nA_{rms}}$ from 1 Hz to 100 kHz. The lower 1 Hz limit is chosen fairly arbitrary, but the presence of $\frac{1}{f}$-noise inhibits a definition down to DC. There should be negligible amounts noise below 1 Hz compared to the upper 100 kHz though.

The final aspect of the current source that needs to be specified, is the bandwidth of the current steering input. The bandwidth in these terms defines a reasonably flat ($\leq$3 dB) response. As it was discussed above, beyond a frequency of 1 MHz, the frequency sensitivity of the laser diode to current modulation drops by an order of magnitude, altering the transfer function and introducing new challenges for control loops. Therefore a minimum bandwidth of 1 MHz is considered sufficient.

Above 1 MHz it is recommended to either use more dedicated solutions like the direct modulation at the laser head presented in [177] or switch to acousto-optic modulators (AOMs) or electro-optic modulators (EOMs).

This leads to the following requirements regarding the current source of the laser driver:

Design requirements 3.2: Current source, electrical

- Maximum output current 300 mA, optionally 500 mA
- **Compliance voltage $\geq$8 V**
- Output impedance $\geq$7.5 MΩ at low frequencies (close to DC)
- **Current noise $\leq$30 $\mathrm{nA_{rms}}$ from DC to 100 kHz**
- 3 dB-bandwidth of the modulation source $\geq$1 MHz

3.2.3. Design Goals: User Interface and Form Factor

The user interface must allow repeatability and reproducibility of the outputs. The reason is that the laser system is intended to be portable to be moved from the university where it is performance tested to the GSI facility. Within the labs, systems are usually moved from test

stands to the actual experiment as well. Requiring as little setup efforts as possible is a big advantage.

The interface must both be accessible both locally and remotely to allow simple adjustment of the parameters while on the bench and also from within the experimental control software. The local controls must be directly accessible to humans without tools to give a better user experience.

The remote user interface is strictly required because the Penning trap and the laser system are spatially separated with the laser system being located in a special laser lab for environmental as well as safety reasons. This separation is about 30 m. Ideally this remote interface is computer controlled to give full access to all features of the laser system. USB or Ethernet is preferred as this does not require extra hardware in the lab.

Regarding the application programming interface (API), support for both Python and optionally LabVIEW is favoured, as most of the group has switched from LabVIEW to labscript suite [214] on Python to run the experiments.

The form factor should allow integration into standard 19-inch racks to allow simple transportation from the experiment location at GSI to the university for testing and calibration.

Design requirements 3.3: Current source, user interface

- Local control via the front end without tools
- Remote access via a digital interface
- Software API supporting **Python** and optionally LabVIEW

3.3. Laser Temperature Controller

The external cavity diode laser (ECDL) design employed at GSI and in this group, based on [28], consists of two parts: The laser diode, mounted in an aluminium frame containing a collimator, which is mounted in an external resonator also made of aluminium. The aluminum used for the external resonator is AlZn4.5Mg1, also called alloy 7200 [241]. It has a moderate thermal coefficient of expansion of $23.1\,\mu\mathrm{m}/(\mathrm{m\,K})$, which is one order of magnitude larger than that of Invar, but is significantly easier to machine.

In order to derive the required stability criteria the laser diode and the external resonator must both be considered. The influence of external parameters on the laser wavelength were discussed in the work of Preuschoff [176]. The temperature sensitivity of a typical near-infrared laser diode at $780\,\mathrm{nm}$ along with the external resonator used in this group were calculated to be

$$K_{T,diode} \approx -3\,\mathrm{GHz/K}$$
$$K_{T,resonator} \approx -9\,\mathrm{GHz/K}\,.$$

From these number it is clear that the resonator marks the lower bound. Going to a blue $441\,\mathrm{nm}$ laser this criterion is even more critical, because $K_{T,resonator}$ is proportional to the laser frequency and the frequency almost doubles, this leads to a sensitivity of the resonator on the order of

$$K_{T,resonator} \approx -16\,\mathrm{GHz/K}\,. \tag{3.4}$$

This implies that in order to match the stability of the laser current driver, the temperate stability should be far better than $1\,\mathrm{mK}$. A temperature stability of better than $100\,\mu\mathrm{K}$ has been demonstrated before [73, 92, 124, 126, 148, 190, 244], but all of these solution have in common that they use either multiple layers of shielding and control or elaborate baths into which the subject is submerged. The controller itself is then typically placed inside the controlled environment to shield it from external effects. This type of setup is not feasible in this situation as it would require a considerable redesign of the laser resonator. The laser resonators in use in this group [176] have been set up over the course of several years and there are dozens of them in use. This existing design must therefore be taken into consideration as well. The resonator in its current state does does not have an airtight seal. The sensitivity of the laser frequency to the barometric pressure can be estimated using the formula developed by Ciddor et al. [53] to be

$$K_{baro} = -75\,\mathrm{MHz/hPa}\,. \tag{3.5}$$

This leads to a frequency drift of several $100\,\mathrm{MHz}$ due to a pressure drift of around $\pm 10\,\mathrm{hPa}$ observed in the lab over a typical day. A long-term drift of $55\,\mathrm{hPa}$ over the year 2022 was also recorded by the monitoring software LabKraken. On shorter time scales the air pressure varies on the order of tens of Pa. This must be matched by the temperature controller. It is therefore sufficient to call for a stability of $<1\,\mathrm{mK}$ when using an unsealed resonator. To guarantee such a stability, the resolution of the driver should be at least $200\,\mu\mathrm{K}$, preferably $100\,\mu\mathrm{K}$.

The type of temperature transducer used in the laser design is a $10\,\mathrm{k}\Omega$ thermistor, so the design must work with this type of sensor, while the support of other sensors like a PT100 is optional.

Finally, a problem often encountered with analog proportional–integral–derivative (PID) controllers when temperature controlling large, well isolated bodies is the long time scales involved. One example found in the lab are high finesse cavities mounted in vacuum enclosures.

These extremely stable cavities are extensively used to reduce the linewidth of lasers to a few Hz. The time scales involved necessitate very long integration times T_i or a rather small gain of the integral term k_i of the PID controller. See section 3.5.3 for details on PID controllers and the terminology. An illustration of the problem encountered with an analog controller can be seen in figure 3.4. It shows the temperature of a Stable Laser Systems `VH 6020` cavity housing used for a high finesse Fabry-Pérot cavity which has a time constant of 4 to $7\,\mathrm{h}$ [230].

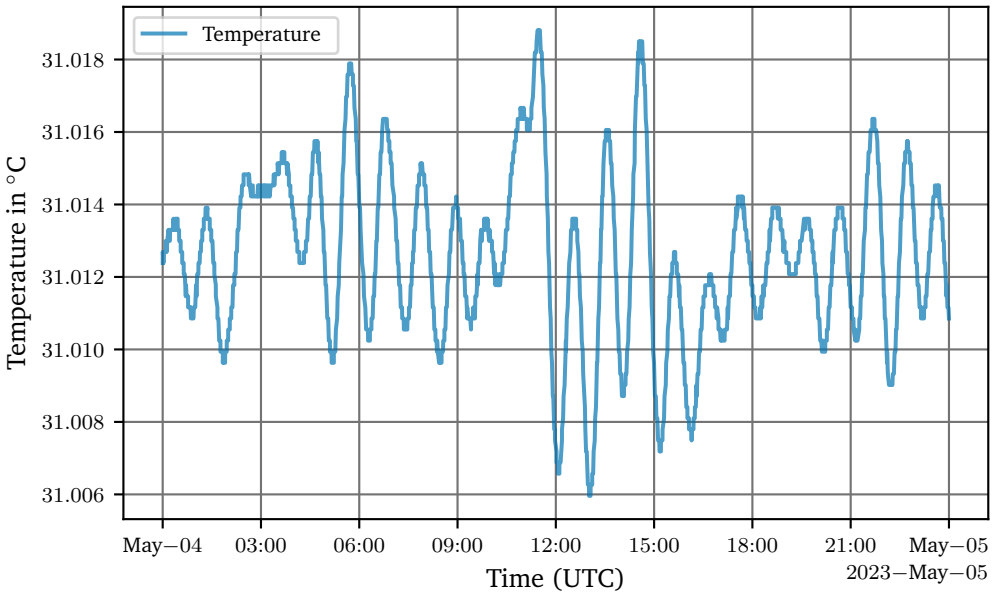

Figure 3.4.: Temperature of a Stable Laser Systems `VH 6020` controlled by a Team Wavelength `HTC1500` temperature controller.

The Team Wavelength `HTC1500` used in this example is an analog PID controller configured for the maximum specified integration time of $10\,\mathrm{s}$ using a $10\,\mu\mathrm{F}$ capacitor. As can be seen by the oscillatory behaviour, this time constant is far too short. Longer time scales can easily be reached by digital controllers which allow very long integration times limited only by the numerical resolution. A digital system can extend the scope of application from lasers to many other systems like those cavities to improve their stability. In addition, a digital system gives more control over the PID tuning parameters, also ensuring repeatability which greatly simplifies setting up new laser systems because a common set of PID parameters can be used a starting point before tuning the controller. Another benefit is the possibility to implement a modified algorithm and additional filters as detailed in section 3.5.3. This versatility to quickly adapt the programming again increases the number of applications. Integrating autotuning algorithms to help the user find a usable set of parameters reduces setup times of new systems. For all of those reasons, the new controller should be based on a digital design.

The final aspect to be considered is the output driver of the controller. The laser design used in this group uses two Peltier elements to cool both the resonator and the laser diode independently. The driver must therefore integrate two channels. While the biggest TECs currently in use are Laird `CP14,127,06,L1,W4.5` which can draw up to $6\,\mathrm{A}$ at $15.4\,\mathrm{V}$ [59] their optimal coefficient of power is between 1–$2\,\mathrm{A}$ and 5–$8\,\mathrm{V}$. Having a driver that can output $4\,\mathrm{A}$ at $12\,\mathrm{V}$ is considered more than sufficient, even for larger TECs and future projects.

Commercial temperature controllers specifying a stability of better than $1\,\mathrm{mK}$ are hard to

come by, especially with multiple channels. Two units were tested for this laser setup. The Vescent `SLICE-QTC` and an ILX Lightwave `LDT-5948`. The latter is specified for a stability of 5 mK, but their application note claims a better performance [192].

The requirements for the temperature controller can be summarised as:

Design requirements 3.4: Temperature controller

- Stability: <1 mK
- Resolution: <200 µK, <100 µK preferred
- Temperature sensor: $10\,\mathrm{k}\Omega$ thermistor
- Two or more channels
- Output power: 4 A at 12 V
- Digital interface to work with long time scales and reproducible PID parameters

3.4. LabKraken

3.4.1. Design Goals

LabKraken is designed to be an asynchronous, resilient data acquisition suite that scales to thousands of sensors and across different networks to serve the need for monitoring and automation required for large scale experiments spanning multiple sites. It is written in Python and supports many sensors and instruments found in a scientific environment. Such sensors include Standard Commands for Programmable Instruments (SCPI) capable devices accessible via Ethernet or GPIB or sensors using a serial protocol. Many other Ethernet capable devices are also supported via a simple driver interface.

3.4.2. Software Architecture

To meet the increasing demand for high quality data, LabKraken needs to scale to thousands of sensors which must to be served concurrently. This problem is commonly referred to as the C10K problem as dubbed by Kegel back in 1999 [113] and refers to handling $10\,000$ concurrent connections via network sockets. While today millions of concurrent connections can be handled by servers, handling $10\,000$ can still be challenging, especially if the data sources are heterogeneous as is typical for sensor networks of diverse sensors from different manufacturers.

In order to meet the design goals, an asynchronous architecture was chosen and several different approaches were implemented over time. All in all, four complete rewrites of the software were made to arrive at the architecture introduced here. The reason for the rewrites is mostly historical and can be explained by the development of the Python programming language which was used to write the code. The first version was written using Python 2.6 and exclusively supported sensors made by Tinkerforge. With the release of Python 3.5 which supported a new syntax for asynchronous coroutines, the software was rewritten from scratch to support this new syntax, because it made the code a lot more verbose and easier to follow. When Python 3.7 was released asynchronous generator expressions where mature enough to be used in productions and the program was again rewritten to use the new syntax. In 2021 a new approach was taken and the program was once more rewritten with a functional programming style. Some of those approaches will be discussed in the next sections to highlight limits of the programming style used and the improvements made to overcome them. This development underlines important steps in the progress of asynchronous programming made by the Python language in recent years that can be applied to many other problems, for example process control. Specifically so since Python is a very popular language among scientists and used in many experiments. Each of the following sections discusses the same program, but written in different programming styles to show the differences. Especially the last example presenting a function programming style is interesting for experimental control as it gives a clean representation of the data flow from the producer to the consumer [71].

The example program that will be discussed does the following job. It opens a network connection to a remote (Tinkerforge) sensor platform, then queries the other side for its sensors. When the sensors are returned it looks for a specific sensor, then starts reading data from that sensor to finally print it. The example itself is designed around the Tinkerforge sensors to present a working example instead of the typically used pseudocode. It does represent a common program flow in a sensor application though and the concept is not limited to the Tinkerforge programming API.

Threaded Design

The first version of LabKraken used a threaded design approach, because the original libraries of the Tinkerforge sensors are built around threads. Most threaded programs make extensive use of callbacks. These are functions that are passed from the main thread to the worker, typically on creation, and are then called by the worker to inform the main thread of its activity. The downside is that main thread has no knowledge about the caller, the callback might have even been passed on by the worker to another thread.

```
1  ipcon = IPConnection()
2
3
4  def cb_temperature(temperature: int) -> None:
5      """Read the temperature data from the device and print it."""
6      print(f"Temperature: {temperature/100.0} °C")
7
8
9  def cb_connected(connect_reason: int) -> None:
10     """Query for sensors as soon as the connection is established."""
11     ipcon.enumerate()
12
13
14 def cb_enumerate(uid: str, *_args) -> None:
15     """Search for OUR_KNOWN_DEVICE and, when found, read from it."""
16     if uid == OUR_KNOWN_DEVICE:
17         device = BrickletTemperatureV2(uid, ipcon)
18         # Register temperature callback as function cb_temperature
19         device.register_callback(device.CALLBACK_TEMPERATURE, cb_temperature)
20         device.set_temperature_callback_configuration(1000, False, "x", 0, 0)
21
22
23 # Connect to the sensor host
24 ipcon.connect(HOST, PORT)
25 # Register connection and enumeration callbacks
26 ipcon.register_callback(IPConnection.CALLBACK_ENUMERATE, cb_enumerate)
27 ipcon.register_callback(IPConnection.CALLBACK_CONNECTED, cb_connected)
28
29 input("Press key to exit\n")
30 ipcon.disconnect()
```

The program starts at line 24 by making a connection to the host, then the first callback functions are registered with the connection object. These callbacks allow the connection thread to signal the program when the connection has been established (*cb_connected*) and when new sensors are found (*cb_enumerate*). The main program is now finished and it waits until terminated by the user. All the work is done inside the thread and the program flow unfortunately looses itself in the callbacks which get called by the connection object and their order can only be guessed from the documentation as the main program has no control over it. As the program continues it first enters the *cb_connected* callback where it will query the host for its sensors in line 9. The answer will be returned through the *cb_enumerate* callback. This function filters the sensor id for a known sensor and then attaches another callback for the sensor to return data. It then configures the sensor. This program flow is typical for a callback driven design and the reader may imagine how more complex tasks are implemented. As the program grows, more and more layers of callbacks will be added and in the end, the code will be impossible to read without intimate knowledge. The effort of maintaining the callback driven code resulted in the decision to redesign the program when moving to Python 3.

To untangle this problem, Python 3.7 introduced so-called generators. This is a type of expression that will produce values from an iterator. An iterator is an (infinite) ordered series of values or events which can be processed by requesting the next value until the series is exhausted, if it is finite. The main advantage is that the logic of the program stays within the main part and only the data gathering is done outside of this scope. A generator based program is shown next.

Generator Design

In addition to a different coding style the code base is moved from a multithreaded to a asynchronous approach using Python asyncio. The difference is that asyncio uses a single thread as opposed to multithreaded code. Multiple threads can run concurrently on multiple processor cores, so different cores can process data at the same time. Asynchronous programs must pause the execution of code paths because they run within a single thread on a single core. This type of programming works best when the tasks are not computationally intensive but input/output bound by external peripherals like a network. While the processor is waiting for the slower network it can work on other tasks. The advantage is that access to shared resources is greatly simplified as these resources will never be accessed at the same time. The code is shown below.

```
async def process_device(device: BrickletTemperatureV2) -> None:
    """Prints the callbacks (filtered by id) of the bricklet."""
    async for temperature in device.read_temperature():
        print(f"Temperature: {temperature} °C")


async def shutdown(tasks: dict[asyncio.Task]) -> None:
    """Clean up by stopping all consumers"""
    for task in tasks:
        task.cancel()
    await asyncio.gather(*tasks)


async def main() -> None:
    """Enumerate the connection, then create workers for each device known."""
    try:
        async with IPConnectionAsync(HOST, PORT) as connection:
            await connection.enumerate()
            async for enum_type, device in connection.read_enumeration():
                if device.uid == OUR_DEVICE:
                    asyncio.create_task(process_device(device))
    finally:
        await shutdown(tasks)


asyncio.run(main())
```

The first impression that can be gather from the new design is that the code has become more concise. To understand it, a few Python language keywords used must be introduced. In order to yield control to the next task, the keyword *await* is used which is put in front of a function call. This will pause the current execution and wait until the function has returned with a result. Another important language feature used is a so-called context. A context is created using the *async with* command and it makes sure that after leaving the context certain commands are executed. This can be used to clean up after the the creation and use of certain

objects like the Ethernet connection. The connection context will make sure that the Ethernet connection will be properly terminated no matter whether enclosed content was shut down gracefully or not. The iterator uses the *async for* keyword and works asynchronously as well. It pauses the code until a new event can be produced.

The code starts at line 26 and runs the *main()* function. This function first connects to the host by creating a context in line 15 where the *connection* variable is usable. Using this connection the sensor platform is queried in line 16. In comparison to the precious example it is now far easier to follow the program flow because the context and generator reveal what is happening next. Unfortunately, reading the sensor still requires passing it to a new task because the generator will keep generating more sensors in the meantime. Although the code is split into multiple tasks, the nesting of callbacks as in the previous example is resolved and the readability of the code has improved tremendously.

The only problem is the error handling, because these worker tasks do not communicate with the original task that created them. This can be solved using the so-called observer pattern where an observer tasks watches the workers and handles such event. Directly implementing this pattern creates a myriad of events and event handler registrations. Missing one such event can break the whole program and leads to bugs that are hard diagnose and fix. To simplify this pattern a stream based approach can be applied. The observable is treated as a stream of events which is being processed by the observer using a chain of operators and actions executed in a certain order. This is much like an assembly line where different tasks are executed as the product passes each station.

Stream Design

The previously mentioned observer pattern is often implemented using data streams representing the subjects observed while the consumers are the observers. Using functional programming style these data streams can be written in a very concise form as shown in the following version of the example program.

```
async def main() -> None:
    """Define a stream, then execute it."""
    async with IPConnectionAsync(HOST, PORT) as connection:
        connection.enumerate()
        reader = (
            stream.iterate(connection.read_enumeration())  # read devices
            | pipe.filter(lambda device: device.uid == OUR_DEVICE)  # keep our
                                                                    device
            | pipe.switchmap(lambda device: device.read_temperature())  # read
                                                                        data
            | pipe.print("Temperature: {} °C")  # Print results
        )
        await reader  # start the stream


asyncio.run(main())
```

The program starts in line 14 and enters the *main()* function. Here, a context is used again to open the connection to the sensor platform. The sensors are queried next and a stream is created to read the reply, then filter for the specified sensor which is then read and the result is printed.

Using this programming style the intent of the program is revealed immediately, even before starting the stream. The syntax uses was borrowed from the Python library *aiostreams* [159],

which is similar to ReactiveX [160], a library developed by Microsoft to operate on data streams. The interesting aspect of this code is the use of the pipe operator which inject the result of one function into the next function as its parameters. This way a chain of function calls is created. The *lambda* keyword denotes a small anonymous function, but regular functions can also be used. In combination with an operator like *filter*, *switchmap*, or *print*, they dictate the program flow, hence the name functional programming. These operators need some introduction though. The *filter* operator is simple to understand as it will only pass on the input when the function, to which the input is passed as well, returns true. The *switchmap* operator is more interesting. It is a combination of a map operator and a switch operator. The former applies a function to the input and then passes on the output of the function, in this case *read_temperature* which creates an iterator. The latter operator will take its most recent input and iterate, producing temperature values. This operator will terminate the iteration when a new input is passed and then iterate the new input. This is handy as it automatically makes sure that there is only one reader per sensor and for example new sensor configurations can be injected into the data stream above the *switchmap* which automatically replace the old sensor reader.

This style of programming was found to be ideal for real-time data processing, as it allows to continuously update configurations or add and remove sensors, or even hosts, without having to worry about what happens along the pipeline.

Device Identifiers

Every sensor network needs device identifiers. Preferably those identifiers should be unique. Typically a device has some kind of internal identifier. Here are a few examples of the sensors used in the authors network:

Device Type	Identifiers	Example
GPIB (SCPI)	**IDN?*	Keysight Technologies,34470A,MYXXXXXXXX,A.03.03-02.40-03.03-00.52-02-01 or Agilent Technologies,34410A,MYXXXXXXXX,A.03.03-02.40-03.03-00.52-02-01
Tinkerforge	A base58 encoded integer device id	QE9 (163684)
LabNode	UUID	cc2f2159-e2fb-4ed9-8021-7771890b37ad

Table 3.3.: Device identifiers used by common devices found in the lab. The serial number of the Keysight `34470A` DMM was obscured on purpose.

As it can be seen in table 3.3, most of these identifiers do not guarantee to uniquely identify a device within a network. The Tinkerforge id is the weakest, as it is a 32 bit integer ($4\,294\,967\,295$ options), which might easily collide with another id from a different manufacturer. For better readability the id is typically presented as a base58 encoded string. An encoder/decoder example can be found in the TinkerforgeAsync library [33].

The id string returned by a SCPI device is slightly more useful, but again does not guarantee uniqueness. As per the SCPI specification it returns a string containing *$manufacturer,$name,$serial,$revision*. Even when ignoring the software revision part which might change on update, the same device might return a different id depending on its settings. The id string shown in table 3.3 relate to the same device, but the latter uses a compatibility flag in the settings.

The only reasonably unique id is used by the LabNodes. The universal unique identifier (UUID) or globally unique identifier (GUID), as dubbed by Microsoft, can be used for networks

with participant numbers going into the millions. There are several versions defined in RFC 4122 [125] and the LabNodes use version 4, which is a random 128 bit identifier with 122 bit of entropy. Of the remaining 6 bit, 4 bit are reserved for the UUID version and 2 bit for the variant. This allows to prove the usefulness as a unique id as below.

Calculating the chance of a collision between two random UUIDs is called the birthday problem [236] in probability theory. The probability of at least one collision in n devices out of $M = 2^{122}$ possibilities can be calculated as follows:

$$\begin{aligned} p(n) &= 1 - 1 \cdot \left(1 - \frac{1}{M}\right) \cdot \left(1 - \frac{2}{M}\right) \dots \left(1 - \frac{n-1}{M}\right) \\ &= 1 - \prod_{k=1}^{n-1} \left(1 - \frac{k}{M}\right) \end{aligned} \tag{3.6}$$

Using the Taylor series $e^x = 1 + x \dots$, assuming $n \ll M$ and approximating we can simplify this to:

$$\begin{aligned} p(n) &\approx 1 - \left(e^{\frac{-1}{M}} \cdot e^{\frac{-2}{M}} \dots e^{\frac{-(n-1)}{M}}\right) \\ &\approx 1 - \left(e^{\frac{-n(n-1)/2}{M}}\right) \\ &\approx 1 - \left(1 - \frac{n^2}{2M}\right) = \frac{n^2}{2M} \end{aligned} \tag{3.7}$$

For one million devices using random UUIDs, this gives a probability of about 2×10^{-25}, which is negligible.

In the LabKraken implementation, all devices, except for the LabNodes which already have a UUID, will be mapped to UUIDs using the underlying configuration database. It is up to the user to ensure the uniqueness of the non-UUID ids reported by the devices to ensure proper mapping. These UUIDs can then be used to address and configure each device on the sensor network.

3.5. Short Introduction to Control Theory

This section will give a very brief introduction to some basic concepts of control theory. Many systems require control over one or more process variables. For example, temperature control of a room or a device, or even creating a programmable current from a voltage is one such problem. All of this requires control over a process and is established through feedback, which allows a controller to be aware of the state of the system.

The focus of this section is narrowed down to the concept of feedback and control with regard to developing and understanding PID controllers for temperature control. Simpler feedback loops like those typically used around op-amps will not be primarily considered in this section and are discussed in the relevant part of the documentation. In the following sections, first general properties of the Laplace transform and useful relationships are introduced, then, a model for the system and its controller will be developed, finally, using the model, tuning of the control parameters using different tuning algorithms will be discussed.

3.5.1. Introduction to the Transfer Function and the Laplace Domain

There are two types of control systems: open- and closed-loop systems. A system is called open loop, if the output of a system does not feed back to its input as in figure 3.5 (a). On the other hand, if the output influences the input of the system via feedback, it is called a closed-loop system, as shown in figure 3.5 (b). Although feedback can be treated in static systems, it is more useful to treat it in dynamic systems, either in the time-domain or the frequency-domain. To discuss these systems, the terminology used in the following section needs to be defined. $G(s)$ is called the transfer function of the system, while $U(s)$ is the input, $Y(s)$ is the output, s is a complex frequency domain variable, β is the feedback parameter, also called feedback fraction, as shown in figure 3.5 (b). In this section, upper case letters are used to denote functions in the Laplace domain, while lower case letters are referring to functions in the time domain. Normally, the transfer function is denoted $H(s)$ but to prevent confusion with the Heaviside function $H(t)$, the letter G is used here for the transfer function. In later chapters the common form $H(s)$ is used.

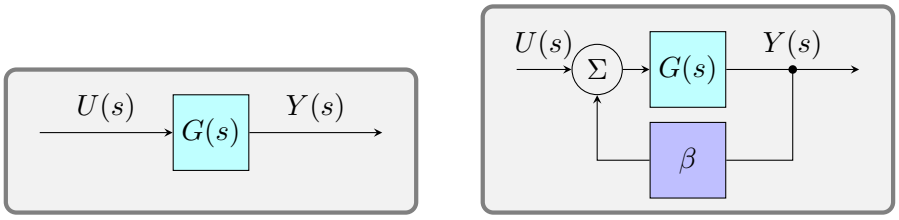

(a) Open-loop system. (b) Closed-loop system.

Figure 3.5.: Block diagram of a closed- and an open-loop control system.

It is convenient to express the transfer function in its Laplace transform for several reasons that will be explained below. The systems to be discussed are physical system and hence are causal. That means the output only depends on past and present inputs, but not future inputs. For this reason, only the one-sided or unilateral Laplace transform needs to be considered. It is defined as:

$$\mathscr{L}\left(f(t)\right) = F(s) = \int_0^\infty f(t)e^{-st}\,dt. \tag{3.8}$$

with $f : \mathbb{R}^+ \to \mathbb{R}$ that is integrable and grows no faster than $c \cdot e^{s_0 t}$ for $s_0, c \in \mathbb{R}$. The latter attribute is important for deriving the rules of differentiation and integration.

To understand the benefits of using the Laplace representation of the transfer function, a few useful properties should be discussed with regard to the PID controller. First of all, the Laplace transform is linear:

$$\begin{aligned}\mathscr{L}\left(a \cdot f(t) + b \cdot g(t)\right) &= \int_0^\infty (a \cdot f(t) + b \cdot g(t)) e^{-st}\, dt \\ &= a \int_0^\infty f(t) e^{-st}\, dt + b \int_0^\infty g(t) e^{-st}\, dt \\ &= a\mathscr{L}\left(f(t)\right) + b\mathscr{L}\left(g(t)\right)\end{aligned} \tag{3.9}$$

Another interesting property is the derivative and integral of a function f. The function f must, of course, be differentiable and grow no faster than the exponential function as defined above:

$$\begin{aligned}\mathscr{L}\left(\frac{df}{dt}\right) &= \int_0^\infty \underbrace{f'(t)}_{v'(t)} \underbrace{e^{-st}}_{u(t)}\, dt \\ &= \left[e^{-st} f(t)\right]_0^\infty - \int_0^\infty (-s) f'(t)\, dt \\ &= -f(0) + s \int_0^\infty f'(t)\, dt \\ &= sF(s) - f(0)\end{aligned} \tag{3.10}$$

$$\begin{aligned}\mathscr{L}\left(\int_0^t f(\tau)\, d\tau\right) &= \int_0^\infty \left(\int_0^t f(\tau)\, d\tau e^{-st}\right) dt \\ &= \int_0^\infty \underbrace{e^{-st}}_{v'(t)} \underbrace{\int_0^t f(t)\, d\tau}_{u(t)}\, dt \\ &= \left[\frac{-1}{s} e^{-st} \int_0^t f(t)\, d\tau\right]_0^\infty - \int_0^\infty \frac{-1}{s} e^{-s\tau} f(\tau)\, d\tau \\ &= 0 + \frac{1}{s} \int_0^\infty e^{-s\tau} f(\tau)\, d\tau \\ &= \frac{1}{s} F(s)\end{aligned} \tag{3.11}$$

If the initial state $f(0)$ can be chosen to be 0, the differentiation becomes a simple multiplication by s, while the integration becomes a division by s. These three properties greatly simplify the calculations required for studying a proportional–integral–derivative controller in section 3.5.3.

Finally, the most important aspect is the possibility to give a simple relation between the input $u(t)$ and the output $y(t)$ of a system. This relationship between input and output of a system as shown in figure 3.5 (a) is given by the convolution, see e.g. [26]. Assuming the system has an initial state of 0 for $t < 0$, hence $u(t < 0) = 0$ and $g(t < 0) = 0$, one can calculate:

$$y(t) = (u * g)(t) = \int_0^\infty u(\tau) g(t - \tau)\, d\tau \tag{3.12}$$

Applying the Laplace transform, greatly simplifies this:

$$\begin{aligned} Y(s) &= \int_0^\infty e^{-st} y(t)\,dt \\ &\overset{3.12}{=} \int_0^\infty \underbrace{e^{-st}}_{e^{-s(t-\tau)}e^{-s\tau}} \int_0^\infty u(\tau) g(t-\tau)\,d\tau\,dt \\ &= \int_0^\infty \int_0^t e^{-s(t-\tau)} e^{-s\tau} g(t-\tau) u(\tau)\,d\tau\,dt \\ &= \int_0^\infty e^{-s\tau} u(\tau)\,d\tau \int_0^\infty e^{-st} g(t)\,dt \\ &= U(s) \cdot G(s) \end{aligned} \tag{3.13}$$

This formula is a lot simpler than the convolution of $u(t)$ and $g(t)$, therefore the use of the Laplace transform has become very popular in control theory.

Having derived some of the most useful properties, it is interesting to look at a few functions, which are heavily used in control theory, like a function delayed by the time interval θ. To demonstrate its properties, let $f(t-\theta)$ be

$$g(t) := \begin{cases} f(t-\theta), & t \geq \theta \\ 0, & t < \theta \end{cases}. \tag{3.14}$$

The reason for this definition is that it is mandatory for the system to be causal. This means, it is impossible to get information from the future ($t < \theta$). To satisfy this requirement, any constant other than 0 may be chosen, as is done later in section 3.5.4, when determining tuning parameters and fitting experimental data to a model. An example of such a time delayed function $g(t)$ is shown in figure 3.6 (b).

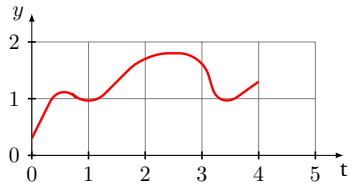

(a) Original signal $f(t)$.

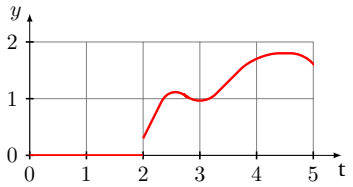

(b) Delayed signal $f(t-2)$.

The Laplace transform of a delayed signal $g(t)$ can be calculated as follows:

$$\begin{aligned} \mathscr{L}\left(g(t)\right) &= \int_0^\infty g(t) e^{-st}\,dt \\ &\overset{3.14}{=} \int_\theta^\infty f(t-\theta) e^{-st}\,dt \\ &\overset{\tau := t-\theta}{=} \int_0^\infty f(\tau) e^{-s(\tau+\theta)}\,d\tau \\ &= e^{-s\theta} \int_0^\infty f(\tau) e^{-s\tau}\,d\tau \\ &= e^{-s\theta} F(s) \end{aligned} \tag{3.15}$$

To satisfy the causality requirement in the time domain, the Heaviside function $H(t)$ can be used to give a more concise representation of $g(t)$:

$$\mathscr{L}\left(f(t-\theta)H(t-\theta)\right) = e^{-s\theta} F(s) \tag{3.16}$$

Lastly, the Laplace transform of e^{at} is given, which is commonly used in differential equations:

$$\mathscr{L}\left(e^{at}\right) = \int_0^\infty e^{(a-s)t}\,dt = \frac{1}{a-s}\left[e^{(a-s)t}\right]_0^\infty = \frac{1}{s-a} \tag{3.17}$$

Using these tools, it is possible calculate the transfer function of a closed-loop temperature controller, which will be done in the next section.

3.5.2. A Model for Temperature Control

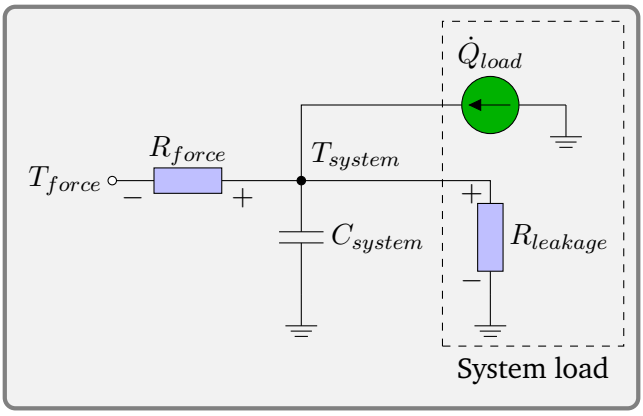

Figure 3.7.: Simple temperature model of a generic system.

In order to describe a closed-loop system using a transfer function $G(s)$, one has to first create a model for the process and the controller involved. This section will derive the simple, but very useful first order model with dead-time. This model can be derived from the idea that the system at temperature T_{system} has a thermal capacitance C_{system}, an influx of heat $\dot{Q}_{load}$ from a thermal load and a controller removing heat from the system through a heat exchanger with a resistance of R_{force}. Additionally, there is some leakage through the walls of the system to the ambient environment via $R_{leakage}$. This analogy of thermodynamics with electrodynamics allows to create the model shown in figure 3.7. Since this model is to be used for a temperature controller, more simplifications can be made and a so-called small-signal model can be developed as opposed to the large-signal model shown above. The small-signal model is an approximation around a working point that is valid for small deviations around it, similar to a Taylor approximation. The small-signal model can be used to calculate the system response to small changes of the controller output in order to estimate the control parameters at that working point.

Using the small-signal approach, the system response can be split into a constant and a dynamic part: the 0^{th} and 1^{st} order of the Taylor approximation. In order to simplify the system shown in figure 3.7, the assumption can be made that the system load $\dot{Q}_{load}$ and the flux through $R_{leakage}$ is *reasonably stable*. *Reasonably stable* means that it can be treated as small deviations and additionally any changes are within the bandwidth of the controller and well suppressed. This allows to treat them as (almost) constant effects. Constant effect can be neglected in the small-signal model because they only manifest as a constant offset applied to the output of the controller and have no dynamics. This leaves only the room with its heat capacity and the heat exchanger as dominant factors in the small-signal model shown in figure

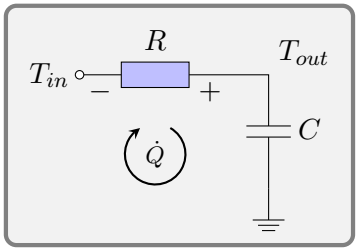

Figure 3.8.: Simplifications of the temperature model of a room lead to this first order model.

3.8. Here T_{force} and T_{system} were replaced by T_{in} and T_{out}, R_{force} and C_{system} were replaced by R and C for better readability.

This is the classic RC circuit. To calculate the transfer function, a relationship between T_{in} and T_{out} is required and exploiting the analogy of thermodynamics and electrodynamics again, using Kirchhoff's second law, following the arrow in figure 3.8 one finds:

$$\sum T_i = 0$$
$$T_{in}(t) - \dot{Q}(t)R - \frac{1}{C}\int \dot{Q}(t)\,dt = 0 \tag{3.18}$$

Taking the Laplace transform, applying equation 3.11, solving for $\dot{Q}(s)$ and using $T_{out} = \frac{1}{sC}\dot{Q}(s)$ to replace $\dot{Q}$, equation 3.18 can be written as:

$$T_{in}(s) - \dot{Q}(s)R - \frac{1}{sC}\dot{Q}(s) = 0$$
$$\dot{Q}(s) = \frac{T_{in}(s)}{R - \frac{1}{sC}} = \frac{T_{out}}{\frac{1}{sC}}$$

This allows to calculate the transfer function of the process P as

$$\begin{aligned} P(s) = \frac{T_{out}}{T_{in}} &= \frac{\frac{1}{sC}}{R - \frac{1}{sC}} \\ &= \frac{1}{sRC + 1} \\ &= \frac{1}{1 + s\tau} = \frac{K}{1 + s\tau}\,. \end{aligned} \tag{3.19}$$

with the system gain K and the time constant τ. In case of the RC circuit, the gain is 1, but other systems may have a gain factor of $K \neq 1$. This is generally the case when using any type of sensor that converts the measurand into the input signal. K is therefore included here for the sake of generality.

Equation 3.19 is called the transfer function of a first order model, because its origin is a differential equation of first order. This model describes homogeneous systems like a room very well, as can be seen in section 4.3.3, but in order to derive the transfer function including the controller and the sensor some more work is required to derive the sensor transfer function.

Expanding on figure 3.5 (a) and equation 3.12 the open-loop transfer function of the process and its sensor becomes:

$$G(s) = P(s) \cdot S(s) \tag{3.20}$$

and the block diagram changes to

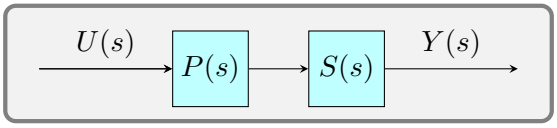

Figure 3.9.: Open-loop system with sensor.

The transfer function of the sensor, given an ideal linear transducer, can be modeled as a delay line with delay θ and $f(t-\theta) = H(t-\theta)$. A sensor gain of 1 is assumed here, because any system gain is assumed be included in the parameter K of the process transfer funciton. Using equation 3.15, $S(s)$ can be written as

$$S(s) = e^{-\theta s}. \tag{3.21}$$

The full system model including the time delay can now be written as:

$$G(s) = \frac{K}{1+s\tau} e^{-\theta s} \tag{3.22}$$

This is called a first order plus dead-time model (FOPDT) or first order plus time-delay model (FOPTD). While the Laplace representation is useful to mathematically explore the mode, in order to fit experimental data to this model it is more convenient to transform the transfer function 3.22 into the time domain. To have a meaningful result, an input $U(s)$ is required, because $G(s)$ is only a transformation. In principal, any function can serve this purpose, but a step function is typically used, for example by Ziegler et al. [253] and many others [26, 154, 173, 207, 208, 209, 235]. The step function is both simple to calculate and to apply to a real system in form of a controller output change. This technique is also explored in more detail in section 4.3.3. Using equations 3.15 and 3.17, the Heaviside $H(t)$ step function transforms into

$$\mathscr{L}\left(u(t)\right) = U(s) = \mathscr{L}\left(\Delta u H(t)\right) = \frac{\Delta u}{s} \tag{3.23}$$

with the step size Δu. The output response $Y(s)$ of the system to the step can then be calculated analytically.

$$\begin{aligned} Y(s) &= U(s) \cdot G(s) \\ &= \frac{\Delta u}{s} \frac{K}{1+s\tau} e^{-\theta s} \\ &= K\Delta u \frac{1}{s(1+s\tau)} e^{-\theta s} \\ &= K\Delta u \left(\frac{1}{s} - \frac{\tau}{s\tau+1} \right) e^{-\theta s} \\ &= K\Delta u \left(\frac{1}{s} - \frac{1}{s+\frac{1}{\tau}} \right) e^{-\theta s} \end{aligned} \tag{3.24}$$

To derive $y(t)$, the inverse Laplace transform of $Y(s)$ is required. Unfortunately, this is not as simple as the Laplace transform. Fortunately though the required equations were already derived in equations 3.11 and 3.17. Making sure causality is guaranteed as shown in equation

3.16, the simple first order model can be transformed back into the time domain.

$$\begin{aligned} y(t) &= \mathscr{L}^{-1}\left(Y(s)\right) \\ &= K\Delta u\mathscr{L}^{-1}\left(\frac{1}{s}e^{-\theta s}\right) - K\mathscr{L}^{-1}\left(\frac{1}{s+\frac{1}{\tau}}e^{-\theta s}\right) \\ &\overset{3.17}{=} K\Delta u \cdot 1 \cdot H(t-\theta) - \left(e^{-\frac{t-\theta}{\tau}}\right)H(t-\theta) \\ &= K\Delta u\left(1-e^{-\frac{t-\theta}{\tau}}\right)H(t-\theta) \end{aligned} \tag{3.25}$$

The time domain solution of the FOPDT model can now be used to extract the parameters τ, θ and K from a real physical system.

The procedure can be summarised from the above as follows. The controller must be set to a constant output and the room must be given time to reach equilibrium. Once the temperature has settled, an output step of Δu is applied. The system will respond after a time delay and then follow an exponential function. A simulation of the step response applied to a first order model with time delay is shown in figure 3.10. The gain is $K = 1$. The solid black line shows the response of the transfer function, including the system and the sensor. The dashed lines show the individual components, the Heaviside function governing the delay and the exponential term of the system. The controller output step $\Delta u = 1$ is applied at $t = 0$ and not shown explicitly. From figure 3.10 it can be clearly seen that the sensor does not register a change until the time delay θ has passed and the Heaviside function changes from 0 to 1. Then the system responds with an exponential decay towards 1.

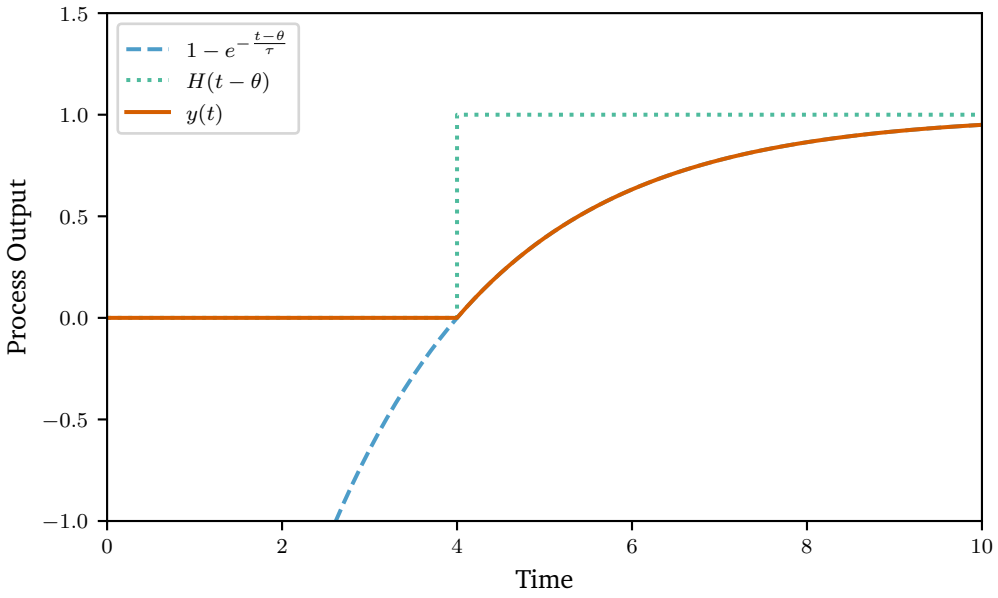

Figure 3.10.: Time domain plot of a first order plus dead time model showing individual components of the model and the composite function $y(t)$. Model parameters used: $K = \Delta u = 1, \tau = 2, \theta = 4$.

So far, only open-loop systems were discussed. Using the FOPDT model, the system parameters can now be extracted from an existing system using a fit to the time domain reaction

of such a system to a step input. Having extracted the system parameters, the next step is to design a controller around the system and close the loop to realize a controlled system. This is shown in the next section.

3.5.3. PID Controller Basics

While there are many different types of controllers, like the bang–bang controller utilized in many temperature controller, which turns on at a certain threshold and turns off at another one, producing the saw-tooth shaped room temperature curve shown in figure 3.3, a continuous control system is desired to keep fluctuations to a minimum. The most commonly used controller type for non-integrating systems is the proportional–integral–derivative (PID) controller [69]. A non-integrating system is a system without memory whose steady state does not depend on previous inputs. The advantage of applying a PID controller is that the controller does not need any special knowledge about the system model. A universal PID is simple to implement and can be tuned to control a wide range of different systems. While there are many variations of the PID algorithm [195], this section only introduces the basic, parallel, PID controller commonly used in digital implementation and deals with some of the shortcomings in practical applications.

In order to extend the FOPDT system derived in the previous section 3.5.2, with the PID controller one has to move to a closed-loop system. Adding to figure 3.5 (b) and inserting a new control block into the transfer function yields figure 3.11.

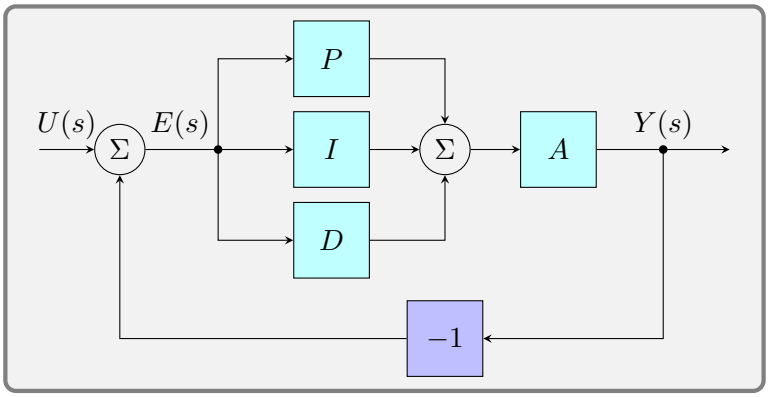

Figure 3.11.: Closed-loop system with a PID controller.

The error signal $E(s)$ used by the PID controller is the difference between the setpoint and the control parameter, in this case the room temperature. The transfer function of the PID controller can be split into three parts. A proportional part that is proportional to the error representing the present state, an integral part that is proportional to the accumulated error, representing the past state, and a derivative part that is proportional to the change in the error, extrapolating into the future. Analytically, it can be written as

$$c(t) = k_p e(t) + k_i \int_0^t e(\tau)\, d\tau + k_d \frac{\mathrm{d}e(t)}{\mathrm{d}t} \tag{3.26}$$

$$C(s) = k_p + k_i \frac{1}{s} + k_d s\,. \tag{3.27}$$

The following discussion will mostly focus on equation 3.26, because, the time-domain equation is the one that can be implemented in software. As hinted above, there are a few

shortcomings with the classic PID equation, when used in a real system which requires dynamic changes of the the setpoint or k_i.

The first problem that needs addressing is occurring when changing the PID parameter k_i, because equation 3.26 is given for a time-independent k_i. Assuming a settled system without external disturbances, the output is fully determined by the integrator value because the error is zero. Now, when k_i is changed, the output immediately changes, due to the change of the integral term. This is unintended. To fix it, the integral term must be changed to

$$k_i \int_0^t e(\tau)\,d\tau \Rightarrow \int_0^t k_i(\tau)e(\tau)\,d\tau\,. \tag{3.28}$$

This way, when adjusting k_i, its new value is applied to future error values only and there is no sudden kick.

The next issue is called derivative kick. When looking at the derivative part of equation 3.26, it can be seen that when instantly changing the setpoint, as in a step function, $\frac{\mathrm{d}e(t)}{\mathrm{d}t} \to \infty$. This behaviour is not intended and to fix this, the derivative part can be modified as follows.

$$\begin{aligned}\frac{\mathrm{d}e(t)}{\mathrm{d}t} &= \frac{\mathrm{d}\left(u(t)-y(t)\right)}{\mathrm{d}t} = \underbrace{\frac{\mathrm{d}u(t)}{\mathrm{d}t}}_{\to\infty} - \frac{\mathrm{d}y(t)}{\mathrm{d}t} \\ &= -\frac{\mathrm{d}y(t)}{\mathrm{d}t}\end{aligned} \tag{3.29}$$

The new derivative term is equal to the unmodified one, except in the case of setpoint changes. Removing the setpoint from the equation, the controller behaves as intended. This solution is sometimes called *derivative on measurement* as opposed to *derivative on error*.

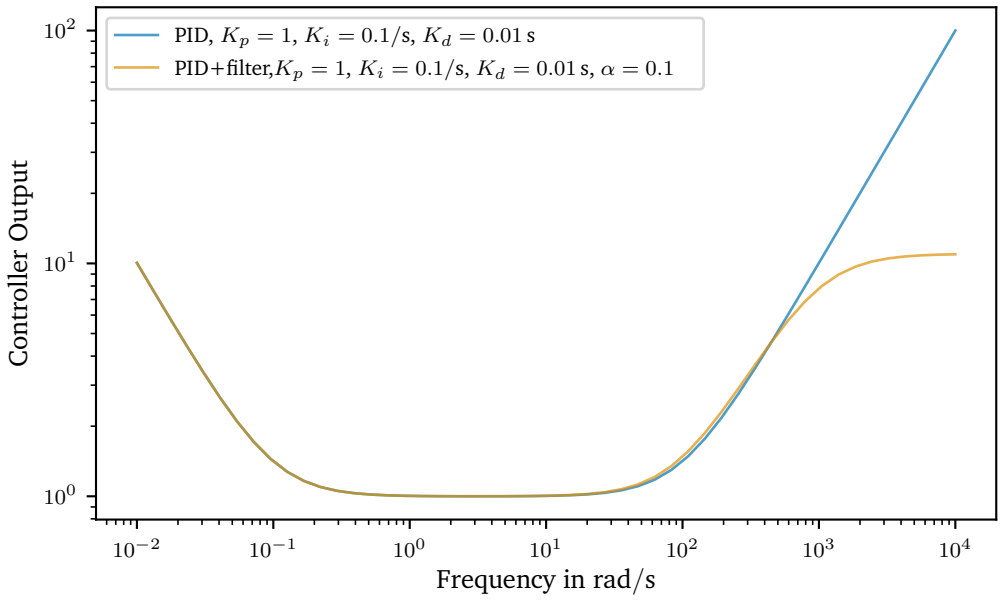

Figure 3.12.: Magnitude plot over frequency of the PID controller transfer function. Both the ideal PID controller and the PID controller with a filtered derivative are shown.

Another issue is caused by the derivative term with noisy inputs. Assuming there is a very short input spike due to noise, the differential of the derivative term will again be sent to very

high values, pushing the output away from the correct value and forcing the controller to slowly rebalance.

To further discuss the problem and its solution it is best to visit the frequency domain and visualize the transfer function of the PID controller as shown in figure 3.12. The ideal PID controller without filtering of the derivative displays a very strong response to low frequency inputs. This is due to the integral action, which removes any (constant) offset. It needs to have infinite gain at DC to push the offset to zero. In reality this is limited by input noise. Then follows a plateau with a magnitude of k_p for the proportional term and finally the differential gain starts growing in magnitude and keeps steadily growing with rising frequency, just as expected.

With some knowledge about the process or the sensor it is possible to define an upper frequency, above which inputs become unrealistic and must therefore be unwanted noise. By filtering the derivative term with a first order filter causes it to roll off and its gain becomes constant as shown in figure 3.12. By adding the filter the PID controller transfer function changes to

$$C(s) = k_p + k_i \frac{1}{s} + \frac{k_d s}{1 + s\alpha k_d}\,. \tag{3.30}$$

Typically α is in the range of 0.05–0.2 [195, p. 129].

An alternative is to filter the whole input. Depending on the filter cutoff, there is not much difference to equation 3.30, because the filter will not touch the proportional and integral part of the transfer function if both are well within its passband.

From figure 3.12 it can also be seen, why in some publications, the gain k_p is applied to all three terms and k_i and k_d are replaced with T_i and T_d to accommodate for that.

$$C(s) = k_p \left(1 + \frac{1}{T_i s} + \frac{T_d s}{1 + s\alpha T_d}\right) \tag{3.31}$$

Using this form allows to shift the overall gain up and down keeping its shape instead of just the k_p part, thus changing the corner frequencies. The alternative form is only given here for the sake of completeness. The author uses the ideal form shown in equation 3.27 with the parameters k_p, k_i, and k_d wherever possible.

This concludes the discussion of the PID controller and the introduction of the basic terms. It now begs the question how the controller interacts with the system and how to derive the optimal PID parameters from a given system or model. Thus, the next section discusses controller tuning rules and their effect on the system performance.

3.5.4. PID Tuning Rules

While many PID tuning rules can be found in the literature, their application depends on the underlying system and the desired system response. This section will discuss several proposed solutions and compare them to the authors use case. The section aims to give a simple method to determine decent PI/PID parameters for the applications found in the lab. Among the methods discussed are the most classic set of tuning rules developed by Ziegler et al. [253], and an improved version called Skogestad Internal Model Control (SIMC) presented by Skogestad [209] which promises better performance for non-integrating systems. These rules all include simple instructions to extract the necessary parameters using pen and paper. Using a computer and fitting algorithms, the bar for *simple* has been raised considerably, so more

complex approaches can be undertaken which extract more parameters from the system. Using these additional parameters, more precise control is promised by Åström et al. [26, 27] with a method called AMIGO. Finally, it is possible to shape the control loop to result in a desired transfer function. This technique is mostly used in motor control [27, 195] and also requires the model parameters.

All of these rules will be compared against a demo model of a room to explain the details. It is the first order model with delay which was derived in equation 3.22. The discussion is limited to the FOPDT model, because the systems treated in this work could be modelled very well using this equation. Higher-order models are discussed in more details for example in [27, 195, 209], in case the reader encounters such a system and feels the need to extract the model parameters.

$$G(s) = \frac{Ke^{-\theta s}}{1 + s\tau} \tag{3.32}$$

The following parameters were extracted from lab 011 of the APQ group, using the techniques shown in section 3.5.2 using equation 3.25. The details are discussed in section 4.3.3. The system gain K was scaled to the full scale output ($4095\,\mathrm{bit}$) of the controller, hence the somewhat strange unit $\mathrm{K\,bit\,bit^{-1}}$.

Gain K	Lag τ	Delay θ
$13.07\,\mathrm{K\,bit\,bit^{-1}}$	$395\,\mathrm{s}$	$187\,\mathrm{s}$

Table 3.4.: Example paramters extracted from lab 011 using the techniques shown here and as applied in section 4.3.3.

.

Before detailing the tuning parameters, the loop shaping method will be explained first, because it cannot only be used to derive custom rules but was also used to create the SIMC rules proposed by Skogestad [209]. The aim of this method is to derive a controller that shapes the model in such a way that a desired system response to setpoint changes is achieved. A general closed-loop system with a controller C and a system G is shown in figure 3.13. This will be used as a basis to find the required controller for a desired transfer function $\frac{Y(s)}{U(s)}$.

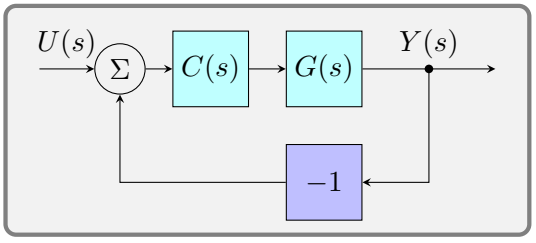

Figure 3.13.: Closed-loop system G with a controller C.

Starting with the transfer function of the controlled system, made up of the controller and the system, most experimenters would, at least in a feverish dream, prefer a transfer function of the following divine form

$$\frac{Y(s)}{U(s)} = 1\,,$$

but unfortunately life is more profane and there is no controller that will always (and with warp speed) force a system to a certain setpoint. One may therefore settle for the second-best

choice, a first order low pass with a slow roll-off and a small delay, which must be added to ensure causality. One therefore arrives at

$$\frac{Y(s)}{U(s)} = \frac{e^{-\theta s}}{1 + s\tau_c}\,, \tag{3.33}$$

where τ_c is the closed-loop time constant and a measure for the aggressiveness of the controller. A small τ_c results in a more aggressive controller with faster response.

For the system shown figure 3.13 the closed-loop transfer function is found to be

$$\begin{aligned} \frac{Y(s)}{U(s)} &= \frac{C(s)G(s)}{C(s)G(s)+1} \\ \Rightarrow C(s) &= \frac{1}{G(s)}\frac{1}{\frac{Y(s)}{U(s)} - 1} \end{aligned}$$

This loop now needs to be shaped into the desired transfer function given in equation 3.33, so substituting $\frac{Y(s)}{U(s)}$ yields

$$C(s) = \frac{1}{G(s)}\frac{e^{-\theta s}}{s\tau_c + 1 - \underbrace{e^{-\theta s}}_{\approx 1-\theta s}} \tag{3.34}$$

$$\approx \frac{1}{G(s)}\frac{e^{-\theta s}}{s(\tau_c + \theta)}\,. \tag{3.35}$$

$e^{-\theta s}$ was approximated using a first order Taylor expansion. The desired controller response now only depends on the system (including the sensor) to be controlled. So, substituting the system equation 3.32 results in

$$\begin{aligned} C(s) &= \frac{1}{K}\frac{s\tau + 1}{(\tau_c + \theta)s} \\ &= \underbrace{\frac{1}{K}\frac{\tau}{\tau_c + \theta}}_{k_p} + \underbrace{\frac{1}{K}\frac{1}{\tau_c + \theta}}_{k_i}\frac{1}{s}\,. \end{aligned} \tag{3.36}$$

This is a PI controller with $k_p = \frac{1}{K}\frac{\tau}{\tau_c+\theta}$ and $k_i = \frac{1}{K}\frac{1}{\tau_c+\theta}$. From these calculations, it can be seen that a first order model can be fully treated using a PI controller. Second order (and higher order) models typically necessitate a PID or more sophisticated controller for optimal control. The problems discussed in this work mainly focus temperature control of (mostly) homogeneous objects, so the focus lies on the PI controller for most of the remaining section but the ideas and simulations can similarly be applied to the PID controller as well. Any caveats to be expected when treating a PID instead of a PI controller will be discussed.

Using the loop shaping technique, it is fairly easy to derive custom rules in case the model parameters can be extracted. As mentioned above, one such loop-shaped tuning rule is the SIMC rule set and the authors of those rules give advice for an ample variety of different models and also investigate the parameter choice regarding stability, load, and setpoint disturbances. Before attempting a custom approach, it is therefore recommended to check [209] for an appropriate set of rules for more complex models in order to save time and effort.

Tuning Rule	k_p	T_i	T_d	Source
Z-N PI	$\frac{0.9\tau}{K\theta}$	$\frac{\theta}{0.3}$	–	[253]
Z-N PID	$\frac{1.2\tau}{K\theta}$	2θ	$\frac{\theta}{2}$	[253]
SIMC PI	$\frac{\tau}{K(\tau_c+\theta)}$	$\min\left(\tau, 4(\tau_c+\theta)\right)$	–	[209]
SIMC PID	$\frac{\tau_1}{K(\tau_c+\theta)}$	$\min\left(\tau_1, 4(\tau_c+\theta)\right)$	τ_2	[209]
AMIGO PI	$\frac{0.15}{K} + \left(0.35 - \frac{\tau\theta}{(\tau+\theta)^2}\right)\frac{\tau}{K\theta}$	$0.35\theta + \frac{13\tau^2\theta}{\tau^2+12\tau\theta+7\theta^2}$	–	[27, p. 228]
AMIGO PID	$\frac{1}{K}\left(0.2 + 0.45\frac{\tau}{\theta}\right)$	$\frac{0.4\theta+0.8\tau}{\theta+0.1\tau}\theta$	$\frac{0.5\tau\theta}{0.3\theta+\tau}$	[27, p. 233]

Table 3.5.: PI/PID parameters for different tuning rules. The PI controllers assume a first order model, the PID rules are required when dealing with a second order model.

For reasons of brevity, in table 3.5, the PID parameters are given as k_p, T_i and T_d as introduced in equation 3.31. k_i and k_d can be calculated from

$$k_i = \frac{k_p}{T_i}$$
$$k_d = k_p T_d \,.$$

Regarding the SIMC PI/PID algorithm, Skogestad [209] and [235, ch. 5] suggests using $\tau_c = \theta$ for "*tightest possible subject to maintaining smooth control*". Following this recommendation, the minimum can be calculated from the parameters given in table 3.4 on page 41 as $\min\left(\tau, 4(\tau_c+\theta)\right) = \min\left(\tau, 8\theta\right) = \tau$.

Using the rules above, the full system can be simulated now. This was done using Python. The simulation source code can be found in data/simulations/sim_pid_controller.py as part of the online supplemental material [42]. The simulation can be used to model arbitrary PI(D) controller and arbitrary models can be used as well. It allows to compare different settings before applying them to a real system. It also considerably shortens deployment times because especially for systems with long time scales, it becomes difficult to test several parameter sets on the fly, thus a simulation can reduce deployment time to a few minutes instead of hours.

The simulation emulates the PID controller developed for the lab temperature controller. By default it has a sampling rate of 1 Hz. The simulation will apply a setpoint change of 1 K 10 s into the simulation. After the simulation, it will plot the time domain response of the controlled system. The setpoint change in this scenario is very similar to the load disturbances that are expected. Typically a noise source is used here instead, but in contrast to the statistical noise, which could be used to test for disturbance rejection, the situation in labs are different and cannot be modelled with stationary noise. While there is some noise coming from the sensor and the lab, the major disturbances are usually caused by the experimenters instead of the lab itself. These are events like a device being switched on or off for an extended period of time, longer than the controller needs to settle. This is equivalent to a setpoint change in terms of the error term in equation 3.26, since there is no difference in the error term between a setpoint and a process variable change. Do note, that this is not true for the PID controller, whose derivative term directly works on the measurement (or process variable) as this was explicitly implemented above. For PID controllers, there is a difference between the setpoint change behaviour and system noise rejection. This must be kept in mind and tested accordingly.

Simulating the model above and using the PI parameters derived from table 3.5, gives the plot shown in figure 3.14.

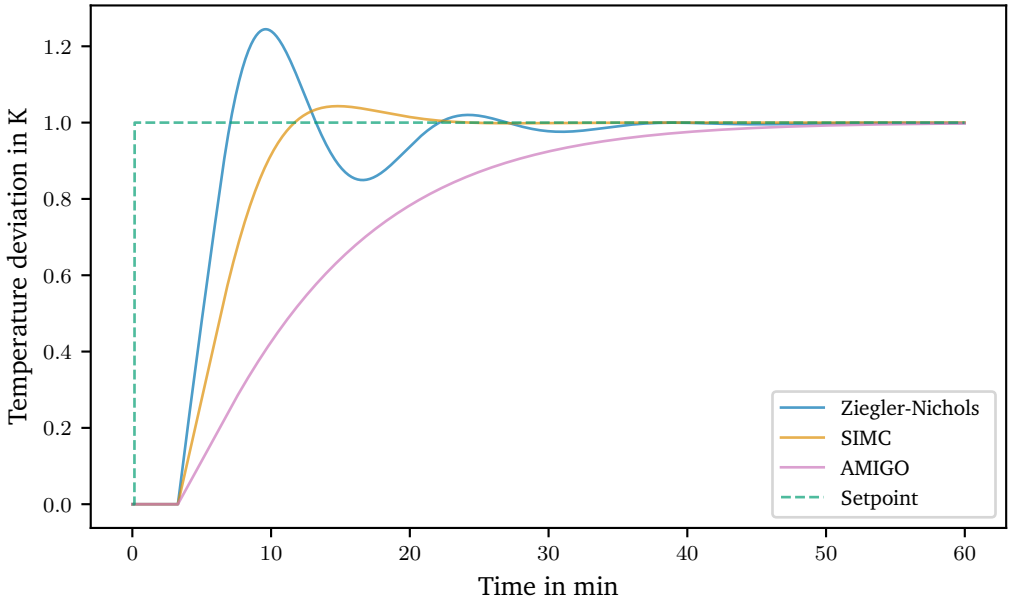

Figure 3.14.: Different PI Controllers tuned with parameter derived using the following methods: Ziegler-Nichols, SIMC and AMIGO. The system model is the FOPTD model for room 011.

As it can be seen in figure 3.14, the Ziegler-Nichols tuning rule produces a very aggressive PI controller that shows quite a bit ringing, which is undesired for this application. The AMIGO rules are rather conservative, but do not produce any overshoot. The SIMC rules have proven the most useful for this application so far. This experience is in line with the results from Liebmann [129], who tested different PID tuning algorithms for their viability for temperature control in the labs discussed here.

To conclude, several PID tuning rules were presented and using a Python simulation tool it is possible to test a set of PID parameters before implementation. Using an example based on parameters extracted from a real environment, the different tuning rules were applied to a model for a real lab and the SIMC tuning rules were found to give the best results for this application. The reader should now be able to extract the model parameters from physical systems and have the tools to choose an optimal set of tuning parameters for the PID controller. Further reading recommendations are for a broad overview [195], and for more details [27].

3.6. Noise and Allan Deviation

The Allan variance [19] $\sigma_A^2(\tau)$ is a two-sample variance and used as a measure of stability. The Allan deviation $\sigma_A(\tau)$ is the square root of the variance. Originally, the Allan variance was used to quantify the performance of oscillators, namely the frequency stability, but it can be used to evaluate any quantity. In order to define the Allan variance, a few terms need to be defined first. A single measurement value of a time series $y(t)$ can be written as

$$\bar{y}_k(t) = \frac{1}{\tau} \int_{t_k}^{t_k+\tau} y(t)\, dt. \tag{3.37}$$

This is the k-th measurement with a measurement time or integration time τ. The latter term is frequently used for digital multimeters (DMM). t_k is the start of the k-th sampling interval including the dead time θ

$$t_{k+1} = t_k + T \tag{3.38}$$

with

$$T := \tau + \theta. \tag{3.39}$$

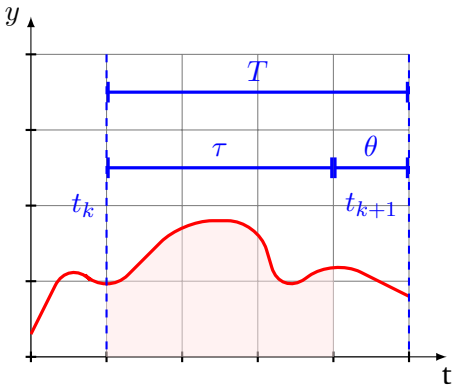

Figure 3.15.: Measurement interval according to equation 3.37. The shaded region is the signal acquisition period.

Using this, the deviation over N samples is defined as [19, 30]

$$\sigma_y^2(N,T,\tau) = \left\langle \frac{1}{N-1} \left(\sum_{k=0}^{N-1} \bar{y}_k^2(t) - \frac{1}{N} \left(\sum_{k=0}^{N-1} \bar{y}_k(t) \right)^2 \right) \right\rangle \tag{3.40}$$

The $\langle\ \rangle$ denotes the (infinite time) average over all measurands y_k or, simply put, the expected value.

The Allan variance is a special case of this definition with zero dead-time ($\theta = 0$) and only 2 samples:

$$\sigma_A^2(\tau) = \sigma_A^2(N=2, T=\tau, \tau) \tag{3.41}$$

$$= \left\langle \frac{(\bar{y}_{k+1} - \bar{y}_k)^2}{2} \right\rangle \tag{3.42}$$

It can be shown [30] that 3.43 is indeed more useful than $\sigma_A^2(N \to \infty, T = \tau, \tau)$, because $\sigma_A^2(N = 2, T = \tau, \tau)$ converges for processes that do not have a convergent $\sigma_A^2(N \to \infty, T = \tau, \tau)$.

In practice, no experiment can take an infinite number of samples, so typically the Allan variance must be estimated using a number of samples m:

$$\sigma_A^2(\tau) \approx \frac{1}{m} \sum_{k=1}^{m} \frac{(\bar{y}_{k+1} - \bar{y}_k)^2}{2} \tag{3.43}$$

This estimation can lead to artifacts in the results as discussed later. In order to derive the Allan variance from a set of data points, the different values of τ are usually obtained by averaging over a number of samples as there is no dead time (by definition of the Allan variance).

Additionally, the Allan variance is mathematically related to the two-sided power spectral density $S_y(f)$ [30]:

$$\sigma_A^2(\tau) = 2 \int_0^\infty S_y(f) \frac{\sin^4(\pi f \tau)}{(\pi f \tau)^2} \, df \tag{3.44}$$

and therefore all processes that can be observed in the power spectral density plot can also be seen in the Allan deviation. The inverse transform however, is not always possible as shown by Greenhall [91].

Distinguishing different noise processes using the Allan deviation will be elaborated in the next section.

3.6.1. Identifying Noise in Allan Deviation Plots

It was already mentioned by Allan in [19] that types of noise, whose spectral density follows a power law

$$S(f) = h_\alpha \cdot f^\alpha \tag{3.45}$$

can be easily identified in the Allan deviation plot. The constant h_α is called the power (intensity) coefficient. The most common types of noise encountered in experimental data and their representations can be found in table 3.6, which serves as a summary of this section. Since those types of noise are present in any measurement or electronic device, it warrants a further discussion to understand their root causes and ideas to minimize them. While not a type of noise, linear drift can also be easily identified in the Allan deviation plot. It is therefore included in table 3.6 as well.

Amplitude noise type	Power-law coefficient α	Allan variance σ_A^2
White noise	0	$\frac{1}{2} h_0 \tau^{-1}$ [20]
Flicker noise	-1	$2 \ln 2 \, h_{-1} \tau^0$ [20]
Random walk noise	-2	$\frac{3}{2} \pi^2 h_{-2} \tau^1$ [20]
Burst noise	0 and -2	$y_{rms}^2 \frac{\bar{\tau}^2}{\tau^2} \left(4e^{-\frac{\tau}{\bar{\tau}}} - e^{-\frac{2\tau}{\bar{\tau}}} + 2\frac{\tau}{\bar{\tau}} - 3 \right)$
Drift	–	$\frac{1}{2} D^2 \tau^2$ [90]

Table 3.6.: Power law representations of different noise types using the Allan variance.

In order to arrive at a good understanding of the features seen in an Allan deviation plot, this section will provide the reader with examples of each type of noise and the corresponding

time domain, power spectral density and Allan deviation plot. Since a complete overview is not available in current literature, all required mathematical descriptions and simulation tools will be discussed here. The simulations were done using Python and the source code is linked to in the discussions. The files are found in the online supplemental material found at [42]. Using these scripts, all the graphs shown can be recreated and explored further.

White Noise

White noise is probably the most common type of noise found in measurement data. Johnson noise found in resistors, caused by the random fluctuation of the charge carriers, is one example of mostly white noise up to a bandwidth of 100 MHz, from where on quantum corrections are required [80]. Amplifiers also tend to have a white noise spectrum at higher frequencies.

For the latter reason, white noise typically makes up for a considerable amount of noise in measurements, unless one works at very low frequencies. White noise is a series of uncorrelated random events and therefore characterised by a uniform power spectral density, which means there is the same power in a given bandwidth at all frequencies up to infinity. White noise therefore has infinite power (variance). In reality a measurement is always limited in bandwidth and hence the above property of a constant power spectral density only holds within that bandwidth. Those bandlimited samples of white noise thus have a finite variance. Since white noise is so common, a few of its properties should be mentioned. One such property is that the variance σ^2_{x+y} of two uncorrelated variables x and y adds as:

$$\sigma^2_{x+y} = \sigma^2_x + \sigma^2_y + \underbrace{2\,\mathrm{Cov}(x,y)}_{\text{uncorrelated}=0} = \sigma^2_x + \sigma^2_y \tag{3.46}$$

This results in simple addition rules for variances from different sources, but it must be stressed here that this property is only valid for uncorrelated sources like white noise, although it is usually incorrectly applied to all measurements which unfortunately obscures rather than clarifies the uncertainties involved.

In order to demonstrate the effect of white noise in Allan deviation plots, it was simulated using the *AllanTools* library written by Wallin [238]. The noise generator is based on the work of Kasdin et al. [109]. The full Python program code is published online [42] and found in data/simulations/sim_allan_variance.py. To allow better comparison, all noise densities are normalised to give an Allan deviation of $\sigma_A(\tau_0) = 1$, with τ_0 being the smallest time interval.

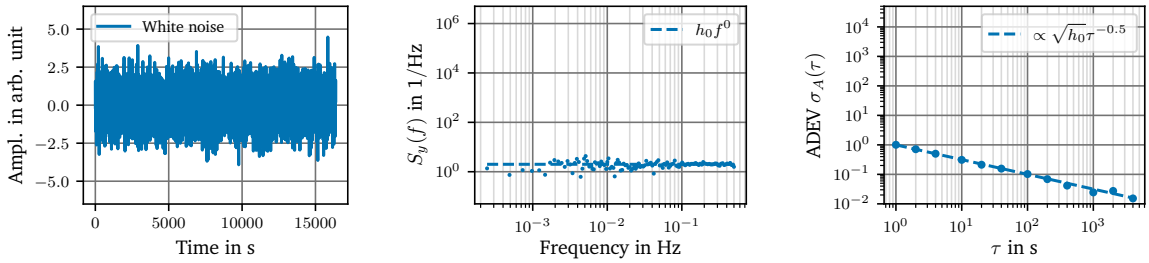

(a) Time domain (b) Power spectral density (c) Allan deviation

Figure 3.16.: Different representations of white noise.

Figure 3.16 shows a sample of white noise in its three different forms. Figure 3.16 (a) is the time series representation from which the power spectral density was calculated and is shown

in figure 3.16 (b). The dashed line shows the expectation value of the power spectral density and the Allan deviation.

From this simulation, several features can be observed. First of all, the power spectral density is flat and constant with $h_0 = 2$, which is in accordance with table 3.6 and the normalisation mentioned earlier. Figure 3.16 (c) shows the typical $\tau^{-\frac{1}{2}}$ dependence of white noise in the Allan deviation plot. This immediately explains, why filtering white noise scales with $\frac{1}{\sqrt{n}}$ with n being the number of samples averaged.

Burst Noise

Burst noise, popcorn noise, or sometimes referred to as random telegraph signal is a random bistable change in a signal and is caused by generation-recombination processes. This happens, for example, in semiconductors if there is a site that can trap an electron for a prolonged period of time and then randomly release it. Impurities causing lattice defects are discussed in this context [55, 111, 112, 178]. Such lattice defects can also be introduced by ion implantation during doping. Fortunately, this type of noise has become less prevalent in modern manufacturing processes, because the quality of the semiconductors has improved. But if a trap site is located very close to an important structure, for example a high precision Zener diode, its effect might be so strong that it can be clearly seen.

The discussion is split into two parts. First the power spectral density is calculated and then the Allan variance is calculated using that result.

The spectral density of burst noise caused by a single trap site was derived in [146] by Machlup. Machlup used the autocorrelation function of the burst noise signal and applied the Wiener-Khinchin (Wiener-Хи́нчин) theorem, which connects the autocorrelation function with the power spectral density. A more detailed derivation can be found in [251], in this paper the preconditions like stationarity of the process, are also discussed. The burst noise signal consists of two energy levels, called 0 and 1, split by Δy. Multiple burst noise signals can be superimposed in a real device. This would then result in multiple levels, but they can be treated separately. The measurement interval over an even number of transitions, so that one ends in the same state as the measurement has started, is the time T. The mean lifetime of the levels is called $\bar{\tau}_0$ and $\bar{\tau}_1$:

$$\bar{\tau}_0 \approx \frac{1}{N}\sum_i^N \tau_{0,i} \qquad \bar{\tau}_1 \approx \frac{1}{N}\sum_i^N \tau_{1,i} \tag{3.47}$$

Figure 3.17 shows a burst noise signal along with the definitions above.

Using these definitions, one can then derive [146]:

$$R_{xx}(T) = \Delta y^2 \cdot \frac{\bar{\tau}_1\bar{\tau}_0 e^{-\left(\frac{1}{\bar{\tau}_1}+\frac{1}{\bar{\tau}_0}\right)T}}{\left(\bar{\tau}_1+\bar{\tau}_0\right)^2} \quad \text{and} \tag{3.48}$$

$$S(\omega) = 4R_{xx}(0)\frac{\frac{\frac{1}{\bar{\tau}_1}+\frac{1}{\bar{\tau}_0}}{\left(\frac{1}{\bar{\tau}_1}+\frac{1}{\bar{\tau}_0}\right)^2+\omega^2}}{} \qquad \omega > 0. \tag{3.49}$$

Note, that the power spectral density is the one-sided version, hence an additional factor of 2 is included. The constant term was omitted here and can usually be neglected, because it is not relevant for calculating the power spectral density as it only contributes a single peak at

$\omega = 0$. Using the following definitions of the average time constant and the duty cycle

$$\frac{1}{\bar{\tau}} = \frac{1}{\bar{\tau}_1} + \frac{1}{\bar{\tau}_0} \quad \text{and} \tag{3.50}$$

$$D_i = \frac{\bar{\tau}_i}{\bar{\tau}_1 + \bar{\tau}_0} \quad i \in \{0; 1\} \tag{3.51}$$

equations 3.48 and 3.49 can be rewritten to give a more intuitive form.

$$R_{xx}(T) = \Delta y^2 D_1 D_0 \, e^{-\left(\frac{1}{\bar{\tau}_1} + \frac{1}{\bar{\tau}_0}\right)T} \tag{3.52}$$

$$S(\omega) = 4R_{xx}(0)\frac{\bar{\tau}}{1 + \omega^2 \bar{\tau}^2} \tag{3.53}$$

The special case $\bar{\tau}_0 = \bar{\tau}_1$ with $D_i = \frac{1}{2}$ is the previously mentioned case of random telegraph noise.

$R_{xx}(0)$ can be identified as the mean squared value of y:

$$y_{rms} = \sqrt{R_{xx}(0)}\,. \tag{3.54}$$

Equation 3.53 is a Lorentzian function and from this, it can be easily seen that a single trap site has a power spectral density that is proportional to $\frac{1}{f^2}$ at high frequencies and is flat at low frequencies.

With the spectral density in hand, it is now possible to calculate the Allan variance as it was done by Van Vliet et al. in [231] for the classic example of random telegraph noise where $\bar{\tau}_1 = \bar{\tau}_0$. Do note that table I given by Van Vliet et al. shows the total number of events instead of the instantaneous number of events typically given. Hence their notation must be multiplied by $\frac{1}{\tau^2}$ (or $\frac{1}{T^2}$ in their notation). For the generic case with $\bar{\tau}_1$, $\bar{\tau}_0$ and the definition of $\bar{\tau}$ given in equation 3.50 one finds for the Allan variance of burst noise:

$$\sigma_A^2(\tau) = R_{xx}(0)\frac{\bar{\tau}^2}{\tau^2}\left(4e^{-\frac{\tau}{\bar{\tau}}} - e^{-\frac{2\tau}{\bar{\tau}}} + 2\frac{\tau}{\bar{\tau}} - 3\right) \tag{3.55}$$

Having arrived at equations 3.53 and 3.55 of the power spectral density and Allan variance, it it now possible to model it. For this purpose, parts of the Python library *qtt* [75] was used. This algorithm written by Eendebak et al. implements continuous-time Markov chains to simulate the burst noise signal. The result can be see in figure 3.18. For these simulations one of

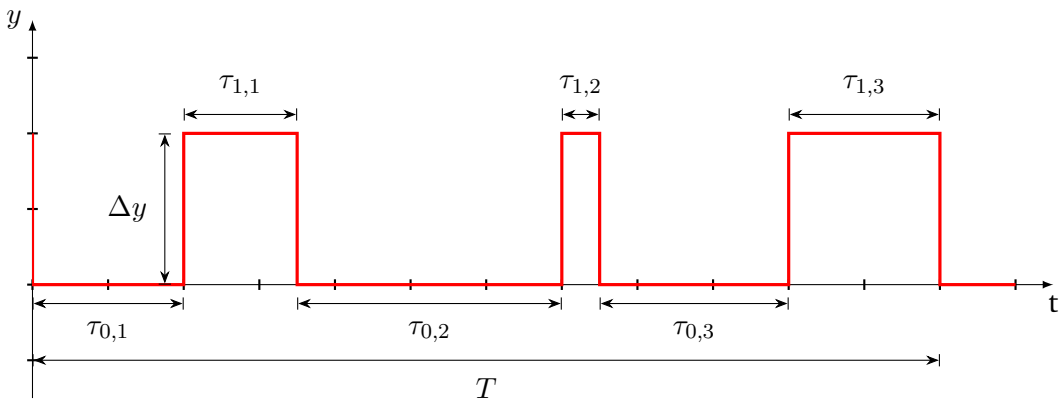

Figure 3.17.: A random burst noise signal.

the time constants, namely the lifetime of the lower state $\bar{\tau}_0$ was held constant, while the lifetime of the upper state was varied to show the effect of different $\bar{\tau}$. By looking at the time domain in figure 3.18 (a) it can be seen that the maximum average number of state changes can be observed, when $\bar{\tau}_1 = \bar{\tau}_0$. If $\bar{\tau}_1 > \bar{\tau}_0$ the system will favour the upper, while if $\bar{\tau}_1 < \bar{\tau}_0$ it will favour the lower state instead. This explains why the noise is strongest for random telegraph noise when $\bar{\tau}_1 = \bar{\tau}_0$, which can also be seen in the power spectral density plot in figure 3.18 (b). Looking at the Allan deviation in figure 3.18 (c) confirms this, but also shows another interesting implication as it shows an obvious maximum. If the application allows a choice over the sampling interval τ, the effect of the burst noise can be mitigated by staying well clear of the maximum.

The small deviation from the analytical solution in figure 3.18 (c) suggesting an upwards trend at large τ is a typical so-called end-of-data error. As it was discussed above, the Allan deviation can only be estimated given a limited number of samples using equation 3.43 and going to longer τ means there are fewer samples to average over.

The burst noise equations can be used to gain further insight into other types of noise. The first one is Shot noise, which is commonly found in photodetectors and lasers. Here, electrons or photons are created at discrete intervals resulting in an instantaneous signal. This means that the lifetime of the upper level is very short in comparison to the lower level ($\tau_1 \ll \tau_0$) equation 3.49 becomes:

$$
\begin{aligned}
S_{Shot}(\omega) = S_{\tau_1 \ll \tau_0}(\omega) &= 4\Delta y^2 \frac{\tau_1}{\tau_0} \frac{\frac{1}{\bar{\tau}_1}}{\left(\frac{1}{\bar{\tau}_1}\right)^2 + \omega^2} \\
&= 4\Delta y^2 \frac{1}{\tau_0} \frac{1}{\frac{1}{\tau_1^2} + \omega^2} \qquad (3.56) \\
&\overset{\omega \ll 1/\tau_0}{\approx} 4\Delta y^2 \frac{\tau_1^2}{\tau_0} = \text{const.} \qquad (3.57)
\end{aligned}
$$

Typically, a very large number of such events happen. When not counting single events, but rather a stream, the relation $\omega \ll 1/\tau_0$ is valid and hence the result is a white spectrum as $S_{Shot}(\omega)$ is constant with respect to ω — just as observed in photodetectors and lasers.

The other interesting occurrence is a case where many trap sites with different time constants are contributing to the noise. This can change the shape of the spectrum from f^{-2} to f^{-1} and is discussed in the next section.

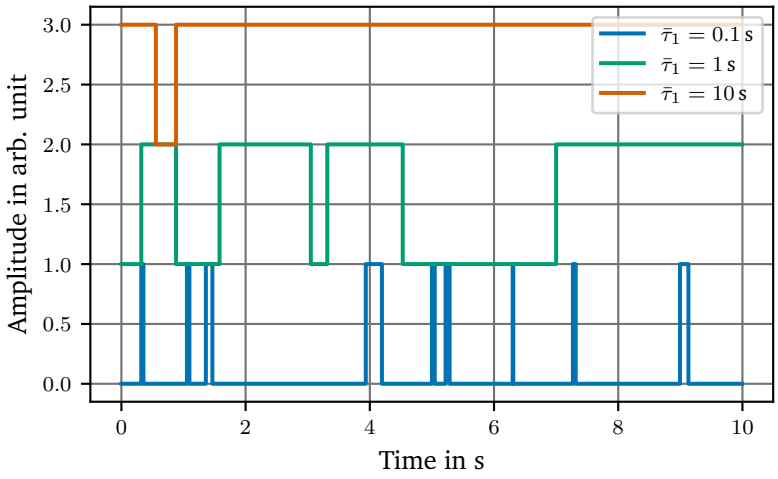

(a) Time domain

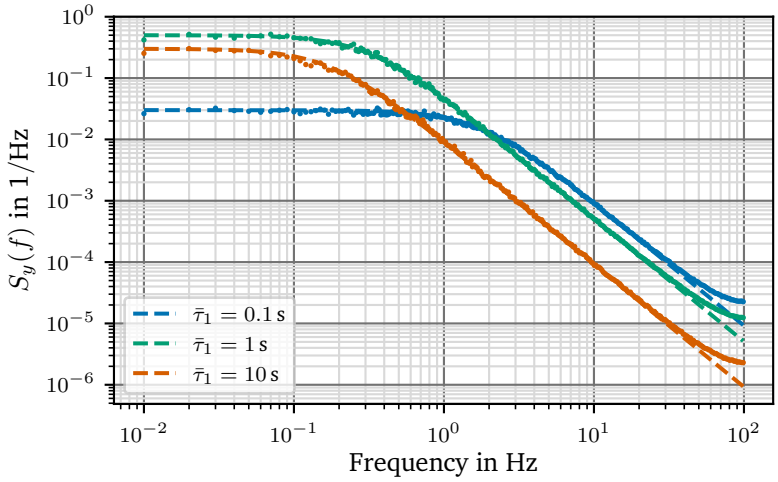

(b) Power spectral density

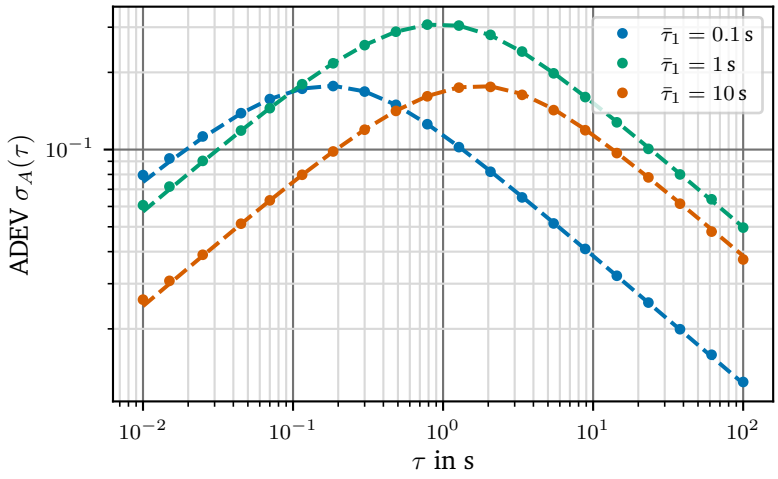

(c) Allan deviation

Figure 3.18.: Different representations of burst noise for different $\bar{\tau}_1$ and fixed $\bar{\tau}_0 = 1\,\mathrm{s}$.

Flicker Noise

Flicker noise is also called $\frac{1}{f}$-noise and it can be observed in many naturally occurring phenomena. Its origin is not clear, even though there have been many explanations. An overview can be found in [78, 163, 175]. This section concentrates on flicker noise in electronic devices. In thick-film resistors, for example, it was shown to extend over at least 6 decades without any visible flattening [172]. In transistors, flicker noise is caused by the existence of generation-recombination noise or burst noise discussed in the previous section [78]. If there are many uncorrelated trap sites which contribute to the total noise, the envelope of the noise spectral density changes from $\frac{1}{f^2}$ to $\frac{1}{f^1}$ as shown in figure 3.19

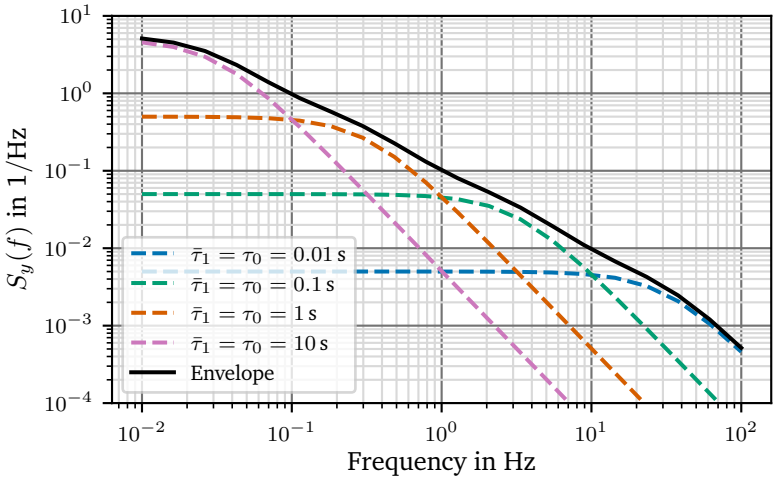

Figure 3.19.: Multiple overlapping Lorentzian noise sources forming a $\frac{1}{f}$-like shape.

Given that no trap site can store an electron indefinitely, the number of trap sites N with a certain time constant $\frac{1}{2}\bar{\tau} = \bar{\tau}_0 = \bar{\tau}_1$ must decline when going to longer time scales. Assuming N is inversely proportional to the time constant $\bar{\tau}$

$$N(\tau) \propto \frac{1}{\bar{\tau}}\,, \tag{3.58}$$

which can be motivated if the trapping process is thermally activated [74] and using equation 3.53 from the previous section, multiplying the weight function 3.58 and integrating over all possible storage times gives:

$$\begin{aligned}
S(\omega) &= \lim_{t\to\infty} \int_0^t N(\bar{\tau})\, 4R_{xx}(0) \frac{\bar{\tau}}{1+\omega^2\bar{\tau}^2}\, d\bar{\tau} \\
&\overset{\bar{\tau}_0=\bar{\tau}_1}{=} 4R_{xx}(0)\, C_N \lim_{t\to\infty} \int_0^t \frac{1}{1+\omega^2\bar{\tau}^2}\, d\bar{\tau} \\
&= \frac{4R_{xx}(0)\, C_N}{\omega} \lim_{t\to\infty} \arctan \bar{\tau}\omega \Big|_{\bar{\tau}=0}^{t} \\
&= \frac{4R_{xx}(0)\, C_N}{\omega} \cdot \frac{\pi}{2} \\
&= \frac{2\pi R_{xx}(0)\, C_N}{\omega} \qquad (3.59) \\
S(f) &= h_{-1} f^{-1} \qquad (3.60)
\end{aligned}$$

C_N is the proportionality constant of 3.58 and h_{-1} is the power coefficient introduced in 3.45. This shows that for a large number of distributed trap sites, a noise spectrum of f^{-1} is found.

Using equation 3.44, the Allan variance can be calculated from the power spectral density:

$$\begin{aligned}\sigma_A^2(\tau) &= 2h_{-1}\int_0^\infty \frac{1}{f}\frac{\sin^4(\pi f\tau)}{(\pi f\tau)^2}\,df \\ &= 2\ln 2\, h_{-1}\end{aligned} \tag{3.61}$$

Again, using the *AllanTools* library [238], flicker noise was simulated to give an impression of its properties.

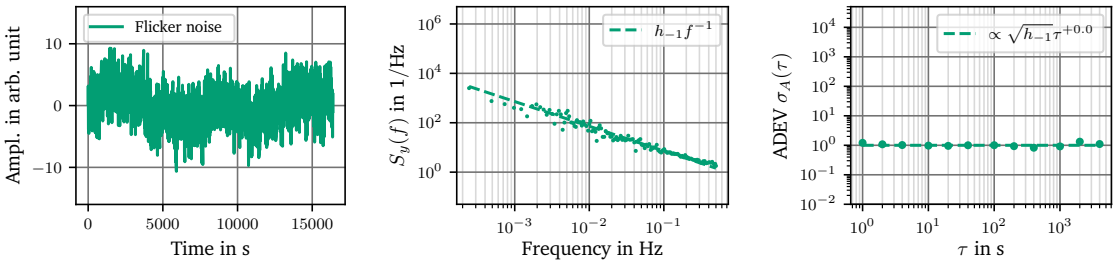

(a) Time domain (b) Power spectral density (c) Allan deviation

Figure 3.20.: Different representations of flicker noise.

While it is not immediately evident from the power spectral density, the Allan deviation plot explains very well, why additional filtering does not affect flicker noise. No matter how long the integration time, the variance will still be the same.

The small wiggles at longer τ are typical end-of-data errors caused by spectral leakage, because there are insufficient samples to average over [99]. As it was discussed above, the Allan deviation can only be estimated using equation 3.43 given a limited number of samples. Therefore, at $\frac{\tau}{2}$ there are only 2 samples left, so there is no averaging possible to improve the estimate of the Allan deviation, which causes the oscillations at low frequencies or large τ.

As a last remark, a commonly used definition in combination with flicker noise is the corner frequency f_c. The corner frequency appears in situations where there is both flicker and white noise present. It is the crossover point in frequency, where the flicker noise is equal compared to the white noise.

$$f_c = \frac{h_{-1}}{h_0} \tag{3.62}$$

It can be graphically extracted from the power spectral density plot by drawing a line trough the flicker noise and the white noise and finding the intersection. This can be seen in figure 3.25 on page 58. The corner frequency can be found where the horizontal dashed blue and green line meet.

Random Walk

Random walk noise can be attributed to environmental factors such as temperature [232] and diffusion processes, the latter contributing to the ageing effect seen in semiconductors. It is a process, where in each time step the change is randomly determined to be either a positve or

negative step with equal probability and a fixed step size. Its mean is

$$\langle y_n \rangle = \langle e_1 + e_2 + \dots e_n \rangle = \underbrace{\langle e_1 \rangle}_{=0} + \langle e_2 \rangle + \dots + \langle e_n \rangle = 0\,, \tag{3.63}$$

but its variance

$$\sigma_y^2 = \langle y_n^2 \rangle - \underbrace{\langle y_n \rangle}_{=0} = \sigma_{e_1}^2 + \sigma_{e_2}^2 + \dots \sigma_{e_n}^2 = n\sigma_e^2 \tag{3.64}$$

goes with n (or t). It therefore is not a stationary process as can also be seen in figure 3.21 (c).

The power spectral density can be calculated [30, 109] to be

$$S(f) = h_{-2}\frac{1}{f^2} \tag{3.65}$$

and the Allan deviation can again be calculated from the spectral density

$$\begin{aligned}\sigma_A^2(\tau) &= 2h_{-2}\int_0^\infty \frac{1}{f^2}\frac{\sin^4(\pi f\tau)}{(\pi f\tau)^2}\,df \\ &= \frac{2}{3}\pi^2 h_{-2}\,\tau\end{aligned} \tag{3.66}$$

The *AllanTools* library [238] can then be used to simulate the random walk.

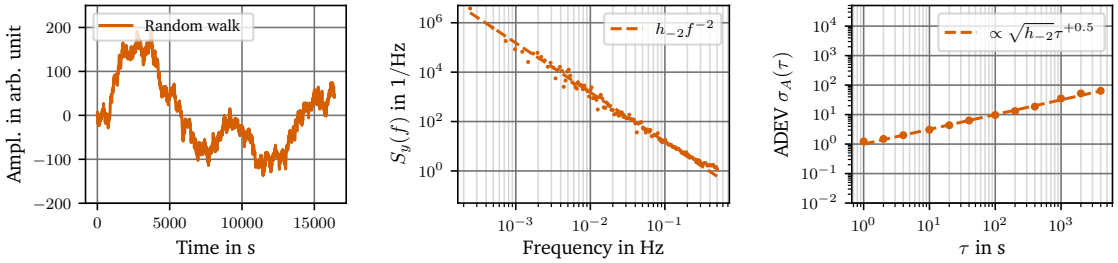

(a) Time domain (b) Power spectral density (c) Allan deviation

Figure 3.21.: Different representations of random walk noise.

Drift

Finally, the last feature of the Allan deviation plot that needs to be discussed is drift. Drift happens at very long time scales and describes a linear dependence of the measurand on time. This is also part of the ageing effect. Greenhall discussed the effect of drift [90] on the Allan variance and found the following relationship:

$$\sigma_A^2(\tau) = \frac{D^2}{2}\tau^2 \tag{3.67}$$

with slope of the drift D.

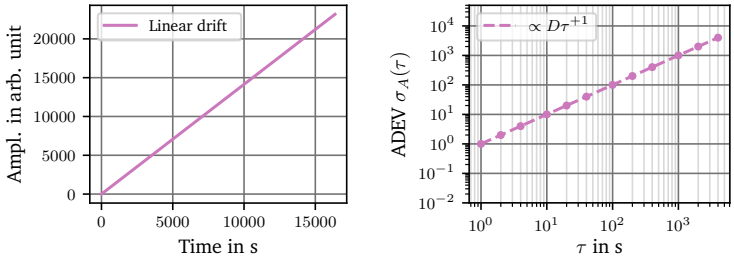

(a) Time domain (b) Allan deviation

Figure 3.22.: Different representations of linear drift.

Dead Time

The coefficients given in the previous examples were derived using the assumption that all samples in a measurement are continuous with a dead time $\theta = 0$. Unfortunately, measurements sometimes have a dead time that is non negligible. This problem was extensively discussed by Barnes et al. [30]. Dawkins et al. even developed special models to account for the algorithms of modern frequency counters [66]. While some frequency counters support gapless measurements, the situation is entirely different for digitizers and digital multimeters. Several settings commonly used affect the dead time, which can be considerable. It is therefore important to discuss typical measurement settings for voltmeters to estimate the errors that arise from those settings. The focus of this discussion lies on the dead time introduced by digital multimeters, but the application is not limited to this field.

The most commonly used settings that affect the dead time of a voltmeter are autozeroing and line synchronization. Autozeroing is done by adding additional measurements to the normal input integration cycle. To correct for the zero offset drift a zero measurement is added where the ADC is switched to the low terminal. Additionally, some devices add a reading of the reference voltage to correct for gain errors. The implementation details and type of measurements are manufacturer dependent.

The other setting, which can be enabled in voltmeters, is the line synchronization to increase the noise rejection of the instrument. This setting synchronizes the start of a measurement to the zero crossing of the power line. Depending on the instrument, this might cause a delay of one power line cycle (PLC) after each measurement if the instrument is not capable of processing the previous measurement while at the same time recording another one.

A simple measurement with dead time is shown in figure 3.15 on page 45. That model assumes that the dead time is constant and is always added after the actual integration time

τ. This is rarely true for real measurement data as many devices and even ADCs use internal averaging and autozeroing to produce a measurement. The actual dead time is therefore spread over the whole measurement and not limited to the end of the measurement. An example is the Keysight 3458A DMM that automatically switches to averaging when selecting integration times greater than 10 PLC. The reason is simple as for longer integration times, more and more flicker noise starts contributing to the measurement. The measurement is therefore split into single measurements of 10 PLC and, using autozeroing, the flicker noise is suppressed. This is discussed in more detail as an example in section 3.7. The mathematical problem of a distributed dead time was already noted by Allan [20] and it is distinctively different from the calculations made by Barnes et al. [30] for a single dead time at the end of the measurement. The exact mathematical treatment is complex and is beyond the scope of this work, especially considering that autozeroing does a lot more than just adding dead time at the end of the measurement. Fortunately, using a few assumptions, the problem can be greatly simplified.

An interesting observation can be made for white noise. Since it is uncorrelated, it makes no difference whether it is sampled in full, or only partially, and therefore the Allan deviation for a white noise process with or without dead time is the same:

$$\sigma^2(N, T, \tau) = \sigma^2(N = 2, T = \tau, \tau) = \sigma_A^2(\tau)\frac{1}{2}h_0\tau^{-1} \tag{3.68}$$

Consequently, if the dead time is added at a frequency high enough, so that the input amplifier output is dominated by white noise, the dead time will have no influence on the Allan variance.

Finally, Barnes et al. [30] notes that for measurement durations or averaging times $T \gg T_0$, the Allan variance with respect to T shows an asymptotic behaviour of $\sigma_A^2(T) \to \sigma_A^2(\tau)$.

3.6.2. Example

Using the results from the previous sections, it is possible to simulate a typical measurement sample containing white noise, flicker noise and random walk behaviour. The simulation was written in Python using the *AllanTools* library [238] to generate the time domain data, which was then converted to a power spectrum using the algorithm developed by Welch [240] to estimate the power spectral density. The Allan deviation was calculated using the *AllanTools* library. The full Python source is available at [42] and found in data/simulations/sim_allan_variance_example.py. The time domain data shown here were downsampled from 2^{25} data points to 2000 points for faster plotting using the Largest-Triangle-Three-Buckets (LTTB) algorithm created by Steinarsson [215] and also available as a Python library. The downsampling algorithm chosen is optimal for this application because it aims to visually keep the result the same by favouring parts of the data where there is more dynamics. The only difference noticeable to the author is that the edges of the white noise plot are a slightly rougher. The full data set can be obtained using the source code given above if one desires. The power spectrum and the Allan deviation were always calculated from the full dataset. The data of the power spectrum were additionally binned to be evenly spaced on a logarithmic scale. This considerably reduced the high frequency noise and made the plot easier to read while not negatively impacting its shape.

The three time series shown in figure 3.23 were sequentially generated using a fixed seed for the random number generator to ensure repeatability as long as the order of creation is kept the same. For generating the noise, the algorithm presented by Kasdin et al. [109], implemented in the *AllanTools* Python library was used. The noise strength parameters were

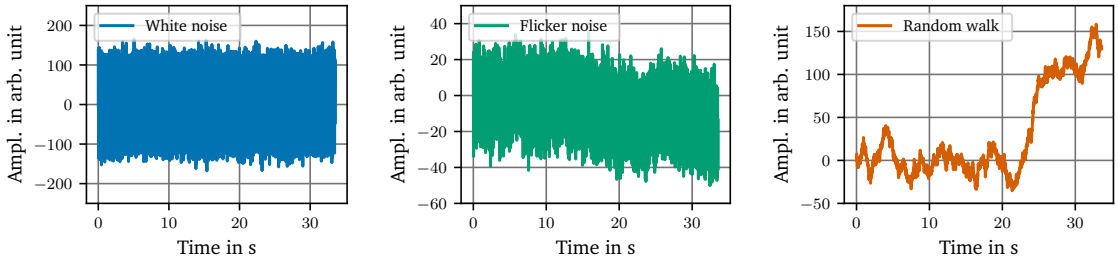

(a) White noise (b) Flicker noise (c) Random walk

Figure 3.23.: Three separate noise components that were summed together to simulate a typical noise source.

deliberately chosen in such a way that both the white noise and the random walk part have more noise power than the flicker noise. This allows to distinguish them in the following plots at both extremes of the frequency scale and time scale. Finally, the three types of noise data were summed together to give the combined signal, which is shown in figure 3.24, again downsampled using LTTB. The summed series clearly shows the white noise content and it is possible to deduce either flicker or random walk noise, but it is highly obscured due to the amount of white noise. Using only the time domain plot makes it very hard to clearly distinguish the type of noise present, let alone estimate the individual noise power of the three components. Therefore, a different analysis tool is called for.

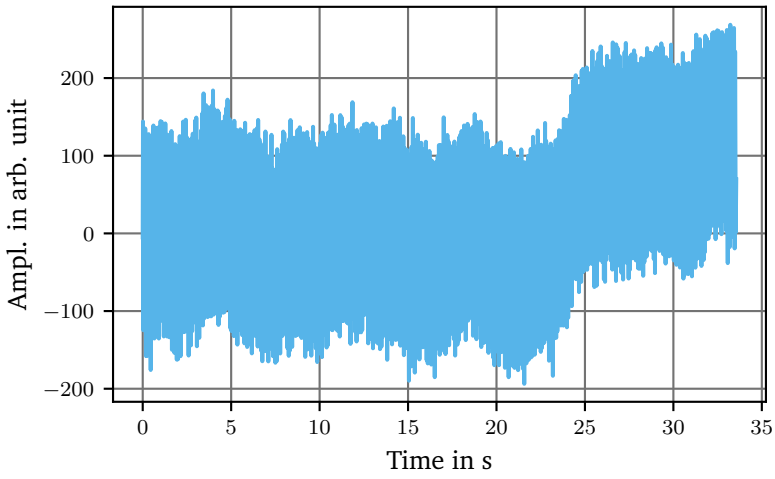

Figure 3.24.: A simulated time series containing white noise, flicker noise and random walk behaviour.

A common approach to identify noise sources is the power spectrum. It is easily accessible, even in real-time using spectrum analysers and, utilizing the computational power of modern computers, large time-domain data sets can be converted using the fast Fourier transform, making this the method of choice in the lab. The power spectral density of figure 3.24 is shown in figure 3.25. It allows to clearly separate the white noise part from the other f^{α} components. The dashed lines representing the individual components were plotted using the h_{α} values calculated from the input parameters of the simulation. The noise spectral density h_0 of the white noise signal can be easily extracted even by hand without resorting to a fit. This yields

$h_0 = 2 \times 10^{-3}/\text{Hz}$. h_{-1} and h_{-2} can be extracted as well using a fit to

$$S(f) = \sum_{\alpha=-2}^{0} h_\alpha f^\alpha \,. \tag{3.69}$$

The noise corner frequency f_c can either be calculated from h_0 and h_{-1} using equation 3.62 or determined graphically by constructing a tangent with a slope of -1 to the spectral density. From the intersection of the blue h_0 line and the green h_{-1} line the corner frequency is found to be $f_c \approx 1.8\,\text{kHz}$.

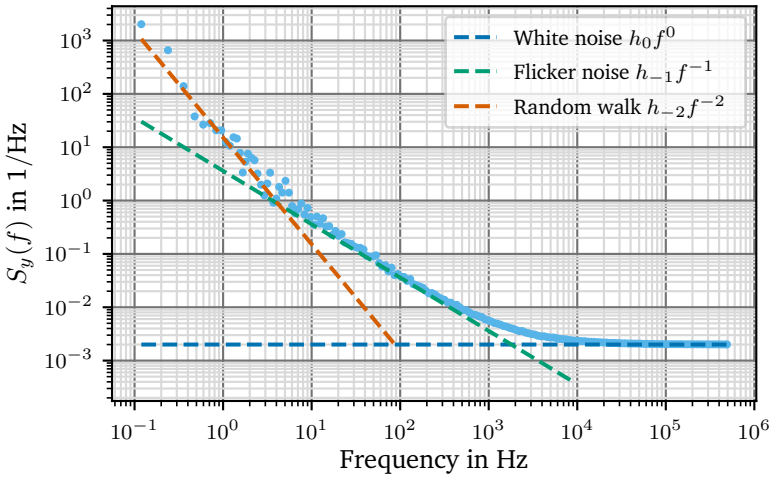

Figure 3.25.: A simulated power spectrum containing white noise, flicker noise and random walk behaviour.

To get an even better representation of the individual noise contributions, the Allan variance or Allan deviation can be used. The Allan deviation plot shown in figure 3.26 gives very clean results and all noise components can be clearly identified. The individual components were plotted using dashed lines as well.

The Allan variance was calculated using the overlapping Allan variance algorithm [184] and only Allan deviation values for frequency values of $(1, 2, 4)$ per decade were plotted. The overlapping Allan variance gives a better confidence at longer intervals or lower frequencies, allowing to identify very low frequency noise like the random walk shown here. Reference [184] also gives a very good comparison of other algorithms to identify even more noise types in data sets like phase noise. Plotting only three values per decade improves the clarity of the plot, because at longer τs, even though the overlapping Allan variance is used, some oscillations inevitably show up. Using fewer values of τ causes less distractions in this case. From the figure 3.26, the Allan deviation of the flicker noise can be estimated from the flat minimum to be around 2.3 or $\sqrt{5}$. Using table 3.6 the Allan variance can be converted to

$$h_{-1} = \frac{5}{2\ln 2} \approx 3.6$$

Using the previously found h_0, this corner frequency is calculated using equation 3.62 to be:

$$f_c = \frac{5}{2 \times 10^{-3}/\text{Hz} \cdot 2\ln 2} \approx 1.8\,\text{kHz}$$

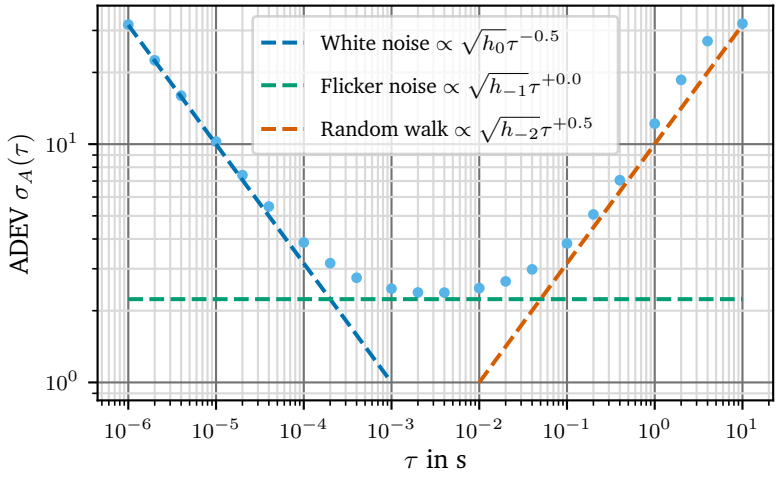

Figure 3.26.: A simulated Allan deviation containing white noise, flicker noise and random walk behaviour.

This is obviously the same result as the one from the geometric approach above.

This concludes the examples section for different noise types. The reader should now be able to identify different types of noise in measurement data and have learnt to appreciate the value that the Allen variance brings to the table. An example was presented that applied all techniques shown in this section to extract information about the noise sources in a dataset. Additionally, Python source code is provided to further explore the topic.

3.7. Autozeroing

Autozeroing (AZ), sometimes called zero-drift or dynamic offset compensation, is such an important concept that it must be discussed in its own right. The need for autozeroing comes from the typical behaviour of amplifiers. Every amplifier has some offset, be it small or large, and especially at high gains, this offset becomes a problem for high precision measurements. To make matters worse, this offset is not stable over time and drifts with both time and temperature. It can therefore not be calibrated out once, it must be permanently adjusted during operation, depending on environmental conditions. This procedure is called autozeroing.

There are many different ways to implement autozeroing and regarding operational amplifiers a good overview can be found in [96]. As an example, the autozero cycle for the Keithley `Model 2002` and the Keysight `3458A` Multimeter is shown in figure 3.27. Keithley uses a more complex and slower algorithm, while HP implemented a simpler but faster algorithm. The most simple (digital) approach is to regularly switch the input from the signal to zero, take a reading, then subtract this reading from all subsequent readings until a new zero reading is taken. An alternative approach adds another measurement of the reference voltage to apply a gain correction as well. This is done by the Keithley `Model 2002` and works very well to suppress gain drift in the input amplifier due to temperature changes but increases the time between samples by another $50\,\%$. The Keysight/HP `3458A` in the other hand calculates those gain corrections only during the manual auto-calibration (ACAL) routine to maintain a higher throughput.

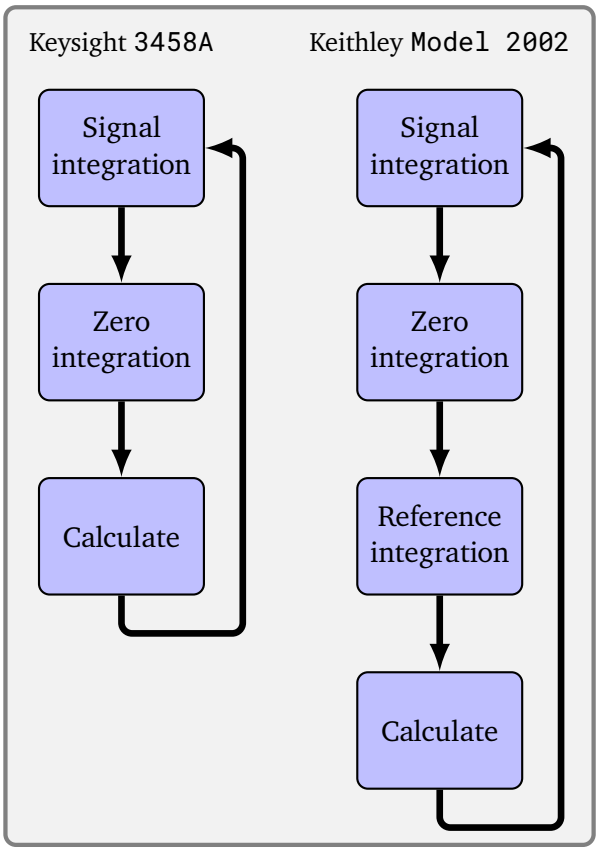

Figure 3.27.: Auto-zero phases of the Keysight `3458A` and Keithley `Model 2002`.

3.7.1. Offset Nulling

Offset nulling is the most basic approach to autozeroing. It aims to remove the offset drift of an amplifier. Especially at high gains, the offset, which is multiplied by the gain, can be substantial. In order to explain how offset nulling works and how it shapes the spectrum, it is best to discuss it based on an example. While this technique can also be found in many integrated circuits, it is more noticeable in DMMs, because it is a switchable option. Therefore, the example data set simulated is based on the parameters of the aforementioned Keysight 3458A multimeter. The corner frequency and the white noise floor is modeled after the $10\,\mathrm{V}$ range of the 3458A [120, 122] with the values given below. Do note that both references [120, 122] contain a typographical error. The corner frequency of the noise floor is erroneously given as $0.5\,\mathrm{Hz}$, but should be $1.5\,\mathrm{Hz}$. This can be seen in figure 2.35 in [120, p. 116], where the noise spectral density is plotted and it was also confirmed with the author [121]. The data used in this section is generated using the Python *AllanTools* library [238] and the simulation source code can be found in data/simulations/sim_autozero.py as part of the online supplemental material [42].

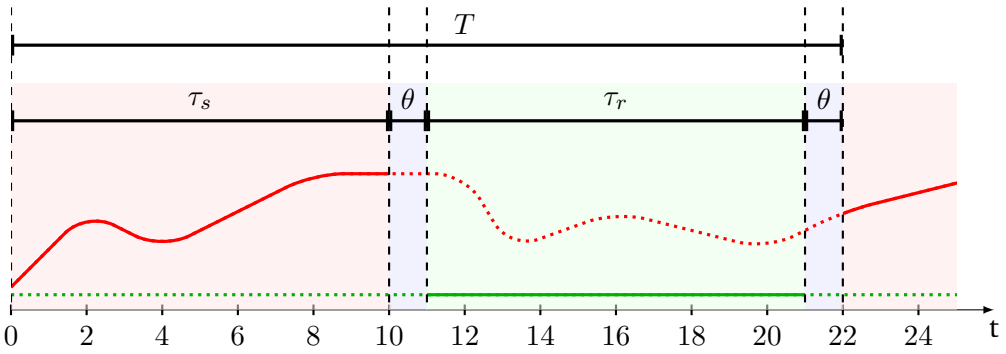

Figure 3.28.: Integration sequences of the offset nulling algorithm. Solid lines denote sampled data. Red is the input signal, green is the zero reading and blue is the dead time required for switching inputs.

For this simulation, a noise-free and arbitrarily chosen $10\,\mathrm{V}$ input is assumed to be sampled by the device at a sampling rate of $10\,\mathrm{PLC}$ at $50\,\mathrm{Hz}$, the same rate discussed previously on page 55. As it will be shown, the actual mean value of the input signal has no bearing on the outcome of the calculation when considering offset nulling, but its value must be considered for other types of autozeroing as discussed in section 3.7.2 and is included here only for the sake of completeness.

Figure 3.28 shows the individual sequences of the offset nulling algorithm. First, the source is sampled for $\tau_s = 10\,\mathrm{PLC}$, then the input is switched to the LO terminal. While this operation is very fast and takes less than $1\,\mathrm{ms}$ [183], if the instrument is synchronized to the line frequency the zero measurement will nonetheless be delayed until the next zero crossing, hence the dead-time $\theta = 1\,\mathrm{PLC}$. Finally, the zero reference is measured for another $\tau_r = 10\,\mathrm{PLC}$ and then the instrument switches back to the HI terminal.

The data is simulated in the following way: First, two sets of noise data are generated, a white noise spectrum with a noise spectral density of $165\,\mathrm{nV}/\sqrt{\mathrm{Hz}}$ and a flicker noise spectrum with an intensity scaled to result in a final spectrum with a corner frequency of $1.5\,\mathrm{Hz}$. The required flicker noise intensity is calculated using equation 3.62. To get a good low frequency estimate, $2^{20} \approx 10^6$ values were generated. Finally, the two noise data sets are summed with

the noise-free input source to give the final result. Other effects, such as power-line hum are neglected in this simple simulation because it would needlessly overcomplicate the example and limit the educational value. The same goes for higher order random-walk f^{-2} noise components, which can be introduced by temperature fluctuations and other environmental effects and would be present in a real measurement.

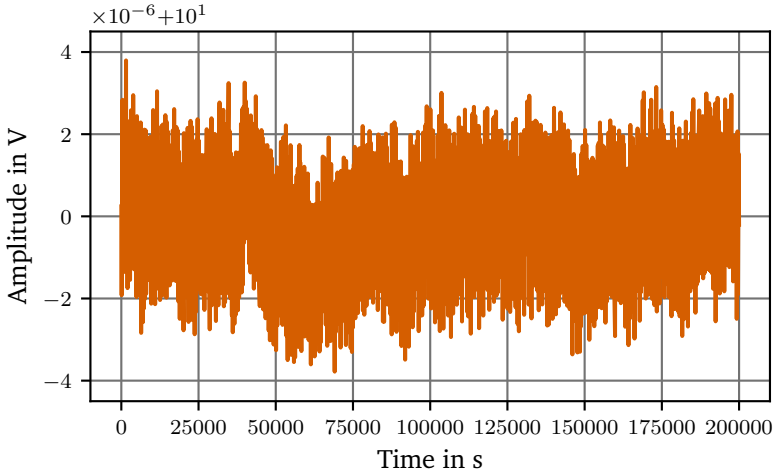

Figure 3.29.: Time series data with white noise and flicker noise.

The time domain plot of the simulation is shown in figure 3.29. The white noise component is clearly visible, while the f^{-1} flicker noise can be recognized, but its strength can hardly be estimated. It was already shown in section 3.6.2 that different types of noise have different frequency components and those can be distinguished in the frequency domain, which leads to the next approach.

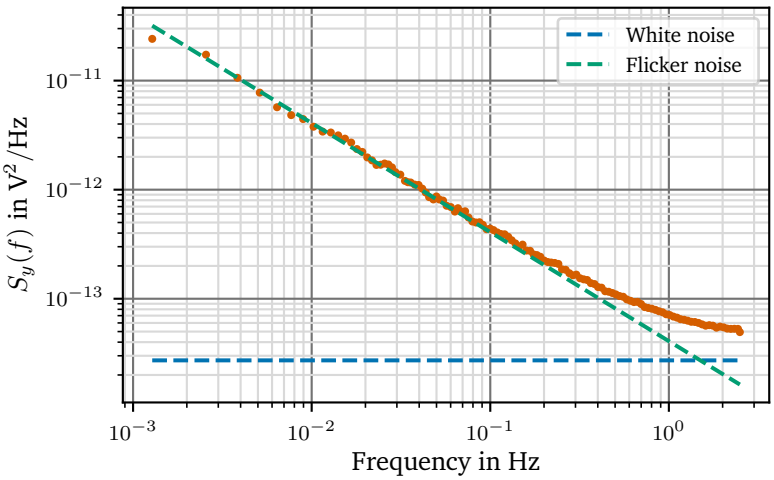

Figure 3.30.: Simulated power spectrum of a Keysight 3458A containing white noise and flicker noise. The line frequency is 50 Hz.

The noise power spectral density shown in figure 3.30 is calculated from the time series given in figure 3.29 and confirms the flicker and white noise content. The theoretical white noise floor is shown as a horizontal dashed blue line and the flicker noise as a dashed green

line. The $1.5\,\mathrm{Hz}$ corner frequency, which is defined as the intersection between the f^{-1} noise and the white noise floor can be easily identified using those lines. It is evident that the $5\,\mathrm{Hz}$ sampling frequency with a $2.5\,\mathrm{Hz}$ bandwidth does not allow the spectral density to fully settle to the white noise floor.

From the power spectral density is can be seen that higher frequencies have a significantly lower noise spectral density than low frequencies. It is therefore most beneficial to do measurements at higher frequencies. To discuss the optimal measurement interval, the Allan deviation is an excellent tool.

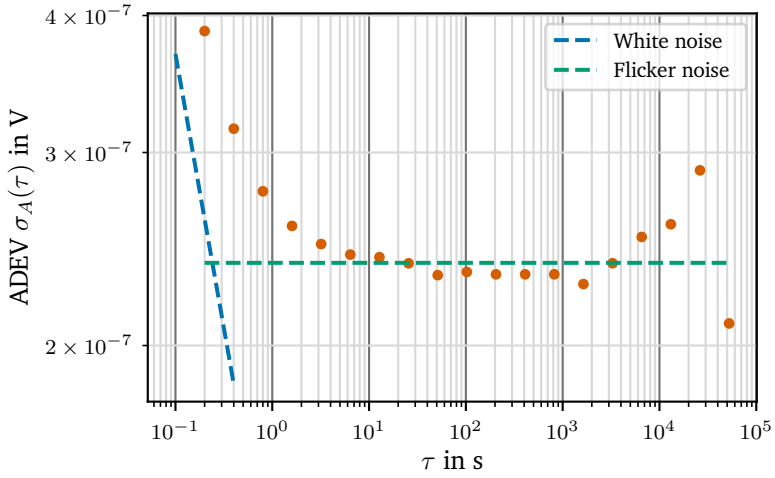

Figure 3.31.: Simulated Allan deviation of the input amplifier of a Keysight 3458A containing white noise and flicker noise. The line frequency is $50\,\mathrm{Hz}$.

The Allan deviation it plotted in figure 3.31 and shows two distinct regions. Short τ display an asymptotic behaviour towards white noise with a $\tau^{-0.5}$ dependence and at longer τ the constant flicker noise region can be identified. At very long τ typical end-of-data oscillations can be seen, which are the result of the limited confidence of the Allan deviation estimator as previously discussed and can therefore be safely ignored. The Allan deviation clearly demonstrates the performance of the device at longer integration times and it is obvious that beyond an integration time of about $1\,\mathrm{s}$ or $50\,\mathrm{PLC}$ no additional information can be extracted from the measurement and the variance is constant. This leads to the need for autozeroing to remove the flicker noise. It can be shown [193] that subtracting a reference measurement from the actual measurement data removes all correlated effects. Since flicker noise is autocorrelated, it can be removed by subtracting a zero measurement.

To demonstrate autozeroing, two cases will be discussed. Going back to figure 3.28 it can be seen that between switching inputs, a dead time θ is added. For a first discussion, this dead time is neglected and then the effect of adding a dead time is discussed in a next step.

Using figure 3.31 it was shown that integrating over flicker noise, does not reduce the variance. In order to have as little flicker noise content in the final measurement values as possible, it is clear that the autozeroing should be done as fast as feasible to keep the flicker noise content out. This allows to calculate the expected variance of the autozeroed measurement. The noise of the input measurement x and the reference measurement y are the same, because in this model the only noise source comes from the input amplifier, as the input signal is assumed to be noise-free. The zero level is, by definition, noise-free. As discussed above, the autozero interval is chosen, in such a way that its variance is dominated by white noise. The variance

σ^2 of the combined measurement of $x - y$ can then be calculated using equation 3.46:

$$\sigma_{x-y}^2 = \sigma_x^2 + \sigma_y^2 \tag{3.70}$$

By subtracting the zero reading the amplifier noise is effectively added twice to the final result, once for the input measurement and once for the zero measurement. Additional noise from the input signal noise would simply be added to this as it is uncorrelated as well.

Do note, that the number of samples is now half the number before applying autozeroing. This leads to an interesting effect. Taking for example a data set containing only white noise with a variance σ^2 and removing half the samples obviously does not change the variance as white noise is not correlated, but subtracting the samples is effectively decimating the data set and since the sampling rate is halved, the Nyquist band is halved as well. Unfortunately the input noise bandwidth stays the same. The second Nyquist band is then folded back into the first, thus doubling the noise power density.

To conclude, it is expected that the variance doubles and the power spectral density quadruples. These considerations can be compared to the simulated data. In order to apply the autozeroing algorithm to the simulated data set, the constant noise-free part, namely the $10\,\mathrm{V}$ signal, of the noisy input signal was nulled for every odd value and the residual noise was subtracted from the signal value. The result in the time domain is shown in figure 3.32.

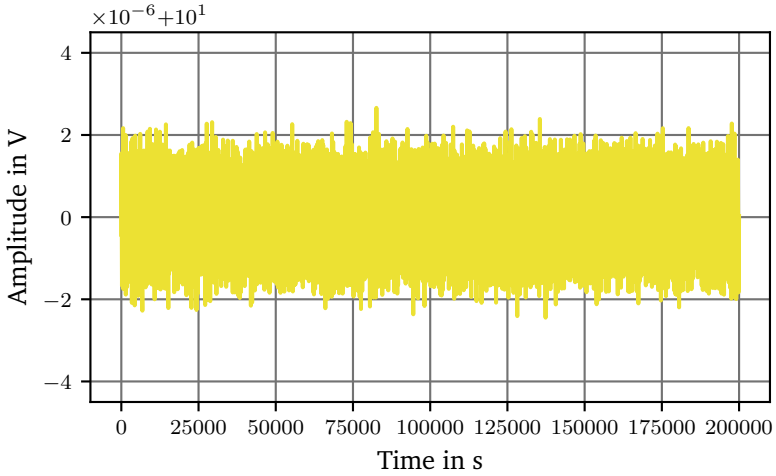

Figure 3.32.: Simulated measurement with autozeroing applied.

When comparing figure 3.32 to figure 3.29 on page 62 it is immediately evident that the f^{-1} flicker noise component is no longer present. The difference in white noise strength is difficult to compare and it must be turned to the power spectral density again. When calculating the spectral density it is important to remember that the sampling rate is now halved because the odd samples were subtracted. The result is shown in figure 3.33 along with dashed lines showing the noise content prior to applying the autozero algorithm as was done in figure 3.30 on page 62.

The power spectral density in figure 3.33 confirms an increase in the white noise power as discussed above and using the graph it can be worked out that the white noise power $\sqrt{h_{-1}}$ has increased from $165\,\mathrm{nV}/\sqrt{\mathrm{Hz}}$ to $489\,\mathrm{nV}/\sqrt{\mathrm{Hz}}$, an increase by a factor of $\sqrt{8.8}$, which is more than estimated from equation 3.70. Including the factor of 2 introduced by the decimation, the increase of $\sqrt{h_{-1}}$ was gauged to be by a factor of $\sqrt{4}$. The cause of the additional noise was already mentioned above. There is still some substantial f^{-1} noise present at the autozero

frequency of $5\,\mathrm{Hz}$. This type of noise is not uncorrelated and therefore the covariance is not zero, hence equation 3.46 does not strictly hold and additional correlated noise is leaking into the result. This hypothesis can be confirmed by increasing the sampling frequency by an order magnitude. Doing this, the white noise floor of the autozero measurement now only increases by a factor of $\sqrt{4.5}$, which is close to the expected factor of $\sqrt{4}$. This means that the autozeroing frequency should be chosen to be at least a decade above the noise corner frequency to be most effective.

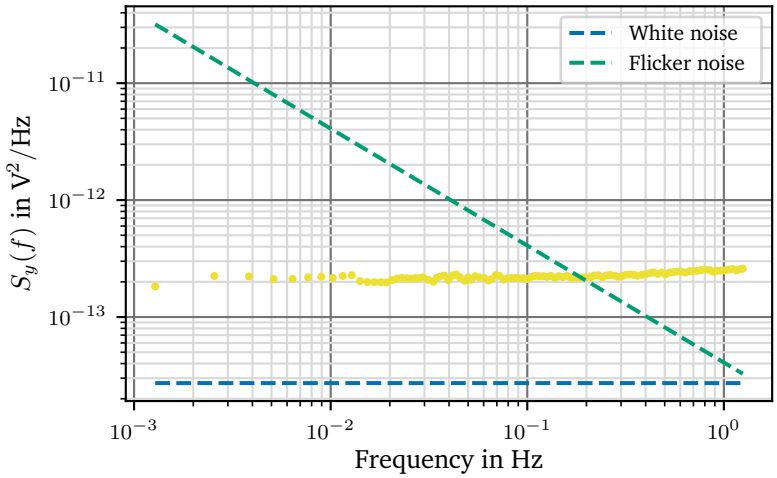

Figure 3.33.: Simulated power spectrum of a Keysight 3458A with autozeroing applied. The dashed lines denote the noise present prior to applying the autozero algorithm. The line frequency is $50\,\mathrm{Hz}$.

Nonetheless, down to very low frequencies, f^{-1} noise is effectively suppressed and the spectral density is almost perfectly flat. For reference, the dashed lines show the noise content that was present in the dataset prior to autozeroing, which is less white noise, but far more flicker noise.

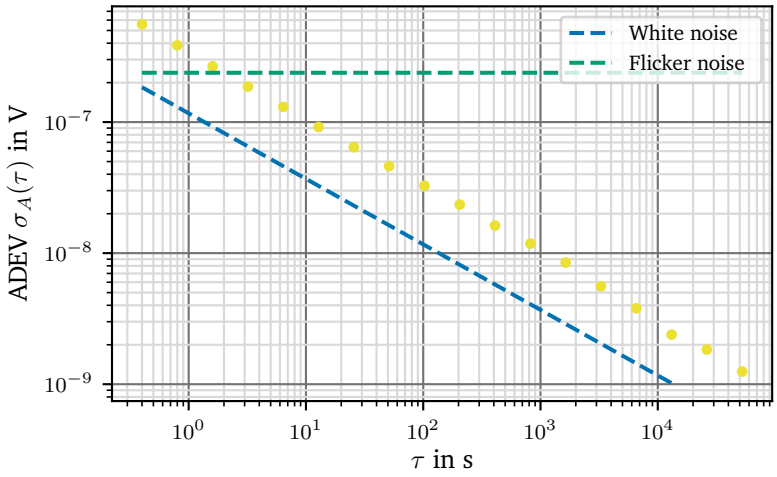

Figure 3.34.: Simulated Allan deviation of a Keysight 3458A with autozeroing applied. The dashed lines denote the deviation prior to applying the autozero algorithm. The line frequency is $50\,\mathrm{Hz}$.

The Allan deviation plot in figure 3.34 also confirms that white noise is the only component and shows a $\tau^{-\frac{1}{2}}$ dependence for the full range of integration times.

From this plot it can be seen that for measurement times longer than about $2\,\mathrm{s}$ or $100\,\mathrm{PLC}$, autozeroing has a clear benefit over a measurement without autozeroing. It must be noted though that, judging from this simulation, the device would reach a noise floor of $0.01\,\mu\mathrm{V/V}$ only at integration times of slightly more than $10\,\mathrm{s}$, while the datasheet claims $2\,\mathrm{s}$. Do note, that this simulation is for the $10\,\mathrm{V}$ range of the DMM and therefore $0.01\,\mu\mathrm{V/V}$ is $0.1\,\mu\mathrm{V_{rms}}$. It is therefore likely that the noise parameters of a real device are better than the numbers used in the simulation. Additionally, the datasheet likely refers to an instrument that is synced to a $60\,\mathrm{Hz}$ power line frequency which shifts the sampling frequency up by $20\,\%$ and, as discussed, reduces the noise floor because more noise content is white noise at the autozero interval. In this simulation the $0.01\,\mu\mathrm{V/V}$ ($0.1\,\mu\mathrm{V_{rms}}$) noise level would be reached at exactly $10\,\mathrm{s}$ when using a line frequency of $60\,\mathrm{Hz}$. For the purpose of demonstrating the autozeroing algorithms these subtleties are irrelevant.

For the comparison of different ADC integration intervals before applying autozeroing figure 3.35 can be consulted. Using the Allan deviation makes it very simple to compare noise figures for identical measurement times τ, yet different integration times, before autozeroing is applied. The simulation source code can be found in data/simulations/sim_optimal_autozero.py as part of the online supplemental material [42].

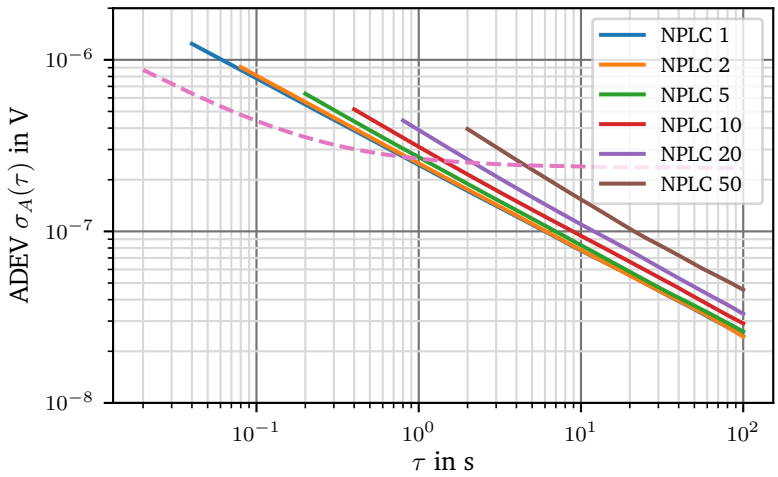

Figure 3.35.: Allan deviation for different ADC integration intervals before applying the AZ algorithm. Dead time $\theta = 0\,\mathrm{s}$. The dashed line denotes the Allan variance without autozeroing. The line frequency is $50\,\mathrm{Hz}$.

It can be seen that with an increasing integration time before applying the AZ algorithm more uncertainty is accumulated due to the f^{-1} content which cannot be filtered. As a result, after removing the f^{-1} content using autozeroing more time is required for filtering until the same Allan deviation can be reached. From these simulations it can be concluded that if there is only a negligible dead time θ involved when switching the inputs, it is advantageous to switch early, while white noise is still dominating the noise content.

Finally, the case of a non-negligible dead time shall be treated. When the dead time has to be considered, it is clear that the autozero frequency cannot be arbitrarily increased, because an increasing proportion of sampling time is lost to the dead time. This effective loss in sampling time then increases the noise spectral density due to aliasing as discussed above. To show this

effect, the simulation above is modified to include a dead time of 1 PLC as detailed in figure 3.28. The dead time is added once after each measurement because the input is switched after each measurement. There are also alternative switching patterns like the one proposed by Schieder et al. [193] splitting the measurement interval in two and instead of measuring HI-LO-HI-LO-HI-LO, to measure HI-LO-LO-HI-HI-LO. This scheme has both advantages and disadvantages, because f^{-1} flicker noise is correlated and its autocorrelation function decays with const. $-\ln(\tau)$ [233, 239]. Therefore constantly changing the order of subtracted samples is not as efficient in removing the noise as the normal autozero procedure because neighbouring samples are highly correlated. Only when the dead time is large in comparison to the measurement time, this method yields an advantage. Some measurements also allow for another scheme. If the measurement is differential, the HI and LO input can be inverted without incurring the noise penalty of equation 3.70 because both measurements taken contain the desired data. This puts the autozeroing closer to a synchronous detection scheme, but this is outside the scope of this discussion. For the sake of simplicity, only the case of a HI-LO-HI-LO measurement mentioned first is treated here. To compare the zero dead time case with the non-negligible dead time case, the Allan deviation for different integration times is again evaluated in the same way as it was in figure 3.35. The results are shown in figure 3.36.

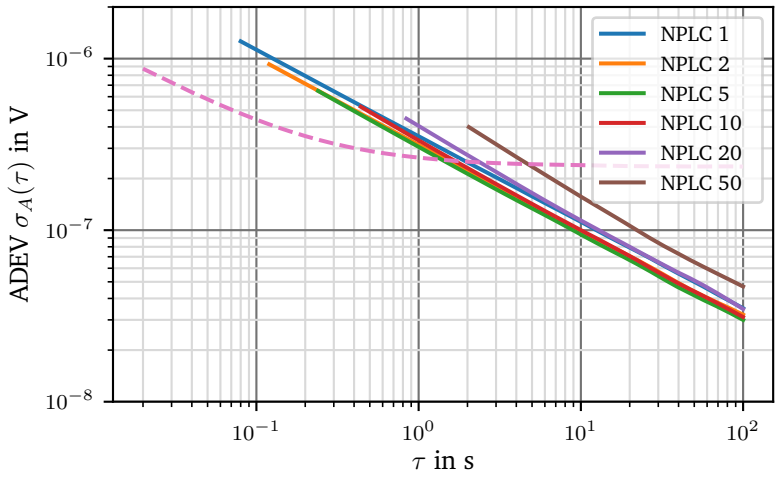

Figure 3.36.: Allan deviation for different ADC integration intervals before applying the AZ algorithm. Dead time $\theta = 1\,\text{PLC}$. The dashed line denotes the Allan variance without AZ. The line frequency is $50\,\text{Hz}$.

Figure 3.36 demonstrates that the effectiveness of the AZ scheme no longer keeps increasing with an ever rising switching frequency. Instead, there is an optimal autozero interval. Above this optimal frequency, the portion of time spent with dead time is getting too large and too little information is collected. For the parameters chosen for this simulation ($f_c = 1.5\,\text{Hz}$ and $165\,\text{nV}/\sqrt{\text{Hz}}$), $5\,\text{PLC}$ at $50\,\text{Hz}$ is the optimal interval. If the corner frequency is shifted to a lower frequency, the optimum shifts more towards $10\,\text{PLC}$. The same goes for a higher line frequency of $60\,\text{Hz}$. This explains, why HP chose $10\,\text{PLC}$ as the maximum integration time. For integration times higher than that, software averaging is used delivering the performance shown in figure 3.36 along the $10\,\text{PLC}$ line.

It should be stressed here that the dead time is not the only factor to consider when choosing the autozero interval. For example, in case of an amplifier, switching the input also adds an error current due to the charge injection of the switching transistors. This may negatively impact the

measurement of a high impedance source. These additional drawbacks are implementation specific and must already be considered during the design phase.

3.7.2. Gain Correction

The effect of the gain correction, where the input value x is scaled by a scaling factor y to adjust the gain error, can be calculated, assuming white noise, as follows:

$$\begin{aligned}
\sigma_{x\cdot y}^2 &= \langle x^2 y^2 \rangle - \langle xy \rangle^2 \\
&= \langle x^2 \rangle \langle y^2 \rangle + \underbrace{2\,\mathrm{Cov}\left(x^2, y^2\right)}_{\text{uncorrelated}=0} - \left(\langle x \rangle \langle y \rangle + \underbrace{2\,\mathrm{Cov}\left(x, y\right)}_{=0} \right)^2 \\
&= \left(\sigma_x^2 + \langle x \rangle^2\right) \cdot \left(\sigma_y^2 + \langle y \rangle^2\right) - \langle x \rangle \langle y \rangle \\
&= \sigma_x^2 \sigma_y^2 + \sigma_x^2 \langle y \rangle^2 + \sigma_y^2 \langle x \rangle^2
\end{aligned} \tag{3.71}$$

With respect to the gain correction, equation 3.71 can be further simplified. The scaling factor is derived from the reference voltage V_{ref} and normalised using $\frac{V_{ref,measured}}{V_{ref}}$. The expected value, therefore is $\langle y \rangle \approx 1$, as the ADC full scale gain should not drift much. Furthermore, σ_y^2 is scaled by the constant $1/V_{ref}$ and $\sigma_x^2 \sigma_y^2 \ll \sigma_x^2$. The latter should be true for any measurement of significance.

$$\sigma_{x\cdot y}^2 \approx \sigma_x^2 + \sigma_y^2 \langle x \rangle^2 \tag{3.72}$$

The gain correction noise therefore behaves similar to the offset correction case, except that it scales with the input voltage x and has no effect with a shorted input, while fully introducing its additional noise when a full scale input is applied.

3.8. Current Sources

Throughout this work the concept of current sources is widely used, for example section 3.2 discusses a current source to drive laser diodes and the temperature controller discussed in section 4.4 uses a current source to measure the resistance of a temperature sensitive resistor. While there are many more use cases, this section will limit the discussion to a few examples used by the devices presented in this work. Namely, a unidirectional transconductance amplifier with an operational-amplifier in conjunction with a field-effect transistor and a bidirectional Howland current pump invented by Bradford Howland in 1962 and first published in 1964 by Sheingold [201]. The discussion will start with the properties of the ideal current source and, based on this, develop a more accurate model. The models developed typically represent the static, time-independent case unless explicitly stated. First, the unidirectional current source is treated, then the bidirectional Howland current pump is discussed.

3.8.1. Current Sink and Current Source

The question whether to use a current source or a current sink is elemental for the design of a laser driver. Figure 3.37 shows different configurations of current sinks and sources with respect to the laser diode.

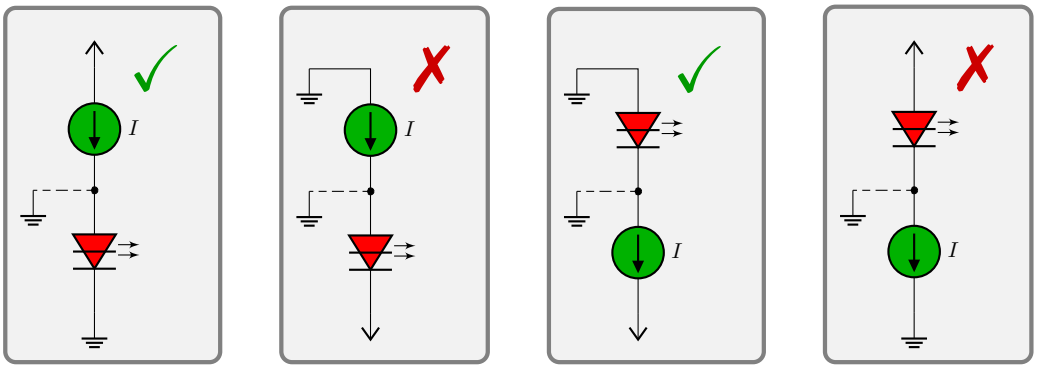

(a) Source with grounded LD. (b) Source with floating LD. (c) Sink with grounded LD. (d) Sink with floating LD.

Figure 3.37.: Different configurations of current sinks and sources with respect to the laser diode. A green check mark denotes a fail-safe configuration when accidentally shorting one or more pins of the diode to the laser chassis, illustrated by a dashed connection.

The optimal configuration depends on the laser diode and safety aspects in terms of protecting the laser diode. The protection of the laser diode is discussed first. The laser resonator is assumed grounded in the setup. This is not the design case, but incorrect assembly can facilitate this condition. While not intended, there are numerous ways to also accidentally short-the diode to ground and since there are no immediate consequences arising from it, when the controller is disconnected, it might easily be overlooked. This blunder should not bear the risk of destroying an expensive laser diode. To ensure this, a configuration where the laser diode is shorted out, instead of the current source or sink, must be chosen. That way, the laser diode is automatically removed from the circuit in case of an error condition. Choosing between a current sink and a current source is more subtle. If the other shell of the laser diode

is connected to the anode, a current sink can be considered to keep the diode can at ground potential. This is not an issue with the laser design in this group though, because the laser diode mount is floating. Another aspect is the electronics. A current source is typically implemented using p-channel field-effect transistors, while current sinks are using n-channel transistors and additionally the input of a current source is referenced to the positive supply, while the sink is referenced to the negative supply. Using the negative supply as a reference for control signals brings more challenges than vice versa, because typically integrated components like digital-to-analog converters prefer working with positive voltages and would need additional support to be floated to a negative reference. This makes a current source simpler to implement in this scenario and this work focuses on the current source. In principle all methods that will be discussed can be applied to a current sink as well.

3.8.2. Ideal Current Source

The ideal current source as shown in figure 3.38 has two major properties besides the output current I_{out}, the output impedance R_{out} and the compliance voltage, which are best understood when looking at the two equivalent representations of a current source separately. On the left in figure 3.38 (a), the Norton representation can be seen. Norton's theorem reduces any linear circuit to a current source, shown in green, with a parallel resistance R_{out}, usually called output resistance or impedance. On the right, the Thévenin representation can be seen, which simplifies a circuit as a voltage source, also shown in green, with a series resistance.

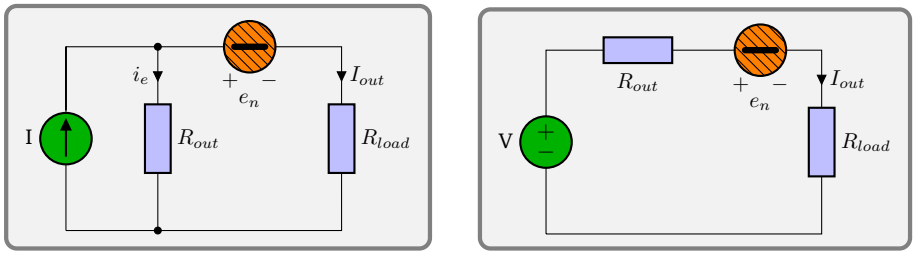

(a) Norton representation. (b) Thévenin representation.

Figure 3.38.: An ideal current source with output impedance R_{out} and noise e_n.

First, the output impedance is discussed. Ideally, R_{out} is infinite and all current is forced to flow through the load. Given a finite output impedance leads to a decreased accuracy of I_{out}, because it is influenced by the load impedance as

$$I_{out} = I_{set} \cdot \frac{R_{out}}{R_{load} + R_{out}} \,. \tag{3.73}$$

In addition to a decreased accuracy, inserting a noise voltage source between the current source and the load as shown in figure 3.38 in orange, has the same effect as a changing load resistance and due to the finite output impedance R_{out}, any voltage noise e_n translates to current noise i_n through the load as

$$i_n = \frac{e_n}{R_{load} + R_{out}} \approx \frac{e_n}{R_{out}} \,, \tag{3.74}$$

again making a high output impedance desirable to suppress noise sources between the current source and the load.

Going to figure 3.38 (b) of a current source in the Thévenin representation allows discussing the compliance voltage property. As it was said above, the output impedance of an ideal current source is infinite and so is the maximum output voltage of said current source. A finite output impedance immediately implies a finite supply voltage to keep the current to a finite limit, which dictates a maximum output voltage. This is called the compliance voltage.

3.8.3. The Field-Effect Transistor Current Source

Given the limited supply voltage of a real current source drives the need for a resistive element that has a finite resistance and infinite, or very high, frequency dependent dynamic impedance to react to load changes. One such pass element, having these properties, is a field-effect-transistor (FET). A junction-gate field-effect transistor (JFET) or metal–oxide–semiconductor field-effect transistor (MOSFET) can be used either as a current source or sink, depending on its doping. A p-channel FET, which uses a positive doping of the channel, is a current source, while an n-channel FET works as a current sink. This discussion is focussing on the p-channel FET with MOSFETs at its centre, because it covers the bulk of the laser current driver design in section 3.2.

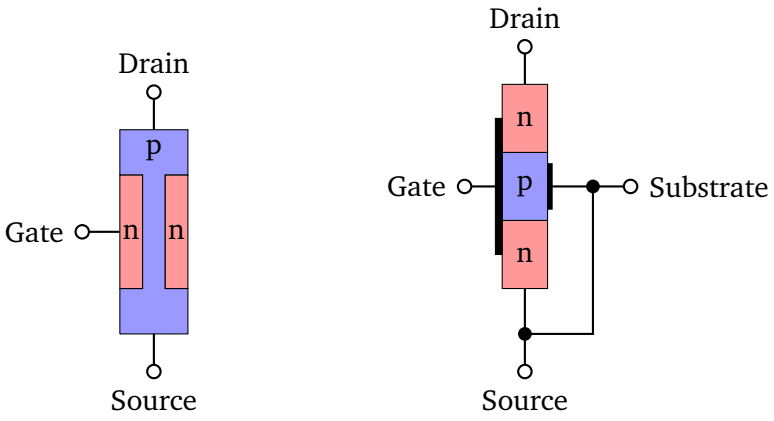

(a) P-Channel JFET. (b) P-Channel MOSFET.

Figure 3.39.: The simplified semiconductor structure of a JFET and a MOSFET.

The difference between a JFET and a MOSFET is the gate structure as illustrated in figure 3.39. While a MOSFET has an insulated gate, the JFET does not. This reduces the gate leakage current, typically by about three orders of magnitude and allows to forward bias the device since there is no diode, resulting in larger current handling capacity. So for low currents up to a few mA or low noise applications, JFETs are preferred, while MOSFETs can handle several hundred ampere. The same mathematical approach can be applied to both types of FETs though. The other difference between a JFET and a MOSFET is the fact that JFETs are only available as depletion-mode (normally-on) devices, while MOSFETs are available as both depletion and enhancement (normally-off) devices. The reason is the gate structure as mentioned above. An enhancement-mode device does not conduct when the gate-to-source voltage $V_{GS} = 0\,\mathrm{V}$, so V_{GS} must be decreased or the junction enhanced for the device to allow conduction. This is not possible with an uninsulated gate like a simple n-p junction of a JFET, which would then start conducting. A p-channel depletion-mode device on the other hand conducts at $V_{GS} = 0\,\mathrm{V}$ and V_{GS} must be increased and the junction depleted to reduce the current, which is possible

with the uninsulated gate, because the n-p junction is reverse biased. The annotated circuit symbol and the quantities used to discuss the device properties are shown in figure 3.40.

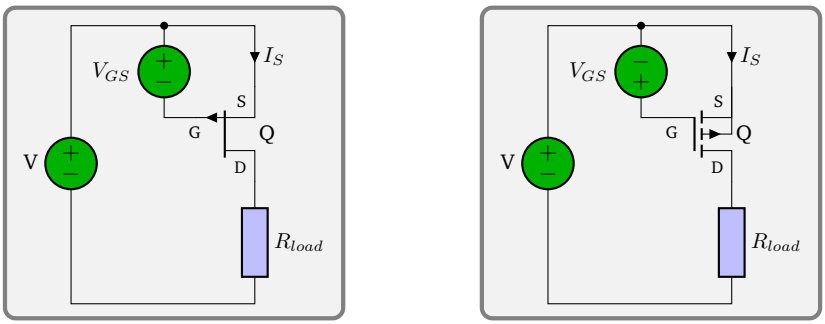

(a) P-channel JFET. (b) P-channel MOSFET.

Figure 3.40.: Basic p-channel FET circuit.

A p-channel FET has its source (S) connected to the positive supply and the drain (D) is connected to a more negative voltage, typically the load. For the MOSFET the gate (G) is biased below the source to allow conduction. The source is usually connected to the substrate for solitary devices as shown in figure 3.39 (b). This will be assumed in all further discussions and the consequences of a substrate that is biased differently are omitted here. The interested reader may look up these details in [21].

As it was hinted above, if appropriately biased, a FET can be considered a voltage controlled current source. This property can be seen in figure 3.41.

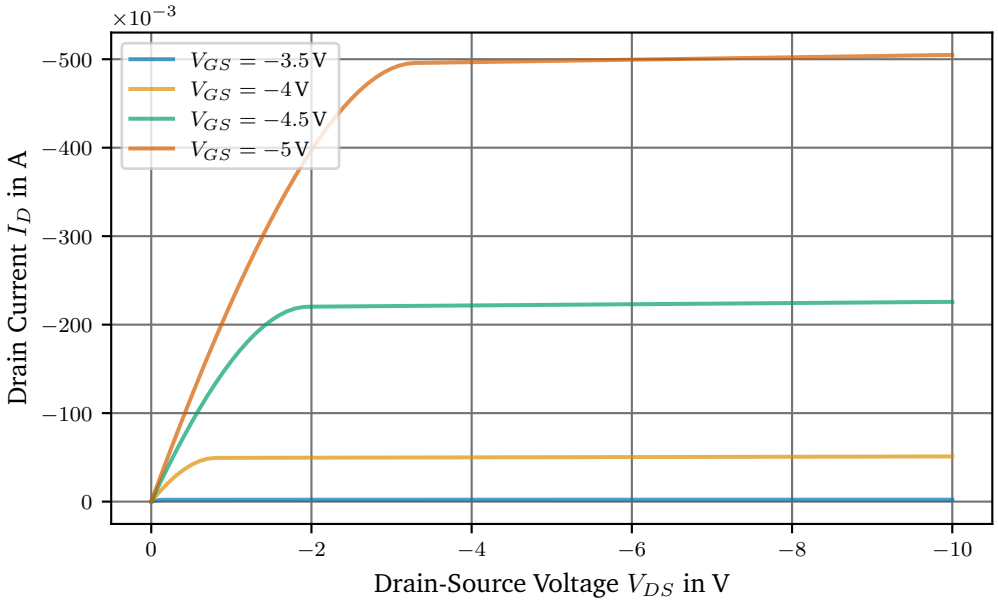

Figure 3.41.: Simulated drain current for different gate bias voltages of an `IRF9610` p-channel MOSFET.

Figure 3.41 shows the current I_D flowing out of the drain of a p-channel MOSFET over the drain-to-source voltage V_{DS} which is applied across the FET. For illustrative purposes an

example p-channel MOSFET was chosen and its *Simulation Program with Integrated Circuit Emphasis* (SPICE) model [45, 95] was used to generate the data, yet the overall shape is the same for all FETs. For more information on modelling MOSFETs in SPICE, [56, p. 442] can be consulted. There are two regions, the first region, where $V_{DS} > V_{GS} - V_{th}$, demonstrates an almost linear correlation of the channel current and the voltage across the device. This is called the ohmic region, where the MOSFET behaves much like a (gate-) voltage controlled resistor and can be described [204] as

$$I_{D,ohmic} = \underbrace{\kappa(V_{GS} - V_{th})V_{DS}}_{\text{ohmic}} - \underbrace{\frac{1}{2}\kappa V_{DS}^2}_{\text{pinch off}} . \tag{3.75}$$

For small voltages V_{DS} the output current is proportional to the applied voltage V_{DS} across the channel just like a normal resistor, giving rise to its name ohmic region. As the voltage increases further I_D starts leveling off because V_{DS} starts affecting the channel conductivity. The channel is slowly getting pinched off at one end and becomes tapered. The reason is that the voltage V_{DS} is dropped across the length of the channel. This voltage drop is linear with V_{DS}, resulting in a $-V_{DS}^2$ dependency of the current, reducing the conductivity of the channel. V_{th} is called the threshold voltage of a MOSFET or pinch-off voltage V_p in case of a JFET and is the voltage at which a current starts flowing.

The parameter κ is a device specific parameter and depends on process parameters and the geometry of the device.

$$\kappa = \kappa' \frac{W}{L} = \mu C_{ox} \frac{W}{L} \tag{3.76}$$

μ is the electron mobility, which is about $1350\,\mathrm{cm}^2/\mathrm{V}$ for n-channel MOSFETs and about $540\,\mathrm{cm}^2/\mathrm{V}$ for p-channel MOSFETs [198]. C_{ox} is the gate-oxide capacitance per unit area and determined by the thickness t_{ox} of the silicon dioxide layer of the gate

$$C_{ox} = \frac{\epsilon_{ox}}{t_{ox}} \approx \frac{3.9 \cdot \epsilon_0}{t_{ox}} \approx \frac{3.45 \times 10^{-11}\,\mathrm{F/m}}{t_{ox}} , \tag{3.77}$$

W is the width of the channel, and L is the length of the channel.

The letter κ is used here instead of the usual k as it is used by Sedra et al. [198] to avoid confusion with the Boltzmann constant k_B. Unfortunately, κ is not well controlled [96], because it is not just determined by the size, but also the doping of the material. While the size of the structure can be well controlled to within a few nm using lithography masks, the doping is a matter of temperature and time in a diffusion furnace. The ohmic mode of operation is, for example, used in switches or linear voltage regulators to control the output voltage of the regulator, forming a low impedance voltage source and not the desired current source. This brings up the next region to discuss.

Once the voltage V_{DS} has reached $V_{GS} - V_{th}$, the channel is fully pinched off, any further increase in V_{DS} will not lead to an increase in I_D, in other words the output resistance becomes infinite. The MOSFET is said to be pinched-off or in saturation. In practice there still is a small influence of V_{DS} on the channel. While the depth can no longer decrease as its length is 0 at one end already, the channel will retract a small amount in length with increasing V_{DS}. This is taken into account by the factor λ, called channel-length modulation. The drain current in saturation can now be described [204] as

$$I_{D,sat} = \underbrace{\frac{1}{2}\kappa \left(V_{GS} - V_{th}\right)^2}_{\text{ideal FET}}(1 + \lambda V_{DS}) . \tag{3.78}$$

The parameter λ is the first order Taylor expansion of the length dependence of κ and typically is small and on the order of 0.01–$0.05\,\mathrm{V}^{-1}$ for p-channel MOSFETs [182, p. 23]. It mainly depends on the length of the channel to which it is inversely proportional, since the channel length defines the slope of the tapered channel. Sometimes the value $\frac{1}{\lambda}$ is also referred to as the Early voltage V_A. It is noteworthy that more modern processes choose a smaller channel length to reduce the on-state resistance of the MOSFET because the main application of a MOSFET nowadays is as a switch. The reduced channel length makes the MOSFET more susceptible to the channel length modulation effect. This will be discussed in more detail in section 3.8.7, when choosing a suitable MOSFET.

Going back to figure 3.41 the effect of the channel-length modulation can be seen as a small slope of I_D in the saturation region.

Combining the previous equations, the FET drain current behaviour can be summed up as

$$I_D = \begin{cases} 0 & \text{if } V_{GS} - V_{th} < 0 \\ \kappa(V_{GS} - V_{th})V_{DS} - \frac{1}{2}\kappa V_{DS}^2 & \text{if } V_{GS} - V_{th} >= 0 \text{ and } V_{DS} < V_{GS} - V_{th} \\ \frac{1}{2}\kappa \left(V_{GS} - V_{th}\right)^2 (1 + \lambda V_{DS}) & \text{if } V_{GS} - V_{th} >= 0 \text{ and } V_{DS} \geq V_{GS} - V_{th} \end{cases} \tag{3.79}$$

The saturation region is the region of interest for building a high output impedance current source, because for a wide range of V_{DS} the current remains almost constant and can be adjusted using the gate voltage V_{GS}. As a reminder, for the p-channel MOSFET, all voltages are reversed. V_{GS}, V_{th}, V_{DS}, κ and I_D are negative. Some datasheets therefore only give the magnitude of those quantities. The important aspect to remember is that for the p-channel enhancement-mode MOSFET the gate must be biased negative with respect to the source pin by a least the threshold voltage ($V_{GS} < V_{th}$ or $|V_{GS}| > |V_{th}|$) to turn the transistor on and allow current to flow.

Before proceeding to the precision current source in section 3.8.4, the concept of conductance and transconductance must be explored. The transconductance describes the relationship of the input voltage with the output current. The conductance is a measure for how well current flows from input to output. The transconductance g_m and the channel conductance g_{DS} are defined as

$$g_{m,sat} \coloneqq \left.\frac{\partial I_{D,sat}}{\partial V_{GS}}\right|_{V_{DS}=const} = \kappa \left(V_{GS} - V_{th}\right)(1 + \lambda V_{DS}), \tag{3.80}$$

$$= \sqrt{2\kappa I_D (1 + \lambda V_{DS})} \approx \sqrt{2\kappa I_D} \tag{3.81}$$

$$g_{DS,sat} \coloneqq \left.\frac{\partial I_{D,sat}}{\partial V_{DS}}\right|_{V_{GS}=const} = \frac{1}{2}\kappa \left(V_{GS} - V_{th}\right)^2 \lambda \tag{3.82}$$

$$= \frac{I_D}{\frac{1}{\lambda} + V_{DS}} = \frac{1}{R_o} \approx I_D \lambda\,. \tag{3.83}$$

The transconductance g_m, as a measure of the current gain with respect to the gate-source voltage of the MOSFET, is proportional to the square root of the drain current I_D. The inverse of the channel conductance g_{DS} is called output resistance R_o and discussed below. Typically the V_{DS} term in the denominator of the output resistance in equation 3.83 can be neglected.

The meaning of g_m and g_{GS} can be best understood when looking at a mathematical model of the MOSFET. These models come in varying complexity and either as a large-signal or small-signal model. Only the latter is used here. The small-signal model, is a first order Taylor approximation around the working point, for a constant gate-source voltage V_{GS} and constant

drain-source V_{DS}, hence both g_m and g_{GS} are constants.

$$I_D \approx \frac{\partial I_D}{\partial V_{GS}} \Delta V_{GS} + \frac{\partial I_D}{\partial V_{DS}} \Delta V_{DS} \tag{3.84}$$

$$= g_m \Delta V_{GS} + g_{DS} \Delta V_{DS} \tag{3.85}$$

$$= g_m v_{GS} + \frac{1}{R_o} v_{DS} = i_D \tag{3.86}$$

The lower case letters denote the variables of the small-signal model as they only change very little compared to the working point parameters. From 3.86 it can be seen that the g_{DS} term adds to the output current and is proportional to v_{DS}. Comparing this with figure 3.38 (a), the proportionality constant can be identified as $\frac{1}{R_o}$ like proposed above. Just like the ideal current source in figure 3.38, the model can be given in the Norton or Thévenin representation, both shown in figure 3.42.

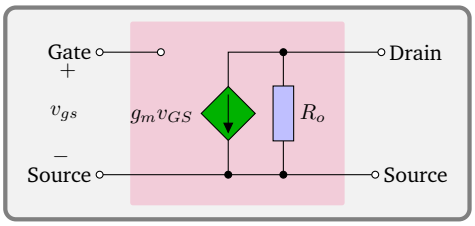

(a) Small-signal model of a saturated MOSFET including the output resistance. The output resistance models the channel-length modulation as given by equation 3.86.

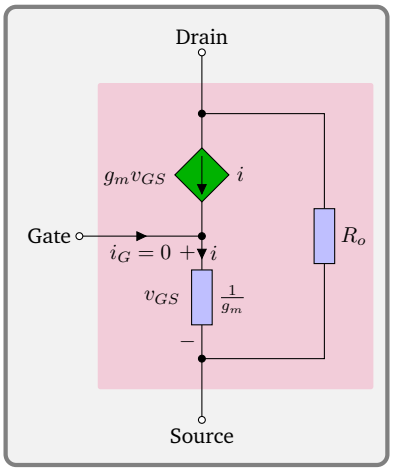

(b) MOSFET model in Thévenin representation.

Figure 3.42.: Equivalent MOSFET models in Norton and Thévenin representations.

A detailed graphic derivation of the Thévenin representation can be found in [198]. The Thévenin representation will prove especially valuable when treating circuits with a resistance in the source leg. The small-signal model now shows that the output impedance is dependent on the channel-length modulation λ and v_{DS}. Typically, $\frac{1}{\lambda} \gg v_{DS}$, so λ is the most important factor governing the output impedance of a MOSFET.

To give an example of the output impedance of a MOSFET, parameters were taken from the aforementioned SPICE model of the `IRF9610`. Do note that these parameters of the model are tuned to match certain operating conditions by their creators and only present an estimation of the real MOSFET. Using the example parameters from table 3.11, $I_D = 250\,\text{mA}$, $\lambda = 4\,\text{mV}^{-1}$, $V_{DS} = 3.5\,\text{V}$ equation 3.83 yields

$$R_{out} = R_o \left(I_D = 250\,\text{mA}, \lambda = 4\,\text{mV}^{-1}\right) = 1014\,\Omega \overset{V_{DS}=0}{\approx} 1\,\text{k}\Omega\,, \tag{3.87}$$

which is not very convincing as a current source. The insignificant impact of V_{DS} on the output impedance can be seen when dropping the V_{DS} term, which leads to an output impedance of $1\,\text{k}\Omega$. In textbooks this dependence is therefore usually neglected. To improve R_{out}, the focus thus lies on the λ dependence. The model derived from equation 3.86 can be used to do so, leading to the precision current source presented next.

3.8.4. Precision Current Source

In the previous section 3.8.3 it was shown in equation 3.86 that the output impedance of a MOSFET depends on the channel-length modulation λ and is too low for practical purposes. On the quest to improve the output impedance of the MOSFET circuit in figure 3.42 (a), the most obvious solution would be to simply add a source resistor R_s into the circuit as shown in in figure 3.43 (a). At first glance this may seem to only add a series resistance to R_o, but the attempt is more intriguing and will lead to an even better solution.

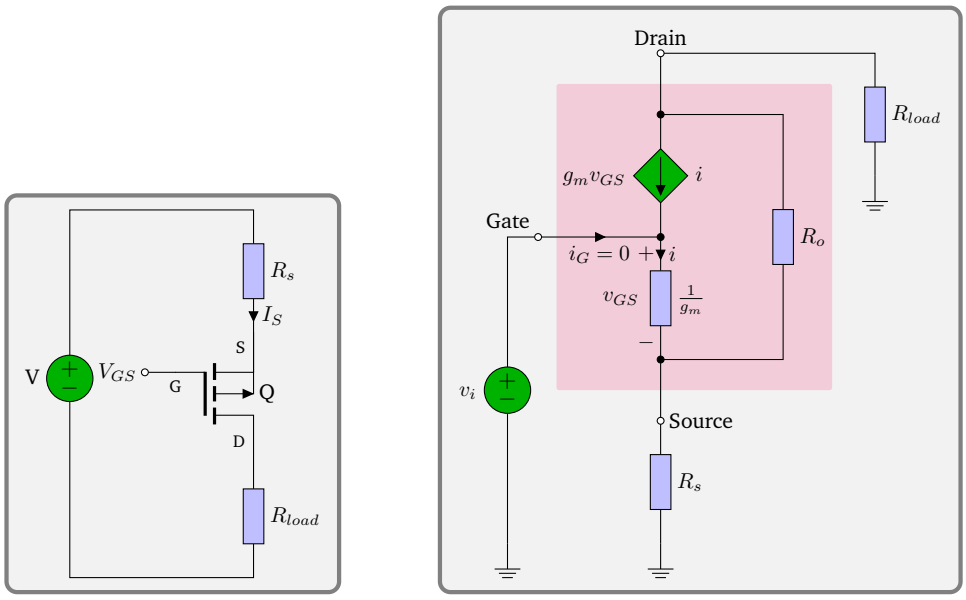

(a) MOSFET with source resistor R_s to improve the output impedance R_{out}.

(b) Small-signal Thévenin model.

Figure 3.43.: Circuit of a MOSFET with source degeneration resistor and equivalent Thévenin model.

Before calculating the output impedance, we shall have a look at v_{GS} and the input signal v_i derived from it. With the introduction of the source resistor R_s, v_i no longer equals v_{GS}, because $\frac{1}{g_m}$ now forms a voltage divider with R_s and it follows

$$v_{GS} = v_i \frac{\frac{1}{g_m}}{R_s + \frac{1}{g_m}} = v_i \frac{1}{1 + g_m R_s} \,. \tag{3.88}$$

This implies a reduction in gain by the factor $\frac{1}{1+R_s g_m}$ compared to the previously discussed approach. The cause of this reduction is negative feedback. To understand this, imagine that with a constant v_i and hence a constant current I_D flowing, a changing load resistance is trying to modulate I_D. Any increase in I_D will cause the voltage across R_s to rise, reducing v_{GS}, because v_i is still constant. The decreasing v_{GS} will then reduce I_D, thus introducing negative feedback. Having realized there is negative feedback present, it can be postulated that the reduction in input sensitivity, or effective transconductance, will be passed on to the output impedance. This very interesting relationship will now be derived.

To calculate the output impedance, figure 3.43 (b) can be simplified by grounding v_i, because there is no AC component as there is no current flowing through the insulated MOSFET gate

and is not modulated. The load R_{load} resistance must is replaced by an AC test voltage v_{load} to modulate I_D. These changes result in the small-signal model shown in figure 3.44. This configuration is also called a common-gate amplifier.

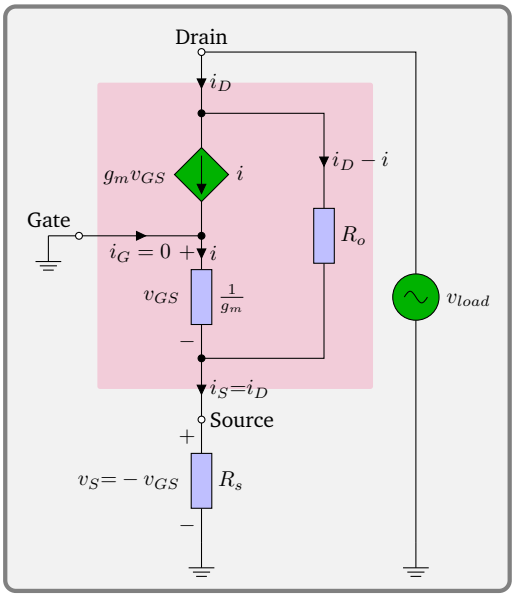

Figure 3.44.: Small-signal model of the common-gate amplifier with source resistance R_s.

The (dynamic) output impedance is given by

$$R_{out,cg} = \frac{v_{load}}{i_D}\,, \tag{3.89}$$

with $i_D = i_S$, since there is no gate current. v_{load} can easily be calculated by looking at figure 3.44 and equals the total voltage across R_o and R_s. v_{GS} can also be found, because the gate is grounded. With the resistance $\frac{1}{g_m}$ at one end, the voltage at the source pin must be $-v_{GS}$.

$$\begin{aligned} v_{load} &= (i_D - i)\, R_o + i_S R_s \\ &= (i_D - g_m v_{gs})\, R_o + i_D R_s \\ &= (i_D + g_m i_D R_s)\, R_o + i_D R_s \end{aligned} \tag{3.90}$$

Using equations 3.89 and 3.90 gives

$$R_{out,cg} = (1 + g_m R_s)\, R_o + R_s \tag{3.91}$$

for the output impedance.

This result is interesting, as it can be be immediately seen that the output impedance scales very quickly with the transconductance g_m and R_s. As it was already speculated above, the reduction in the transconductance $\frac{1}{1+g_m R_s}$ of the MOSFET is transferred to the output impedance, which is increasing by the inverse of the loss in transconductance.

Going back to the quest for an increased output impedance, it is apparent that increasing R_s quickly raises the output impedance, as it scales with $gm_m R_o$, but it would come at the cost of a significantly reduced compliance voltage. Therefore, other means need to be explored. As we have seen, the scale factor $gm_m R_o$ is explained by feedback and this leads to another solution.

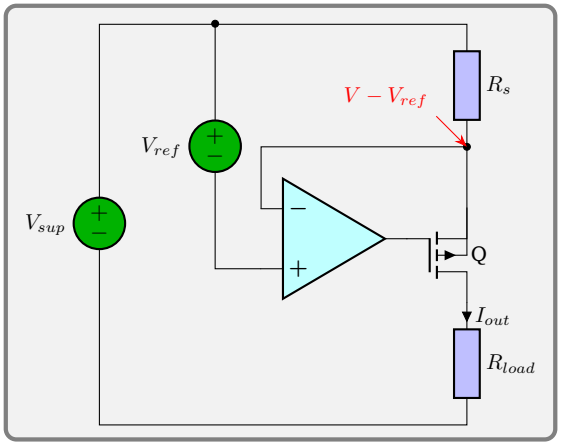

Figure 3.45.: Transconductance amplifier with a p-channel MOSFET.

The amount of feedback can be increased further using an operational amplifier (op-amp) as shown in figure 3.45.

The output impedance of this transconductance amplifier is amplified by the open-loop gain of the op-amp as shown in appendix A.3, while the transfer function greatly simplifies to

$$\begin{aligned} R_{out} &\approx A_{ol} \left(g_m R_o R_s + R_o + R_s \right) \\ I_{out} &\approx \frac{V_{ref}}{R_s} \end{aligned} \tag{3.92}$$

In addition to the increased output impedance, the current $I_D = I_{out}$ can now steered by adjusting V_{ref} and is, given sufficient loop gain of the op-amp, no longer dependent on the MOSFET but rather only on the sense resistor R_s.

This has the added benefit that it is possible to leverage the tight accuracy and precision of a resistor over the poor specifications of a MOSFET. Resistors can be manufactured with tolerances of less than $100\,\mu\Omega/\Omega$, which is orders of magnitude better than FETs, which can be matched to low % values with patience.

Using the example parameters from table 3.11, the output impedance in saturation can now be calculated again for $I_{out} = 250\,\text{mA}$ and the ideal `IRF9610` model with the addition of an idealized `AD797` op-amp using the worst-case specifications.

$$R_{out} \approx 2\,\text{V}\,\mu\text{V}^{-1} \left(0.64\,\text{S} \cdot 1014\,\Omega \cdot 30\,\Omega + 1014\,\Omega + 30\,\Omega \right) \approx 40\,\text{G}\Omega \tag{3.93}$$

From these consideration, it can be seen that the open-loop gain and the unity-gain bandwidth of the op-amp essentially determine the properties of the current source, given that $R_{id} \gg R_s$ and $R_o \gg R_s$. This will be important for selecting an operational amplifier later.

The next section will focus on the MOSFET and discuss the compliance voltage of the current source, which was only briefly touched during the introduction. It will give rise to criteria for selecting a MOSFET for the precision current source.

3.8.5. Compliance Voltage

The compliance voltage of a current source is the maximum voltage it can output to maintain the requested output current. For an ideal current source, the compliance voltage is infinite, but it is obviously limited in the physical world.

The precision current source discussed in section 3.8.4 has several limiting factors of the compliance voltage, which shall be discussed now. The compliance voltage is taxed most at the maximum output current $I_{out,max}$. Thus for the following discussion, the output is always treated as set to maximum.

Looking at figure 3.45 of the precision current source it is immediately evident that the output voltage can be calculated by subtracting the voltage across the source resistor V_{R_s} and the MOSFET V_{DS} from the supply voltage V_{sup}

$$V_{out} = V_{sup} - V_{R_s} - V_{DS} = V_{sup} - V_{ref} - V_{DS}\,.$$

The voltage V_{R_s} is given by equation 3.92 and equal to the setpoint voltage and hence given by the system parameters. This leads to the question of the minimum working point voltage V_{DS} at $I_{out,max}$. As a reminder, from equation 3.79 and figure 3.41 one can see that the drain current is almost constant over V_{DS} in the saturation region, and in the ohmic region is proportional to V_{DS}. The transition point from the ohmic region to the saturation region is at $V_{DS} = V_{GS} - V_{th}$ and putting this into equation 3.79 yields for the drain current

$$\begin{aligned} I_D &= \frac{1}{2}\kappa V_{DS}^2\,(1 + \lambda V_{DS}) \\ \Rightarrow V_{DS} &\approx \sqrt{\frac{2I_D}{\kappa}} && (3.94) \\ &\approx 784\,\text{mV} && (3.95) \end{aligned}$$

The latter result was calculated using the example parameters from table 3.11. At this point it can already be postulated that the MOSFET will severely change in its function as a current source for $V_{DS} < 0.78\,\text{V}$. To quantify this, one has to look at the output impedance of the transconductance amplifier once again. In the last section, the output impedance was only treated for the saturation region, but this time, R_{out} must be considered over a wide range of V_{DS}, thus not only in the saturation region but also in the ohmic region. Instead of using the small-signal model as before, which assumed only small changes of V_{DS}, a large-signal model must be applied, which also includes the non-linear nature of the piece-wise defined equation 3.79 of the drain current.

For the sake of simplicity, a SPICE simulation of figure 3.45 was carried out in LTSpice [162]. Solving this analytically bears no educational value over the numerical solution shown below as will be seen. Additionally, the SPICE simulation also offers the opportunity to add additional, parasitic elements to the model to evaluate their effect, for example, the capacitive nature of the MOSFET gate.

The simulation itself is numerically challenging and the typical approaches will lead to the limits of the numerical precision. To make the simulation feasible, the large-signal model is broken down into several small segments. For each of these segments, the small-signal model at its respective working point is evaluated and then the result joined back together to reconstruct the large-signal model sought. How this is done in detail, is shown in appendix A.4 as it is beyond the scope of this section. The final result was calculated for two different frequencies, one frequency was deliberately chosen so low ($1\,\mu\text{Hz}$) that it is well below the dominant pole of the op-amp, meaning that the full open-loop gain applies and the other frequency chosen was $1\,\text{MHz}$, were the gain had dropped to $10\,\text{V/V}$. This is shown in figure 3.46.

Looking at figure 3.46 clearly shows the effect of entering the ohmic region of the MOSFET. Over a range of $100\,\text{mV}$ starting at the $0.78\,\text{V}$ calculated above, the output impedance drops by two orders of magnitude and then keeps dropping at an exponential rate with decreasing V_{DS}.

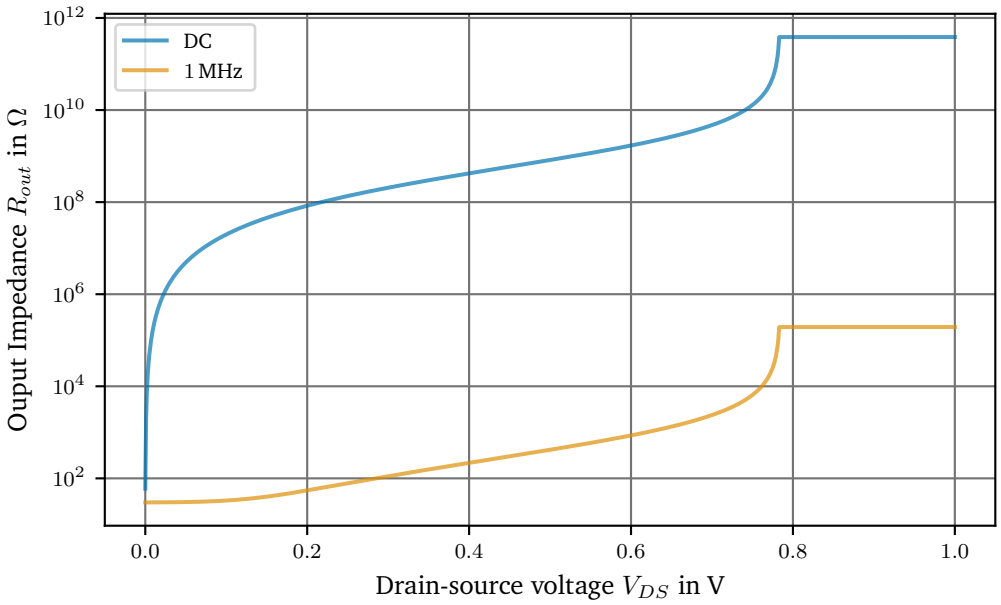

Figure 3.46.: Simulated output impedance for the precision current source from figure 3.45 at DC and 1 MHz over the drain-source voltage.

The same effect applies to the output impedance at 1 MHz, although the starting value of the output impedance is around 200 kΩ due to the reduced gain from the op-amp at 1 MHz. It can also be seen that R_{out} levels off at 30 Ω, the value of the sense resistor.

This overall effect of leaving the saturation region is so drastic that the compliance voltage must be defined in such a way that the MOSFET remains in saturation and this leads to

$$V_{comp} = V_{sup} - V_{ref} - \sqrt{\frac{2I_D}{\kappa}}\,. \tag{3.96}$$

Now turning to the supply voltage, it is limited by the op-amp which must drive the gate of the MOSFET all the way up to the supply to turn off the current source. The reference voltage is, unless one divides it down dictated by the reference chosen. This, unfortunately, leaves only little room for the MOSFET and it must be carefully chosen not limit the compliance voltage too much.

At this point a fallacy the author has observed multiple times must be addressed. In order to address the limited compliance voltage, one may be tempted to use multiple MOSFETs in parallel to divide the current between the MOSFETs and thereby reduce the voltage that needs to be dropped across the FET proportional to $\frac{1}{\sqrt{N}}$, where N is the number of MOSFETs paralleled.

Imagine the following modified circuit of the precision current source shown in figure 3.47 with two MOSFETs in parallel. For clarity the gate resistors required are not included.

While at first this seems like a solution to the limited V_{DS}, it is not recommended for a number of reasons given here.

The first reason is, MOSFET specifications are very loose, notably the threshold voltage V_{th}, the transconductance g_m and the capacitances, but the latter is of little concern here. These tolerances limit the usefulness of paralleling MOSFETs to certain conditions, for example, when

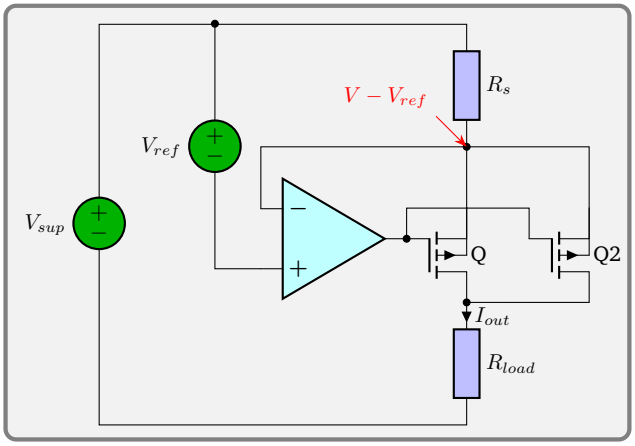

Figure 3.47.: Transconductance amplifier with two p-channel MOSFETs in parallel.

using the MOSFETs as a switch ad not as a current source. The difference between its use as a switch and a current source is the thermal load, which is a lot higher when using the MOSFET as current source. In this respect it seems to be a common misunderstanding that MOSFETs are immune to thermal runaway. This is mostly true when using them as a switch, fully turned on and in the ohmic region. In this case, there are two effects occurring, the first is that the (absolute) value of V_{th} decreases with temperature, thus increasing I_D and the second effect is, $R_{DS,on}$ is rising with temperature [48]. The latter effect is, depending on the physical design, stronger, but it depends on the specific MOSFET. A detailed analysis of paralleling MOSFETs as switches can be found in [81]. In case the MOSFET is operating in pinch-off and not the ohmic region, $R_{DS,on}$ has no influence on the current, therefore, the only effect at work is the decreasing V_{th}. Depending on the difference in V_{th} between the paralleled MOSFETs, one MOSFET will take most of the current and power. Adding source resistors can compensate for this by pushing down the source voltage as the current goes up. This will then reduce V_{GS}. The size of the resistor depends on the transconductance g_m and the temperature coefficient of V_{GS}, which is around 1.5–$2\,\mathrm{mV/K}$ [84]. Unfortunately, $1\,\Omega$ or $2\,\Omega$, will already use up, most of the benefits gained in compliance voltage as will be shown below.

The second reason why paralleling MOSFETs is not desirable can be seen when remembering equation 3.79. It is known that the transition from the unwanted ohmic region to the saturation region is

$$V_{DS} \geq V_{GS} - V_{th}\,. \tag{3.97}$$

Looking at 3.47, it can be seen that V_{GS} is set by the op-amp and is the same for both MOSFETs because their gates and sources are connected. However, V_{th} is device specific and according to the datasheet of the example `IRF9610` [104] V_{th} values can show a spread of as much as -2 to $-4\,\mathrm{V}$, although [170] suggests that MOSFETs from the same reel show a spread of only $\pm 125\,\mathrm{mV}$ of V_{th} within the same batch for consecutive devices. The $125\,\mathrm{mV}$ was found for the `BUK7S1R5-40H` [50], which was sampled in this report. The number given in the report is for 3σ and, assuming the datasheet values for the spread are also referring to 3σ, the spread found in the report is about twice as high as the datasheet value of 2.4–$3.6\,\mathrm{V}$. Assuming similar numbers for `IRF9610` MOSFET used in our examples, this leads to $\pm 208\,\mathrm{mV}$ for the `IRF9610`, again applying 3σ. Using this number, a Monte Carlo simulation (not quite, because the dice were biased to yield a Gaussian distribution instead of equal probabilities) was run using LTSpice, simulating the circuit shown in figure 3.47 and also the original circuit using

only one MOSFET. For this simulation the current source was set to $250\,\text{mA}$ as per table 3.11. The load voltage was set to

$$V_{DS,parallel} = \sqrt{\frac{2\frac{I_d}{2}}{\kappa}} \approx 555\,\text{mV}\,, V_{DS,single} = \sqrt{\frac{2I_d}{\kappa}} \approx 784\,\text{mV}\,.$$

$\frac{I_D}{2}$ was used to calculate $V_{DS,parallel}$ for the parallel configuration to show the effect assuming perfect current sharing between the MOSFETs. Additionally, a configuration with an increased safety margin of $1\sigma = 70\,\text{mV}$ added to $V_{DS,parallel}$ was investigated. 4000 samples were drawn and the spread of the output impedance was calculated for each circuit. The results are shown as a histogram in figure 3.48. The counts give the number of cases for each bin of the output impedance.

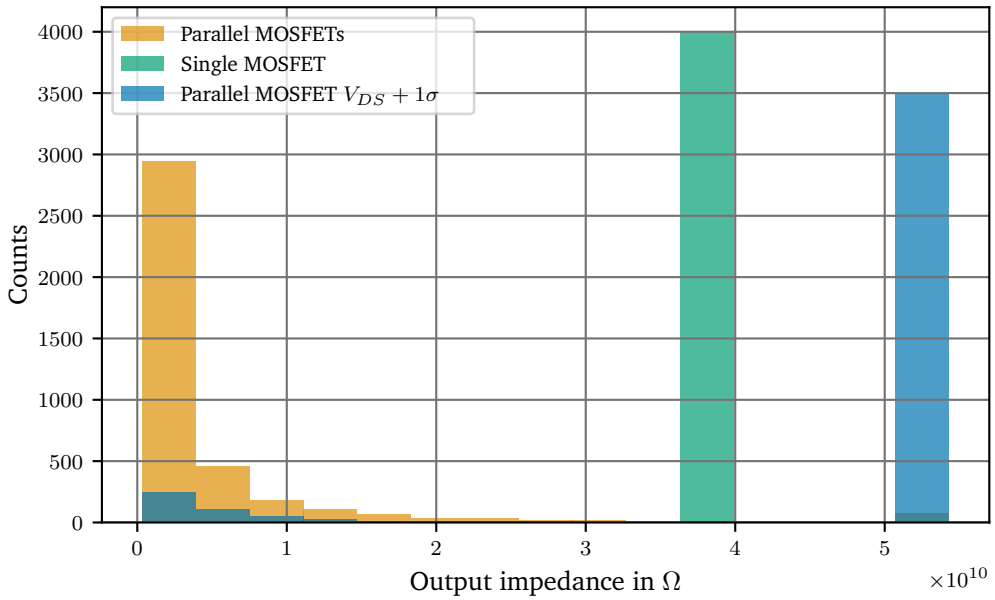

Figure 3.48.: Results of a Monte Carlo simulation of the output impedance for different configurations of MOSFETs.

Unsurprisingly, there is no variance of the output impedance in the single MOSFET case in accordance to what can be seen in appendix A.3. The op-amp gain simply suppresses all device properties of the MOSFET. The slight variation of g_m for different samples was not simulated, because this variation stems from the variation of κ and goes as $\frac{1}{\sqrt{\kappa}}$, so its effect is not as pronounced as the threshold.

In case of two MOSFETs, the output impedance varies over an order of magnitude from about 1.8–$52\,\text{G}\Omega$. Even when increasing the drain-source voltage by $1\sigma = 70\,\text{mV}$ to $625\,\text{mV}$ on average, the spread is still an order of magnitude. Only when increasing V_{DS} to around $700\,\text{mV}$, the situation stabilises, but then the net gain from this measure has shrunk to a meager $84\,\text{mV}$. It can be seen from this simulation that the system-to-system spread becomes very unstable in tough situations. Such instability can also be brought into the system by temperature effects as V_{th} is temperature dependent as discussed above. Additionally, it may suffer from thermal runaway unless each individual MOSFET is laid out to carry the full current.

3.8.6. Noise Sources

The fundamentals of different types of noise were already introduced in section 3.6. Here, a subset of those noise types is revisited. It is expected that the dominant noise observed in the current source circuit is $\frac{1}{f}$-noise at low frequencies and white noise towards higher frequencies. All noise components will be converted to the so-called input referred notation to make the noise sources comparable. This can be easily understood when looking at two amplifiers with different gain. If both of them add a fixed amount of noise to the output signal, the absolute amount of noise may be the same, but the signal to noise ratio shows a different picture. To compare these amplifiers it is useful to divide the noise by the transfer function (gain) of the amplifier. This is called the input-referred noise, since it treats the noise in relation to the input signal. Additionally, when calculating noise figures, the noise bandwidth is always considered to be 1 Hz unless specified otherwise.

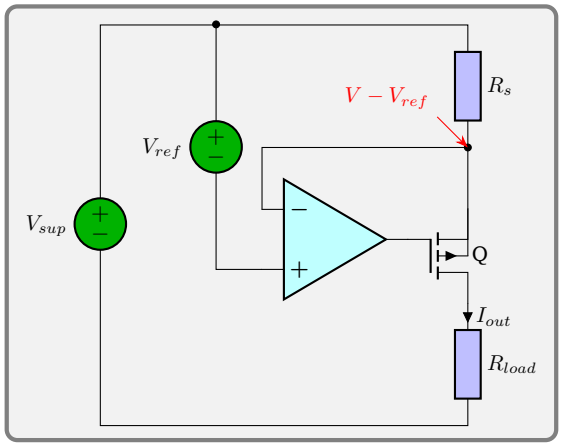

Figure 3.49.: Transconductance amplifier with a p-channel MOSFET. Copied from page 78.

Noise sources are ubiquitous in the circuit shown in figure 3.49, which is repeated here from figure 3.45 on page 78 for clarity. The resistor R_s, the MOSFET, the op-amp, the setpoint voltage V_{ref} and the supply voltage V_{sup} can all contribute noise to the output current. Fortunately, some of those noise contributions are either very small or well suppressed in this design, so each component must be briefly discussed to see if they can indeed be safely neglected.

Starting with the supply voltage V_{sup}, it can be seen that any change of this voltage affects the string R_s-Q-R_{load}. From equation A.8, it is known that if the op-amp gain is high (true within the bandwidth of the op-amp) all disturbances of the voltage across R_s will be suppressed and the output current is only defined by the reference input and R_s. Looking closer, the supply noise is present at the inverting and non-inverting input of the op-amp with the same magnitude. If there is no current flowing into the op-amp pins, which is true for low frequencies, the noise is affecting both pins equally and it will be suppressed by the common-mode-rejection ratio (CMRR) of the device. Fortunately, this is a strong quality of precision op-amps and values of more than $1\,\mu V V^{-1}$ are not uncommon. The op-amp will therefore take care of the supply noise at low frequencies. At high frequencies the parasitic capacitance of the input pins and the reduced gain and CMRR come into play. To take care of this, it is therefore prudent to filter the supply voltage for high frequency noise.

The next noise source is the reference voltage. The reference is directly connected to the input and its noise dictates most of the circuit noise. While the high-frequency noise can again be filtered to some extend, the low frequency noise, which is mostly $\frac{1}{f}$-noise cannot be filtered

as was shown in section 3.6.1, so it must be kept low from the start and the reference selected for low flicker noise.

The MOSFET as a noise source is considered in appendix A.5 and the interested reader may find the derivation of the MOSFET noise component there. The two types of noise that need to be considered are the flicker noise of the MOSFET and its wideband thermal noise as calculated in equation A.20 on page 228

$$i_n = \sqrt{\underbrace{4k_BT\frac{2}{3}g_m}_{\text{thermal}} + \underbrace{\frac{K_f I_D}{C_{ox}L^2}\frac{1}{f}}_{\text{flicker}}}\,.$$

To calculate the input referred noise in order to show that the MOSFET noise will be suppressed by the op-amp, the current noise needs to be divided by the open-loop gain derived as equation A.7 on page 220

$$e_{n,FET} = \frac{i_n}{A_f} = \frac{\sqrt{4k_BT\frac{2}{3}g_m + \frac{K_f I_D}{C_{ox}L^2}\frac{1}{f}}}{\frac{A_{op}}{R_s}\frac{g_m(R_o||R_s||R_{id})}{g_m(R_o||R_s||R_{id})+1}}\,. \tag{3.98}$$

Looking at the parameters from table 3.11, it is found that $(R_o||R_s||R_{id}) \approx R_s$ and e_n can be simplified to

$$\begin{aligned} e_{n,FET} &\approx \frac{\sqrt{4k_BT\frac{2}{3}g_m + \frac{K_f I_D}{C_{ox}L^2}\frac{1}{f}}}{A_1\frac{1}{R_s+\frac{1}{g_m}}} \\ &\approx \frac{R_s+\frac{1}{g_m}}{A_1}\sqrt{4k_BT\frac{2}{3}g_m + \frac{K_f I_D}{C_{ox}L^2}\frac{1}{f}} \\ &\overset{A_1\to\infty}{=} 0 \end{aligned}$$

Unless the MOSFET transconductance g_m or the gain of the op-amp A_1 become very small, the noise of the MOSFET is very well suppressed. If the wideband thermal noise contribution is small (which it is, see A.5) and the flicker noise corner frequency is within the bandwidth of the op-amp, the noise contribution from the MOSFET can be neglected.

The noise contribution from the sense resistor R_s is the Johnson–Nyquist noise, see section 3.6.1, which when transformed to its Norton representation can be written as a current noise

$$i_{n,R} = \sqrt{\frac{4k_BT}{R_s}}\,. \tag{3.99}$$

Additionally, it was shown that depending on the material of the resistive element, a flicker noise component can also be present. This is especially prevalent in carbon and thick-film resistors [79, 172]. While thin-film resistors are less noisy, their performance varies greatly between different models [199], so their make and model must be carefully selected for the application. Metal foil and wirewound resistors were shown to perform best and have almost no flicker noise [44, 199]. Using a high quality resistor, the flicker noise can be neglected and only the thermal noise must be taken into account.

The sense resistor is part of the feedback network and therefore it contributes fully to the noise of the transconductance amplifier. Input referred, the current noise must be divided by the closed-loop gain A_f given by A.2 on page 219.

$$e_{n,R} = i_{n,R}\cdot\beta \approx i_n \cdot R_s = \sqrt{4k_BTR_s} \tag{3.100}$$

The final component to be discussed is the operational amplifier. Although the op-amp is a rather complex device, its noise can be modeled with sufficient accuracy by a small number of noise sources. The typical noise model of an op-amp is shown in figure 3.50.

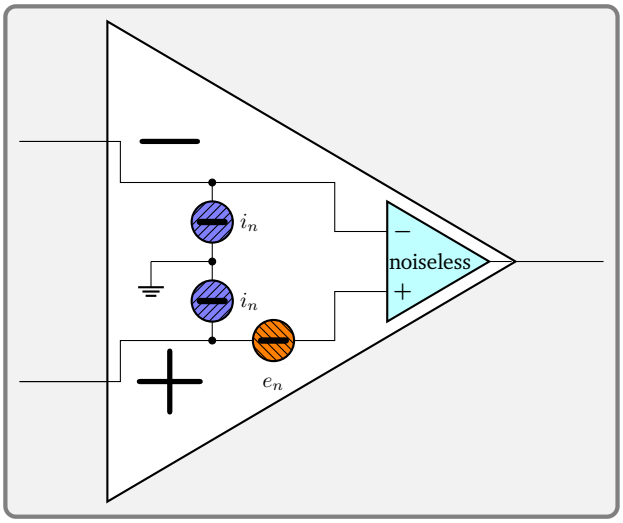

Figure 3.50.: Noise model of the operational amplifier.

In figure 3.50 one can see that there are three noise sources required to treat the op-amp. The input voltage noise source e_n and two input current noise sources i_n. The current noise noise sources i_n are assumed to be mostly uncorrelated. This assumption leads to an upper bound as can be seen from figure 3.51, which shows the input differential amplifier, which is the first stage of a typical bipolar op-amp.

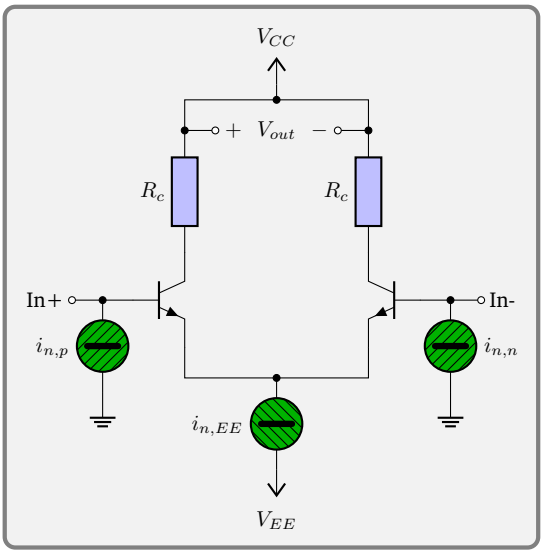

Figure 3.51.: Bipolar op-amp input stage with noise sources.

Of the three noise sources $i_{n,p}$, $i_{n,n}$ and $i_{n,EE}$ only $i_{n,p}$ and $i_{n,n}$ are uncorrelated, because it is the input bias current of the individual transistors, and only the effect of $i_{n,EE}$ is correlated, because the current of the emitter bias current source is equally distributed between the two input transistors. Since effects of equal magnitude and sign cancel out due to the differential

nature of the input stage, correlated effects are suppressed. An equal magnitude can be assumed, because the gain of the two transistors is well matched, due to their close proximity on the semiconductor die. Therefore assuming all noise is uncorrelated presents an upper bound for the current noise i_n. A more detailed analysis can be found in [88]. Due to the matching of the transistors, the magnitude $i_{n,p}$ and $i_{n,n}$ are also closely matched, hence, in the model used here, they are assumed equal and referred to as i_n from now on. These two current noise sources cannot be combined with the voltage noise source, because they depend on the external impedance connected to the op-amp, so this final step must be done by the circuit designer as shown next.

Both the voltage noise e_n and the current noise i_n can be found in the datasheet of the op-amp. Typically, these values given are input-referred values. For the complete circuit as in figure 3.49 it is possible to calculate the full noise contribution of the op-amp as

$$e_{n,op} = \sqrt{e_n^2 + e_{n,+}^2 + e_{n,-}^2}\,, \tag{3.101}$$

assuming the noise sources are uncorrelated. The input referred voltage noise $e_{n,-}$ of the inverting input resulting from the current noise can be calculated in a similar fashion as e_{n_R} in equation 3.100. It is likewise part of the feedback network and must therefore be divided by the closed-loop gain A_f as before.

$$e_{n,-} \approx i_n \cdot R_s \tag{3.102}$$

The current noise of the non-inverting input can be translated by considering its input impedance. This is determined by the filter circuit of the reference voltage which is required to remove the high frequency noise as discussed above. Assuming an RC-filter of first order, the output impedance can be calculated from the transfer function of the low-pass filter, derived in equation 3.19

$$R_{out,f} = R_f \cdot A = \frac{R_f}{1 + sR_fC} \tag{3.103}$$

$$\lim_{s\to 0} R_{out,f} = R_f$$

$$\lim_{s\to \infty} R_{out,f} = 0\,.$$

$$e_{n,+} \approx \frac{i_n R_f}{1 + sR_fC} \tag{3.104}$$

Looking at the output impedance of the filter, it can be seen that for high frequencies, the output impedance approaches 0, while for low frequencies it is R_f. This has the effect that if the filter corner frequency $\omega_0 = \frac{1}{RC}$ is close to the flicker noise corner frequency of the reference voltage there is is almost no wideband current noise contribution from $e_{n,+}$ as well. Only the $\frac{1}{f}$ component of the op-amp current noise multiplied with R_f is left. Ideally, this is lower than the reference noise to have negligible impact and must be kept in mind when selecting an op-amp. This leads to the total noise of the op amp

$$e_{n,op} = \sqrt{e_n^2 + (i_n R_s)^2 + \left|\frac{i_n R_f}{1 + sRC}\right|^2}\,. \tag{3.105}$$

To conclude, table 3.7 is given as a reference for the noise contributions in the low-frequency and also the wideband domain. From this table, it can be seen that the only wideband-noise contributors are the reference resistor and the op-amp. The low-frequency contributors are

the voltage reference and the op-amp, since they have a strong flicker noise component. A low-noise, precision op-amp typically has far less low frequency noise than a voltage reference and the dominant low frequency contributor remains the voltage reference.

Noise component	Low frequency	Wideband
V_{sup}	≈ 0	≈ 0
MOSFET	≈ 0	≈ 0
V_{ref}	$\sqrt{e_{n,ref}^2 + 4k_B T R_f}$	≈ 0
R_s	$\sqrt{4k_B T R_s}$	$\sqrt{4k_B T R_s}$
Op-amp	$\sqrt{e_n^2 + i_n^2(R_s^2 + R_f^2)}$	$\sqrt{e_n^2 + i_n^2 R_s^2}$

Table 3.7.: Input referred noise components of the transconductance amplifier. Multiply by $\frac{1}{R_s}$ to get the output referred current noise.

From those findings it is clear that the most important choices regarding the noise contributions are a good quality metal-foil or wirewound sense resistor R_s, a low noise voltage reference and a low noise op-amp. Regarding the low-noise op-amp it is critical to decide between low voltage noise or low current noise. This choice depends on the value of R_s. For typical values of R_s below $1\,\mathrm{k\Omega}$, voltage noise is the dominating effect. The reference should be chosen for low flicker noise.

3.8.7. Component Selection

This section deals with selecting the right components for the precision current source presented in section 3.8.4. The focus lies on the requirements defined in section 3.2, notably specifications 3.1 and 3.2. Most attention will be on the MOSFET, the operational amplifier, and the voltage reference. For these components examples from literature are given and are compared to the requirements. Discussed first is the voltage reference, because this will define several parameters down the road. Then the op-amp is considered, for which several examples from scientific publications and other alternatives are shown and the best solution is presented. Finally, the selection parameters for the MOSFET will be elaborated. The reader must be warned though that the lineup of p-channel MOSFETs in production is decreasing, with more and more products being discontinued in favour of n-channel MOSFETs. The component recommendations may therefore already be outdated.

Numerous laser driver designs for different applications and laser diodes can be found in literature [77, 94, 128, 196, 221, 222, 227]. Even though Libbrecht et al. [128] were not the first to present their circuit, a similar solution can already be found in [51], their design stands out for its simplicity. The designs mentioned can be divided into two groups. High power drivers for quantum cascade lasers (QCL) typically featuring a compliance voltage V_c of more than $10\,\mathrm{V}$ and output currents of up to several ampere based on the work of Taubman [221] and medium power devices for laser diodes having a lower compliance voltage of around $2\,\mathrm{V}$ and capable of driving a few hundred mA based on the work of Libbrecht et al. [128]. The requirements of this work mostly fall into the latter category, except for the compliance voltage, which is targeted for blue laser diodes and $V_c \geq 8\,\mathrm{V}$. All these designs share one common aspect though, the type of voltage reference. Most laser drivers in literature and also commercial products are designed around low-noise, low-drift buried Zener diode voltage

references, namely the Analog Devices (ADI) LM399 [133] or ADI LTZ1000 [143].

The buried types of voltage references are Zener diodes. that are created within the bulk silicon using ion implantation. This reduces noise caused by surface contamination [202]. These diodes are not true Zener diodes though, but called Zeners nonetheless, and use a mix of Zener and avalanche breakdown to compensate the temperature coefficient.

The Zener effect is the tunneling of electrons through the barrier formed between the valence band and conduction band. It has a negative temperature coefficient, because an increase in temperature reduces the size of the band gap. This effect dominates at low currents.

Avalanche breakdown, on the other, hand describes a mechanism in which free electrons (due to temperature) are accelerated to such energies that they knock out other electrons, causing an avalanche of electrons. This effect has a positive temperature coefficient [108] and occurs at higher currents. While the zero temperature coefficient point is around $5\,\mathrm{V}$, this operating point implies a high susceptibility to changes in the reverse current. Typically, the Zener voltage is shifted slightly upwards to result in a net positive coefficient, which is then compensated by the negative temperature coefficient of a forward biased diode [202]. This results in the common Zener diode voltage of around $6.2\,\mathrm{V} + 0.7\,\mathrm{V} = 6.9\,\mathrm{V}$. In comparison to other types of diodes, buried Zeners have the best stability and lowest noise. $V_{ref} \approx 7\,\mathrm{V}$ is therefore set in stone for the reasons given above. Table 3.8 lists some commercially available buried Zener diodes. All of these diodes are manufactured by ADI as they are the sole manufacturer left on the market to produce this kind of diodes.

Component	Voltage	Temperature coefficient	Stability	Package
LT1021	$7\,\mathrm{V}$	2–$5\,\mu\mathrm{V}/(\mathrm{V\,K})$	$15\,\mu\mathrm{V}/(\mathrm{V}\sqrt{\mathrm{kh}})$	SO-8
LT1027	$5\,\mathrm{V}$	1–$2\,\mu\mathrm{V}/(\mathrm{V\,K})$	not specified	SO-8
LM399	$7\,\mathrm{V}$	0.3–$1\,\mu\mathrm{V}/(\mathrm{V\,K})$	$8\,\mu\mathrm{V}/(\mathrm{V}\sqrt{\mathrm{kh}})$	TO-46
ADR1399	$7\,\mathrm{V}$	0.2–$1\,\mu\mathrm{V}/(\mathrm{V\,K})$	$7\,\mu\mathrm{V}/(\mathrm{V}\sqrt{\mathrm{kh}})$	TO-46
LTZ1000	$7.2\,\mathrm{V}$	$0.05\,\mu\mathrm{V}/(\mathrm{V\,K})$	$0.3\,\mu\mathrm{V}/(\mathrm{V}\sqrt{\mathrm{kh}})$	TO-99
ADR1000	$6.6\,\mathrm{V}$	$<0.2\,\mu\mathrm{V}/(\mathrm{V\,K})$	$0.2\,\mu\mathrm{V}/(\mathrm{V}\sqrt{\mathrm{kh}})$	TO-99

Table 3.8.: List of commercially available buried Zener diodes and selected properties.

Choosing a voltage reference can be done according to specification 3.1. A temperature coefficient of $\leq 1\,\mu\mathrm{A}/(\mathrm{A\,K})$ rules out any non-hermetic unheated voltage reference. Using a hermetic package also improves the stability against humidity as the epoxy used for an SO-8 package is hydrophilic and swells when exposed to water vapour causing pressure on the die, resulting in a change of the output voltage. The hermetic voltage references can be divided into two groups, the LM399 and the newer ADR1399 in one group and the LTZ1000 and its newer counterpart ADR1000 in another. While the LM399 requires very few external components, the external circuit for the LTZ1000 is far more elaborate requiring more parts and space. Additionally, the LTZ1000 is more than four times the price of the LM399 in quantities of 10 at the time of writing. Last but not least, the stability and temperature coefficient of the LTZ1000 cannot be matched by the performance of the sense resistor in the precision current source, so the sense resistor gives a lower bound of about $0.5\,\mu\mathrm{A}/(\mathrm{A\,K})$. Unless the better low frequency noise performance is required, the LM399 and ADR1399 are the more economical parts. The performance of the latter two references will be discussed in section 4.1.13 and the sense resistor is considered next.

With the maximum reference voltage of $7\,\mathrm{V}$ known, a sense resistor between $14\,\Omega$ ($500\,\mathrm{mA}$)

and $28\,\Omega$ (250 mA) is required. The Vishay VPR221Z are high power low drift metal foil resistors in a TO-220 package and a solid choice here. The low value resistors, combined with the requirement for a low current noise output of the source, limits the choice of op-amps to bipolar low-noise devices or discrete implementations. Table 3.9 lists some choices compiled from the literature sources, which will now be discussed.

Component	Wideband-noise	Low frequency noise	Temperature coefficient
LT1028	$0.85\,\mathrm{nV}/\sqrt{\mathrm{Hz}}$	$35\,\mathrm{nV_{p-p}}$	$0.2\,\mu\mathrm{V/K}$
AD797	$0.9\,\mathrm{nV}/\sqrt{\mathrm{Hz}}$	$50\,\mathrm{nV_{p-p}}$	$0.2\,\mu\mathrm{V/K}$
ADA4898	$0.9\,\mathrm{nV}/\sqrt{\mathrm{Hz}}$	not specified	$1\,\mu\mathrm{V/K}$
ADA4004	$1.8\,\mathrm{nV}/\sqrt{\mathrm{Hz}}$	$150\,\mathrm{nV_{p-p}}$	$0.7\,\mu\mathrm{V/K}$
AD8671	$2.8\,\mathrm{nV}/\sqrt{\mathrm{Hz}}$	$77\,\mathrm{nV_{p-p}}$	$0.3\,\mu\mathrm{V/K}$

Table 3.9.: List of low-noise precision bipolar operational amplifiers with typical performance properties.

The low value of the sense resistor makes a bipolar op-amp the preferred choice, because they have a very low voltage noise and their current noise and input bias current do not interfere with such a low value resistor. While a discrete solution using matched JFETs or bipolar transistors may push the input noise even lower, the temperature stability, circuit complexity and again the size speaks against this option, so the discussion will be limited to integrated solutions only.

To find a reference point for the choice of op-amp, the thermal noise of the sense resistor must be looked at. A $28\,\Omega$ sense resistor has a thermal noise of

$$e_n\,(R = 28\,\Omega T = 23\,^\circ\mathrm{C}) = 0.67\,\mathrm{nV}/\sqrt{\mathrm{Hz}}\,.$$

This means that even the lowest noise op-amp from table 3.9 dominates the wideband-noise. With this said, the component choices made in literate can be discussed. The AD8671 chosen by Erickson et al. [77] only makes sense, because they have chosen a very large filter resistor R_f of $2 \times 3\,\mathrm{k}\Omega$. The ADA4004 was used by Moglabs in the DLC-102, again likely due to the high values of R_f used. The ADA4898 might seem like a good choice at first sight but the very limited (in terms of precision op-amps) open-loop gain of $0.14\,\mathrm{V/\mu V}$ makes this op-amp an inexpensive, but poor choice. The final choice is between the AD797 and the LT1028, both op-amps have very similar specifications, but there is a peculiarity in the datasheet of the LT1028 [136]. The *High Frequency Voltage Noise vs Frequency* plot shows a noise bump at around $400\,\mathrm{kHz}$. The original application of the LT1x28 is for audio frequencies, which is well below that bump, but in this case poses a problem. The publication by Libbrecht et al. [128] also blames the LT1028 for the noise peak around $400\,\mathrm{kHz}$. Moreover, this peak is the reason why Seck et al. [196] found the LT1028 to have a higher integrated noise than the AD797. Additionally to the superior noise performance, the AD797 (B-grade) has excellent specifications overall. The open-loop gain is between 2–$20\,\mathrm{V/\mu V}$, the supply rejection is greater than $1\,\mu\mathrm{V/V}$, the bias current is almost constant between 20–$100\,^\circ\mathrm{C}$ and the unity gain bandwidth is around $10\,\mathrm{MHz}$. Finally it does have a high output drive capability of $50\,\mathrm{mA}$, which allows to drive large MOSFETs. These features make the AD797 the ideal op-amp for low-value sense resistors, although it puts limits on the maximum filter resistor to limit the low frequency current noise contribution.

Finally, the choice of MOSFETs can be discussed. As it was shown in section 3.8.3 in equation 3.78, the channel length modulation plays an important role in increasing the channel conductance g_{DS} and limiting the output impedance. To reduce the channel length modulation a longer channel is preferred. Manufacturers do not give these numbers, nor information on the manufacturing process. Older technologies like the planar (lateral) FET are better suited for operating in the saturation region than the modern trench (vertical) FET. Trench MOSFETs are geared towards a low on-state resistance $R_{DS,on}$, which is important for switching applications, but their lower resistance comes from a shorter channel. One of the few planar MOSFETs still available on the market is the HEXFET, which was designed for switching applications, but proves useful nonetheless. High voltage MOSFETs also have longer channels than low voltage MOSFETs, so searching for MOSFETs that are rated for 60–$100\,\mathrm{V}$ or more can narrow down the candidates. While the output impedance is a factor worth keeping in mind, the most important aspect is whether the MOSFET can drive the load regarding the compliance voltage. To outline the problem, one can refer again to the example parameters from table 3.11.

Assuming a supply voltage of $15\,\mathrm{V}$ and the `AD797` op-amp, the current source supply voltage V_{sup} is limited to about 11–$12\,\mathrm{V}$, because the `AD797` is no rail-to-rail op-amp and its output only swings within $3\,\mathrm{V}$ of the rail (minimum) and the input is limited to within $2\,\mathrm{V}$ of the rail (minimum). Considering the maximum V_{ref} at full output of $7\,\mathrm{V}$ and a load voltage of $3\,\mathrm{V}$ in case of the `L785H1` [118] laser diode used as an example in this section leaves only

$$V_{DS,min} = V_{sup} - V_{ref} - V_{load} = 12\,\mathrm{V} - 7\,\mathrm{V} - 3\,\mathrm{V} = 2\,\mathrm{V} \tag{3.106}$$

for the MOSFET – a serious challenge.

To find a suitable MOSFET, one has to consult the *Typical Output Characteristics* graph in the datasheet. By using the maximum output current specification it is possible to estimate the minimum drain-source voltage V_{DS} to keep the MOSFET in saturation at the given maximum output current. This again narrows down the list of candidates.

The final aspect is the capacitive nature of the MOSFET gate. This property was briefly brushed in appendix A.5 and the parasitic capacitances can be found in figure A.8. The `AD797` can drive fairly large capacitive loads and several hundred pF are possible. It is best to keep the input capacitance C_{iss} below $500\,\mathrm{pF}$. The output impedance of the `AD797`, is about $10\,\Omega$ at $1\,\mathrm{MHz}$ and rising by an order of magnitude at $10\,\mathrm{MHz}$. $500\,\mathrm{pF}$ results in an impedance of around $300\,\Omega$ dropping by an order of magnitude at $10\,\mathrm{MHz}$, so keeping the capacitance low, allows for a higher bandwidth of the current source.

Using these guidelines, searching a MOSFET across a lot of manufactures can still be tedious, but the distributor Digikey, for example, allows filtering and sorting by voltage and input capacitance. The following MOSFETs in table are given as an example and can be chosen for their respective current ranges.

MOSFET	Maximum V_{DS}	Input capacitance C_{iss}	Current range
`IRF9610`	$200\,\mathrm{V}$	$170\,\mathrm{pF}$	100–$250\,\mathrm{mA}$
`IRF9Z10`	$50\,\mathrm{V}$	$270\,\mathrm{pF}$	250–$500\,\mathrm{mA}$
`IRF9Z14`	$60\,\mathrm{V}$	$270\,\mathrm{pF}$	250–$500\,\mathrm{mA}$

Table 3.10.: Example MOSFETs for a current source and recommended current ranges.

The current range of the MOSFETs in table 3.10 is given based on the datasheet, making sure that the MOSFET can be biased into saturation for the estimated minimum V_{DS} according

to 3.106. The IRF9Z10 is a lower voltage version of the IRF9Z14 and the IRF9Z14 should be preferred if available. Those MOSFETs starting with *IRF* are all HEXFETs formerly made by International Rectifier, whose MOSFET business was bought by Vishay in 2007.

To summarize the component selection. The ADI AD797 op-amp is a superior choice among the op-amps compared and the recommended choice for being low noise with enormous gain, high bandwidth and a strong drive current. A MOSFET based on an older process, to ensure stable performance in saturation, like the Vishay IRF9Z14 is a good choice for medium power applications. The reference of choice is a a buried Zener diode, because of their low noise and high stability. The ADI LM399 or ADR1399 is the most economical choice. Regarding the sense resistor, it must be able to dissipate up to $500\,\mathrm{mA} \cdot 7\,\mathrm{V} = 3.5\,\mathrm{W}$ with minimal drift, making the Vishay VPR221Z a very good choice.

3.8.8. Current Source Example Parameters

Throughout this section, example calculations are performed to give the reader an idea of real-life parameters that can be applied with the theoretical models. These parameters are summarised in table 3.11, including their origin.

Parameter	Value	Source
MOSFET drain current I_D	$250\,\mathrm{mA}$	L785H1 [118]
MOSFET κ	$0.813\,\mathrm{A\,V^{-2}}$	IRF9610 SPICE model [45]
MOSFET channel length modulation λ	$4\,\mathrm{mV^{-1}}$	IRF9610 SPICE model [45]
MOSFET source voltage	$3.5\,\mathrm{V}$–$4\,\mathrm{V}$	section 3.8.7
Source/Sense Resistor R_s	$14\,\Omega$ or $28\,\Omega$	section 3.8.7
Op-amp differential input impedance R_{id}	$7.5\,\mathrm{k\Omega}$	AD797 [9]
Op-amp open-loop gain A_{ol}	$2\,\mathrm{V\,\mu V^{-1}}$	AD797 [9]
Op-amp gain bandwidth product GBP	$10\,\mathrm{MHz}$	AD797 [9]

Table 3.11.: Parameters used throughout this section and their sources.

3.8.9. Howland Current Pump

This section will discuss two versions of the popular Howland current source (HCS) [201]. Both the traditional Howland current pump and the so-called *improved* Howland current pump which is similar, but changes some of its properties for good and bad. Both are bidirectional current sources and can be used for high frequency current modulation or the generation of a precision floating current source. The Howland current source is most useful for small currents of up to a few mA, because its output impedance is limited and mostly depends on the resistors surrounding the op-amp as will be shown below. The design discussed here aims at an output current gain of $1\,\mathrm{mA/V}$, which has proven useful for diode lasers over time. The full circuit is shown in figure 3.52. It is shown as the improved Howland current source but can be configured as the classic Howland current source by shorting out R_{2a}.

As can be seen, these two current sources designs require a set of either 4 or 5 resistors depending on the desired configuration as the classic Howland current source does not need R_{2a}. The output impedance of the Howland current source is derived in appendix A.7 and the

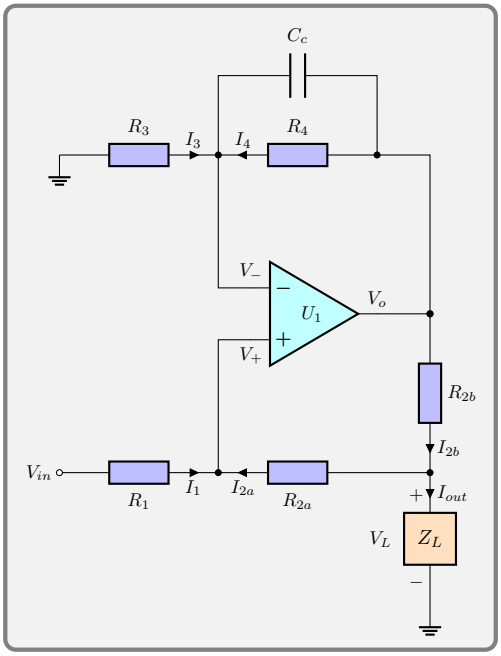

Figure 3.52.: The Howland current source. Using $R_{2a} = 0\,\Omega$ is the classic version, while $R_{2a} \neq 0\,\Omega$ is the *improved* version. C_c is a compensation capacitor to enhance stability.

result is equation A.40 repeated here,

$$R_{o,m,A} = \left(\frac{R^2 - R_{2a}^2}{R}\right) \frac{(AR + R - \epsilon + 1)}{A\,(R + \epsilon - 1) + 2R - 2\epsilon + 2}\,, \tag{3.107}$$

where A is the frequency dependent gain of the op-amp as discussed in equation A.11, $R = R_1 = R_2 = R_3 = R_4$ and ϵ is the resistor mismatch factor introduced in A.31. The mismatch factor can be applied for worst-case calculations for a given resistor tolerance T using equation A.33.

By using the formula above, it is possible to calculate the output impedance for a modulation current source of a laser driver. Since the the output impedance of the *improved* Howland current source is worse than that of the classic Howland current source according to equation 3.107, the discussion will begin here. Experience has shown that an input sensitivity of $1\,\mathrm{mA/V}$ is a reasonable choice, giving enough headroom to steer the laser and apply a modulation as mentioned above. The resistor value can be calculated from this input sensitivity to be $1\,\mathrm{k\Omega}$. To reduce manual labor it is recommended to use an array of 4 matched resistors like the Vishay `MORN` [165] or the ADI `LT5400` [138], both quad resistor arrays offering a ratio matching between $0.5\,\%$ and $0.01\,\%$. Commonly available is the `MORN` array with $0.05\,\%$ tolerance and the `LT5400` with $0.01\,\%$ tolerance and even $0.005\,\%$ between neighbouring resistor pairs. For such arrays and an amplifier with $A = 10^7$, the worst case output impedance can be calculated as

$$R_{out}(R = 1\,\mathrm{k\Omega}, T = 0.05\,\%) \approx 499\,\mathrm{k\Omega} \qquad R_{out}(R = 1\,\mathrm{k\Omega}, T = 0.01\,\%) \approx 2.5\,\mathrm{M\Omega}\,.$$

R_{out} is proportional to $\frac{1}{T}$, since the amplifier gain is very high and the tolerances are small. The upper limit imposed by the op-amp gain can be calculated according to equation A.39 as

$$R_{out,max}(A = 10\,\mathrm{V/\mu V}) \approx 2.5\,\mathrm{G\Omega}\,.$$

Comparing these values with the requirements from specification 3.2, $R_{out} \geq 7.5\,\mathrm{M\Omega}$, it is obvious that the Howland current source can meet them, but not without extra trimming or a tighter matched resistor array (T $\leq 0.01\,\%$) which is hard to come by and expensive. In order to get a better understanding of the output impedance and to show the effect of different tolerances, a Monte Carlo simulation was conducted. The parameters assumed a Gaussian distribution of the resistor values with $3\sigma = T$ due to the tolerance. The Monte Carlo simulation was then run 10^5 times and the output impedance was extracted for each run. Finally, the absolute value (there are positive and negative values, see below) was binned into 100 bins of $500\,\mathrm{k\Omega}$ width and plotted as a histogram.

The LTSpice simulation file can be found at source/spice/howland_current_source_ideal.asc and the result, limited to bin values $\leq 50\,\mathrm{M\Omega}$ for better readability, is shown in figure 3.53.

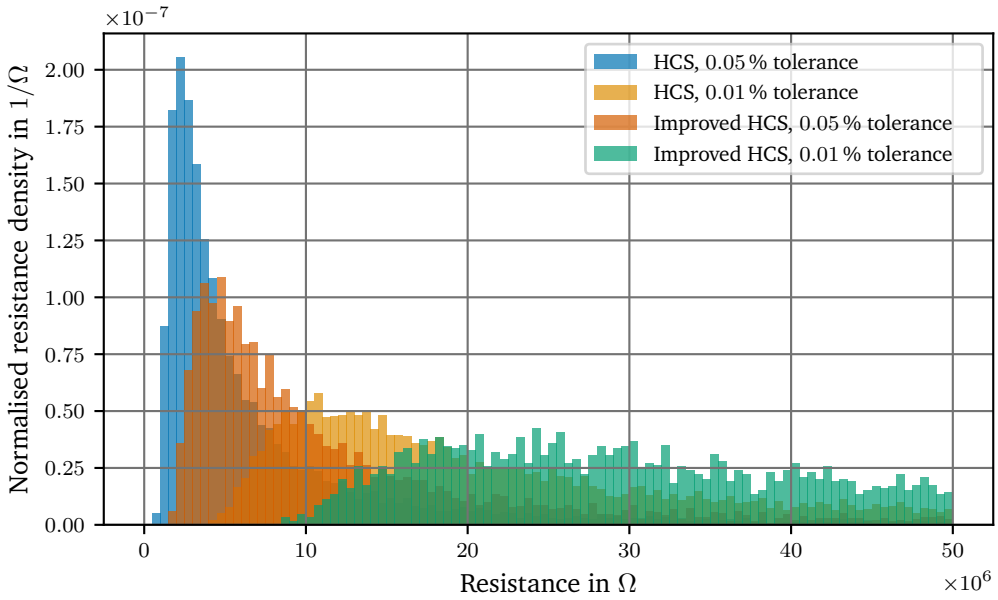

Figure 3.53.: Histogram of the Monte Carlo simulations of the output impedance for the classic Howland current source with different resistor tolerances, assuming $A = \infty$, $3\sigma = T$, $R = 1\,\mathrm{k\Omega}$. The improved Howland current sources uses $R = 10\,\mathrm{k\Omega}$ and $R_{2b} = 1\,\mathrm{k\Omega}$. The number of simulation runs was 10^5.

Figure 3.53 gives a more complete picture of the expected output impedance distribution when implementing an (improved) Howland current source without trimming. Do note, that figure 3.53 only shows the absolute value of the output impedance. The impedance can be either positive or negative, depending on the resistor ratios. The probability is evenly distributed between negative and positive impedance, producing a left-handed negative copy of the plot in figure 3.53. For the purpose of improving readability of the plot, only the absolute value is plotted. A negative impedance means that with increasing load voltage, the output current increases as well. For the purpose of of driving laser diodes, this distinction is irrelevant as the output impedance mostly determines the noise immunity.

First, the basic Howland current source is discussed. Using $0.05\,\%$ tolerance resistors the lower limit of $500\,\mathrm{k\Omega}$ can be easily identified as the leftmost bin of the histogram that contains a non-zero number of counts. The maximum probability is reached at around $2\,\mathrm{M\Omega}$. Integrating over the probability density of the values gives a $31.5\,\%$ probability to end up with an output

impedance of at least $7.5\,\mathrm{M\Omega}$. This is not nearly enough to meet the specificaction. Going to $0.01\,\%$ tolerance resistors, the lower limit of $2.5\,\mathrm{M\Omega}$ can again be identified by the absence of counts in the lower bins. The maximum probability is around $10\,\mathrm{M\Omega}$–$20\,\mathrm{M\Omega}$ and the chance of getting an output impedance of more than the targeted $7.5\,\mathrm{M\Omega}$ is $95.6\,\%$, a number far closer to the desired 3σ value ($99.7\,\%$) and can be considered acceptable given the high cost of acquiring a resistor array with better specifications.

The improved Howland current source was simulated with $R = 10\,\mathrm{k\Omega}$ and $R_{2b} = 1\,\mathrm{k\Omega}$. It is therefore expected that according to equation A.36 the minimum output impedance is about a factor of two higher than compared to the basic Howland current source. Looking at figure 3.53, this assumption holds. For a resistor tolerance of $T = 0.05\,\%$, the minimum bin is $1.5\,\mathrm{M\Omega}$, with the maximum probability at $4.5\,\mathrm{M\Omega}$. The chance of having an output impedance of more than $7.5\,\mathrm{M\Omega}$ is $79.7\,\%$, which is quite an improvement over the $31.5\,\%$ of the basic current source, but still not usable. Using $T = 0.01\,\%$ resistors, the improved Howland current source has a minimum impedance of $8.5\,\mathrm{M\Omega}$, which is sufficient to meet the requirements and the maximum is between $20\,\mathrm{G\Omega}$ and $30\,\mathrm{G\Omega}$. The results are summarised again in table 3.12.

Configuration	Tolerance T	$R_{out,min}$ Bin	P($R_{out} \geq 7.5\,\mathrm{M\Omega}$)
HCS	$0.05\,\%$	$500\,\mathrm{k\Omega}$	$31.5\,\%$
	$0.01\,\%$	$4\,\mathrm{M\Omega}$	$95.6\,\%$
Improved HCS	$0.05\,\%$	$1.5\,\mathrm{M\Omega}$	$79.7\,\%$
	$0.01\,\%$	$8.5\,\mathrm{M\Omega}$	$100\,\%$

Table 3.12.: Summary of the Monte Carlo simulations for different current source configurations.

In comparison to the MOSFET based precision current source, for which an output impedance of $40\,\mathrm{G\Omega}$ was calculated in equation 3.93, the Howland current source is the weak link, when both are combined in a laser driver. To improve this situation the resistors can either be trimmed or a JFET or MOSFET cascode can be added to improve the output impedance. Do note a cascode is not bidirectional though. Several trimming options were discussed by Pease [171], but trimming at this level will prove difficult. The desired trim for the classic Howland current source and $R = 1\,\mathrm{k\Omega}$ can be calculated as

$$\begin{aligned} R_{out} &\approx \frac{R}{\epsilon} \approx \frac{R}{4T} \geq 7.5\,\mathrm{M\Omega} \\ \Rightarrow T &\approx 33\,\mathrm{\mu\Omega/\Omega}\,. \end{aligned}$$

The final aspect that needs to be discussed is the compliance voltage. The compliance voltage of the HCS and improved HCS was calculated in equations A.42 and A.43 as

$$V_{c,HCS} \leq \frac{1}{2} V_{o,max} \qquad\qquad V_{c,iHCS} \leq V_{o,max} - V_{in}$$

From those equations it can be seen that there is a significant difference between the the basic Howland current source and the improved HCS. The compliance voltage of the basic Howland current source only depends on the maximum output voltage of the op amp and hence the supply voltage. The improved HCS depends on both the supply voltage and the input voltage. This makes it unsuitable for a laser driver modulation source, because the maximum modulation input typically is roughly the same voltage as the maximum output of a typical

op-amp, since the laser driver is modulated or steered by another box using the same power rail. The improved Howland current source can only by employed in situations, where the input is well defined and a lot lower than the power supply rail of the HCS op-amp. For a laser driver modulation current source, the basic HCS is more suitable since it is independent of the input. To achieve a high output impedance, a high quality matched array is necessary, or alternatively, a difference amplifier like the ADI LT1997 [137] can be used. Those amplifiers contain both the amplifier and a resistor network that is tightly matched. In case of the LT1997, the matching is better than $60\,\mu\Omega/\Omega$. Unfortunately, the choice of resistor values in this case is even more limited than the range of resistor arrays.

The problem of a limited choice of resistor values as arrays or integrated resistors can be addressed by a circuit that combines both the basic HCS and the improved HCS. This circuit is shown in figure 3.54.

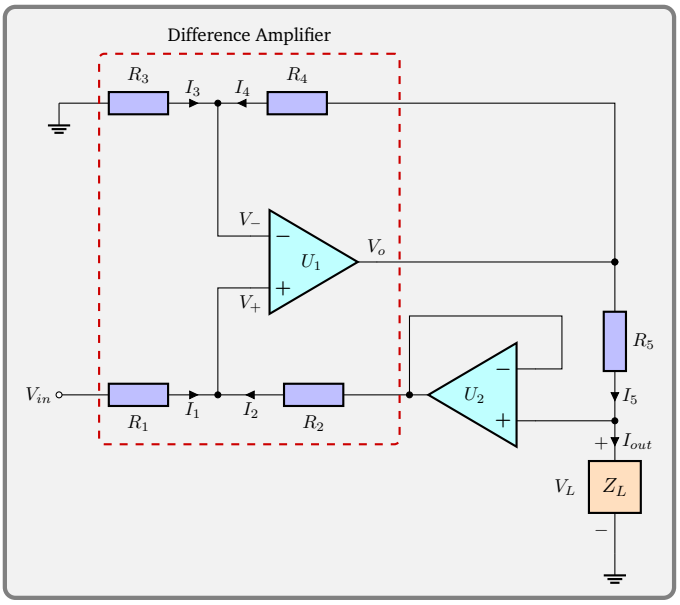

Figure 3.54.: A buffered Howland current source combining the improved HCS and the basic HCS.

By adding another op-amp R_2a is now connected to a low impedance node, just like in case of the basic Howland current source. This leads to the same formulae regarding the output impedance and the compliance voltage as the improved HCS, but removes the matching requirement of R_2a and R_2b. The full derivation can be found in the Python notebook at data/simulations/howland_current_source.ipynb as part of the online supplemental material [42].

With the buffered HCS it is possible to use either 4 matched resistors or a difference amplifier with integrated resistors. The single resistor R_5 is used to set the output current and can be chosen independently to result in

$$I_{out} = \frac{V_{in}}{R_5}\,. \tag{3.108}$$

4. Results

"It's still magic even if you know how it's done."

– Sir Terry Pratchett, *A Hat Full of Sky*

4.1. Laser Current Driver

For this project several commercial and in scientific literature publicly available laser current drivers were evaluated to assess their performance for the laser system discussed in section 3.1. The following devices were tested for the requirements listed in 3.1 and 3.2.

- Moglabs `DLC-102`
- Newport `TLB-6800-LN`
- Sisyph `SMC11 Puy Mary`
- Toptica `DCC 110`
- Vescent `D2-105`
- LQO `LQprO` [86]
- A driver based on the work of Erickson et al. [77]

As a disclaimer, Moglabs, Vescent and Sisyph provided demo units, free of charge, to the author and without any obligations regarding this work. The opinions and measurements in this work are in no way biased by this service.

All of the drivers presented claim to produce a very low-noise output current, but vary in features. The `DLC-102`, the `TLB-6800-LN` and the `D2-105` additionally include a Peltier controller. The former two also have an integrated modulation source that can, for example, be used to lock the laser to an external reference. The `TLB-6800-LN`, the `DCC 110` and the design by Erickson et al. also feature a digital interface.

All drivers were compared to the requirements. although not all drivers have the required features, for example, like a remote accessible interface. Their performance was evaluated nonetheless to have a broader range of choices. A performance comparison can be found in the sections 4.1.9, 4.1.10 and 4.1.11 . Unfortunately, not a single driver was able to properly drive the high compliance voltage required by the blue laser diode `PL 450B` [174] of about 6 to $7\,\mathrm{V}$ [174]. As it was discussed in section 3.8.5, the compliance voltage of all laser drivers based on the design of Libbrecht et al. [128] is limited to around 2 to $3\,\mathrm{V}$ at full output, see 3.106 for details. Since the compliance voltage increases roughly proportional to the reciprocal of the output current multiplied by $7\,\mathrm{V}$, limiting the maximum output current to about 30–$40\,\%$ boosts the compliance voltage by up to $5\,\mathrm{V}$. Not only does this limit the choice of drivers, but

also requiring a 500 mA driver for a 150 mA laser diode seems excessive and does not help with the noise requirements because the output noise of the drivers scales with I_{max} as detailed in section 3.8.6 as the op-amp noise is the limiting factor. This lead to the decision to design a current source that meets all of the requirements, while surpassing the available alternatives and at the same time tackling the compliance voltage limit. This design and its individual components are discussed in the following sections. First, the state of the art is presented, then the problems encountered are outlined and finally the design that resolves these issues is presented and the technical challenges are discussed.

4.1.1. The State of the Art in Laser Current Drivers

Prior to this work, all laser drivers commonly used for scientific purposes, were more or less strictly following the design proposed by Libbrecht et al. [128]. This design was presented in 1993 and back then, blue laser diodes were not available as these were only developed in 1996. Maruska et al. [152] gives an interesting historic summary for the interested reader. In 2014, the efforts of Isamu Akasaki, Hiroshi Amano and Shuji Nakamura were then rewarded with the Nobel Prize in Physics. The original laser driver circuit was therefore designed for laser diodes requiring a low current and low compliance voltage compared to modern laser diodes. While the design remains useful for many low power near-infrared (NIR) laser diodes, these shortcomings were never addressed or even acknowledged by commercial alternatives. Sadly, the topic of the compliance voltage is usually not even mentioned in the datasheets – the Moglabs `DLC-102` and Sisyph `SMC11` are notable exceptions, but it is unclear from the specification to which version and/or output currents of the devices the numbers relate. A comparison of features of these drivers is shown in table 4.1. Do note, the Newport `TLB-6800-LN` is special with regard to the other drivers as it only works with certain Newport laser heads. At startup it communicates with the laser head to determine parameters like the maximum current and voltage and refuses to start without the correct laser. It is included in the table for reference only because it came with the Newport `Vantage` laser that is part of the laser system presented in section 4.5 and its performance was assessed for this reason.

Laser driver	Output current	Compliance voltage	Additional features
Moglabs `DLC-102`	**100 mA**, 250 mA, 500 mA	**6 V**, 3.2 V	TEC, PID, Piezo
Newport `TLB-6800-LN`		–	TEC, Piezo, Digital
Sisyph `SMC11`	210 mA, **470 mA**	5 V	
Toptica `DCC 110`	**100 mA**, 500 mA, 3 A, 5 A	–	
Vescent `D2-105`	200 mA, **500 mA**	–	TEC
LQO `LQpr0`	**140 mA**, 400 mA	–	

Table 4.1.: Overview of laser current drivers tested. Marked in bold is the version tested in this work. A dash denotes that no specification is given by the manufacturer.

A quick overview of the individual drivers will now be given before proceeding to the performance test. This allows to better understand some of the design decisions affecting the

device performance discussed later.

Starting with the Moglabs DLC-102, which is a fully integrated unit that includes a current driver, a piezo actuator (piezo) driver, a temperature controller for a thermoelectric cooler (TEC) and also a lock-in amplifier with a PID controller. It is the only driver that comes close to the required 7 V for the compliance voltage as it is specified for 6 V. It does not have any remote control capabilities though, but there is a monitoring output available. The high degree of integration makes this a very competitive solution.

The Vescent D2-105 current source also features more than just the laser driver and includes a TEC controller as well, like the DLC-102. The output current can be adjusted via a 10-turn potentiometer, but also steered via an external input although this is not recommended by the manufacturer as it might degrade stability. It is also the most expensive solution tested.

The Sisyph SMC11 is a rack-mountable unit, unlike the drivers discussed so far. The setpoint of the driver is adjusted via a recessed trimpot using a screwdriver and also externally using an input connector. The driver does not have any display and to read out the setpoints a voltmeter must be attached to the monitoring connector. It is the least expensive unit though.

The Toptica DCC 110 is rack-mounted as well. It comes with a separate display module, which connects via the backplane. The setpoint is adjusted with a 10-turn potentiometer and can additionally be adjusted via the backplane with an external signal.

The LQO LQprO is a solution that comes closest to the requirements, apart from the compliance voltage issue, as it is rack mounted and its output current cannot only be adjusted via an analog input, but also using a 10-turn potentiometer.

The Newport TLB-6800-LN is the only driver that has a digital interface and supports Standard Commands for Programmable Instruments (SCPI). It also incorporates a TEC controller and a piezo controller. As mentioned before this driver only works with the Newport Vantage laser it was sold with.

4.1.2. Laser Driver: Design Concept

It was outlined in the previous section that none of the low noise laser drivers commercially available or described in scientific literature can properly drive the new generations of laser diodes with higher voltage requirements currently entering the market. These diodes include, for example, blue laser diodes or high power laser diodes like the 780 nm Thorlabs L785H1, which requires 250 mA at 3 V maximum. Since the ARTEMIS experiment requires a laser at 441 nm and novel quantum computing experiments need more laser power at 780 nm a new laser driver design is presented in this work to cope with the high supply voltage demands without degrading other performance aspects, additionally fulfilling the requirements outlined in tables 3.1 and 3.2. The concept is, nonetheless, similar to the laser driver design presented by Libbrecht et al. [128] because the application is related. To get a better understanding of the advances implemented, the previous state of the art proposed by Libbrecht et al. will now be compared to the new system. The simplified version of the original design shown in figure 4.1 can be split into four building blocks. A supply voltage input filter, a reference voltage to create the setpoint, a unidirectional current source and some form of bidirectional current source used for modulating the laser current at high frequency. Each of these sections will be discussed in more detail. The chapters also list problems discovered and the solution proposed in the design presented here.

The original design is a straightforward approach and it is possible to reproduce it even on prototype printed circuit boards (PCBs), a key factor for its widespread use. This initial design was modified and improved in several publications by other authors. Erickson et al.

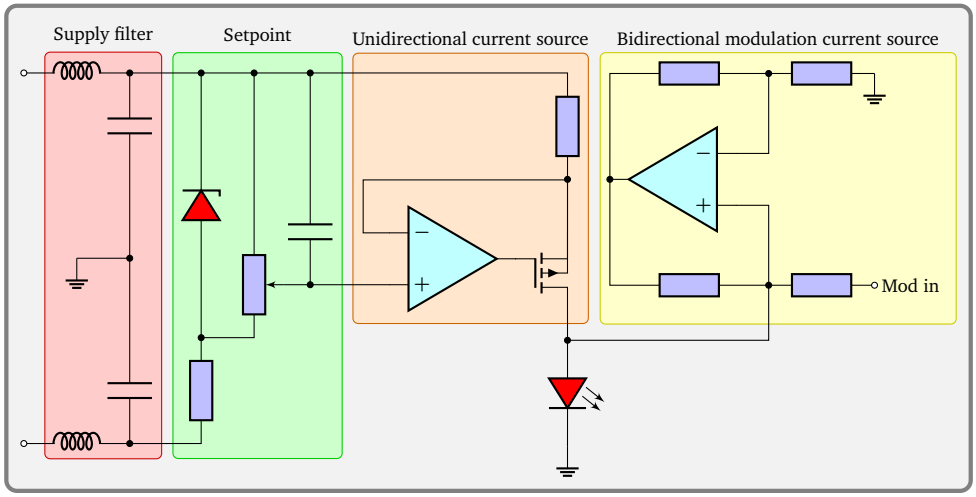

Figure 4.1.: Building blocks of a laser driver based on [128].

[77] replaced the potentiometer with a DAC, but left the other parts untouched. Taubman [221, 222] published some extensive modifications, which not only replaced the reference circuit with a DAC and an `LTZ1000` reference, but also added extensive filtering of the supply. The changes introduced in this work go beyond any of the smaller modifications and present a fully revised system going beyond the capabilities of the original design.

4.1.3. Power Supply

Before moving to the discussion of the power supply filter, the power supply input is shown, which also contains additional safety features. As the device is rack mounted, it is installed in a slot of a 19-inch subrack. The standard power supply scheme used for most devices in this group is a dual $\pm 15\,\mathrm{V}$ supply. It is distributed using a backplane in a 19-inch subrack. The subracks are, for example, Fischer Elektronik `BGT 384`. Into these, a backplane PCB [39] can be fitted. The backplane has connectors for different modules and power connectors are laid out as standard $4\,\mathrm{mm}$ connectors allowing the use of rack mounted power supplies like a Keysight `6632B` or similar linear supplies. Each module in the subrack uses a male DIN41612 Type C, 64-pin connector to mate with the backplane. The pinout of this connector as used by the laser current drivers, is shown in figure 4.2.

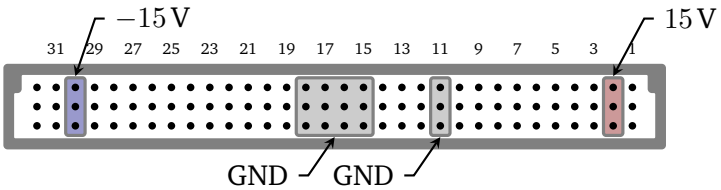

Figure 4.2.: The default male DIN41612 backplane connector pin layout of the digital current controller.

This layout is the default layout and configured on all standard units. Pins not marked either in figure 4.2 or 4.3, are internally not connected and it does not pose a problem to connect other low voltage signals to those pins. For example, due to legacy compatibility with other

devices, pins 30–32 are normally tied together to −15 V on the backplane and the same goes for pins 1–3, which are connected to 15 V.

There is also an alternative layout available, which can be configured using solder jumpers on the PCB. The secondary layout is similar to the layout used by Toptica and allows an upgrade path to replace existing hardware, but keeping the same subrack.

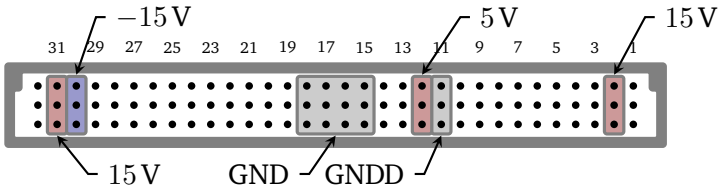

Figure 4.3.: The alternative male DIN41612 backplane connector pin layout of the digital current controller.

In order to switch from one layout to the other, consult table 4.2.

Jumper	Default Layout	Alternative Layout	Function
JP1 (bottom)	open	closed	Connect pin 31 to pin 2
JP2	closed	open[1]	Disconnect pin 11 from pin 15
JP3	open	closed[1]	Connect digital supply to pin 12
JP4	closed	open[1]	Discconect digital supply from pin 2

Table 4.2.: Jumper positions to enable different layouts. JP2 to JP3 are optional, see text.

Jumper 1 is situated on the backside of the PCB while the others are on the top side. Jumper 1 connects pins 2 to 31. This layout is similar to the Toptica `DCC 110` current driver and allows the use of the `DgDrive` in existing racks. Do note however, that the alternative layout is not fully compatible as the control pins are not supported. The manual of the `DCC 110` should be consulted first if other Toptica devices are still being used in the same rack. The system ground of the Toptica rack via pin 1 is currently not supported and must by wired using a small cable.

The alternative layout also offers an option for the digital supply, typically only used for development purposes. The digital power rail is normally fed from the same rail as the analog part and there is no disadvantage in doing so. Should the user nonetheless desire to drive the digital section from a separate supply, jumpers 2–4 can be used to disconnect the digital supply from the analog side. The digital part of the laser driver is galvanically isolated and can be driven from a separate supply. Jumper 2 disconnects the digital ground at pin 11 from the system ground at pins 15–18 and jumpers 3–4 change the digital power supply over to pin 12. A lower input voltage of 5 V is sufficient for the digital supply.

The digital current controller is equipped with advanced power supply protection features that ensure the device is not damaged due to incorrect handling. These protection features include over- and undervoltage protection, reverse polarity protection, reverse current protection, surge protection and circuitry that handles the correct power supply sequencing. The supply protection is available on all power pins and depends on the pin voltage rating. Table 4.3 can be consulted for details regarding each rail.

[1] optional, see text

Supply Rail	Working Range	Absolute Maximum
15 V	15 V to 18 V	±40 V
−15 V	−15 V to −18 V	±40 V
5 V (layout 2)	5 V to 18 V	±20 V

Table 4.3.: Voltages above or below the absolute maximum rating may cause permanent damage to the device.

These types of protection are important in the context of the operating environment. Typically, in this lab, the subracks do not have an integrated power supply and are driven using an external laboratory bench supply like an HP/Keysight 6632B [2], which is also mounted in the rack. Using this solution, there is no inherent protection against incorrectly setting up the power supply and no means to establish a foolproof procedure. These types of faults are furthered by the need to wire up two single channel power supplies for dual polarity. The most common error encountered by the author in this regard was an incorrect polarity. Another problem experienced is associated with hot swapping.

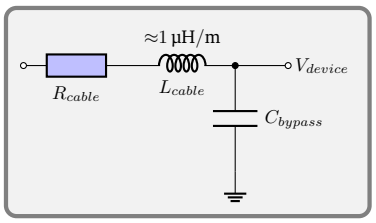

(a) Power supply input parasitic elements forming an underdamped oscillator.

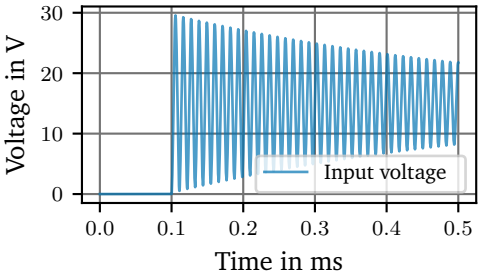

(b) Simulated connection to a hot 15 V rail. The parameters were $L = 3\,\mu\text{H}$, $R = 10\,\text{m}\Omega$ and $C = 1\,\mu\text{F}$.

Figure 4.4.: Oscillations of the supply voltage caused by the parasitic cable inductance and hot swapping modules.

The issue arising from hot swapping is founded in the parasitic inductance of the power supply cable and the input capacitors of the device module. Figure 4.4 (a) shows a simplified model of those parasitic elements. The very low cable resistance is not enough to damp the LC resonator and upon insertion of a module into the subrack there will be strong oscillations, easily surpassing the maximum voltage rating. Figure 4.4 (b) shows a simulation with a 3 m cable between the power supply and the subrack having an estimated inductance of $L = 3\,\mu\text{H}$ and a resistance of $R = 10\,\text{m}\Omega$. The input capacitance of the device is a 1 µF ceramic capacitor with a low equivalent series resistance (ESR). The latter value was taken from the circuit used by Libbrecht et al. [128] as shown in figure 4.5. The circuit designer must make sure that this LC circuit is at best critically damped. This is further discussed in section 4.1.4 on page 106. Unfortunately, the length of the power supply cable is not under control and neither are neighbouring rack modules.

Ideally, hot swapping is therefore addressed by the backplane. Currently, most of the subracks in use do not have a dedicated backplane, but rather use directly wired connectors bolted to

the subrack chassis. The backplane PCB mentioned above, will, in future, address this problem by adding bulk capacitors (and a damping network) directly on the backplane to bypass the inductance of the power supply cable. Additionally, inrush current limiting per port can be implemented to prevent modules with a large input capacitance loading the rail too much. This is part of the ongoing development and hot swapping is currently not supported for devices without proper inrush current limiting.

Experience has shown though, that contrary to advice, hot swapping is practised in the field, even if not supported. It is therefore mandatory to include a robust over- and undervoltage protection to safeguard against transient events like the one shown in figure 4.4 as harm to either the driver or laser diode can be costly. The protection system is designed to safely shut down the laser in case of a fault of any type.

The overvoltage protection against voltage spikes is realised using a `SMBJ40CA` [211] $40\,\mathrm{V}$ bi-directional transient voltage suppressor (TVS) diode, while the undervoltage and reverse polarity protection uses an ADI `LTC4365` [140] controller and a Diodes Inc. `DMN6040SSD` [72] dual $60\,\mathrm{V}$ MOSFET connected back-to-back. One MOSFET is used for reverse polarity protection, the other for overvoltage protection. The `LTC4365` controller will typically shut down the driver within $<5\,\mu\mathrm{s}$ after detecting the fault, preventing most, if not all, transient events to reach critical parts of the system. The $40\,\mathrm{V}$ limit was chosen because this is the upper voltage limit of most power supplies used for these applications in the lab. This makes sure that even considering worst case scenarios no damage to the driver or the laser diode can occur.

Another feature worth mentioning is the built-in inrush current limit. The current driver does have roughly $1.1\,\mathrm{mF}$ of capacitance on each rail, which needs to be charged at startup. This calls for inrush current limiting to prevent currents of several ampere from flowing. The `LTC4365` limits the inrush current to $<100\,\mathrm{mA}$ in order to prevent loading the power rails too much, affecting other devices sharing the same supply.

The full schematic of the input protection can be found in the GitHub repository at [43].

4.1.4. Supply Filtering

The supply section of the design by Libbrecht et al. [128] as shown in figure 4.1 is simplified. The full input filter consists of a CLC filter or sometimes called π-filter shown in figure 4.5. Due to the small input capacitance, the filter is basically just an LC filter regarding the filtering, but do note the use of low ESR ceramic capacitors as discussed in the previous section.

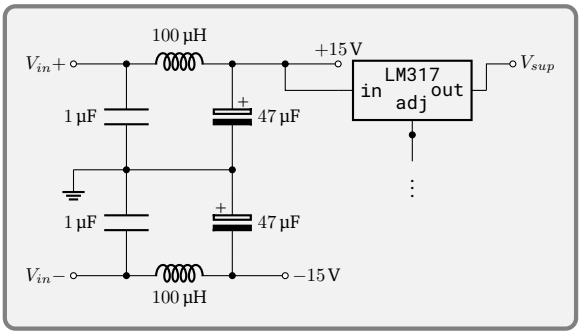

Figure 4.5.: Power supply filter of a laser driver based on [128]. The op-amps are driven by the unregulated filtered voltage and the current source is supplied by the `LM317`.

An LC filter is well suited for a low impedance source like a power supply, because it has a

high input impedance. From the transfer function

$$H(s) = \frac{\frac{1}{sC}}{sL + \frac{1}{sC}} = \frac{1}{s^2LC + 1} = \frac{\frac{1}{LC}}{s^2 + \frac{1}{LC}} = \frac{\frac{1}{LC}}{\left(s + i\frac{1}{\sqrt{LC}}\right)\left(s - i\frac{1}{\sqrt{LC}}\right)}, \tag{4.1}$$

one can deduce, that the passband gain at DC is 1 and additionally, there are two complex poles in the imaginary plane at $s = \frac{\pm i}{\sqrt{LC}}$, putting the cutoff frequency of the 2nd order filter at $f_c = 2.3\,\text{kHz}$. Due to the imaginary poles, there is some gain peaking at f_c. This can be solved by damping the filter as discussed later. An LC filter is fairly efficient at removing high frequency noise, if properly implemented, but low frequency noise like mains hum is left for the op-amp CMRR to suppress as discussed in section 3.8.6 on page 83. The paper of Libbrecht et al. [128] shows some $60\,\text{Hz}$ hum, but it is not clear wether is is introduced by the noise measurement setup or actually part of the laser current.

To push the corner frequency of the filter below $50\,\text{Hz}$ the product of the inductor value and the filter capacitor value has to be increased by about 6 orders of magnitude. Not an easy feat. The paper presented by Taubman [221] shows a brute-force approach. They applied very high values for the capacitor C_{LC} and the inductor L of the LC filter of $10\,\text{mF}$ and $1\,\text{mH}$. The cutoff frequency of this LC filter is about $50\,\text{Hz}$. The filter is then followed by a second filter with an even lower cutoff frequency. This implementation is shown in a simplified form in figure 4.6 and is briefly discussed now. For a more detailed schematic and part names see [221].

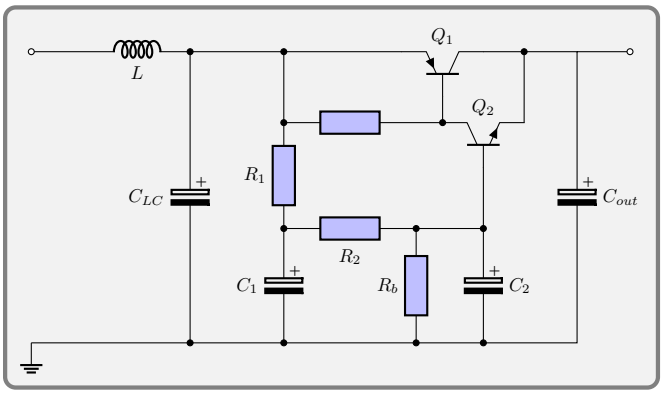

Figure 4.6.: Power supply filter using a capacitance multiplier for a cutoff frequency of $0.5\,\text{Hz}$. This is a simplified schematic based on [221]. Only the positive rail is shown.

The second stage of the filter is comprised of a capacitance multiplier, which is formed by wrapping a feedback loop around the 2nd order filter created by R_1C_1 and R_2C_2. This feedback loop and the gain of the transistor allows to use only a very small part of the current to filter the main current going through Q_1, which in turn allows to use large values for R_1 and R_2 while maintaining a low output impedance of the filter. The properties of this construction will be analysed now, but the reader must be warned beforehand that the term capacitance multiplier is misleading. It neither multiplies the capacitance, nor does is behave like a real 2nd order filter. This circuit was given the name capacitance multiplier because the output does not see R_1 (or R_2), but rather the fraction $\frac{1}{1+\beta}$ of it (roughly). Since the RC constant is still the same, the capacitor looks bigger on the output. Unfortunately, this effect highly depends on the characteristics of the transistor, which in turn depends on the operating conditions. The gain β (or h_{fe}) of a transistor, for example, drops with increasing output current although it rises with temperature. Since the transistor does not store energy like a capacitor the maximum

ripple voltage that can be filtered by the capacitance multiplier depends on the voltage dropped across the transistor as its regulation headroom. This means the maximum input ripple must stay below the output voltage plus a diode drop of $0.6\,\mathrm{V}$ for the base-emitter diode. If more ripple rejection is required, an additional resistor R_b from the base of Q_2 to ground shown in figure 4.6 can be applied. This increases the voltage dropped across Q_1. The downside is a reduced output voltage and more power burnt in the transistor. Another issue stems from the Early effect, which is similar to the channel-length modulation discussed in section 3.8.3. The Early effect can be represented as an output impedance R_o in the small-signal model as well, just like the MOSFET model shown in figure 3.42 (a) on page 75. This connection from collector to emitter typically limits the suppression to 500–1000 ($50\,\mathrm{dB}$ to $60\,\mathrm{dB}$). For more details on the Early effect and bipolar transistors in general see [67, 198]. The capacitance multiplier is very useful at low frequencies though because it can reach cutoff frequencies otherwise unreachable as it is shown in the publication of Taubman [221].

To sum it up, the capacitance multiplier behaves like an ordinary RC filter, but with a lower output impedance compared to the RC filter and only works at low ripple voltages The filtering performance is limited by the Early effect, but it is very effective at low frequencies, which cannot be reached otherwise.

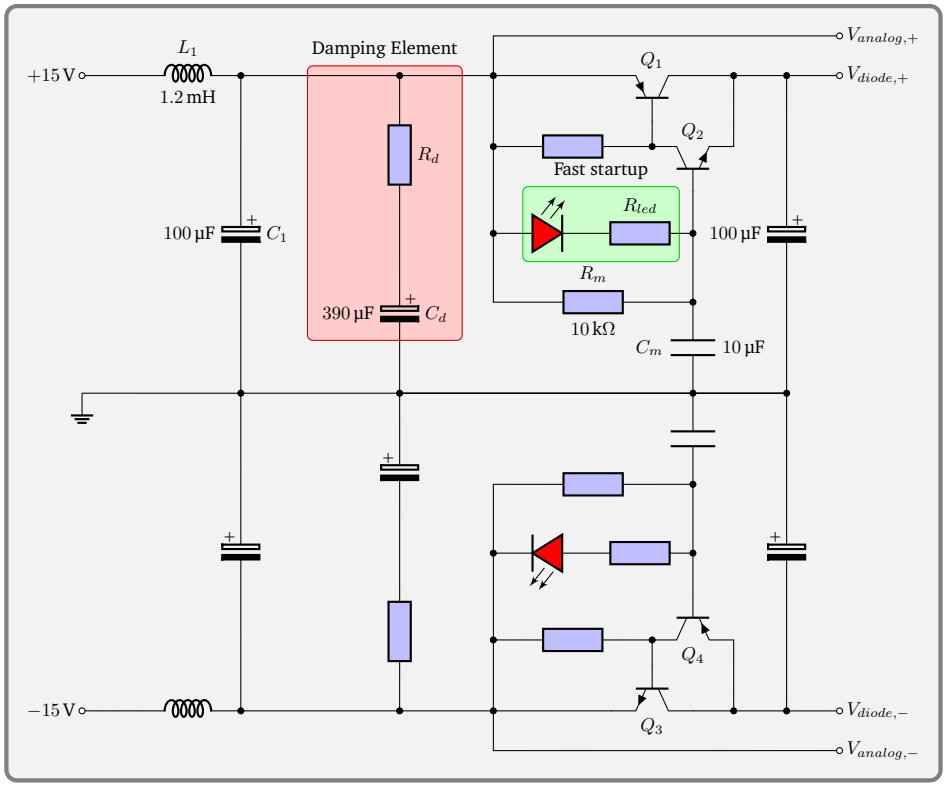

Figure 4.7.: Power supply filter of the digital current driver. The component values are only given for the positive side. The passive components are same for both rails.

The power supply filter of the digital current driver shown in figure 4.7 uses a similar design. The design shown in figure 4.7 is only valid for PCB revisions <2.4.0, which comprises the first batch of units. Later revisions use a revised circuit as discussed below. A passive LC filter is applied first, then the analog supply rail for the op-amps and other monitoring functions is branched off while the laser diode supply voltage is fed into a capacitance multiplier. The

negative rail is mirrored from the positive rail with same passive components but PNP instead of NPN transistors and vice versa. The diode supply and the analog rail, which is taken before the capacitance multiplier, are both going to low noise post-regulators, the ADI `LT3045` and its negative counterpart, the ADI `LT3094`. Both regulators have excellent power supply ripple rejection (PSRR) out to at least $1\,\mathrm{MHz}$ of more than 10^3. At low frequency the PSRR is even higher and more than 10^5 can be expected. This allows a combined PSRR of better than 10^6 from low to high frequencies, even beyond $1\,\mathrm{MHz}$. The design and the choice of components for this filter will now be explored in more detail before proceeding to the measurement of the rejection ratio.

Going back to equation 4.1, it was shown that the undamped LC filter is prone to ringing at the cutoff frequency because the filter poles are imaginary. To address this, there are several solutions. The most simple one is to add a damping element either in parallel to the capacitor or in parallel to the inductor. In this case a damping element in parallel to the capacitor was chosen, because placing such an element in parallel with the inductor will degrade the filter performance by making the blocking inductor lossy. Such a damping element is typically a capacitor with a series resistor or a simple lossy capacitor with a high ESR. Using the arrangement shown in figure 4.7, the new transfer function can be calculated.

$$
\begin{aligned}
H(s) &= \frac{Z_2}{Z_1 + Z_2} \\
Z_1 &= sL_1 \\
Z_2 &= (R_d + Z_{C_d}) \,||\, Z_{C_1} = \left(R_d + \frac{1}{sC_d}\right) || \frac{1}{sC_1} = \left(\left(R_d + \frac{1}{sC_d}\right)^{-1} + sC_1\right)^{-1} \\
&= \frac{sC_dR_d + 1}{s^2C_1C_dR_d + s\left(C_1C_d\right)} \qquad (4.2) \\
H(s) &= \frac{\frac{sC_dR_d+1}{s^2C_1C_dR_d+s(C_1C_d)}}{sL_1 + \frac{sC_dR_d+1}{s^2C_1C_dR_d+s(C_1C_d)}} = \frac{sC_dR_d + 1}{s^3L_1C_1C_dR_d + s^2L_1\left(C_1 + C_d\right) + sC_dR_d + 1} \qquad (4.3)
\end{aligned}
$$

This is the transfer function of a 3rd order filter as there are three energy storage elements. This type of filter was discussed by Middlebrook [161] (reprinted in [60] and [61]). Middlebrook concluded, that there is an optimal value for the series resistance R_d given a capacitance C_d and the filter components L_1 and C_1. This optimal value has minimal gain peaking, hence a minimal quality factor Q at the resonance frequency. The existence of such an optimal value can be easily understood from the fact, that if $R_d = \infty$ the resonance frequency is $\omega_0 = \frac{1}{\sqrt{L_1C_1}}$ and in case $R_d = 0$ it is $\omega_1 = \frac{1}{\sqrt{L_1(C_1+C_d)}}$. In between ω_0 and ω_1, there is a lossy zone, where R_d due to its lossy nature reduces Q, but at both ends $Q = \infty$, so there must be a minimum in between. By calculating the minimum value of the output impedance at the point of resonance, Middlebrook [161] found the following results:

$$R_0 \coloneqq \sqrt{\frac{L_1}{C_1}} \qquad (4.4)$$

$$n \coloneqq \frac{C_d}{C_1} \Rightarrow C_d = nC_1 \qquad (4.5)$$

$$Q_{optimal} = \sqrt{\frac{(4+3n)(2+n)}{2n^2(4+n)}} \qquad (4.6)$$

$$R_d = R_0 \cdot Q_{optimal} \qquad (4.7)$$

From these equations, it can be seen, that the damping capacitor C_d needs to be fairly large, depending on n. A critically damped system with $Q = 0.5$ would be preferred, but this would require $n \approx 5.9$ making C_d prohibitively large. For this filter $n = 3.9$ was chosen because there was a capacitor with a small diameter available at this capacitance, making the filter slightly underdamped. A bit of gain peaking at the resonance can therefore be expected. The following components were chosen. First, a large, low resistance inductor L_1 capable of carrying at least 1 A was selected, in this case a Coilcraft `MSS1210-125KEB`. High reliability capacitors were chosen to ensure a long lifetime of the device. Using capacitors rated with a lifetime of 5000 h at 105 °C gives an expected service life at 60 °C of more than 10 a, when assuming an Arrhenius law with a doubling of the lifetime every 10 K. Apart from the reliability of the capacitors, there are no special requirements for them as there is little ripple current to be expected. The input power supply is supposed to be a filtered low noise supply and not the unfiltered output of a DC/DC regulator. So it is possible to maximize L_1 and choose a physically smaller C_1 since board space is limited. This results in the following design values, calculated from equations 4.5 and 4.7, given the components values discussed above.

$$\begin{aligned} L_1 &= 1.2\,\text{mF} & C_1 &= 100\,\mu\text{F} \\ C_d &= 400\,\mu\text{F} \approx 390\,\mu\text{F} & n &= 3.9 \\ Q_{optimal} &\approx 0.62 & R_d &\approx 2.15\,\Omega \\ f_c &\approx 300\,\text{Hz} \end{aligned}$$

Do note, that R_d does include the ESR of C_d, so the ESR of the capacitor must be subtracted from the final value of the damping resistor placed on the board. This may even absolve one from the need for a discrete resistor if the ESR of the capacitor is high enough.

While the LC filter has a cutoff frequency of 300 Hz the capacitance multiplier can go far lower. The RC filter with 10 kΩ and 10 µF formed by R_m and C_m has a cutoff frequency of 1.6 Hz. Only a single order filter was chosen because of the suppression limit imposed by the Early voltage discussed above. The attainable suppression of 30 (30 dB) at 50 Hz is sufficient. The transistors chosen were a combination of a Toshiba `TTA004B/TTC004B` and Onsemi `BC817-40/BC807-40` for the positive/negative rail. The `TTA004B/TTC004B` are good up to about 500 mA. At this point the gains start dropping. A higher power transistor like the Onsemi `D45H8/D44H8` is recommended for currents above 500 mA. The two transistors are configured as a Sziklai pair, which is similar to a Darlington pair but reduces the voltage drop across the transistors from two base-emitter diode drops of 1.2 V to 0.6 V.

A low cutoff frequency always implies a long start up time until the filter has settled. To reduce this time a fast startup circuit highlighted in green in figure 4.7 is used. At startup, the capacitor C_m at the base of Q_2 is still discharged and 15 V will be applied. It will then begin to charge with a current of 1.5 mA through the 10 kΩ resistor R_m. Since Q_2 is an emitter follower configuration, the emitter follows the voltage at the base (minus a diode drop for the base-emitter diode) and the output voltage rises like the voltage of the RC filter. To reduce the rise time, R_m needs to be bypassed. This is the purpose of the LED, a 625 nm Würth Elektronik `150080RS75000`. Applying the input voltage of 15 V at startup the LED it will start conducting immediately while dropping 1.8–2 V. The current flowing into C_m is then dependent on the diode series resistor, which was chosen to be 680 Ω, a value particularly important in this case because it limits the inrush current of the whole circuit. At startup about 20 mA will flow into C_m through the LED. Remembering that Q_2 and Q_1 act as an emitter follower the output voltage rises like the voltage of the base. So for every 10 µF of capacitance in the system a current of 20 mA will flow through Q_1 into the system. With a 100 µF capacitor at the output

and assuming another 100 µF of distributed bypassing capacitance around the board, this is around 400 mA, which is still well below the damage threshold of the transistors (2.5 A and 0.5 A), while 20 mA is below that of the LED (30 mA), but these values must be kept in mind and R_{led} increased accordingly when adding larger output capacitors. The fast startup circuit ensures an output voltage of 13 V within 220 ms instead of around 0.5 s, reducing the time to boot and leaving more time for self-checks without impacting the user experience.

To get a better understanding of the full frequency response of the filter, it was simulated using LTSpice. The simulation was conducted with a load current of 500 mA running through the capacitance multiplier to simulate the worst case because as discussed above, the current gain β of the transistor drops at higher currents as the transistor saturates. The simulation source file can be found at source/spice/input_filter_dgdrive.asc. The simulation also includes the series resistance and parasitic parallel capacitance of the filter inductor L_1. The latter is the cause of the self resonance frequency of the inductor at 1 MHz and marks the usable upper bound of the filter after which the attenuation drops due to the capacitive coupling between the conductor windings.

The suppression of this LC filter is an order of magnitude better than the filter used by Libbrecht et al. not including the high performance regulators that follow. The transfer function for both the damped LC filter and the filter with the capacitance multiplier in series is plotted in figure 4.8. The LC filter shows the expected self resonance peak at 1 MHz that is not damped by the inductor resistance. This is not critical and only marks the limit of the filter as can be seen from the output impedance plot. There is enough capacitance present to make up for the increasing output impedance of the inductor. The output impedance above 1 MHz is dominated by local bypass capacitors and not accurately represented by the simulation. It can be expected to be even lower than the simulated results, which do not include these distributed capacitors.

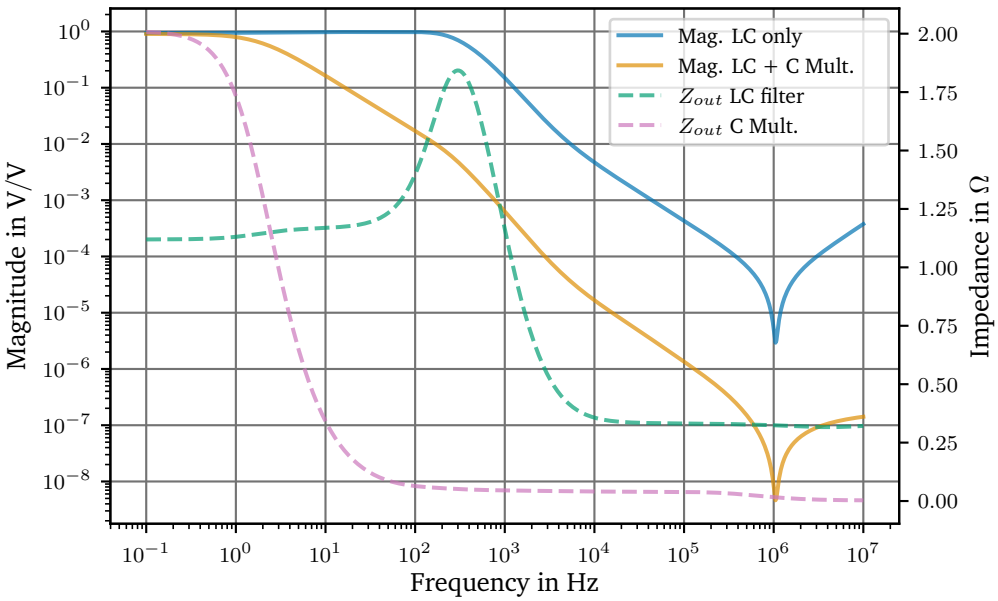

Figure 4.8.: Simulated transfer function of the two stage input filter used in the digital current driver. Both magnitude and output impedance of the stages are shown.

As discussed above the LC filter is not critically but rather underdamped, which can also be seen in the output impedance that peaks at the corner frequency of 300 Hz. This peaking

increases the output impedance of $1.2\,\Omega$ in the passband, which is mostly the resistance of the inductor, to a total of $1.8\,\Omega$.

The rejection ratio of the LC filter and the capacitance multiplier combined is better than 10^6 at $100\,\text{kHz}$ and beyond. This can be anticipated to keep switch-mode noise away from the laser driver current.

The high rejection ratio of the filter is expected to make the the experimental validation rather challenging because there are a number of complications that derive from the active nature of the circuit. The capacitance multiplier must be loaded, preferably at the maximum current to show the worst case and additionally, the ripple voltage must be low enough to not saturate the capacitance multiplier.

This requires a highly sensitive vector network analyser (VNA) that has a low frequency range. This setup uses an Omicron Lab `Bode 100`, which can measure from $1\,\text{Hz}$ to $50\,\text{MHz}$ with an exceptionally low noise floor of about $180\,\text{nV}/\sqrt{\text{Hz}}$ [223]. Additionally a Stanford Research `SR560` was used as a preamplifier. To apply the ripple voltage to the power supply rails a Picotest `J2123A` negative line injector and a self-designed positive line injector was used. The positive line injector design is available open-source and can be found in a GitHub repository at [37]. This injector is called `PB02`. During the measurement, it was found, that since the expected signal is extremely small, ground currents became an issue. There is an inherent ground loop issue built into the VNA. The output and the two inputs of the `Bode 100` are not isolated. The measurement is a 3-port measurement as shown in figure 4.9. The `Bode 100` is driving the line injectors, measuring the signal going into the line injector and also sampling the signal across the output capacitor of the filter. The ground current now has two possibilities of flowing. One is through the low side of the measurement cables and their resistance, or through the ground plane of the VNA. The latter is the dreaded ground loop. This ground loop becomes more pronounced at higher frequencies because the return path trough the cable is inductive and its impedance increases with frequency. Typically this problem would be addressed using a common-mode choke inserted into CH2. CH2 is the VNA input measuring the filter output. This common-mode choke prevents any current flowing through CH2 that has not flown through the cable.

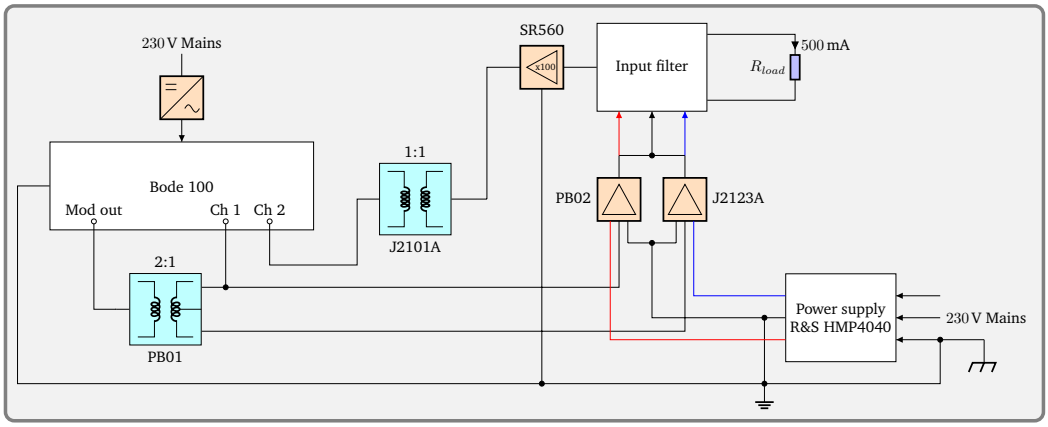

Figure 4.9.: Power and grounding scheme for a low noise measurement of the line filter rejection ratio, minimizing the interfernce of circuit return currents.

Unfortunately, the author did not have a suitable common mode choke at hand, so the only feasible solution to at least suppress the ground loop at low frequencies was to add transformers at the output and the input of CH2. This isolates the output while the battery powered `SR560`

is driving the VNA via the transformer, isolating the input as well. The transformer used for isolating the VNA output, was an injection transformer named `PB01` by the author. It is center tapped to create an anti-symmetrical output for the line injectors. The center tap reduces the output amplitude by one half. The details regarding this device and its construction can be found in annex A.6. The transformer used at the output of the `SR560` is a Picotest `J2123A`. Both transformers are unfortunately injection transformers and not dedicated isolation transformers as discussed in annex A.6, yet the only transformers available at the time. The consequences of this subtle detail will become imminent in a moment.

The digital current driver is powered by a Rohde & Schwarz `HMP4040` and there is a single point of ground connected to protective earth at the power supply. The power supply feeds into the line injectors, through which the current driver is powered. The output current is set to $500\,\mathrm{mA}$ across a $10\,\Omega$ dummy resistor. The SR560 measures the ripple voltage after the LC filter and drives the VNA input via the transformer. The measurement cable used is a short twisted pair to reduce noise pickup.

The output of the VNA was set to $-27\,\mathrm{dBm}$ ($10\,\mathrm{mV_{rms}}$), which must by multiplied by about $0.5 \cdot 0.975 = 0.485$ to give the ripple voltage seen on the positive supply, the latter term comes from the line injector [37]. To put this into perspective, given a $-60\,\mathrm{dB}$ (10^{-3}) suppression, results in a ripple voltage of only $4.9\,\mu\mathrm{V_{rms}}$.

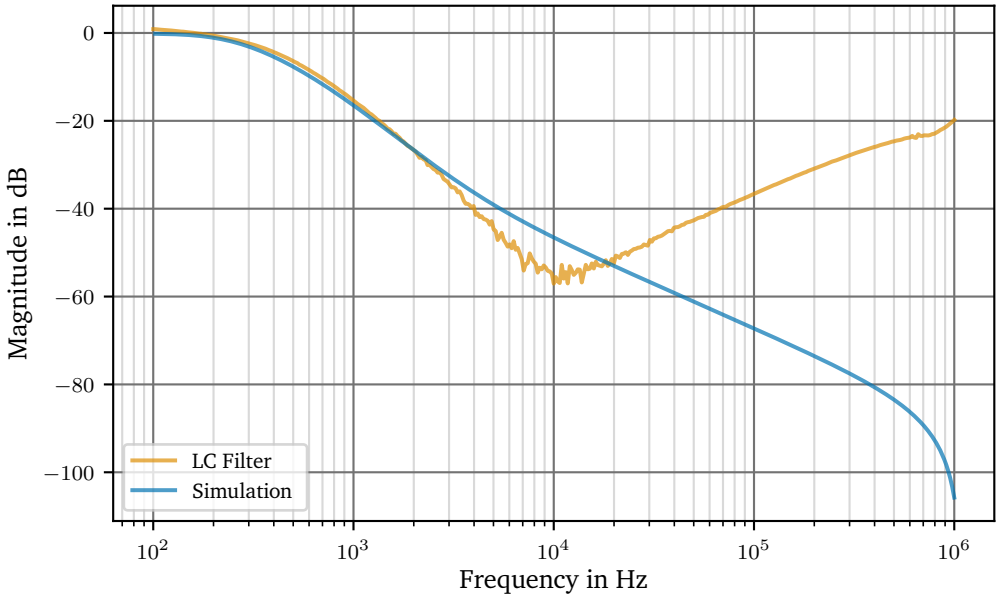

Figure 4.10.: Measured response of input filter used in the digital current driver. Above $10\,\mathrm{kHz}$ capacitive coupling through the transformer can be seen.

Figure 4.10 shows the measurement of the LC filter output. At low frequencies, there is good agreement with the simulation and the filter rolls off with $-40\,\mathrm{dB/decade}$. At around $10\,\mathrm{kHz}$ and $-55\,\mathrm{dB}$ the noise floor of the measurement is reached. Then the ground loop manifests itself again coupling through the transformers. The magnitude rising with $20\,\mathrm{dB/decade}$ is an artifact, which can be significantly influenced by changing the type of probing and the location of probing. To record any usable data above $10\,\mathrm{kHz}$ a common-mode choke is required. Additionally the noise floor of the measurement is reached at around the same frequency, requiring a lower noise amplifier. Due to the lack of another amplifier and the choke, the

author left the measurement as is. It is still a good example to show the ground loop pitfalls of a 2 or 3-port measurement. This topic will be revisited later in section 4.1.10 when measuring the current noise of the driver.

To conclude, the measurements show that the LC supply filter is correctly damped with the expected corner frequency of $300\,\mathrm{Hz}$ and it will likely perform as intended, but above $10\,\mathrm{kHz}$ the filter performance cannot be accurately measured due to limits of the setup.

4.1.5. Voltage Reference and Setpoint Adjustment

The voltage reference used in this Design is the ADI `LM399` and alternatively the ADI `ADR1399`, but the latter was not available in sufficient quantities for production. Only preliminary tests were conducted on this reference. The `LM399` is also used by most current drivers tested for the laser system of highly charged ions, because, as discussed in section 3.8.7, it is the most economical solution, although this statement will by qualified again in section 4.1.13 with regard to the Zener diode selection process.

For the `LM399` used in this design there are two approaches to integrate it as a voltage reference. The first concept is the one used by Libbrecht et al. [128] and shown in figure 4.1. It is a simple arrangement of a resistor in series with the Zener diode. The resistor is used to regulate the current through the diode. According to the data sheet around $1\,\mathrm{mA}$ [133] should be used. The circuit presented by [128] and carried over unmodified by Seck et al. [196] uses a variable current of up to $2\,\mathrm{mA}$ at the maximum diode supply voltage of $12\,\mathrm{V}$ as this voltage is user-adjustable. It can be adjusted up to voltage the input supply voltage of $15\,\mathrm{V}$ minus the minimum dropout voltage of the `LM317`, which is $3\,\mathrm{V}$ [134]. This is used to limit the compliance voltage as discussed below, but also reduces the Zener current accordingly.

On a sidenote, the diode supply voltage adjustment circuitry is rather peculiar because it would allow output adjustment of the `LM317` up to a maximum $24\,\mathrm{V}$, although there is only a $15\,\mathrm{V}$ input. Maybe the trimmer resistance value R_{trim} of $5\,\mathrm{k\Omega}$ was intended for a higher input voltage or was a left-over from a previous design phase. Using the equation given in the datasheet [134]

$$V_{out} = 1.25\,\mathrm{V}\left(1 + \frac{R_2}{R_1}\right) = 1.25\,\mathrm{V}\left(1 + \frac{R_{trim}}{275\,\Omega}\right) ,$$

it can be seen that half the value of R_{trim} would have sufficed to provide the $12\,\mathrm{V}$ minimum output.

This voltage adjustment option is advertised as a current/voltage limit, but its use is particularly deceitful. As discussed in section 3.8.5 the MOSFET needs a certain voltage to remain in saturation for correct operation with good performance, but it will work at lower voltages as a variable resistor. As shown by the output impedance over V_{DS} graph in figure 3.46 on page 80 there is considerable leeway between the saturated zone on the right and the current being limited on the left because V_{DS} has reached $0\,\mathrm{V}$. This can be illustrated with an example. The `VP0106` MOSFET [65] used by Libbrecht et al. [128] requires about $2\,\mathrm{V}$ for correct operation. The voltage limit would be adjusted to include the voltage required by the diode, the sense resistor voltage drop at the maximum allowable diode current and the $2\,\mathrm{V}$ for the MOSFET. In an overcurrent event the latter $2\,\mathrm{V}$ would shift to the $50\,\Omega$ sense resistor. This means that an extra current of $\frac{2\,\mathrm{V}}{50\,\Omega} = 40\,\mathrm{mA}$ can flow before the current limits engages. This is $40\,\%$ of the total range of the driver. The typical $100\,\mathrm{mA}$ laser diode will likely be damaged by then. This feature is therefore best not relied on.

Going back to the Zener diode, the adjustable supply voltage has another drawback, because it influences the Zener voltage of the reference. The `LM399` has a dynamic impedance of $1.5\,\Omega$

[133] which means that the Zener voltage changes $1.5\,\mathrm{mV/mA}$. The Zener diode impedance and the bias resistor $R_{bias} = 7.5\,\mathrm{k\Omega}$ given in [128] forms a voltage divider from which the a suppression of

$$\frac{1.5}{7500 + 1.5} \approx \frac{1.5}{7500} = \frac{1}{5000}$$

can be calculated, totally obliterating the stability of the diode. So it is best adjusted once, then left alone.

Fortunately, this has little bearing on the high frequency performance due to the filter that follows. Moving on to the filter, there is another issue in the original design due to the filter impedance. As shown in equation 3.103 on page 86, the output impedance of an RC filter at low frequency is R_f. For the filter circuit shown in figure 4.1 taken from [128] $R_f = 6\,\mathrm{k\Omega} + (0 \text{ to } 5)\,\mathrm{k\Omega}$, depending on the potentiometer setting, with the maximum of $5\,\mathrm{k\Omega}$ in the center position. Considering the `LT1028` op-amp after the filter results in $47\,\mathrm{nV}/\sqrt{\mathrm{Hz}}$ at $10\,\mathrm{Hz}$ from the op-amp input current noise compared to the voltage input noise contribution of only $1\,\mathrm{nV}/\sqrt{\mathrm{Hz}}$. The current noise is therefore clearly dominating the noise of the op-amp below the filter cutoff. This number is, thankfully, still a lot less than the $170\,\mathrm{nV}/\sqrt{\mathrm{Hz}}$ at $10\,\mathrm{Hz}$ of the `LM399`, but when considering the `ADR1399`, which has a noise density of $65\,\mathrm{nV}/\sqrt{\mathrm{Hz}}$ at $10\,\mathrm{Hz}$, it is no longer negligible, especially given that this number is attenuated by the potentiometer setting.

All of these issues were addressed in the design detailed now. A condensed version of the setpoint generation circuit is shown in figure 4.11, which is reduced to the most important components. The full schematic can be found in the Git repositories of the reference module and the laser driver [32, 43].

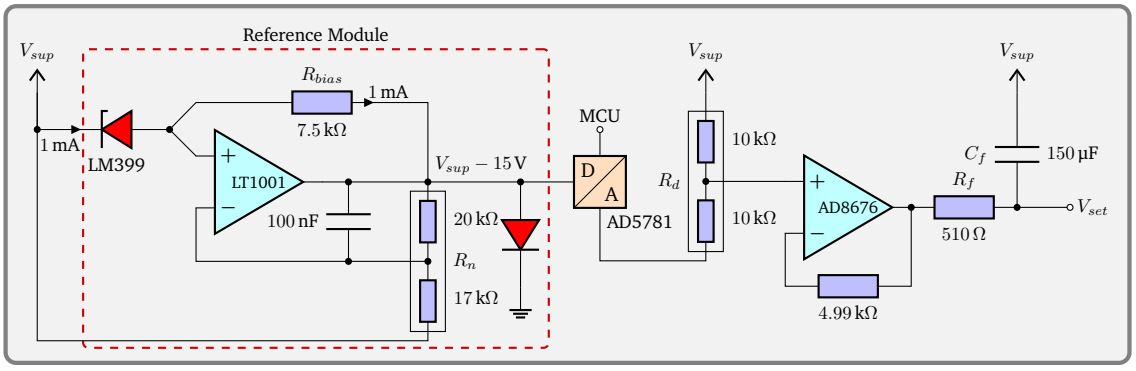

Figure 4.11.: Setpoint generation using the `LM399` reference module and an `AD5781` DAC followed by a 2:1 divider and an RC filter.

To better follow the discussion of figure 4.11 it is essential to remember that the setpoint voltage is referenced to the diode voltage supply V_{sup} as opposed to ground like in a normal circuit. For example the $-7\,\mathrm{V}$ Zener voltage becomes $V_{sup} + (-7\,\mathrm{V})$ and so on. Due to the use of a p-channel FET, as it was shown in figure 3.45 on page 78 where the precision current source was introduced, the setpoint to adjust the current must be referenced to V_{sup}. For reasons of simplicity, the author only refers to these values as $-7\,\mathrm{V}$.

The circuit shown in figure 4.11 is best split into two parts, the voltage reference, which is a separate module shown in a red dashed box and the setpoint generation using a DAC. The DAC circuit will be discussed first, because some of the design decisions are rooted there.

While there are many DACs available on the market, fine grained adjustment of the laser current is desired limiting the choice of DACs. Erickson et al. [77] used an ADI `AD5541` 16 bit

DAC in their design, which can provide up to $100\,\text{mA}$, having a resolution of about $1.5\,\mu\text{A}$. Taubman et al. [222] presented a higher power $1\,\text{A}$ controller with an 18 bit Texas Instruments (TI) `DAC9881SB` DAC, granting a resolution of $4\,\mu\text{A}$. The resolution required by this design is mostly defined by the blue laser and, as it was mentioned in section 3.2.1, the laser is stable over the range of a few tens of µA and requires up to $145\,\text{mA}$. A 16 bit DAC offers a resolution of $2\,\mu\text{A}$, which would only allow a few DAC codes of stable operation. Therefore a DAC with 18 bit or more is desirable. The choice between an 18 bit and a 20 bit DAC is predetermined by the given reference. A 20 bit DAC has a resolution of 1 ppm while the noise of the `LM399` is around $0.5\,\mu\text{V/V}$ at low frequency. The noise and drift performance [133] of the `LM399` makes an 18 bit DAC the more reasonable selection. The type of current source circuit limits the choice of DACs further. Using a current source, which is referenced to V_{sup} requires the DAC to either accept V_{sup} as the positive reference voltage directly or one must float the DAC like Erickson et al. [77] did. Additionally both Erickson et al. [77] and Taubman et al. [222] divided down the reference voltage from $-7\,\text{V}$ to $-5\,\text{V}$ to match the maximum input voltage of the DAC. Floating the DAC brings about a number of problems, like having to level-shift all control signals as Erickson et al. [77] did. Correct power supply sequencing also becomes vital.

A simpler approach can be taken if the DAC can accept both V_{sup} as the positive reference and $V_{sup}+V_{ref}$ as the negative reference without being floated to $V_{sup}+V_{ref}$. A typical bipolar output DAC almost matches those requirements. The only problem is a constraint typically imposed by the negative reference input, which must be at a potential lower than ground. This problem can be solved by amplifying the reference voltage to ensure $|V_{ref}| \geq V_{sup}$. This also has the added benefit of reducing the noise contribution and offset drifts of the added circuitry, like thermal electromotive force (EMF). The suppression is inversely proportional to the gain. This approach is pursued here and its implementation is explained below.

The only bipolar DACs meeting the requirements are the TI `DAC91001` [63] and the ADI `AD5781` [8]. Both are 18 bit devices with a pin compatible upgrade path to a 20 bit version should the need arise. The two devices are fairly similar in regard to this application. The device chosen was based on the availability, the `DAC91001` is only available through TI, while the `AD5781` is available through multiple distributors. Additionally, the author has worked with multiple DACs from ADI before and the implementation details are similar, which cut down the development time.

The DAC reference inputs and the output is buffered using an ADI `ADA4077-4` quad op-amp in a remote sensing arrangement as per the data sheet recommendation [8]. V_{sup} is taken directly from the four-wire sense resistor, a Vishay `VPR221Z` (see section 4.1.6 for details). The negative reference voltage $V_{sup}+V_{ref}$ is the amplified Zener voltage taken from the reference module output. Typically, $V_{ref}=-15\,\text{V}$ is used, because this ensures that $|V_{ref}| \geq V_{sup}$ at all times. The typical supply voltage of the current driver is $\pm 15\,\text{V}$ (maximum $\pm 18\,\text{V}$) and therefore $V_{sup} \leq 15\,\text{V}$ due to required headroom of $3\,\text{V}$ for the op-amps used as discussed in section 3.8.7.

The $-15\,\text{V}$ reference must be divided down after the DAC because the setpoint, which is the voltage dropped across the sense resistor, must be between GND and V_{sup}. The resistor network forming a 2:1 divider is a Vishay `DSMZ` $10\,\text{k}\Omega/10\,\text{k}\Omega$ network. The factor of $\frac{1}{2}$ is chosen because it is the most stable ratio, as both resistor values are of the same magnitude. An ADI `AD8676` [11] dual op-amp buffers both V_{sup} to supply one arm of the divider and also the output of the divider using the second op-amp. The output buffer uses a $5\,\text{k}\Omega$ compensation resistor in the feedback path to match the input resistance as shown in figure 4.11. This compensates for an input offset drift due to changes in the input bias current of the op-amp to cover the worst-case specifications ($\pm 4.5\,\text{nA}$). If there there were no compensation resistor a drift would result from

the difference of the two input bias currents because one input sees $5\,\mathrm{k\Omega}$, while the other input sees zero resistance. The divider is then followed by single pole filter and discussed next.

In contrast to the second order filter used by [77, 128, 196] and shown in figure 4.12, this design uses a simpler first order filter.

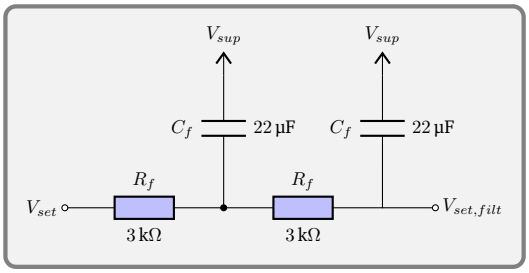

Figure 4.12.: Setpoint filter used in [77, 128, 196].

The second order filter shown in figure 4.12 is overdamped ($\zeta = 1.5$) with a cutoff frequency of $2.4\,\mathrm{Hz}$. The likely reason such a filter is applied is due the `LT1028` used in the design by Libbrecht et al. [128]. It does have a very low flicker noise corner of $3.5\,\mathrm{Hz}$ [136], which matches the filter corner frequency.

There are two problems with the approach though. First, the current noise of the `LT1028` is dominating at low frequencies with more than $5\,\mathrm{k\Omega}$ of input resistance and second the bias current cancelling circuit inside the op-amp, which requires a matched source resistance. The bias current cancelling circuit is injecting a small amount of correlated current noise into both inputs. Using a large input resistance, this noise needs to be considered as well. With unmatched source resistances it is not suppressed by the common mode rejection as explained in section 3.8.6. Therefore, contrary to intuition, using no resistor further increases the noise. The inputs in the original design are not balanced and therefore the low frequency performance of the circuit below the filter cutoff is degraded. The issues encountered when designing a high performance and high stability filter are discussed next.

A filter designed for the ADI `AD797` needs to be less aggressive, because the flicker noise corner frequency is about an order of magnitude higher and around $30\,\mathrm{Hz}$ [9]. Therefore, a first order filter as shown in figure 4.14 can be used. According to the discussion regarding the current noise above, the capacitor size should be maximized so that the resistive part R_f of the RC filter can be reduced. Ideally R_f is kept well below $1\,\mathrm{k\Omega}$ to make sure that the total noise

$$\begin{aligned} e_{total} &= \left(e_n^2 + 4k_BTR_{total} + i_nR_{total}\right)^{\frac{1}{2}} \\ &= \left(e_n^2 + 4k_BT\left(R_f + R_s\right) + i_n\left(R_f + R_s\right)\right)^{\frac{1}{2}} \end{aligned} \tag{4.8}$$

is minimized. e_n is the voltage noise of the op-amp, i_n the current noise, R_f the filter resistor and R_s the sense resistor used for the current source as shown in figure 3.45. In order to determine the optimal filter components several options were simulated and also verified experimentally. The simulation results are shown in figure 4.13.

The simulation is a simplified simulation of the circuit shown in figure 4.11. The reference module, including the DAC is replaced by a noise model, which includes the flicker noise and the white noise of the Zener reference and the DAC. The noise of most op-amps is neglected here, because the noise figure of the DAC as quoted in the datasheet [8] already includes the buffers. The noise of the Zener module buffer can also be neglected as is an order of magnitude less than the Zener diode noise. The ADI `AD8676` buffer following the resistive divider is

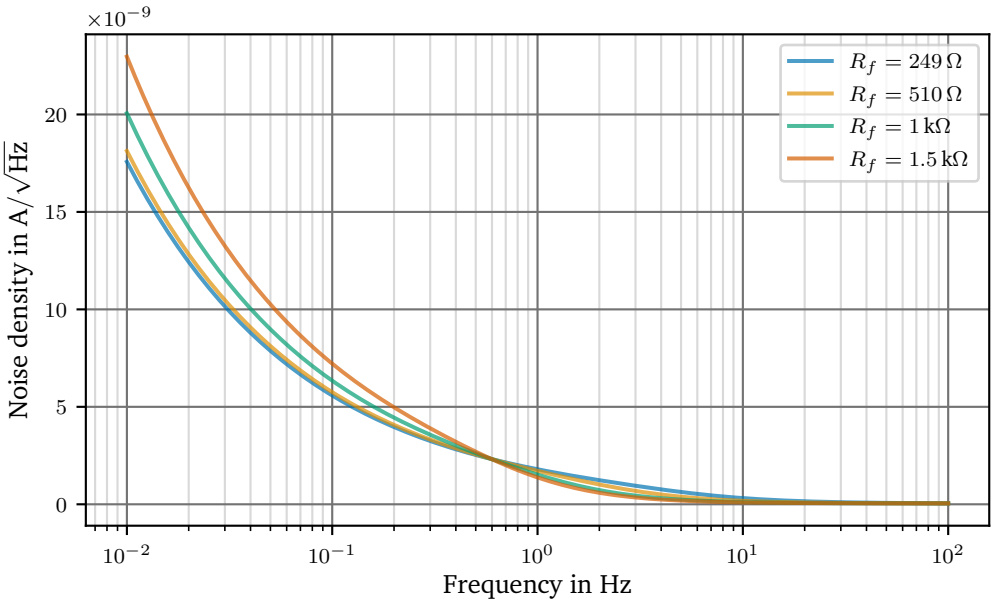

Figure 4.13.: Simulated noise density of a $250\,\mathrm{mA}$ current source running at $50\,\mathrm{mA}$ built according to figure 4.11. Compared are different values of the filter resistor.

included and so is the AD797 current source. The sense resistor value is $30\,\Omega$. The output current was set to $50\,\mathrm{mA}$. The full LTSpice simulation can be found among the supplemental material at source/spice/current_regulator_AD797_noise.asc.

The simulation was conducted for several different values of R_f. A range of values between $249\,\Omega$ and $1.5\,\mathrm{k}\Omega$ were simulated. The values chosen reflect resistor values that are commonly available. It can be seen that for higher values of R_f, the current noise starts dominating the low frequency noise of the AD797 amplifier as discussed above. The inflection point is around $0.6\,\mathrm{Hz}$ and the current source becomes increasing noisy below this frequency with increasing filter resistance. The choice of the capacitor ($150\,\mu\mathrm{F}$) is explained below.

As expected, the difference between a $249\,\Omega$ and a $510\,\Omega$ resistor is small and the noise contribution only becomes noticeable for $R_f \geq 1\,\mathrm{k}\Omega$ underpinning the statement above. Using a larger resistor R_f, does improve the noise contribution above $0.6\,\mathrm{Hz}$ though. However, this advantage is limited to a small frequency range and hence negligible. Table 4.4 shows the integrated noise of the plot shown in figure 4.13 and it can be seen that the numbers are close together, yet there is a slight improvement with a value of $510\,\Omega$. In order to derive these values from the simulation, it is important to remember, that LTSpice can only deal with voltage noise, so a shunt resistor for the current source output is used for the simulation. Its thermal noise was subtracted from the result. This procedure is documented in the simulation file.

Using the simulation as a guideline, several values of R_f were tested and $510\,\Omega$ was also found to be optimal in the final circuit regarding the noise and the temperature coefficient of the filter. The latter is discussed in more detail below. The resistor is a high quality Susumu RG3216P-5100-B-T1 $0.1\,\%$ resistor in a large 3216 package because Seifert [199] has shown, that larger resistors are of consistently higher quality and exhibiting less noise. Having settled on the optimal resistor value, the filter capacitor must be considered.

The capacitor value can be estimated from the required suppression. The AD797 reaches $1\,\mathrm{nV}/\sqrt{\mathrm{Hz}}$ at $100\,\mathrm{Hz}$ and the LM399 has a noise density of about $90\,\mathrm{nV}/\sqrt{\mathrm{Hz}}$ at $100\,\mathrm{Hz}$. This

R_f	Integrated noise, 10^{-2} Hz to 10^{2} Hz
$249\,\Omega$	$4.58\,\mathrm{nA_{rms}}$
$510\,\Omega$	$4.34\,\mathrm{nA_{rms}}$
$1\,\mathrm{k}\Omega$	$4.43\,\mathrm{nA_{rms}}$
$1.5\,\mathrm{k}\Omega$	$4.81\,\mathrm{nA_{rms}}$

Table 4.4.: Integrated noise of the current source for different values of R_f. The integration range is 10^{-2} Hz–10^{2} Hz.

means, that a cutoff frequency of $1.1\,\mathrm{Hz}$ is desired for about two order of magnitude of suppression at $100\,\mathrm{Hz}$, requiring a filter capacitor of $280\,\mu\mathrm{F}$. Taking into account the limited board space, it is clear, that the $280\,\mu\mathrm{F}$ marks an upper bound when considering capacitors with low volumetric efficiency. This warrants the examination of different types of capacitors and their properties. Libbrecht et al. [128] for example used special hermetically sealed tantalum capacitors, but there are also other options available. Modern low-leakage electrolytic capacitors and film capacitors were also investigated. Ceramic capacitors were not considered for this filter, because they are either piezoelectric (X5R, X7R, etc.) or too big in physical size (C0G). The properties studied are the leakage current and its temperature stability, while optimizing volumetric efficiency. Table 4.5 shows an overview of different dielectric materials and their suitability according to those properties. More information on other types of capacitors can also be found in [256] or [255].

Capacitor type	Volumetric efficiency	Leakage	Temperature stability
Electrolytic	$++$	$--$	$--$
Tantalum	$+$	$-$	$-$
Film	$-$	$+$	$+$
Ceramic C0G	$--$	$++$	$++$

Table 4.5.: Capacitor properties of different dielectrics.

The leakage current of a capacitor is of concern, because it affects the filter performance at low frequency. Figure 4.14 shows the first order filter of the digital current driver and two major sources of error currents. The leakage of the capacitor and the input bias current of the op-amp. Due to the filter resistor, both currents create an error offset voltage seen by the op-amp.

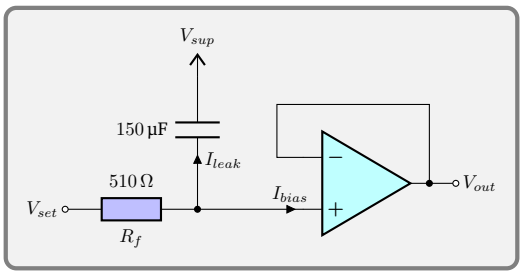

Figure 4.14.: Setpoint filter and error currents. The ADI AD797 is depicted as a buffer instead of the precision current source circuit.

According to the datasheet, the AD797 op-amp [9] has temperature dependent input bias current of about $+2\,\mathrm{nA/K}$, which results in a drift of about $-1\,\mu\mathrm{V/K}$ when using a $510\,\Omega$ resistor. Do note, that an increase in the leakage and bias current causes a negative temperature coefficient. The temperature coefficient of the bias current can only be influenced by using the better and more expensive B grade devices but must otherwise be accepted as given if not additional binning process is applied. All in all, the drift caused by the leakage and bias current should not exceed the reference drift of about $0.3\,\mu\mathrm{V/(V\,K)}$ ($2.25\,\mu\mathrm{V/K}$ for a $-7.5\,\mathrm{V}$ reference voltage), which results in a change in leakage current of $4.4\,\mathrm{nA/K}$. Using a larger filter resistor like the $6\,\mathrm{k\Omega}$ in the second order filter used by Libbrecht et al. [128], the same bias current of $2\,\mathrm{nA/K}$ would cause an offset of $12\,\mu\mathrm{V/K}$, almost $1.7\,\mu\mathrm{V/(V\,K)}$ considering the reference voltage of $-7\,\mathrm{V}$. The leakage current of a capacitor in this context is comprised of two effects, the first is leakage through the bulk resistance of the capacitor and the second is dielectric absorption. Dielectric absorption is an effect that describes how the molecules of the dielectric material slowly align to the external electric field applied. It can be modelled as a parallel RC circuit with a very large resistance. Depending on the type of capacitor, this effect can take several days to subside.

Electrolytic capacitors do have the highest capacitance per volume, but suffer from dielectric absorption and large changes in capacitance over temperature. Tantalum capacitors also exhibit large leakage currents [83] that depend on temperature, but they are more compact than film or ceramic capacitors. Film capacitors are very stable capacitors along with paraelectric NP0 ceramic capacitors. NP0 capacitors, being the most stable, unfortunately have the worst volumetric efficiency. Polyester film capacitors are a compromise between stability and size.

In order to asses the magnitude of the problem, the leakage current over temperature was measured for several capacitors.

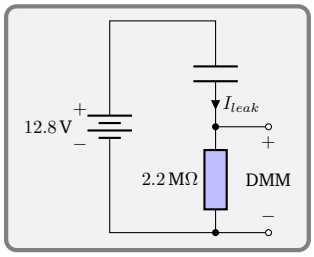

Figure 4.15.: Setup for measuring the leakage current of a capacitor.

The simple measurement setup shown in figure 4.15 was placed in a thermal chamber. A Vishay MRS25 $2.2\,\mathrm{M\Omega}$ resistor was placed in series with the capacitor and a $12.8\,\mathrm{V}$ test voltage from a low noise DC supply was applied. – in this case a stack of 8 alkaline batteries. Batteries were used to ensure, that no AC line noise is mistakenly recorded as leakage. The voltage drop across the resistor was measured using an HP 3458A digital multimeter (DMM). The input bias current of the 3458A is on the order of a few pA [127, 183], which is small compared to the leakage current measured in this setup and henceforth neglected. The capacitor was first allowed to settle for $24\,\mathrm{h}$ so that dielectric absorption can subside. The initial temperature was set to $24\,^\circ\mathrm{C}$ and then stepped to $45\,^\circ\mathrm{C}$ and left until the reading had settled again, then stepped down to $24\,^\circ\mathrm{C}$. This was done to observe the settling behaviour, which would cause a low frequency random walk in a filter arrangement as outlined in section 3.6.1. This setup forms a low-pass filter with a settling time of several minutes due to the large value resistor and capacitor. This means, that any fast settling dielectric absorption like that of a film capacitor cannot be observed.

Three samples each from the same batch of the following capacitors where compared:

- Nichicon UKL1V331KHD low leakage 330 µF, 35 V electrolytic capacitor
- Kemet T491X157K020AT 150 µF, 20 V tantalum capacitor
- WIMA MKS4B061507G00JSSD 150 µF, 50 V polyester (PET) film capacitor

The capacitors were chosen to have at least 150 µF and a voltage rating of ≥16 V, because the maximum setpoint voltage applied is −7.5 V and a derating of at least 50 % is applied to improve reliability.

This test was conducted with all capacitors and the results are summarised in table 4.6.

Capacitor	Capacitance	DC leakage at 12.8 V, 24 °C	Temperature stability
Nichicon UKL1V331KHD	330 µF	1.1 nA	390 pA/K
Kemet T491X157K020AT	150 µF	19 µA	16 nA/K
WIMA MKS4B061507G00JSSD	150 µF	2.2 nA	150 pA/K

Table 4.6.: Capacitor leakage current and temperature stability of the leakage current for different types of capacitors.

The electrolytic capacitor showed strong dielectric absorption and it took about 24 h to settle from about 500 nA to 1 nA. After settling, stability was surprisingly good, although long relaxation constants was observed when changing the temperature. These are due to a change in capacitance. A measurement of a typical sample is shown in figure 4.16.

The tantalum capacitor was a standard industrial grade capacitor and not a special low leakage version. The reason was that low leakage wet slug tantalum capacitors are very costly and similar in size to the PET film capacitor. The Kemet T491 capacitor was tested to get an idea about the performance of standard tantalum capacitors. The leakage current observed for the tantalum capacitor was the highest of the components tested. Especially the temperature stability was unacceptable, as it was almost an order of magnitude larger than was considered acceptable above.

The type of film capacitor was chosen because its size was still possible to fit onto the PCB. The 150 µF WIMA MKS4B061507G00JSSD is the 50 V version. There is also a 63 V available, but these were not available in small quantities for testing. If available the 63 V version should be preferred, because higher voltage capacitors have better leakage specifications, when biased at the same voltage. Dielectric absorption was not observed during testing, but could haven been masked by the large $RC = 330$ s time constant, as the initial current takes about 40 min to decay to 3 nA. The measurement is shown in figure 4.17. The PET film capacitor gave the best results with very good repeatability and very little capacitance change due to temperature. Its leakage current was also the lowest of the three types of capacitors tested.

Based on the results summarised in table 4.6 the 150 µF WIMA MKS4B061507G00JSSD capacitor and a 510 Ω Susumu RG3216P-5100-B-T1 resistor were chosen for the filter.

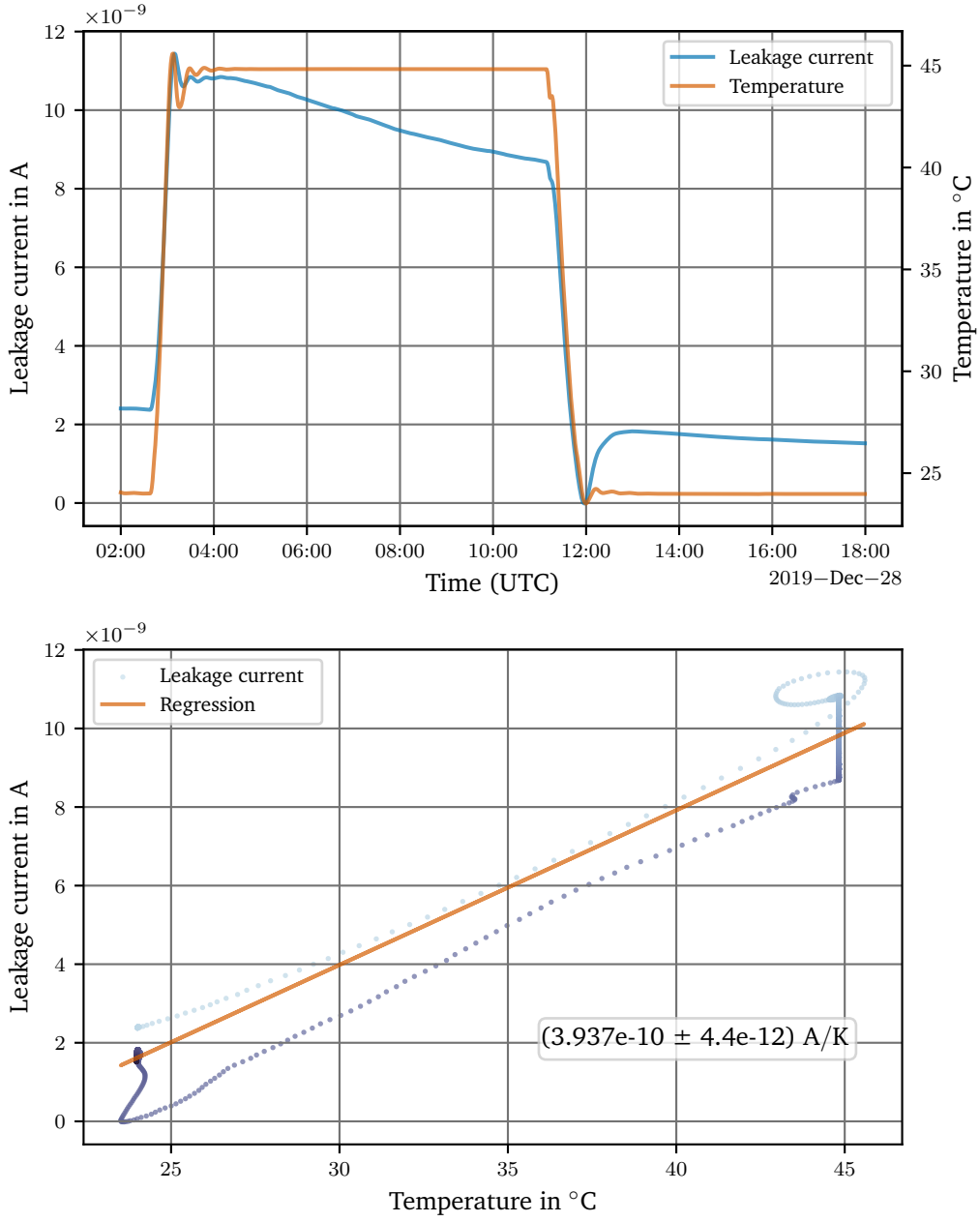

Figure 4.16.: Leakage current over temperature of a Nichicon UKL1V331KHD $330\,\mu F$ electrolytic capacitor biased at $12.8\,V$. The capacitor was allowed to soak for $24\,h$ prior to the measurement.

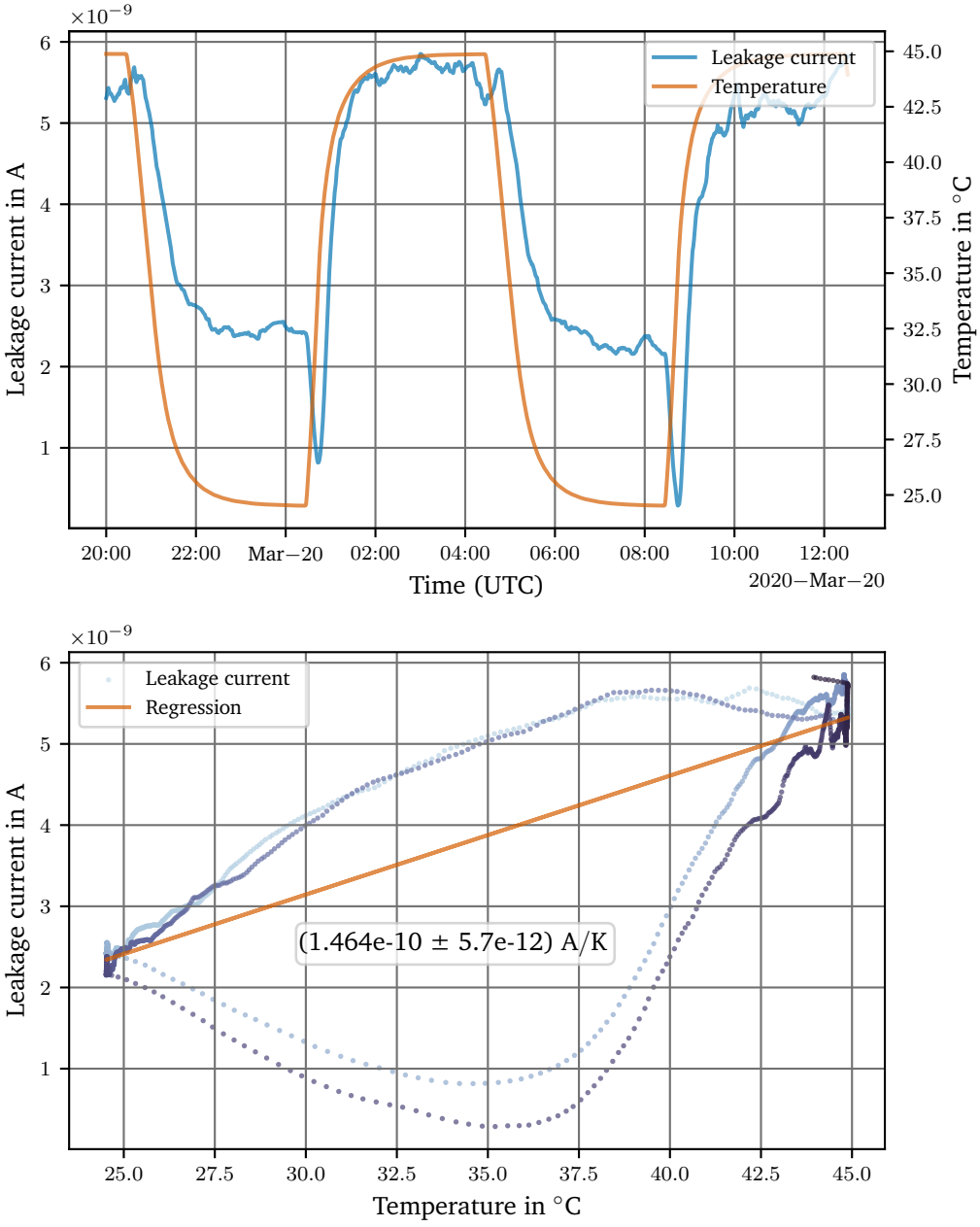

Figure 4.17.: Leakage current over temperature of a WIMA MKS4B061507G00JSSD 150 µF PET capacitor biased at 12.8 V.

Having discussed the DAC it is clear, that the Zener voltage must be amplified to meet the requirements of the negative reference input of the DAC. An optimal value of $-15\,\mathrm{V}$ was also found above.

The voltage reference was realised as an additional reference module that is connected to the main PCB via a pin header. This allows additional testing of the much simpler reference module in a special test bench. These tests are detailed in section 4.1.13, but the circuit is discussed here first.

Amplifying the Zener voltage has the advantage that it is possible to bootstrap the Zener diode to produce its own reference current. The `LM399` only has a limited rejection of $\frac{1}{5000}$ against changes of the supply voltage when connected like shown in figure 4.1 on page 100 because any change in the supply voltage results in a change of the Zener current. Bootstrapping the Zener improves the rejection ratio towards changes of the diode supply voltage and noise, because the Zener current is now produced by the amplified Zener voltage. Any noise and ripple has to additionally get past the amplifier CMRR as discussed in 3.8.6.

The bootstrapped circuit is shown in figure 4.11 on page 112 and can be divided into an upper part with R_{bias} and a lower part with a feedback network. The feedback network, based on a Vishay `300144Z` [1] resistor network, is used to amplify the $-7\,\mathrm{V}$ Zener voltage to

$$-7\,\mathrm{V} \cdot \left(1 + \frac{Rn_1}{Rn_2}\right) = -7\,\mathrm{V} \cdot \left(1 + \frac{20\,\mathrm{k\Omega}}{17\,\mathrm{k\Omega}}\right) = -15.2\,\mathrm{V}\,,$$

again referenced to V_{sup}. With $-15.2\,\mathrm{V}$ at the output and $-7\,\mathrm{V}$ at the Zener diode, R_{bias} will then provide

$$I_{bias} = \frac{-15.2\,\mathrm{V} - (-7\,\mathrm{V})}{7.5\,\mathrm{k\Omega}} \approx 1.1\,\mathrm{mA}\,,$$

which is independent of V_{sup}, just as desired. R_{bias} is a $0.1\,\%$, $10\,\mu\Omega/(\Omega\,\mathrm{K})$ Panasonic `ERA-6ARB752V` resistor, but in principal any $100\,\mu\Omega/(\Omega\,\mathrm{K})$ resistor can be used, because the sensitivity of R_{bias} is roughly

$$\frac{-1\,\mathrm{mA} \cdot 1.5\,\Omega}{7\,\mathrm{V}} \frac{\mathrm{d}R_{bias}}{R_{bias}} \approx 215 \times 10^{-6} \cdot \frac{\mathrm{d}R_{bias}}{R_{bias}}\,. \tag{4.9}$$

Using a $100\,\mu\Omega/(\Omega\,\mathrm{K})$ resistor instead, would cause a temperature coefficient of $-20\,\mathrm{nV/(V\,K)}$, which is small compared to the $0.3\,\mu\mathrm{V/(V\,K)}$ of the `LM399`. The higher quality resistor was chosen to limit long-term drift. The feedback network is far more critical in this regard, hence the use of the Vishay `300144Z` high-precision network. All capacitors used in this circuit are NP0 capacitors, which are very stable over the whole temperature range.

There is one last issue to address. Unfortunately, the bootstrapped reference circuit is not guaranteed to start up correctly. The self-biased circuit has two stable points of operation. The desired one is at $V_{sup} - V_z$ and the other is $V_{sup} + V_f$, when the Zener diode is forward biased. The cause of this is the positive feedback to the `LT1001`. At startup, the Zener diode has a very high impedance (see the typical Zener diode I-V curve, e.g. [198]) and can be considered open, while R_{bias} is small compared to the feedback network. The op-amp inputs are slightly capacitive and the non-inverting input then pulls high faster, delivering positive feedback. This unwanted operating point can be reached if the op-amp supply comes up before V_{sup}. The Zener diode will then be forward biased by the op-amp. Of course this can only happen if the op-amp supply voltage is higher than V_{sup}, which in this case is true. This situation is critical, because the output would then go above $0\,\mathrm{V}$. This output is connected to the negative reference input of the DAC, which must not be positively biased. To prevent this case and damage to the

DAC, the second diode at the output of the op-amp is used. It ensures that the output cannot go above ground and the gain of the positive feedback is drastically reduced and the negative feedback takes over quickly.

The setpoint circuitry can be summarised as follows. The reference module outputs an amplified reference voltage of $-15\,\mathrm{V}$, which is fed to the negative reference input of an ADI `AD5781` $18\,\mathrm{bit}$ DAC, which is used to create a setpoint voltage between V_{sup} and $V_{sup} - 15\,\mathrm{V}$. The DAC output voltage is divided down by a factor of two (with regard to V_{sup}) using a Vishay `DSMZ` resistor network. The resulting voltage between V_{sup} and $V_{sup} - 7.5\,\mathrm{V}$ is then buffered and low-pass filtered using a $510\,\Omega$ and $150\,\mu\mathrm{F}$ RC low pass. The filter capacitor, a WIMA `MKS4B061507G00JSSD`, was tested for low leakage to ensure stability of the filter. The filtered voltage is at last fed to the precision current source discussed in the next section.

The reference module, mounted on a standoff, secured with a screw, is shown in figure 4.18. The reference is on the right hand side with slots surrounding it for better thermal isolation. The serial number and red dot can be seen on can. This is the serial number of the Zener diode and the dot shows that it passed the burn-in test. The Vishay `300144Z` divider is far away from the heated reference in the upper left corner to reduce thermal EMF.

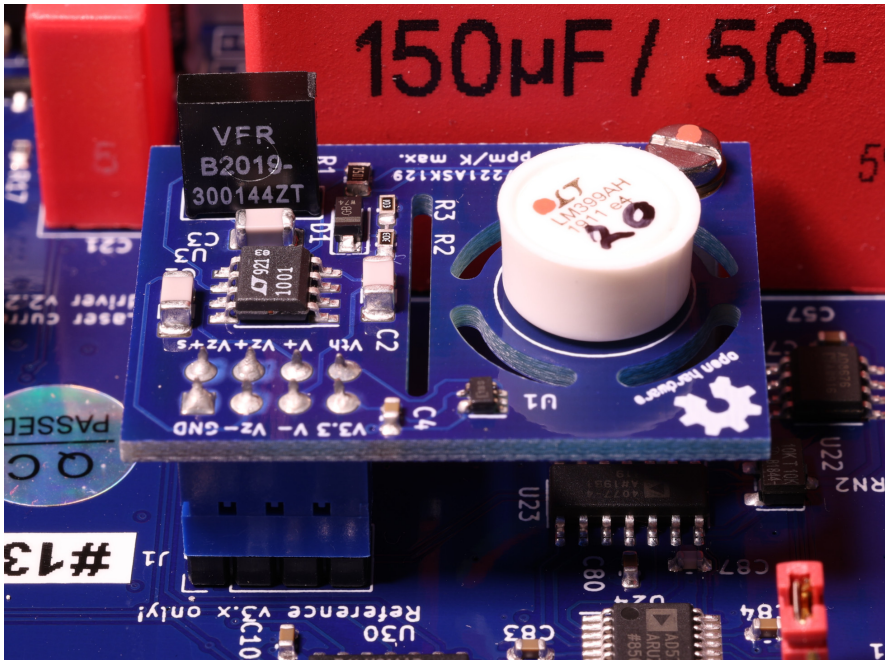

Figure 4.18.: The voltage reference module mounted on its socket on the main current driver PCB. `LM399` no. 20 is marked with a red dot because it passed quality control. In the background, the large red filter capacitor can be seen.

4.1.6. Precision Current Source

The theory behind the precision current source was laid out in section 3.8.4, but some interesting details were not discussed yet. One of the main drawbacks of the current source from section 3.8.4 is that the setpoint has a direct impact on the compliance voltage as discussed in section 3.8.5. Given an input supply voltage of $15\,\mathrm{V}$ it is immediately evident that with a reference voltage of $7.5\,\mathrm{V}$ a compliance voltage of $8\,\mathrm{V}$ as defined in specification 3.2 is impossible to reach.

One solution would be to increase the division ratio after the DAC to three, for example, and thereby reduce the reference voltage to $5\,\mathrm{V}$. Unfortunately, this solution increases the current noise by a factor of $\frac{7.5}{5} = 1.5$ according to table 3.7, because the sense resistor has to be scaled by the factor of $\frac{2}{3}$ to get the same output current.

Another option is to use the negative $-15\,\mathrm{V}$ rail instead of ground to connect the cathode of the laser diode. This would directly increase the compliance voltage by $15\,\mathrm{V}$ and include enough headroom for other components of the current source, like the MOSFET. This solution, however, brings along the problem, which was discussed in section 3.8.1. Directly connecting the laser diode to a voltage rail can have catastrophic consequences for the diode in case the other side is accidentally connected to ground.

This work therefore presents a novel third option, which separates the current source from the compliance voltage requirement and enhances the current source shown in figure 3.45 on page 78. This circuit is shown in figure 4.19.

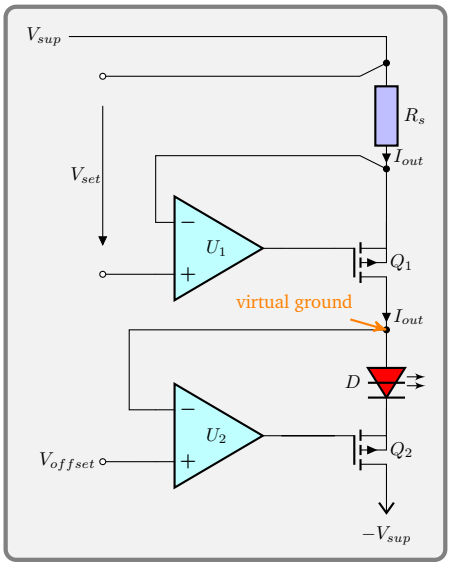

Figure 4.19.: Simplified current source implemented in the digital current driver. The voltage across R_s is Kelvin sensed. The laser diode is wrapped in a feedback loop and the current source is shielded from the load. U_1 is an ADI `AD797B` and U_2 is an ADI `ADA4625-1`.

This circuit consists of the current source introduced in section 3.8.4 and a current sink that wraps the laser diode in a feedback loop to shield the current source from the load. In addition to the circuit shown in section 3.8.4 in figure 3.45 on page 78, the sense resistor is connected differently. The sense resistor used is a Vishay `VPR221Z` [237], a four-terminal device. This allows Kelvin sensing of the voltage across R_s. The positive voltage is buffered using several precision ADI `ADA4077-4` [12] op-amps. This voltage is then supplied to the voltage reference circuit, the DAC and the divider that follows. It is important that no current is drawn from this net. The negative voltage is sensed by U_1, an ADI `AD797` (B grade), to close the feedback loop around R_s.

To understand the current sink, it is easiest to assume, for now, $V_{offset} = 0\,\mathrm{V}$ and the non-inverting input of U_2, an ADI `ADA4625-1`, is grounded. Applying a setpoint voltage V_{set} to U_1 will cause the upper current source to source a current into the virtual ground and the laser diode. This will cause the virtual ground potential to rise and the op-amp U_2 will see a positive

voltage at its inverting input. U_2 will then pull its output low, pulling the gate of the p-channel MOSFET Q_2 low as well, causing the current sink to drain the appropriate amount of current. U_2 will always steer Q_2 in such a way that the virtual ground is maintained. Do note, that using a p-channel MOSFET for Q_2 will put an extra burden on the op-amp U_2, because it has to follow the load voltage with its output. Fortunately, remembering the Shockley equation 3.2 it is clear that the voltage of a diode changes little with the current and this issue can therefore be neglected. On the other hand, using a p-channel MOSFET does not require the op-amp output to go down all the way to the negative diode supply to turn off the MOSFET. The p-channel MOSFET turns off at $V_{offset} - V_{th}$, which is close to $0\,\mathrm{V}$. This arrangement is similar to the concept of a transimpedance amplifier, except that instead of a resistive element in the feedback path, a (laser) diode is used. Putting the laser diode into a feedback loop has a number of advantages, which are discussed below.

The most important one is that the current source does no longer see the load and only has to source the current into a virtual ground. The compliance voltage required from the upper current source is reduced to V_{offset}, because this is the voltage at the virtual ground. This also important for the modulation current source because its compliance voltage is limited as well as shown in equation A.42. The compliance voltage, which can be provided by the combined source is increased to more than $10\,\mathrm{V}$ with this design, more than adequate to meet the design specifications of $8\,\mathrm{V}$ given in specification 3.2. Using a higher voltage negative supply is also possible to further increase the compliance voltage. The compliance voltage is essentially independent of the upper current source.

The circuitry supplying the voltage for the current source is essentially a voltage source, so additional care must be taken to protect the laser diode. This is where the offset voltage comes into play. Choosing a positive offset is interesting because if the virtual ground is accidentally shorted to the system ground, the inverting input of U_2 will be pulled low and the output of U_2 will go high, closing the MOSFET Q_2, protecting the laser diode. If V_{offset} were negative, U_2 would open Q_2, likely destroying the laser diode. V_{offset} must therefore always be $\geq 0\,\mathrm{V}$. In this design $V_{offset} = 500\,\mathrm{mV}$ has proven successful, but in future, it may be reduced to around $100\,\mathrm{mV}$ for an increased headroom for the MOSFET Q_1 in higher current designs. The reduced load voltage seen by the current source is also important for the modulation current source discussed in section 3.8.9.

In addition to solving compliance voltage related problems, there is another benefit from this configuration. Since the current source does not see the load, but rather the constant virtual ground, the output impedance is considerably improved. In essence, any change of the virtual ground potential is suppressed by the gain of the op-amp U_2, which means the output impedance is multiplied by the open-loop gain of U_2. Typically, a gain of 10^7 at low frequencies can be expected from the `ADA4625-1` [13]. The output impedance at this level is no longer limited by the current source, but rather other circuit parasitics. This helps the rather poor output impedance of the Howland current source to meet the requirements stated in specification 3.2.

There is one downside of this solution though. The laser diode is wrapped in a feedback loop that needs to close around the diode. This means, that the physical size of the loop is (regarding op-amps) enormous, because the laser head is not located on the PCB, but rather separated by several meters of cable, located on an optical table next to the rack. This introduces a considerable phase shift into the control loop at high frequencies. The details of the cabling are discussed in more detail in section 4.1.8. For now only the propagation speed of light is of interest. The DVI cables used have a velocity factor of 0.8 and a typical $3\,\mathrm{m}$ cable will therefore cause a delay of about $\tau = 12.5\,\mathrm{ns}$. The signal has to go through the cable twice, so at $1\,\mathrm{MHz}$,

this will introduce a phase delay of

$$\theta = 2\pi \cdot 2\tau \cdot 1\,\text{MHz} \approx \frac{\pi}{20} = 9^\circ\,.$$

While at $1\,\text{MHz}$, this is not yet critical. The phase delay of $\frac{\pi}{2}$ introduced at $10\,\text{MHz}$ will send the control loop into oscillations. The bandwidth of U_2 is therefore limited to $1\,\text{MHz}$, which works well with cables of up to $3\,\text{m}$. Longer cables are not compatible with this device and should not be used. More details about the circuit surrounding U_2 can be found in the schematics [43].

The last issue that needs to be discussed is the power dissipation in the sense resistor. This is less problematic for low currents, but at currents of several hundred mA it becomes more and more of a problem. The power lost in the resistors scales linearly with the maximum output current as the maximum setpoint voltage of $7.5\,\text{V}$ is fixed. At a full scale output of $500\,\text{mA}$, for example, the sense resistor is required to dissipate $3.75\,\text{W}$. The resistors used are rated for $8\,\text{W}$ when mounted on a heat sink, but only at $25\,^\circ\text{C}$ ambient, which is illusory when mounted inside a box without active cooling. The chassis to which the resistors are bolted will already be warmer than $25\,^\circ\text{C}$ inside a typical rack.

The $8\,\text{W}$ maximum is also detrimental to the long-term stability target. The datasheet of the sense resistor gives a maximum load life stability of $150\,\mu\Omega/\Omega$ for $2000\,\text{h}$ at $8\,\text{W}$ [237] when using a proper heat sink. A technical note from Vishay [219] gives some hints regarding the long-term drift of the older C-Foil resistors. Assuming the Z-foil `VPR221Z` resistors behave in a similar way, the load life drift for $30\,\text{d}$ ($720\,\text{h}$) can be estimated as

$$\frac{\Delta R}{R}(30\,\text{d}, 3\sigma) = 150\,\mu\Omega/\Omega \cdot \sqrt[3]{\frac{720}{2009}} = 107\,\mu\Omega/\Omega\,.$$

Using the power derating curve in the datasheet [237] to estimate a thermal resistance of $14\,\text{K/W}$ from the metal foil to ambient gives a temperature of $112\,\text{K}$ above ambient for an $8\,\text{W}$ load. Consulting [219], such a temperature causes in increase in the drift by a factor of 15 when compared to room temperature. Reducing the load to $2\,\text{W}$ will decrease the internal temperature of the metal foil considerably to $28\,\text{K}$ above ambient and therefore reduces the drift to less than a factor of 4 when compared to room temperature. The drift estimated above would then reduce to about $29\,\mu\Omega/\Omega$, far less than the required $240\,\mu\Omega/\Omega$ as given by specification 3.1, leaving a safe headroom for higher ambient temperatures.

In order to reduce the power lost in the resistor to the desired $2\,\text{W}$, R_s can be split into multiple resistors to distribute the current. While this idea is neither novel nor interesting, it does become so, when looking at it in a different context. Splitting the sense resistor only becomes necessary at currents above a few hundred mA. At these currents the sense resistor is of a fairly low value, typically $<50\,\Omega$, and the current noise of the current source is no longer dominated by the sense resistor. As a reminder, the voltage noise of the `AD797` op-amp is $0.9\,\text{nV}/\sqrt{\text{Hz}}$. This is the equivalent to a $50\,\Omega$ resistor at room temperature. With $R_s < 50\,\Omega$, the op-amp becomes the dominant noise source of the current source. The voltage noise of the op-amp, in contrast to the thermal noise of the resistor, does see an improvement when averaged. Using n op-amps improves the high frequency noise by a factor of $\sqrt{n}$. This assumes, that the wideband noise is uncorrelated, which should be the case, as any power supply noise is effectively filtered out and the noise is only produced inside the op-amp. At low frequencies, the reference noise still dominates the noise and using a single reference and setpoint DAC, which is fed into both current sources, the noise is correlated and therefore adds normally, so it does not see any improvement using this technique.

The simulation found at source/current_regulator_AD797_noise.asc can be used to estimate the potential improvement. The simulation gives a more complete picture, because it includes the noise created by the resistors and the feedback network around U_1. Table 4.7 gives the simulated output noise for two solutions of a $500\,\mathrm{mA}$ laser driver, one with a single current source and the other with two current sources. The sense resistors in this case are smaller than the $50\,\Omega$ discussed above. The single source uses a $15\,\Omega$ resistor, while the dual current source solution employs two $30\,\Omega$ resistors.

	LF Noise $10^{-2}\,\mathrm{Hz}$ to $10^{2}\,\mathrm{Hz}$	HF noise, $10^{2}\,\mathrm{Hz}$ to $10^{5}\,\mathrm{Hz}$
Single	$27.2\,\mathrm{nA_{rms}}$	$21.7\,\mathrm{nA_{rms}}$
Dual	$27.2\,\mathrm{nA_{rms}}$	$17.0\,\mathrm{nA_{rms}}$

Table 4.7.: Noise comparison of a single current source with $R_s = 15\,\Omega$ and dual current source with $2 \times 30\,\Omega$, both at $500\,\mathrm{mA}$.

From the simulation it can be easily gathered that the high frequency noise of a dual current source design is about $\frac{1}{\sqrt{2}}$ that of a single source design, just as predicted above. The low frequency noise is also not affected, as discussed above. In order to improve the frequency noise, a lower noise reference like the `ADR1399` must be used. Judging from the datasheet of the `LM399` and `ADR1399` [15, 133] and preliminary tests, the `ADR1399` has $30\,\%$ less noise. While the dual current source design is already very close to the desired $30\,\mathrm{nA_{rms}}$ in $100\,\mathrm{kHz}$ bandwidth, it is still slightly above the desired target with a total noise of $31.9\,\mathrm{nA_{rms}}$. A low noise reference is therefore key and given the loose datasheet specifications of those references, selecting them for low noise is important. This is discussed in section 4.1.13.

Using a second current source also helps with reducing the statistical spread of both the drift and the temperature coefficient of the sense resistor and the `AD797` op-amp U_1. While the datasheet of the sense resistor gives a *typical* value of $\pm 0.05\,\mu\Omega/(\Omega\,\mathrm{K})$, the 3σ range is more like $\pm 2\,\mu\Omega/(\Omega\,\mathrm{K})$ [252]. Using two current sources results an inherent statistical averaging regarding the temperature coefficient, making the $1\,\mu\mathrm{A}/(\mathrm{A\,K})$ target of specification 3.1 easier to reach.

Configuration	Sense resistor value	Maximum current
`DgDrive-150`	$50\,\Omega$	$150\,\mathrm{mA}$
`DgDrive-250`	$30\,\Omega$	$250\,\mathrm{mA}$
`DgDrive-300-LN`	$2 \times 50\,\Omega$	$300\,\mathrm{mA}$
`DgDrive-500-LN`	$2 \times 30\,\Omega$	$500\,\mathrm{mA}$

Table 4.8.: Different configurations of the digital current driver current tested and built.

Combining more than two current sources unfortunately yields diminishing returns as the noise scales as $\frac{1}{\sqrt{n}}$, whereas cost and complexity goes with n. Therefore a maximum of two current sources are used in this design. Table 4.8 lists the current source configurations that were built for this project. The `DgDrive-300-LN`, which is using a $50\,\Omega$ resistor is at the limit of where adding a second current source has any benefits regarding the wideband noise. The difference in wideband noise is about $15\,\%$ ($13.8\,\mathrm{nA_{rms}}$ versus $11.6\,\mathrm{nA_{rms}}$) when comparing the simulation against a $25\,\Omega$ configuration. Only two of these units were built to test the extra stability added by the statistical averaging scheme.

A final note regarding the second current source and the Kelvin sensing mentioned above. As discussed above and shown in figure 4.19 one side of the sense resistor feeds the voltage reference to create the setpoint, the other goes to the AD797 to create the current. This is different for the second resistor. The upper sense pin is not used in this case. One could, in theory, connect the sense pins of both resistors via another resistor to the op-amp and average the voltage, but the voltage difference between both pins is small because a copper pour on the PCB connects both resistors and the chance to introduce thermocouples is large.

Noise measurements of the digital current driver in comparison to other current drivers and the simulation results shown above are presented in section 4.1.10.

To summarize the results, a novel current source configuration was presented that addresses the limited compliance voltage by removing the load seen by the current source. The compliance voltage in this design is more than $10\,\mathrm{V}$, limited by the power supply rails of $\pm 15\,\mathrm{V}$. In addition, a solution was given to limit the increasing current noise contribution of the op-amp in high output current configurations that use small sense resistors. These results were underpinned by simulations and a simulation model was provided to estimate the expected improvements.

Device Properties 4.1: DgDrive current source

- Compliance voltage: $10\,\mathrm{V}$
- Long-term drift over $30\,\mathrm{d}$: $<100\,\mu\Omega/\Omega$
- Current noise ($1\,\mathrm{Hz}$ to $100\,\mathrm{kHz}$), `DgDrive-250`: $19\,\mathrm{nA_{rms}}$
- Current noise ($1\,\mathrm{Hz}$ to $100\,\mathrm{kHz}$), `DgDrive-500-LN`: $19\,\mathrm{nA_{rms}}$

4.1.7. Modulation Current Source

Several options for the modulation current source are presented in literature. Some designs use a simple AC coupled input [128, 242], which drastically reduces the high-frequency output impedance of the current source. Others use a JFET in parallel to the laser diode to divert some of the current [24, 225, 249], which causes poor DC performance due to the missing feedback loop. Libbrecht et al. [77, 128] in addition to the AC coupled input also presented a more rugged approach similar to a Howland current source, which delivers a reasonable DC performance and a claimed bandwidth of more than $10\,\mathrm{MHz}$. The modulation circuit shown by Libbrecht et al. is likely an update of an earlier version of the same laser driver printed in the paper of Wieman et al. [242], which would explain the rather peculiar arrangement. This circuit is shown in figure 4.20 and will be discussed in more detail, because it also used in the legacy laser drivers found in the APQ group.

Looking at figure 4.20, the current source can be identified as the classic HCS. The Howland current source does require a very low impedance input V_{in}, because otherwise the tight matching of the four resistors $R_1 = R_2 = R_3 = R_4$ is imbalanced. This brings about a problem with an external input, having to either short the input to ground or keep it connected to a low impedance source at all times. If the input were kept open, one side of the Howland current source would be imbalanced, thus creating an offset current. Libbrecht et al. [128] addressed this problem by using an inverting amplifier U_2 to invert the output of U_1. Since the output current of U_1 is equally divided between one trace going to the inverting input of U_1 via R_4 and R_3 and the other trace with R_1 and R_2, the current that U_2 injects into the input trace must be divided by half, hence $R_5 = 2 \cdot R_x$. R_x being the value used by the Howland current

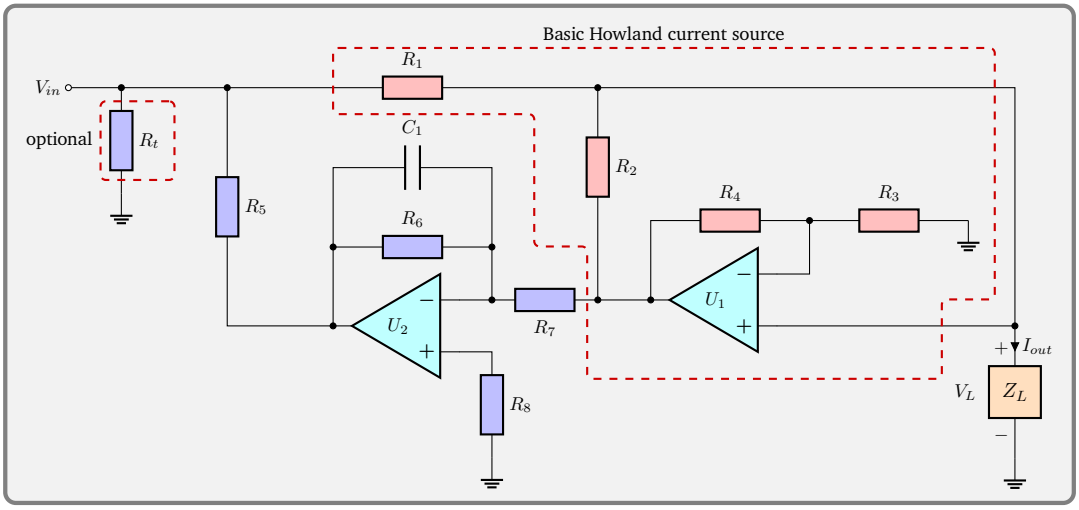

Figure 4.20.: The modulation current source used by [77, 128]. $R_1 = R_2 = R_3 = R_4 = 1\,\text{k}\Omega$ are matched resistors. $\frac{R_5}{2} = R_6 = R_7 = R_8 = 1\,\text{k}\Omega$. $C_1 = 1\,\mu\text{F}$ $R_t = 54\,\Omega$ is optional.

source. The resistor R_8 does not serve any immediate purpose. The design by Libbrecht et al. uses the `OP07` [167] precision op-amp for both U_1 and U_2. This op-amp does have an internal bias current compensation scheme[2] therefore its input bias current is very low and on the order of a few nA. This makes one wonder about the purpose of the resistor R_8, which is not only the wrong value for a compensation resistor, as it should be $R_8 = R_6||R_7 = 500\,\Omega$, but also pretty much unneeded. That could be a relic from an earlier design stage with different op-amps. The matching of the resistors $\frac{R_5}{2} = R_6 = R_7 = R_x$ fortunately does not need to be as tight as the ones of the HCS as discussed in section 3.8.9, because U_2 forms an inverting amplifier with gain $A_2 = \frac{R_6}{R_7} \approx -1$ and feeds back a current of $\frac{A_2 \cdot V_{o,U1}}{R_5}$ into the input node. The error current is then distributed between the input source and the HCS, so only the fraction $R_1||R_{in}$ of the error current flows into R_1 and the HCS. For example, assuming a modulation source has an output impedance of $50\,\Omega$, the error current flowing into R_1 is attenuated by a factor of $\frac{1}{47}$, relaxing the requirements of the matched resistor network by the same factor.

An issue that can be identified with the above circuit is the capacitor C_1. It forms a low-pass filter with the cutoff frequency

$$f_c = \frac{1}{2\pi R_6 C_1} \approx 159\,\text{Hz}$$

for $R_6 = 1\,\text{k}\Omega$ and $C_1 = 1\,\mu\text{F}$ as given in [77, 128]. This has two detrimental effects as it offsets the careful balance created by the feedback of U_2. First, it will dramatically decrease the output impedance of the current source. It was already shown in appendix A.7, that the Howland current source is very sensitive to an imbalance of the resistor ratios and if the feedback of U_2 is reduced, the output impedance of the source starts playing a role. This effect can be seen in figure 4.21, which shows an LTSpice simulation of the circuit shown in figure 4.20 with a $50\,\Omega$ source at the modulation input. The fast modulation input found in [128] was omitted in the

[2]This detail can either be read from the simplified schematic as there is a current source feeding into both inputs or from the input offset current and input bias current specification. The offset current is about the same as the bias current and does not have a defined polarity indicating the possibility of over- and undercompensation.

simulation, but it would introduce an additional limit of $10\,\mathrm{k\Omega}$ above $1.59\,\mathrm{kHz}$ to ($CR = 10\,\mathrm{nF} \cdot 10\,\mathrm{k\Omega}$). The simulation file can be found at source/spice/modulation_input_LibrechtHall.asc.

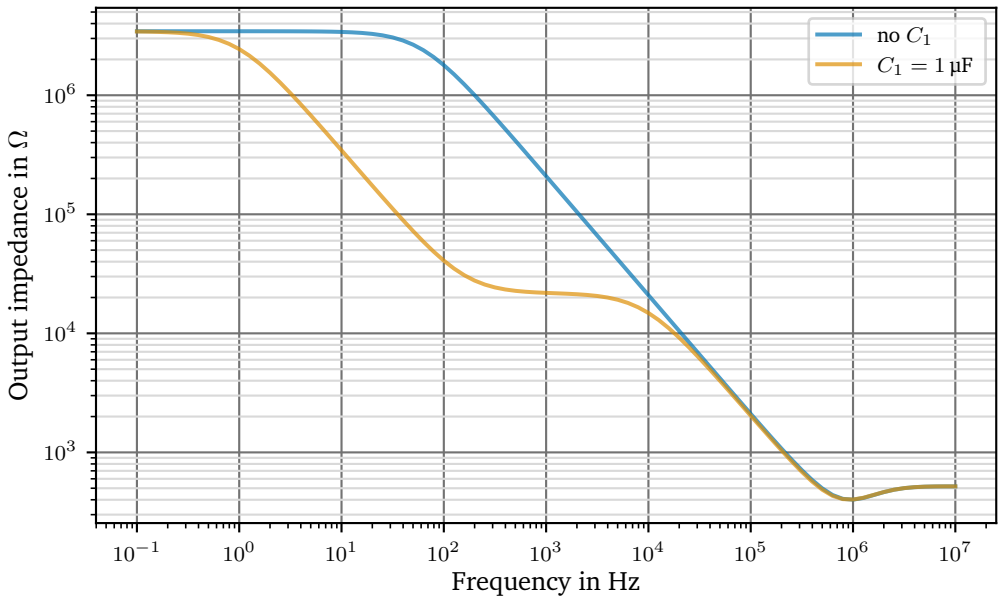

Figure 4.21.: The output impedance of the HCS from figure 4.20 with $0.01\,\%$ worst-case resistor matching and a $50\,\Omega$ source. The simulation was repeated with and without the capacitor C_1.

Figure 4.21 gives the output impedance for two configurations. With and without the capacitor C_1. The output impedance at low frequencies is around $3.5\,\mathrm{M\Omega}$ for both configurations, which is the limit found due to the op-amp gain and the resistor array mismatch. This changes rapidly when inserting the capacitor. The output impedance drops to around $20\,\mathrm{k\Omega}$ at $1\,\mathrm{kHz}$, created by the $50\,\Omega$ mismatch added to R_1. At even higher frequencies, the results converge again, because the op-amp gain is the more limiting factor.

The second effect of the capacitor C_1 is more subtle, but poses a serious problem for a high bandwidth servo. This has to do with the input impedance presented by the circuit. By inspection of figure 4.20, one finds the input impedance to be $R_6||R_1 \approx 667\,\Omega$. The required termination resistor R_t would be $54\,\Omega$, or two $27\,\Omega$ resistors in series, which can be bought off-the-shelf. Unfortunately as soon as the current source balance is disturbed by the gain of the circuit surrounding U_2 rolling off, its input impedance changes. This makes proper input matching impossible and causes unpredictable high frequency behaviour depending on the load. This was also mentioned by [77] and investigated closer by Preuschoff [176] and therefore not covered here. Preuschoff showed that this type modulation current source shows a highly load dependent behaviour above $1\,\mathrm{MHz}$.

This work proposes a different approach to the problem. Instead of using the more complicated approach above, a simple buffer as part of a dual op-amp (Texas Instruments `OPA2140` [168]) is used. Earlier PCB revisions used an ADI `AD8672` [10], which was replaced because the `OPA2140` has similar specifications, but a lower bias current and a rail-to-rail output. A buffer allows proper termination and has no bandwidth dependent issues. The design focuses on a maximally flat response up to $1\,\mathrm{MHz}$ and a well defined roll-off afterwards because the integrated modulation current source is typically used to steer the laser or lock it to an atomic

transition. The former requires a well defined amplitude transfer function while the latter depends on a fast response with litte phase lag. The full circuit is shown in figure 4.22.

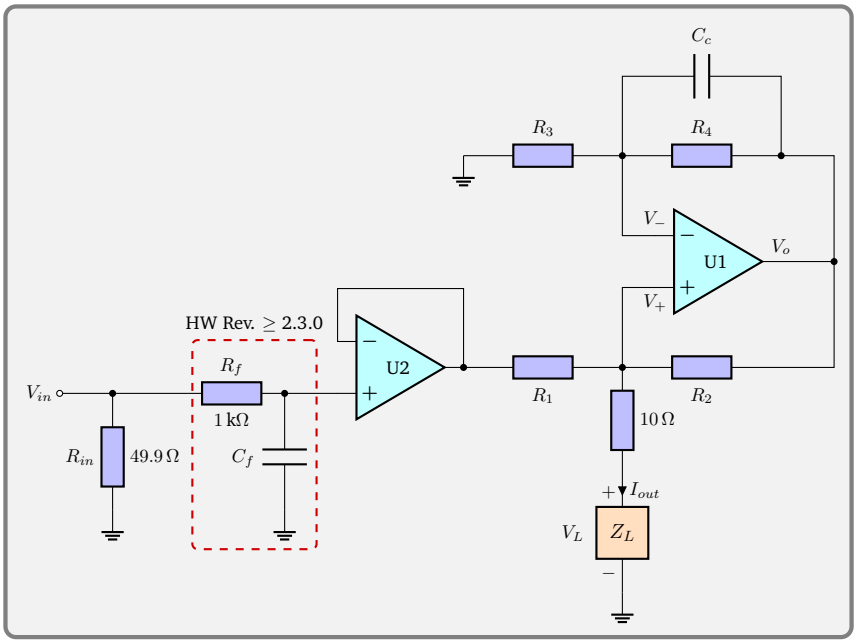

Figure 4.22.: The modulation current source used by digital laser driver DgDrive. $R_1 = R_2 = R_3 = R_4 = 1\,\text{k}\Omega$ and $C_c = 10\,\text{pF}$. The op-amp is a Texas Instruments `OPA2140`.

The idea behind this design is simple. A current source is, by definition, a high impedance source. It cannot be matched to the typical $50\,\Omega$ transmission line. Reflections, cable, and load dependent behaviour are an inevitable consequence. By deliberately limiting the bandwidth to around $1\,\text{MHz}$ these problems can be avoided. If a faster solution is desired it is best to move the current source directly into the laser head like it was done in [177].

As discussed in section 3.8.9, the four resistors R_1, R_2, R_3 and R_4 need to be closely matched. This is achieved using a Vishay `MORNTA1001AT5` [165] array. The ratio matching is $0.05\,\%$ and according to table 3.12 on page 94 one can expect a mediocre worst case output impedance of $500\,\text{k}\Omega$, which is in parallel with the precision current source that generates the bulk current. As discussed in section 3.8.4 this current source has an output impedance of several $\text{G}\Omega$ and easily surpasses the requirement of $7.5\,\text{M}\Omega$ listed in table 3.2 on page 20. The modulation current source on the other hand fails to meet that target.

Normally this would be disastrous and either a better resistor array or trimming would be required to restore the output impedance, but in this implementation it is less of a problem because as shown in the last section 4.1.6, the modulation output is sinked into a virtual ground node created by a current sink. The final output impedance is therefore multiplied by the gain of the `ADA4625-1`, which has plenty of bandwidth and open-loop gain with a unity-gain-bandwidth of $45\,\text{MHz}$ and a gain of 10^7. The output impedance of the combined current source is therefore independent from the performance of the modulation current source and limited only by the physical properties of the cable as discussed in section 4.1.9. This brings up the next subject to be discussed, the bandwidth of the current source.

The bandwidth of the modulation source is limited by the op-amp bandwidth and circuit parasitics. Erickson et al. [77] used a $50\,\Omega$ dummy load (and likely a very short cable) to test their modulation current source. This gives a better performance due to the impedance

matching of the cable and the load. To give a more realistic picture of the performance, a real laser was used in this work and the modulation was recorded using a photodiode.

Figure 4.23 shows a frequency sweep of the modulation input of the DgDrive using a Keysight DSOX1102G oscilloscope, which has a signal generator output to create simple Bode plots. The DgDrive current source was driving an in-house ECDL with a Thorlabs LD785-H1 laser diode via a 2 m cable. The laser diode was impedance matched using a matching network in the laser head as presented in [177]. The laser output amplitude was recorded using a Hamamatsu S9055-01 [188] photodiode with a transimpedance amplifier as discussed in [176] and a $1\,V_{rms} \equiv 1\,mA_{rms}$ modulation was applied. The laser power is proportional to the current modulation [242] and can therefore be used to test the modulation capability of the driver. The amplitude shown in the graph was normalised to the average of the flat part below 100 kHz to calibrate out the transimpedance amplifier gain of the photodiode. The op-amp used by the DgDrive modulation current source was an ADI AD8672 and not the OPA2140 discussed above because a hardware revision 2.2.1 laser driver was used.

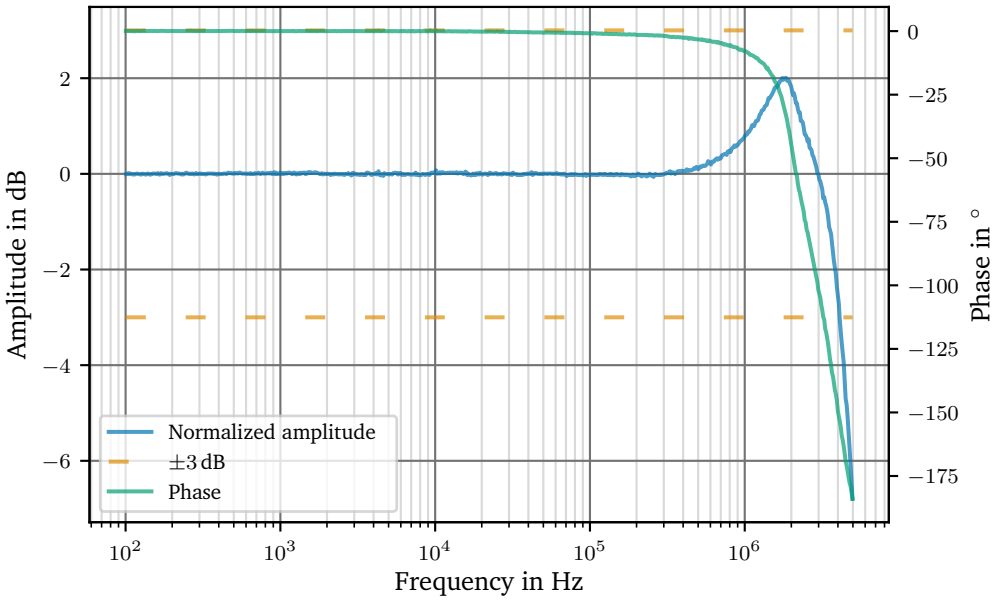

Figure 4.23.: Modulated output current over frequency, measured using a Thorlabs LD785-H1 laser diode as the load. Source: [176].

The frequency response of the modulation shown in figure 4.23 demonstrates the excellent capability of the integrated modulation current source for the purpose of frequency stabilisation or frequency steering. It has a very flat and predictable amplitude and phase response up to 1 MHz. A slight gain peaking of 2 dB (26 %) is seen at 1.8 MHz, due to the op-amp input capacitance and other parasitic capacitance of the PCB. At 1 MHz the gain peaking is 0.78 dB (9 %) with a phase shift of $-8°$. The 3 dB bandwidth is 4 MHz. Due to the gain peaking, the phase shift is $-150°$ – unsuitable for a control loop, but it may still be used for modulation purposes. These values provide excellent behaviour in a control loop up to 1 MHz as desired in specification 3.2. Future revisions > 2.3.0 include an additional input resistor R_f, which serves two purposes, first it makes the design more robust against electrostatic discharge (ESD) and second, it can be configured as a low pass filter using C_f. This can help mitigate gain peaking if a faster op-amp is used. The optional capacitor C_c was added in case a faster op-amp needs

some compensation to prevent oscillations. It is normally unpopulated but makes the design more flexible.

To summarize the modulation current source properties, the following list is given.

Device Properties 4.2: DgDrive modulation input

- Transconductance $1\,\mathrm{mA/V}$
- $3\,\mathrm{dB}$-bandwidth $4\,\mathrm{MHz}$
- Recommended maximum control loop bandwidth $1\,\mathrm{MHz}$ with $8°$ phase shift

4.1.8. Cables and Connectors

This section covers the cables used for the digital current driver. These include the external connection to the laser head and the internal connection of the analog board with the front end user interface board.

Several cabling options for connecting the current driver with the laser head were investigated while testing different current drivers. Both twisted pair cables and coaxial solutions are employed in the field by different solutions. Vescent, for example, uses an SMA connector and a coaxial cable. This solution is a universal approach as an abundance of SMA cables can be found in any lab. On the other hand, the typical RG-316 cable used with SMA connectors is geared towards high frequency applications. This is reflected in the rather poor capacitance of around $100\,\mathrm{pF/m}$, which can be improved to $75\,\mathrm{pF/m}$ by using larger RG-58X cables with a polyethylene (PE) foam dielectric [3]. A coaxial cable works well, if only a single conductor is required.

During the design of the new digital laser driver it was clear, that the number of conductors would increase. The past has shown that additional features like protection circuitry and a fast current modulation input should be moved into the laser head. The laser head design was presented in [177] and shall not be discussed here, but this design requires a dual voltage supply and a signal line to actuate the protection relay. On top of that, the voltage of the laser diode is remote sensed, directly at the laser diode, adding another pair of conductors.

In addition to the need for more conductors, experience has shown, that self-made cables are a common source of problems in the lab. The legacy laser driver design, employed in this group, used a LEMO `ERA.0S.303.CLL` socket at the laser and the driver. For these sockets, cables were typically self-made using a LEMO `FFA.0S.303.CLAC44` plug on both ends. While the quality of the connectors is excellent, their assembly requires skilled hands, which resulted in fluctuating quality. Switching to professionally made cables considerably improved the situation in the past. Using custom specialty cables has the disadvantage of limited availability, high cost and likely longer lead times, so an off-the-shelf solution was preferred.

The laser head connector must be mechanically secure, be able to handle a current of $500\,\mathrm{mA}$ or more and ideally be widely available. Moglabs and Troxel et al. [227] both propose a Digital Visual Interface (DVI) connector and the same approach was also adopted in this work. The DVI cable, which nowadays is a DVI-D cable, only contains twisted pairs. There are also DVI-I cables, which carry legacy analog signals through coaxial conductors, but these are obsolete. This brings up the question of the difference between a twisted pair cable and a coaxial cable, which needs to be addressed.

The most mundane difference is that twisted pairs are cheaper to manufacture than coaxial cables and they require less space, allowing more conductors in a cable. On the other hand, at high frequencies, the impedance of a coaxial cable is more uniform than that of the twisted pair. Fortunately, the latter property has greatly improved in recent years and, for example, the DVI cable is rated for clock rates of $165\,\text{MHz}$, far more than is needed for this application. While the price difference and space savings are interesting for large installations, it is less critical for this application, where signal integrity is premium.

Regarding noise immunity, there is a profound difference between the two types of cables and electric and magnetic field coupling must be distinguished. A coaxial cable grounded at one end with a floating load offers fairly good protection against low frequency electric and magnetic field coupling, while at frequencies above about $100\,\text{kHz}$, the shield forms an antenna. For the floating shield to work, the laser head construction must ensure that it does not have a ground connection because as soon as both ends are grounded, a ground loop is formed. At low frequencies, magnetically induced noise current can then flow in the shield which also serves as the return conductor. This introduces a noise voltage via the shield resistance, which must be minimized with a thick braid to reduce the resistance. On the other hand, high frequency noise above around $100\,\text{kHz}$ is kept out and the skin effect helps to confine the current loop closer to the inner conductor, thereby reducing magnetic pickup. With a coaxial cable one must choose between good low frequency protection or high frequency noise attenuation.

Looking at the twisted pair cable, it has very good magnetic shielding due to the twisted wires as long as there are enough turns per unit length [58, 169]. The mutual capacitance between the two conductors of a twisted pair is also lower, although the conductors are closer together, but the different geometry helps. In case of a shielded twisted pair there is also the capacitance between the shield and the two conductors in addition to the mutual capacitance. Through this capacitance, electric field interference can still couple into the cable. In order to reduce the susceptibility, it is important to keep the cable capacitance as low as possible, which can be achieved using an insulating material with a low relative permittivity ϵ_r for the twisted pairs. To meet their high frequency specification, DVI cables typically use a low ϵ_r dielectric, namely air injected PE foam. Another option would be expanded PTFE (ePTFE), which is a microporous structure that contains air and is held together by strands of PTFE. Finally, having a dedicated shield allows to use a hybrid grounding scheme by only capacitively coupling the shield at one end. This breaks the ground loop yet keeps the shield effectively grounded at high frequency. A good overview of different grounding schemes can be found in [169, p. 72]. In order to find a suitable cable several options were explored.

The cables tested for the laser driver are a DVIGear `SHR` [205], a SUPRA Cables `DVI-DVI Single-Link` [218], an unbranded DVI cable for comparison and a Gore `RCN9034-24` Category 6a Ethernet cable [89]. The former three cables have a PE foam dielectric and 17 conductors while the latter is an ePTFE cable with 8 conductors. The DVIGear `SHR` cable does have the largest conductors with $0.33\,\text{mm}^2$ (AWG22) followed by the SUPRA cable with $0.26\,\text{mm}^2$ (AWG23), then the Gore `RCN9034-24` with a conductor diameter of $0.20\,\text{mm}^2$ (AWG24) and finally the unbranded cable with just $0.05\,\text{mm}^2$ (AWG30).

The twisted pairs of all DVI cables are triple shielded, using a foil around the pairs, then another foil around all conductors and finally a braid over the outer foil. The Gore Category 6a cable has a foil shield around the 4 pairs and a braid around all conductors. The braid helps with low frequency shielding and the more coverage it has, the better. Since the braid can never fully shield a cable, the foil is added to help with high frequency shielding. Figure 4.24 shows the shielding of several cables tested. The Supra Cables `DVI-DVI Single-Link` is not shown, because the braid coverage is similar to the DVIGear cable and a photo can also be

found in the datasheet [218].

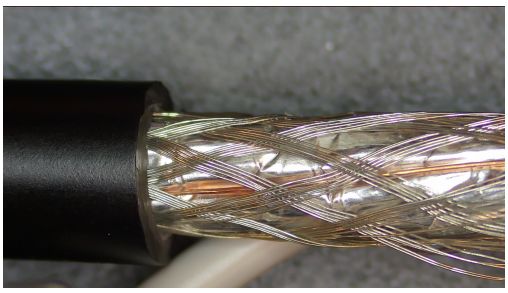

(a) Unbranded DVI cable. 60 % braid coverage.

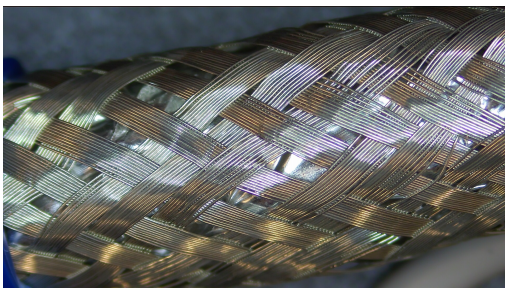

(b) DVIGear SHR. 80 % braid coverage.

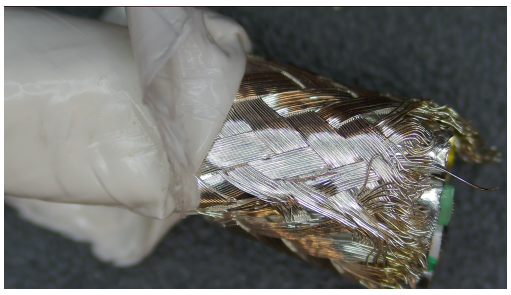

(c) Gore RCN9034-24. 95 % braid coverage.

Figure 4.24.: Braid coverage of several DVI cables and a Category 6a cable.

The braid of the unbranded cable has the least coverage with about 60 % calculated according to ANSI/SCTE 51 2018 [158]. In addition, the braid is made of aluminium instead of copper. This increases the impedance and typically reduces the effectiveness by about 20 dB [245]. The other cables have an 80 % and a 95 % copper braid coverage. The braid and foil shield combination is fairly effective up to several dozen MHz [169, p. 84] covering the most important frequency range for this device if a decent copper braid is used.

As it was mentioned above, using a shielded cable adds more capacitance to the cable. A factor that needs to be considered when shielding a current source as it reduces the output impedance. It is therefore important to have a more detailed look at the cable capacitance in this application. Neglecting the parasitic capacitances to earth ground, the two capacitances most interesting are the mutual capacitance between the conductors C_m and the capacitance between each conductor and the shield C_{ws}, for details see [116]. The cable capacitances of all cables were measured using an LCR Research `LCR Pro 1 Plus` and the results are given in table 4.9. To measure the capacitance between the conductor and the shield, one of the twisted pairs was shorted to the shield using a DVI connector with a solder joint connecting both the shield and the conductor. The Category 6a cable was soldered together without a connector. The capacitance was then measured between the shorted pins and the remaining conductor. The measured total capacitance C_{tot} is the paralleled capacitance between the shield and the conductor C_{ws} and the mutual capacitance C_m. C_{ws} can then be calculated as

$$C_{ws} = C_{tot} - C_m \,.$$

All DVI cables tested fared well regarding the capacitance and gave a similar performance of the mutual capacitance when compared to the ePTFE Category 6a Gore `RCN9034`. Given the

DVIGear SHR	C_m	C_{ws}	Conductor Size
DVIGear SHR	$(49 \pm 1)\,\mathrm{pF/m}$	$(46.0 \pm 1.5)\,\mathrm{pF/m}$	$0.33\,\mathrm{mm}^2$
SUPRA DVI Single-Link	$(42 \pm 1)\,\mathrm{pF/m}$	$(36.0 \pm 1.5)\,\mathrm{pF/m}$	$0.26\,\mathrm{mm}^2$
Gore RCN9034	$(43 \pm 1)\,\mathrm{pF/m}$	$(95.0 \pm 1.5)\,\mathrm{pF/m}$	$0.20\,\mathrm{mm}^2$
Unbranded DVI dual link	$(42 \pm 1)\,\mathrm{pF/m}$	$(41.0 \pm 1.5)\,\mathrm{pF/m}$	$0.05\,\mathrm{mm}^2$

Table 4.9.: Measured cable capacitance for two DVI cables using a PE foam dielectric and an ePTFE Category 6a cable. All values were measured at $10\,\mathrm{kHz}$.

measurement uncertainties of the LCR Pro 1 Plus no distinction can be made. Due to the smaller outer diameter of the Gore cable the shield capacitance unfortunately doubles.

To give a figure for the capacitance seen by the current source, it must be determined, whether the circuit is balanced or unbalanced. Remembering section 4.1.6 and especially figure 4.19 on page 123 where the current source schematic was shown, it is clear, that the circuit is not balanced. The virtual ground has very little impedance, while the other conductor presents a high impedance current source via the MOSFET of the current sink. The virtual ground is the most sensitive node. Any noise current injected into it cannot be distinguished from the drive current. Noise current is injected via capacitive coupling, so the capacitance seen by the virtual ground node is the most important. This is analogous to transimpedance amplifier input node. This capacitance seen is C_{tot} measured above. Looking at the number it can be seen that a DVI cable is indeed a good choice for this use case as it has the least capacitance when compared to the Gore Cat6a cable or a typical coaxial cable, which has about $100\,\mathrm{pF/m}$.

The final decision was made in favor of the SUPRA DVI Single-Link cable, because of its decent shielding and very low capacitance, while being readily available in contrast to the DVIGear cables, some of which have already been given the end-of-life status. A word of caution regarding the unbranded DVI cable needs be said. In addition to the meager shielding, the $0.05\,\mathrm{mm}^2$ wire is not recommended for carrying $500\,\mathrm{mA}$ because it has a resistance of about $330\,\mathrm{m\Omega/m}$, Using a cable of $3\,\mathrm{m}$ length would already drop $1\,\mathrm{V}$ (or $500\,\mathrm{mV}$ when using a dual link cable) at $500\,\mathrm{mA}$. The $0.26\,\mathrm{mm}^2$ cable chosen, for comparison, only drops $82\,\mathrm{mV}$ using a single link.

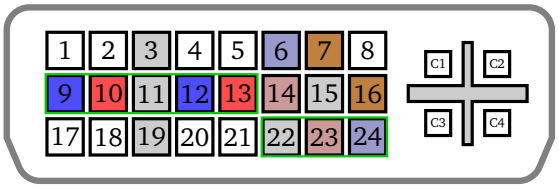

Figure 4.25.: Pin layout of the DgDrive DVI connector. Ground is gray, positive voltages red, negative voltages blue, digital i/o pins brown. White pins are not connected.

With the cable chosen, the connector layout needs to be discussed. DVI-D cables come in two flavours, single link and dual link cables. Dual link cables have twice the number of data lines. These data lines are called TMDS data lines. Those pairs and the clock line are shielded twisted pairs, each pair wrapped in an aluminium foil. Depending on the type of cable, it has 17 or 23 pins with either 3 or 6 TMDS lines. Each shield is brought out with a separate pin except for the additional TMDS lines in the dual link configuration. The shields of

the additional neighbouring TMDS lines is connected together so only 4 pins are required to connect the shields of the TMDS and clock line twisted pairs as shown in figure 4.25. Apart from the shielded twisted pairs, there are 5 conductors available for additional functions. Theses conductors are neither shielded nor twisted. The connector layout of the DVI port of the digital current driver is shown in figure 4.25. A number of twisted pairs are left unconnected (NC) for future applications and some cannot be used because they are part of the legacy analog function of the DVI connector. Pin 8 and pins C1 to C5 are can only be used with a DVI-I digital and analog cable. As mentioned above, these cables have became rare as analog displays are mostly extinct.

Pin	Function	Pin	Function
1–2	NC	14	$+12\,\mathrm{V}$
3	Shield, GND	15	GND
4–5	NC	16	Open-collector, enable laser
6	$-12\,\mathrm{V}$	17–18	NC
7	EEPROM	19	Shield, GND
8	NC	20–21	NC
9	LD cathode	22	Shield, GND
10	LD anode	23	LD voltage sense positive
11	Shield, GND	24	LD voltage sense negative
12	LD cathode	C5	GND
13	LD anode		

Table 4.10.: DVI connector pin layout. See figure 4.25 for the pin labels.

Pin 9 and 10 are used to deliver the laser diode drive current, while the shielded clock line on pins 23 and 24 are used to sense the diode voltage. When a dual link cable is used, pin 12 and 13 are also used to carry current. Using a single link cables reduces the capacitance in comparison to a dual link cable.

The other conductors are used to supply the laser head with a $\pm 12\,\mathrm{V}$ rail and to actuate the protection relay in the laser head. Additionally, there is an electrically erasable programmable read-only memory (EEPROM) chip inside the laser to identify it. This chip can be read using a one-wire protocol via pin 7 and contains information about the laser diode and maximum current settings, the date of assembly of the laser and more.

As discussed above, the shielding and grounding plays an important role to suppress noise. The digital current driver uses a floating DC power supply to supply the sub rack. The subrack is connected to chassis ground and so is the front panel of the current driver through the SMA connectors. The DVI cable shield is also connected to the front panel of the current driver and the system ground. This chassis forms the path of least impedance for any noise current present and diverts it around the PCB ground plane. On the laser side the shield is connected to the laser head, which is grounded as well to protect the laser from electrostatic discharge (ESD). The PCB inside the laser head is only connected to the return conductor, effectively staying inside the shield.

Finally the cable for connecting the display board with the analog board is presented. The analog board and the front panel are two separate boards as the current driver design is a modular concept. Both PCBs feature separate microcontrollers that communicate via a digital Inter-Integrated Circuit (I^2C) bus. The cable is shielded as well and is grounded on the analog

board as well as capacitively coupled via a 10 nF capacitor on the digital front panel board to keep the digital signals from interfering with the analog board. It is a 5 conductor cable as shown in figure 4.26. For example, a Belden 9535 cable can be used, but any other foil shielded cable can be used. The use of a foil is recommended because it is most effective for shielding against high frequency signals. The connectors are from the JST PHR series and currently the cable features an asymmetric layout. Initially the front panel board did not contain a separate microcontroller and the display required more control lines. It was found during development that a self-sufficient board is easier to maintain and also able to support more features like USB. The number of connectors was therefore reduced. The 7-pin header on the analog side will be replaced with a 6-pin header on both side with revision 2.4.0 of the analog board.

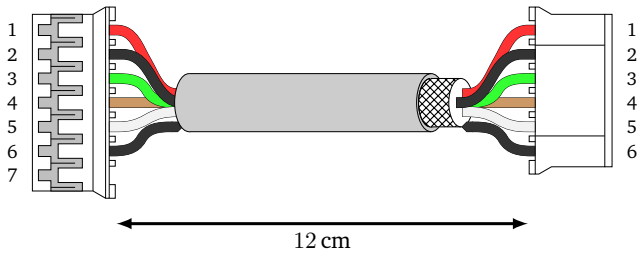

Figure 4.26.: Display cable used to internally connect the display board with the analog board. The 7-pin header is deprecated and will be replaced with a 6-pin header.

Pin	Function	Colour	Pin	Function	Colour
1	+3.3 V	Red	4	I²C SCL	Green
2	GND	Black	5	Interrupt	White
3	I²C SDA	Brown	6	Shield	–

Table 4.11.: Display cable pin layout. See figure 4.26 for the connector layout.

4.1.9. Test Results: Output Impedance

There are several ways of measuring the output impedance of a current source. Two such methods were used to test the output impedance of the current source and are shown in figure 4.27. Figure 4.27 (a) shows the simpler scheme. It can be used to determine the static output impedance at DC and its setup only requires three components, an ammeter or multimeter, a resistor, and a switch. The resistor value should be scaled such that $R_{shunt} \cdot I_{out}$ is just below the compliance voltage of the current source to maximize the resolution. To calculate the output impedance, the following steps are required. The current flowing through the shunt is measured using the ammeter and then the switch is closed to short out the resistor and the current is measured again. Assuming the resistance of the switch and the internal shunt of the ammeter is very small in comparison to R_{out} the current source is essentially shorted and it can be seen in figure 4.27 (a) that all current I_{out} is flowing through the switch and the ammeter when the switch is closed. When opened, the current is split between R_{shunt} and R_{out}. This allows calculating R_{out} as

$$R_{out} = \frac{R_{shunt} \cdot I_{shunt}}{I_{out} - I_{shunt}} = \frac{V_{shunt}}{\Delta I} \,. \tag{4.10}$$

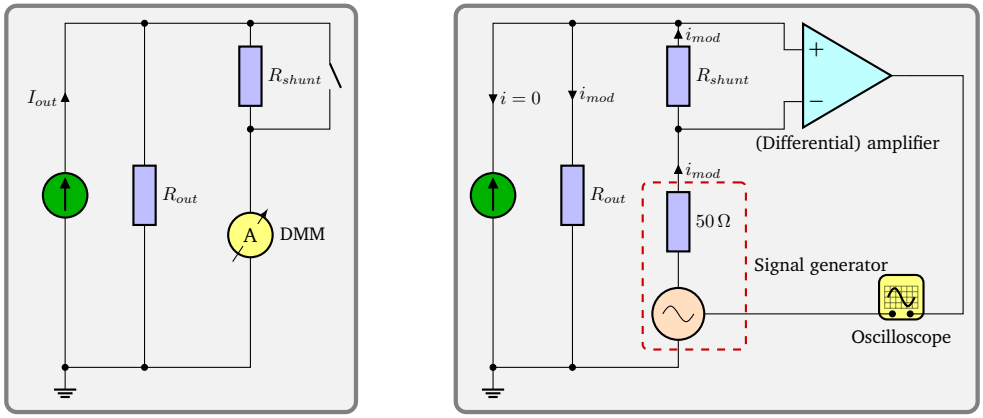

(a) DC scheme. (b) AC scheme.

Figure 4.27.: Two methods for measuring the output impedance of a current source.

The shunt resistance R_{shunt} can usually be determined with sufficient accuracy, but the difference in ΔI between to current with and without R_{shunt} is an entirely different matter though. Given a high impedance source, ΔI is naturally small. For educational purposes this problem can be illustrated by measuring the output impedance of the digital laser driver, which is expected to be very high due to the novel current source configuration discussed in the last section.

The measurement shown in 4.28 was conducted according to figure 4.27 (a). The ammeter was a 7.5 digit Keysight `34470A` multimeter and the shunt resistor value was $R_{shunt} = (3.298 \pm 0.002)\,\mathrm{M\Omega}$, which was measured using a Keysight `3458A`. The output current was chosen as low as reasonably possible to allow for a larger shunt resistor to improve the sensitivity. The DMM settings were 10 PLC with autozeroing enabled. To further improve the sensitivity a $30\,\mathrm{s}$ sample was taken for both switch positions to allow for additional averaging. Using the same settings, the measurement noise floor was determined first. A $30\,\mathrm{s}$ sample with open inputs resulted in a noise floor of $7.1\,\mathrm{pA_{rms}}$ using the `34470A` on the $10\,\mu\mathrm{A}$ range. This noise floor is low enough to be neglected as can be seen below. The measurement was then repeated with the setup shown in figure 4.27 (a). Since the output impedance of the current source is so high and even though the noise of the current source is extremely low with only $1.5\,\mathrm{nA_{rms}}$ ($\equiv 6\,\mathrm{nA/A}$ referred to full scale output) over $30\,\mathrm{s}$, the difference between the two switch settings is hardly recognizable. Figure 4.28 shows, in orange, the mean value of both measurements before and after switching in the shunt resistor. Longer measurement or integration times in an attempting suppress more noise are ineffective due to the presence of flicker noise in the current source, rendering longer integration times futile.

The results nulled to $2.72\,\mu\mathrm{A}$ and extracted from figure 4.28 are

$$I_{out} = 2.72\,\mu\mathrm{A} + (-0.31 \pm 1.48)\,\mathrm{nA} \qquad I_{shunt} = 2.72\,\mu\mathrm{A} + (1.54 \pm 1.10)\,\mathrm{nA}\,. \tag{4.11}$$

There are two things to note about the result $\Delta I = -1.85\,\mathrm{nA}$. First, the output current increases when the resistor is switched in which can also be seen from the negative sign of ΔI. This means the output impedance is negative, which will be discussed below in more detail. The other issue concerns the statistical uncertainty. As it can be seen, the uncertainty of ΔI is in excess of $50\,\%$ of its value. This means that applying the conventional approach of using the

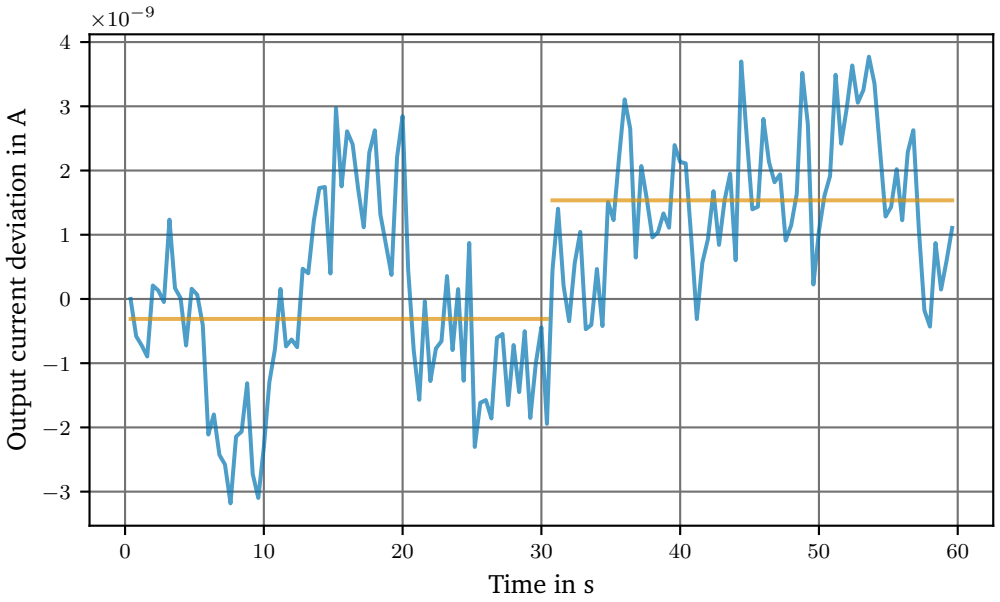

Figure 4.28.: Measurement of the output current using the technique illustrated in figure 4.27 (a). $R_{shunt} = (3.298 \pm 0.002)\,\mathrm{M\Omega}$, $I_{out} = (2.7200 \pm 0.0015)\,\mu\mathrm{A}$. The shunt resistor was switched in at $T = 30\,\mathrm{s}$. The DMM was nulled before the measurement.

mean value and applying the simplified formula for the propagation of uncertainty

$$\sigma_f(x, y, ...) \approx \sqrt{\left(\frac{\partial f}{\partial x}\sigma_x\right)^2 + \left(\frac{\partial f}{\partial x}\sigma_y\right)^2 + \dots}$$

will yield improper results for the calculation of R_{out} since it requires the uncertainty to be limited to a close neighbourhood around the mean because the formula is only an approximation. More background information on working with asymmetric or large uncertainties can be found in [29].

There are several ways to address the problem and a common solution is a Monte Carlo simulation to calculate both the expected value of R_{out} and its uncertainty. Such a simulation was prepared in Python and the source file can be found at data/simulations/sim_output_impedance_mc.py as part of the online supplemental material [42]. For the simulation, the uncertainties of R_{shunt} and the measurement noise floor were neglected because they are very small in comparison to the uncertainty of ΔI. The same goes for the systematic uncertainty resulting from the DMM calibration error of R_{shunt} and I_{out}. The simulation uses 10^8 samples, which are drawn from a normal distribution of $(1.85 \pm 1.56)\,\mathrm{nA}$ to calculate the output impedance applying equation 4.10. Drawing from a normal distribution is technically not correct because the measurement noise contains significant flicker noise, which is not white. Since the result is expected to have considerable uncertainty anyway, which gives a result of questionable significance, this is acceptable though. Using the samples drawn, R_{out} was calculated and 81.6×10^6 results were found the range $[0, 20\,\mathrm{G\Omega}]$. Those are shown in the histogram given in figure 4.29.

From the largest bin of the histogram and the one-σ range the following result for the static

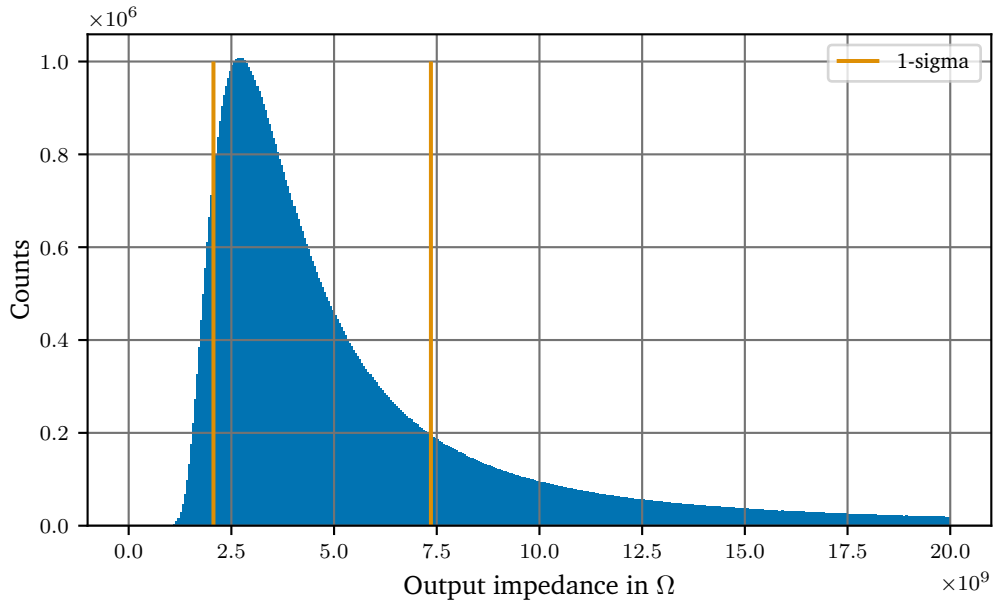

Figure 4.29.: Monte Carlo simulation to derive the output impedance of the DgDrive from the parameters given in 4.11.

output impedance

$$R_{out} = 2.7^{+4.70}_{-0.64}\,\mathrm{G\Omega}$$

was found.

From the simulation results one can gather that the DC output impedance is likely a lot higher than $2\,\mathrm{G\Omega}$. Given the high value of R_{out} measurement technique can only yield limited results. These limits are imposed by the current noise of the source and its flicker noise character. As explained in section 3.6.1 this type of noise cannot be averaged out or filtered to yield a better uncertainty. It must be stressed though that this is not a problem with the source, but rather the measurement technique. The source itself allows measurements down to $6\,\mathrm{nA/A}$ over $30\,\mathrm{s}$, which is a very low noise figure. To get more conclusive results a different approach is therefore needed. Using the method shown in figure 4.27 (b), a signal generator in combination with an oscilloscope or a network analyser can be used to determine the output impedance over a wide frequency range. Moving away from DC is beneficial since the laser driver current source relies on op-amps and their gain. The output impedance therefore declines with increasing frequency. This way, the limited resolution of the previous measurement can be evaded. Additionally, the output impedance frequency spectrum can reveal a lot more details about the current source as will be discussed next.

The setup shown in figure 4.27 (b) puts a few requirements on the signal generator/VNA and the amplifier that need to be addressed first. The measurement setup can be configured in two ways as shown in figure 4.30 below. One approach requires a floating signal generator because the resistor is ground referenced and the other technique requires a floating or differential amplifier because the signal generator is grounded. Due to this nature, the whole measurement becomes more of a test of CMRR and ground isolation than anything else. This statement will be briefly elucidated to help understand the final solution implemented.

Starting with a ground referenced amplifier as shown in figure 4.30 (a), it is clear that

the amplifier sees the common-mode voltage V_{cm} produced by the signal generator on both inputs. An ideal amplifier is unaffected by V_{cm} and has a common-mode gain $A_{cm} = 0$, but any amplifier existing in reality has both a common-mode and a differential mode gain A_d with the CMRR defined as [226, p. 328]

$$CMRR \coloneqq \frac{A_d}{A_{cm}} .$$

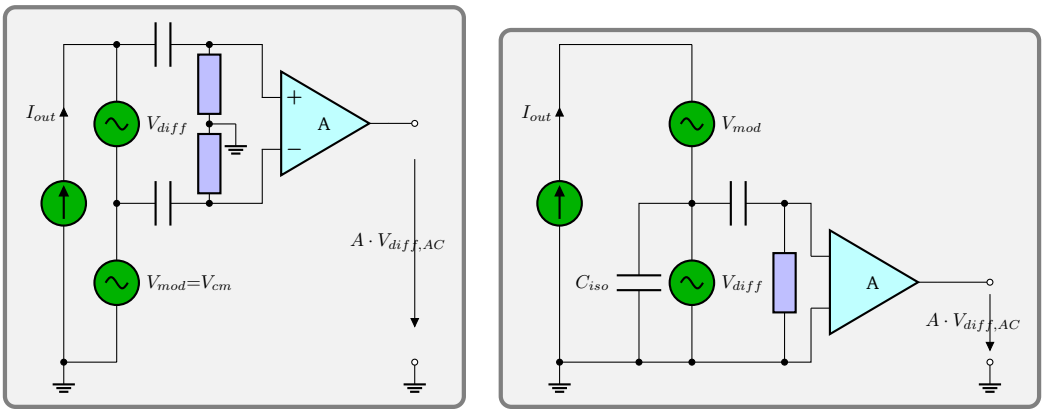

(a) Grounded signal generator.

(b) Floating signal generator.

Figure 4.30.: Different configurations of the amplifier have a profound effect on the measurement. Placing the signal generator on top gives significant coupling to ground, yet allows a single-ended amplifier.

The common-mode rejection quickly becomes a problem, because a larger output impedance implies a smaller differential signal albeit the same common-mode signal. Therefore the CMRR of the amplifier presents an upper limit to the sensitivity in this configuration. The most frequently used amplifier for this situation is a so-called instrumentation amplifier, which is a difference amplifier with buffered high impedance inputs [226]. It is a design based on three op-amps and the CMRR is mostly limited by the matching of four internal resistors. To give some numbers, a $1\,\mathrm{k\Omega}$ shunt resistor in combination with a modern high precision instrumentation amplifier like the Texas instruments `INA821` [101] will give a CMRR of around $120\,\mathrm{dB}$ limiting the maximum output impedance that can be measured to $R_{out} \ll 1\,\mathrm{G\Omega}$. Increasing R_{shunt} is impractical, because the CMRR will also drop with increasing source imbalance due to the input impedance of the instrumentation amplifier. AC coupling the amplifier as shown in figure 4.30 (a) aggrandizes the CMRR problem discussed before. In addition to the common-mode rejection of the amplifier, the transfer function of both high-pass filters has to be closely matched as well, because a gain mismatch translates into a decreased CMRR. Matching those filters to 10^{-6} is a tedious venture.

Alternatively, the signal generator can be floated and placed above the shunt resistor as shown in figure 4.30 (b). This allows to use a singled ended amplifier, which can be easily AC coupled to remove the DC offset. While this takes care of the CMRR issues, it creates another one. The signal generator may have a isolated outputs, but there is still a capacitive coupling C_{iso} to earth and if either the amplifier, the current source, or the oscilloscope is connected to protective earth an AC leakage current can be observed. Using a high value shunt resistor of several $\mathrm{M\Omega}$ to improve the signal-to-noise ratio (SNR) of the measurement exaggerates

the problem, especially around the line frequency, and multiples thereof. This foiled any attempts to measure the output resistance at low frequencies. Using a low capacitance isolation transformer could solve this issue, but there is a solution, that promises fewer sources of error.

Instead of floating the signal generator or using a differential amplifier, the amplifier can be floated as well. Battery driven amplifiers, like the Stanford Research SR560 or the Signal Recovery 5113 are available off-the-shelf and include additional filters and a variable gain. Using a floating amplifier either requires an isolated oscilloscope or an isolated differential probe to connect a grounded oscilloscope. Amplifying the signal first greatly relaxes the common-mode rejection and noise requirement of the active probe allowing the use of commercial off-the-shelf solutions. The performance difference between an isolated oscilloscope and isolated probe only depends on the input capacitance of the device or probe as the capabilities of battery driven scopes has vastly improved in recent years and their performance matches that of mains powered scopes in this application. Both option will be compared below.

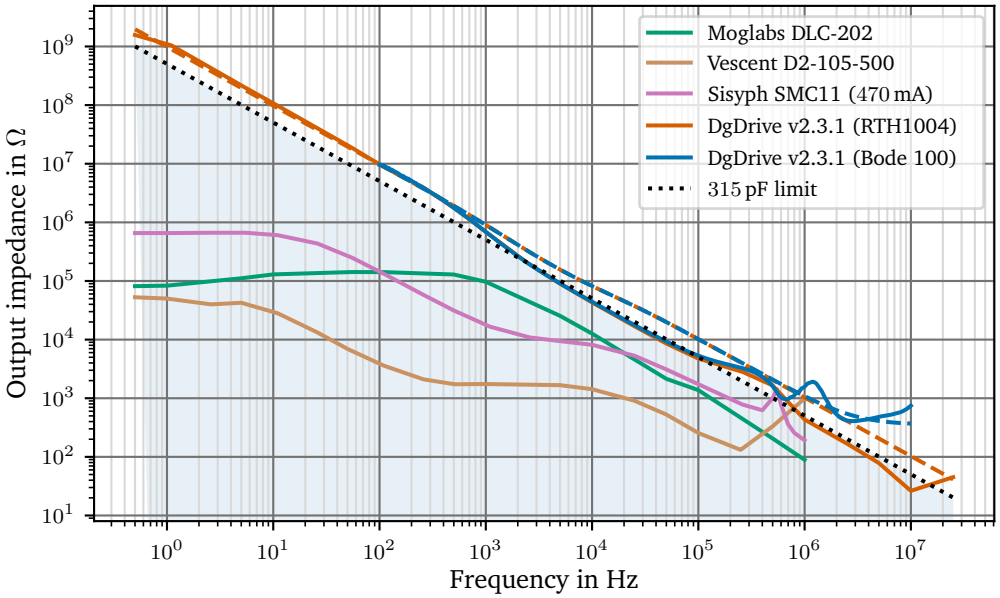

Figure 4.31.: Measured output impedance of several laser diode drivers. The shaded region is the limit imposed by a 3 m RG-213 coaxial cable with a capacitance of 315 pF between conductor and shield. The coloured dashed lines show the results of an LTSpice simulation.

The instruments used for the dynamic output impedance measurement were a Keysight 33522B signal generator, a Stanford Research SR560 [213], a Sapphire HVP70 differential probe and a Keysight MSO9254A oscilloscope. Additionally, a Rohde & Schwarz RTH1004 [180] isolated battery powered oscilloscope and an Omicron Bode 100 [223] VNA was used for parts of the measurement. The devices tested were the Vescent D2-105-500, the Moglabs DLC-102, the Sisyph SMC11 and the DgDrive-250, a 250 mA version of the current driver. An overview of all versions is shown in table 4.8 on page 126. The shunt resistor was mounted in a test fixture and connected via a 1 m RG-213 coaxial cable to the driver, either directly or via a DVI adaptor. The cable length was deliberately kept short to limit the cable capacitance as the impedance of that capacitance is in parallel with the output impedance of the current source and therefore presents an upper limit to the output impedance measurable at high frequencies.

The commercial drivers were tested using a $10\,\Omega$ shunt resistor while the DgDrive-250 required several different shunt resistors to meet the signal-to-noise requirements. The results of the measurements are shown in figure 4.31.

Both the Sisyph SMC11 and the Vescent D2-105-500 show a familiar characteristic. The output impedance is reminiscent of the simulation shown in figure 4.21 on page 4.21. This is not surprising as Vescent claims, in the datasheet [62], that the heritage of their driver is the design by Libbrecht et al. [128]. Regarding the SMC11 this is unknown but it is likely that a similar circuit for the modulation current source is used. Moglabs on the other hands employs a different circuit as confirmed by the author. The output impedance of those three drivers is nonetheless limited, at low frequencies, by the resistor matching of the modulation current source. Going above $1\,$kHz the op-amp gain becomes the major limiting factor as discussed in section 4.1.7. The peaking of the output impedance seen with both the D2-105-500 and the SMC11 around $1\,$MHz stem from the test fixture and its parasitic effects, including the impedance mismatch from connecting a current source to a low impedance sink. Some of the parasitic effects are shown in figure 4.32 and will discussed along with the output impedance of the DgDrive-250.

All commercial current drivers share the same problem, the limited output impedance of the modulation current source confines the combined current source to below $1\,\mathrm{M}\Omega$. Assuming a $3\,$m cable length required to connect the laser with the laser driver, none of these drivers manage to get close to the physical limit imposed by a $3\,$m RG-213 coaxial cable. RG-213 cables are commonly used in experimental setups and the ones used in the group have a measured capacitance of $105\,\mathrm{pF/m}$. Do note, the DLC-102 and the DgDrive-250 use a DVI cable with less capacitance, but both the SMC11 and the D2-105-500 have an SMA output for the laser current and such a connection would likely be adopted in a real situation. The $315\,$pF-limit is shown as a dotted black line with a light blue fill below in figure 4.31. The values within the blue shaded region marks the output impedance physically realisable when a $315\,$pF capacitor is connected in parallel to a high impedance current source. This means that the commercial drivers do not utilize the full potential to suppress external noise sources because a higher output impedance serves the purpose of suppressing current noise as detailed in section 3.8.2 on page 70. The topic of noise will be discussed in depth in the next section 4.1.10.

The DgDrive-250 (serial number: #13) required special attention when measuring its output impedance. First of all, this current source has a floating output, which makes a floating output of the signal generator mandatory. It also means that the oscilloscope measuring the signal generator voltage needs two isolated inputs one for the signal generator and one for the shunt resistor signal. To facilitate this, the MSO9254A was replaced with the fully isolated, battery powered RTH1004. In addition to that complication, the output impedance of the laser driver is so high that at low frequencies between $0.5\,$Hz and $110\,$Hz a $1\,\mathrm{M}\Omega$ resistor had to be used to reach the required signal-to-noise ratio. The test current was set to $5\,\mu$A for the $1\,\mathrm{M}\Omega$ resistor, which had no bearing on the result due to the novel current source design. This can be confirmed using the LTSpice simulation found at source/spice/current_regulator_TIA_simple_output_impedance.asc. Between $260\,$Hz and $250\,$kHz the $1\,\mathrm{M}\Omega$ shunt was replaced by a $1\,\mathrm{k}\Omega$ resistor and the current was increased to $5\,$mA. Beyond that, a $49.9\,\Omega$ shunt resistor was used and the current again increased to $50\,$mA. Along with the change to a $49.9\,\Omega$ shunt resistor the amplifier was removed and the signal was directly fed into the RTH1004, because the bandwidth of the SR560 is limited to $1\,$MHz [213]. The low noise $10\,$bit ADC of the RTH1004 [180] was able to compensate for the loss in gain. In order to reduce parasitic effects, the shunt resistor was a small 0805 SMD high power ($250\,$mW) resistor, that was soldered between the pins of an isolated BNC connector. Using this scheme it was possible to measure

the output impedance between $0.5\,\mathrm{Hz}$ and $10\,\mathrm{MHz}$ without significant distortion. Towards lower frequencies, the measurement is limited by noise and the minimum cutoff frequency of $0.03\,\mathrm{Hz}$ of the band-pass filter in the SR560 [213]. Nonetheless $1\,\mathrm{G\Omega}$ at $1\,\mathrm{Hz}$ was measured, which agrees well with the results from the DC measurement shown above. Towards higher frequencies, the output impedance drops by an order of magnitude per decade of frequency – the typical behaviour of an RC filter. This RC filter is created by the parasitic capacitance of the test fixture and the $1\,\mathrm{m}$ coaxial cable used to connect the driver to the fixture. That cable is an RG-213 coaxial cable soldered to pins of a DVI connector. The test fixture including the cable was measured as having a capacitance of $155\,\mathrm{pF}$. This capacitance is between the output and the return path of the current source. Additionally, the input capacitance of the RTH1004 must be considered. Its value is $12\,\mathrm{pF}$ [180] and it is connected in parallel with the shunt resistor. These parasitic capacitances are shown in figure 4.32 for better illustration.

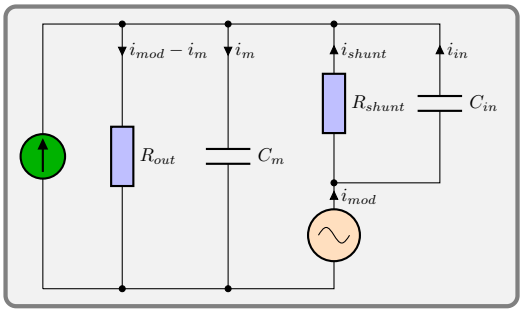

Figure 4.32.: Simplified setup for measuring the output impedance including the mutual capacitance of the cable C_m and the parasitic input capacitance C_{in} of the instrument.

Figure 4.32 shows a model of the test setup along with the most prominent parasitic effects. The mutual capacitance between the two conductors C_m of the current driver output lead is in parallel with the output resistance R_{out}. In addition, the input capacitance C_{in} of the measurement instrument is in parallel with the shunt resistor R_{shunt}. The measurement instrument is either the Bode 100 VNA, the SR560 amplifier, or the RTH1004 oscilloscope along with a $25\,\mathrm{cm}$ RG-213 coaxial cable.

Using these numbers a simulation in LTSpice was conducted and the results are also shown in figure 4.31 as dashed lines of the same colour as the corresponding measurement trace. From the agreement of the simulation, when the parasitics are included, with the impedance measurement, it can be inferred that this measurement only delivers a lower bound, constrained by the test setup. Nonetheless, the $155\,\mathrm{pF}$ capacitance of the test setup gives a reasonable approximation of the real-life situation. As measured in section 4.1.8 and presented in table 4.9 on page 135, the DVI cable has a mutual capacitance of 42–$49\,\mathrm{pF/m}$, depending on the model. The $155\,\mathrm{pF}$ therefore represents a typical value for a $3\,\mathrm{m}$ cable and the results presented in figure 4.31 can be anticipated in real-life situations.

To confirm the results obtained using the signal generator and the oscilloscope, the measurement was repeated using a different setup. The generator and the oscilloscope was replaced by an Omicron Bode 100 VNA. This setup needs some introduction because, as before, the signals of interest have different ground potentials. The VNA itself can be floated but its inputs and outputs share the same ground reference and must therefore be individually isolated. To inject the modulation, a Picotest J2101A injection transformer was used to isolate the output. The injected signal behind the transformer, referenced to the low side of the current source, was sampled using a Sapphire HVP70 differential probe. The second input, sampling the shunt

voltage, was floated to the shunt resistor potential. The shunt was a $1\,\mathrm{k\Omega}$ resistor without the SR560 preamplifier to simplify the setup. Therefore, is was only possible to cover the frequency range between $100\,\mathrm{Hz}$ and $10\,\mathrm{MHz}$. The lower limit comes from the signal to noise ratio and the upper limit is given by the injection transformer bandwidth of about $10\,\mathrm{MHz}$ [64]. As can be seen in figure 4.31, both measurements agree very well. The only difference is visible at frequencies above $1\,\mathrm{MHz}$. The flattening of the output impedance curve is caused by the input capacitance of the VNA ($55\,\mathrm{pF}$, [223]). To understand this, figure 4.32 can again be consulted to aid with the following explanation.

The output impedance shown in figure 4.31 is calculated without parasitics and only valid if the assumption

$$R_{out} = \frac{v_{mod}}{i_{shunt}} - R_{shunt} \qquad i_m \ll i_{shunt} \qquad i_{in} \ll i_{shunt} \tag{4.12}$$

holds. As can be seen from the parasitics shown in figure 4.32 the validity of the assumptions made about the parasitic currents is frequency dependent as the impedance of the parasitic capacitances is determined by frequency. It also depends on the respective resistances R_{out} and R_{shunt}. The current i_m, flowing into the cable capacitance, is the most sensitive parasitic because R_{out} is very large. C_m must therefore be kept very low. If $i_m \ll i_{shunt}$ cannot be satisfied, a substantial current flows around R_{out} and applying equation 4.12 without taking this into account makes the output impedance look smaller. This is responsible for the one decade per decade roll-off seen in figure 4.31 as already mentioned above. The effect of i_{in} can only be seen at high frequencies or large values of R_{shunt}. For this reason, R_{shunt} must be reduced with increasing frequency. This was done by going from a $1\,\mathrm{M\Omega}$ resistor to a $1\,\mathrm{k\Omega}$ and then to a $50\,\Omega$ resistor. Skipping this procedure causes the effect seen in the measurement conducted with the VNA. Using a fixed $1\,\mathrm{k\Omega}$ resistor in combination with the larger input capacitance of the VNA leads to an apparent increase of the output impedance at frequencies above $1\,\mathrm{MHz}$, which is entirely due a systematic measurement error. This can also be reproduced in the simulation by inserting the capacitor $C_{in} = 55\,\mathrm{pF}$ into the model as shown in figure 4.32. Those simulation results are shown as a dashed blue line in figure 4.31.

When comparing the simulation with the measured results a drop in the output impedance by a factor of 2 at $1\,\mathrm{kHz}$ is currently not well understood. It could be due of the test fixture, which was already found to be the limiting element of the measurement. There are plans to revise the test fixture and replace it with a dedicated PCB along with amplifiers directly on the board to reduce the capacitance seen by the current source. This would give a clearer picture on the source of this phenomenon.

The results shown in this section can be summarized as follows. A high output impedance is desirable to ensure a good noise immunity of the current source as shown in figure 3.38 (b) on page 70. The output impedance of all commercial laser drivers tested were limited by the output impedance of the modulation current source and measured below $1\,\mathrm{M\Omega}$ at low frequencies. This limit was shown to be result of the resistor matching in the modulation current source. It can be expected to vary widely between individual samples of the devices as explained in figure 3.53 on page 93. The DgDrive-250 was demonstrated to have a very high output impedance of at least $1\,\mathrm{G\Omega}$ at $1\,\mathrm{Hz}$, which was the limit of the test setup, rather than that of the DgDrive-250. At higher frequencies, the field of tested drivers moves closer together, because the output impedance is limited by the bandwidth of the op-amps used. All drivers are within a range of $100\,\Omega$ to $1\,\mathrm{k\Omega}$ at $1\,\mathrm{MHz}$.

None of the commercial current drivers tested reached the physical limits imposed by the external cabling. A typical $3\,\mathrm{m}$ RG-213 coaxial cable was chosen as an example for connecting

the laser driver. Of the drivers tested, the Moglabs `DLC-102` has shown the best performance between 100 Hz and 100 kHz, a range containing a lot of noise sources like fluorescent overhead lights and switch mode power supplies. The Vescent `D2-105` and Sisyph `SMC11` demonstrated a similar behaviour as seen with the design of the original paper presented by Libbrecht et al. [128]. Those drivers could do lot better by improving on the modulation current source circuit. The Vescent `D2-105` driver has generally shown the worst performance in this test, so a poor noise immunity is expected in later tests.

The DgDrive in turn managed to push the limits of a low capacitance DVI cable and delivered a performance only limited by the cable capacitance which translates in a superior noise rejection capability compared to the commercial devices. The noise performance will be discussed next.

Device Properties 4.3: DgDrive output impedance

- $R_{out} \geq 1\,\mathrm{G\Omega}$ at 1 Hz
- R_{out} is limited by the capacitance of the DVI cable not the driver

4.1.10. Test Results: Current Noise

The spectral current noise density is a quantity, that is both seemingly trivial to measure and also easy to understand and graphically compare. Therefore, it is a figure widely used by manufacturers and many devices are emblazoned by such graphs. The upside is that these numbers can used for reference although comparing devices is not trivial, because the noise depends on the output current range as discussed in section 3.8.6.

Defining the bandwidth of such a measurement is a matter of debate and depends on the future use-case of the current driver. In this work an upper frequency of 1 MHz was chosen for two reasons, first, to limit the number of amplifiers required. As the noise power rises with the bandwidth (in the best case as $\sqrt{\Delta f}$ for white noise) and impedance matching comes into play, a higher power amplifier is required, a trait that does not bode well with low noise, low frequency front ends. So for frequencies above a few MHz more than one amplifier is called for. Additional amplifiers make the whole measurement more intricate, because the amplifiers are the most critical parts in the whole chain.

The second reason does not root in the laziness of the researcher, but has a physical origin. Cables used in the lab like RG-58 or RG-223 have a capacitance of about $100\,\mathrm{pF/m}$. With a cable length of 3 m, resulting in 300 pF, one finds that at 10 MHz the impedance seen by the laser diode approaches $50\,\Omega$. Not unsurprising, given that the cable design impedance is $50\,\Omega$ and a signal at 10 MHz has a wavelength of $\lambda \approx 2$ m calling for impedance matching. At this point the performance of a current source is naturally limited as discussed in the previous section and the laser should be stabilized to an external reference using a current source closer to the laser diode like in the laser head as demonstrated by Preuschoff et al. [177].

The measurement technique used in this section is a simple shunt resistor, through which the current is sourced to convert the current noise into a voltage noise. An AC coupled amplifier is then used to amplify the voltage noise. This measurement setup is owed to the fact, that most publications [77, 128, 196, 221] and commercial drivers [62, 86, 142] use this method and it therefore allows intercomparison. A better signal-to-noise ratio could be achieved using a transimpedance amplifier configuration, which would provide more gain and less noise. Nonetheless, sufficient SNR can be achieved using a $10\,\Omega$ resistor and a low noise amplifier (LNA). A $10\,\Omega$ resistor was chosen to keep the load on the current driver low to exclude any

compliance voltage related effects. These will be discussed separately at the end of this section. Using a test current of $50\,\mathrm{mA}$ gives a voltage drop of only $500\,\mathrm{mV}$, well below the typical forward voltage of a laser diode, compliance voltage related effect should therefore not be visible. In addition, using $250\,\mathrm{mA}$ and $2.5\,\mathrm{V}$ is close to the specifications of the Thorlabs `L785H1` [118] laser diode used in the group. Both scenarios can be covered using a single resistor, simplifying the setup.

A $10\,\Omega$ resistor creates a thermal noise density of $400\,\mathrm{pV}/\sqrt{\mathrm{Hz}}$. This excludes the `SR560` as an amplifier, because it would severely limit the measurement by its own noise figure of $4\,\mathrm{nV}/\sqrt{\mathrm{Hz}}$ [213], the equivalent of a $1\,\mathrm{k}\Omega$ resistor. While the `SR560` uses a FET input amplifier with a very high input impedance and low input current noise, the $10\,\Omega$ input impedance allows the use of bipolar transistors at the input of the amplifier similar to the front end shown in figure 3.51 on page 85. Bipolar transistors are more sensitive to the source impedance since they do not present a high impedance input like a JFET, resulting in a higher input current noise, but achieving a lower voltage noise in return. A design based on the amplifier presented in [156] with a noise floor of $460\,\mathrm{pV}/\sqrt{\mathrm{Hz}}$, a $3\,\mathrm{dB}$-bandwidth of $10\,\mathrm{Hz}$ to $1.5\,\mathrm{MHz}$ and a fixed gain of $80\,\mathrm{dB}$ (10^4) was built for this purpose. The amplifier is powered by alkaline batteries to prevent mains hum from entering the amplifier through the power supply. The input impedance is only $500\,\Omega$, so this has to be taken into account for the source impedance of $10\,\Omega$ as proposed above. The voltage divider formed will reduces the gain to about 9800.

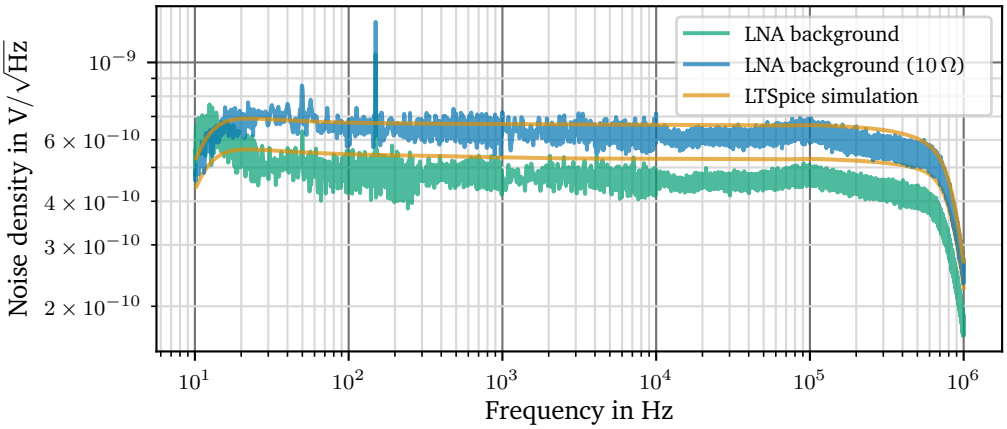

Figure 4.33.: Noise floor of the low noise amplifier based on [156].

Figure 4.33 shows the noise of the amplifier in two configurations. One with the input shorted and the other with a $10\,\Omega$ resistor between the inputs. The latter was corrected for the reduced gain and presents the intrinsic noise of the current noise measurement setup. The white noise floor including the $10\,\Omega$ resistor is at $615\,\mathrm{pV}/\sqrt{\mathrm{Hz}}$, which agrees well with theory, which predicts

$$\sqrt{\left(400\,\mathrm{pV}/\sqrt{\mathrm{Hz}}\right)^2 + \left(450\,\mathrm{pV}/\sqrt{\mathrm{Hz}}\right)^2} = 610\,\mathrm{pV}/\sqrt{\mathrm{Hz}}\,.$$

The noise floor is mostly white with two exceptions. Even though the amplifier is battery powered, the $50\,\mathrm{Hz}$ mains frequency and its third harmonic highlights a weakness of such low noise amplifiers. They are very susceptible to magnetic pickup and must be shielded (preferably in mild steel) and kept away from linear power supplies with large transformers. In practice, a distance of $3\,\mathrm{m}$ from any linear power supply was found to be sufficient. One potential issue

regarding the amplifier noise must be mentioned here. The amplifier does not use a voltage regulator and is directly powered from the batteries. This has the advantage of requiring fewer batteries but comes at the cost of affecting the amplifier performance. As can be seen in figure 3.51, the current flowing through the transistors is not regulated with a current source and only relies on a resistor and the supply voltage. With a decreasing supply voltage the current through the input transistors reduces and the amplifier noise increases. To reach the performance shown in figure 4.33 a fresh set of batteries is required.

To measure the spectral density shown in figure 4.33, multiple recording devices were used since no low frequency FFT analyser or the like was available. At low frequency the digitizing function of a Keysight `34470A` DMM with a sampling rate of up to $10\,\mathrm{kHz}$ was utilised for the range of $0.1\,\mathrm{Hz}$ to $260\,\mathrm{Hz}$. A Keysight `MSO9254A` oscilloscope was used between $260\,\mathrm{Hz}$ and $40\,\mathrm{kHz}$, and above that, a Tektronix `RSA306` USB spectrum analyser (SA) served to measure up to $1\,\mathrm{MHz}$. Each range was band-pass filtered using an SRS `SR560` connected after the LNA. The `SR560` is also responsible for the gain dropping off towards $1\,\mathrm{MHz}$. The time-domain data collected by the DMM and the oscilloscope, was converted into its frequency representation using an algorithm developed by Welch [240] to estimate the power spectrum.

An LTSpice simulation of the circuit was also conducted, but it slightly overestimates the noise figure of the `THAT300` NPN transistor array yet still gives reasonable results. The SPICE model used was the noise model provided by the manufacturer [57]. The simulated data is included in figure 4.33 as solid orange lines for reference.

The system noise floor of $615\,\mathrm{pV}/\sqrt{\mathrm{Hz}}$ or $61.5\,\mathrm{pA}/\sqrt{\mathrm{Hz}}$ obtained from figure 4.33 limits the resolution of the test setup to laser drivers with a current noise of about $100\,\mathrm{pA}/\sqrt{\mathrm{Hz}}$. In this case an error of $17\,\%$ is incurred, which must be kept in mind. Lower noise drivers require a larger resistor as the resistor noise scales with $\sqrt{R}$ while the gain scales with R. For the very low noise drivers a $1\,\mathrm{k\Omega}$ resistor was chosen and the test current was reduced to $5\,\mathrm{mA}$. Since the LNA does not work well with a source impedance of $1\,\mathrm{k\Omega}$ and the thermal noise of the resistor is $4\,\mathrm{nV}/\sqrt{\mathrm{Hz}}$, on par with the `SR560`, the latter can be used standalone without the additional low noise preamplifier.

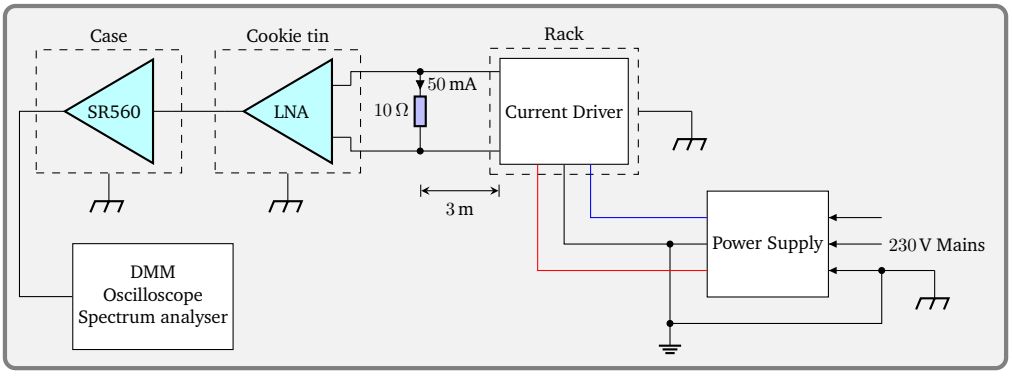

Figure 4.34.: Power and grounding scheme for the current noise measurement. The shunt and amplifier are located $3\,\mathrm{m}$ away from the power supply to prevent magnetic coupling.

The test setup shown in figure 4.34 requires utmost care in order to not introduce ground loops that erroneously show up as noise from the current source. To ensure this, all measurement instruments either had floating inputs or were battery powered without a direct connection to earth. The Keysight `34470A` DMM has floating inputs, the Keysight `MSO9254A`

oscilloscope was used with an isolated differential probe and the Tektronix RSA306 SA was powered via an ALLDAQ ADQ-USB 3.0-ISO-W USB 3.0 isolator to remove the high frequency noise coming from the host computer. The isolated side of the USB 3.0 isolator connected to the RSA306 was supplied through an Agilent E3631A linear power supply. All amplifiers were always powered from battery. The full setup including grounding is shown in figure 4.34. All laser drivers except the DgDrive-500-LN used the power supply that came with the unit to give an example of the full system performance that can be expected out of the box. The DgDrive-500-LN, which does not come with a power supply of its own, was tested with both an Agilent E3631A linear supply and a R&S HMP4040 switch-mode supply to demonstrate the suppression of the input filter, which was already examined in section 4.1.4. As mentioned before, the custom low noise amplifier and the SR560 as well are very sensitive to magnetic coupling. Since shielding at this level either requires an expensive mu-metal box or a thick steel box, the amplifier was instead moved away from any large transformers, namely the power supplies of the drivers. The shunt resistor was connected via a $3\,\mathrm{m}$ cable as shown in figure 4.34, also resulting in a more realistic scenario when compared to a typical laser setup. The effect of different cables and lengths on the current source output was discussed in the previous section 4.1.9.

The results of the measurements are shown in figure 4.35 and the performance each device will now be discussed, starting with the Toptica DCC 110. Although the DCC 110 is a legacy device no longer sold by Toptica, it was widely adopted and is still used in many labs, including the $441\,\mathrm{nm}$ diode laser system intended for the ARTEMIS experiment. Unfortunately, the driver has shown the worst performance of all devices tested. A whole range of mains harmonics can be seen. Additionally, there is substantial interference around $15\,\mathrm{kHz}$ and its harmonics. On top of that, the baseline noise density is around $10\,\mathrm{nA}/\sqrt{\mathrm{Hz}}$ dropping off at $10\,\mathrm{kHz}$ probably due filtering of the reference. The noise floor then levels off at $300\,\mathrm{pA}/\sqrt{\mathrm{Hz}}$.

The next device evaluated was the LQO LQprO-140 developed at the neighbouring group *Laser und Quantenoptik* [85]. The author would like to thank the group for providing a demo device for testing. The unit came in small rack with an integrated power supply. The author was pleasantly surprise of the little mains hum or harmonics present from this supply. Apart from the few mains harmonics up to $350\,\mathrm{Hz}$ there are no other noise present. The noise floor itself was lower than the one presented by Toptica, but unfortunately the $<300\,\mathrm{pA}/\sqrt{\mathrm{Hz}}$ claimed in the datasheet [86] cannot be confirmed. A feature of this driver might be a boon and a bane at the same time and be responsible for the high noise floor. The driver has a full-scale modulation input with a bandwidth of $200\,\mathrm{kHz}$ [86], so aggressive filtering of the current source setpoint with a low cutoff is not possible and therefore quite some noise is present up to $200\,\mathrm{kHz}$. Some of this noise is introduced by its linear regulators and with this feedback considerable improvements were made by John [106], bringing the driver closer to the performance of the Moglabs DLC-102 discussed next.

The Moglabs DLC-102 displays a flat noise floor of $500\,\mathrm{pA}/\sqrt{\mathrm{Hz}}$. Moglabs gives several numbers for the output noise of their drivers between $100\,\mathrm{pA}/\sqrt{\mathrm{Hz}}$ and $250\,\mathrm{pA}/\sqrt{\mathrm{Hz}}$, but it is not clear to which version of the driver these numbers refer. This number is likely owned to the fact that the DLC-102 has a high compliance voltage of $6\,\mathrm{V}$, which is the highest of all drivers tested. With a circuit architecture like the precision current source discussed in 3.8.4, a low value sense resistor must be employed. This in turn results in less transconductance gain, which increases the current noise as discussed in section 3.8.6 and shown in table 3.7 on page 87. The $50\,\mathrm{Hz}$ noise and harmonics are likely due to the unshielded transformer integrated into the unit as part of the power supply. The large, solitary peak at $250\,\mathrm{kHz}$ is due to the local oscillator of the integrated lock-in amplifier. The oscillator can be disabled completely by

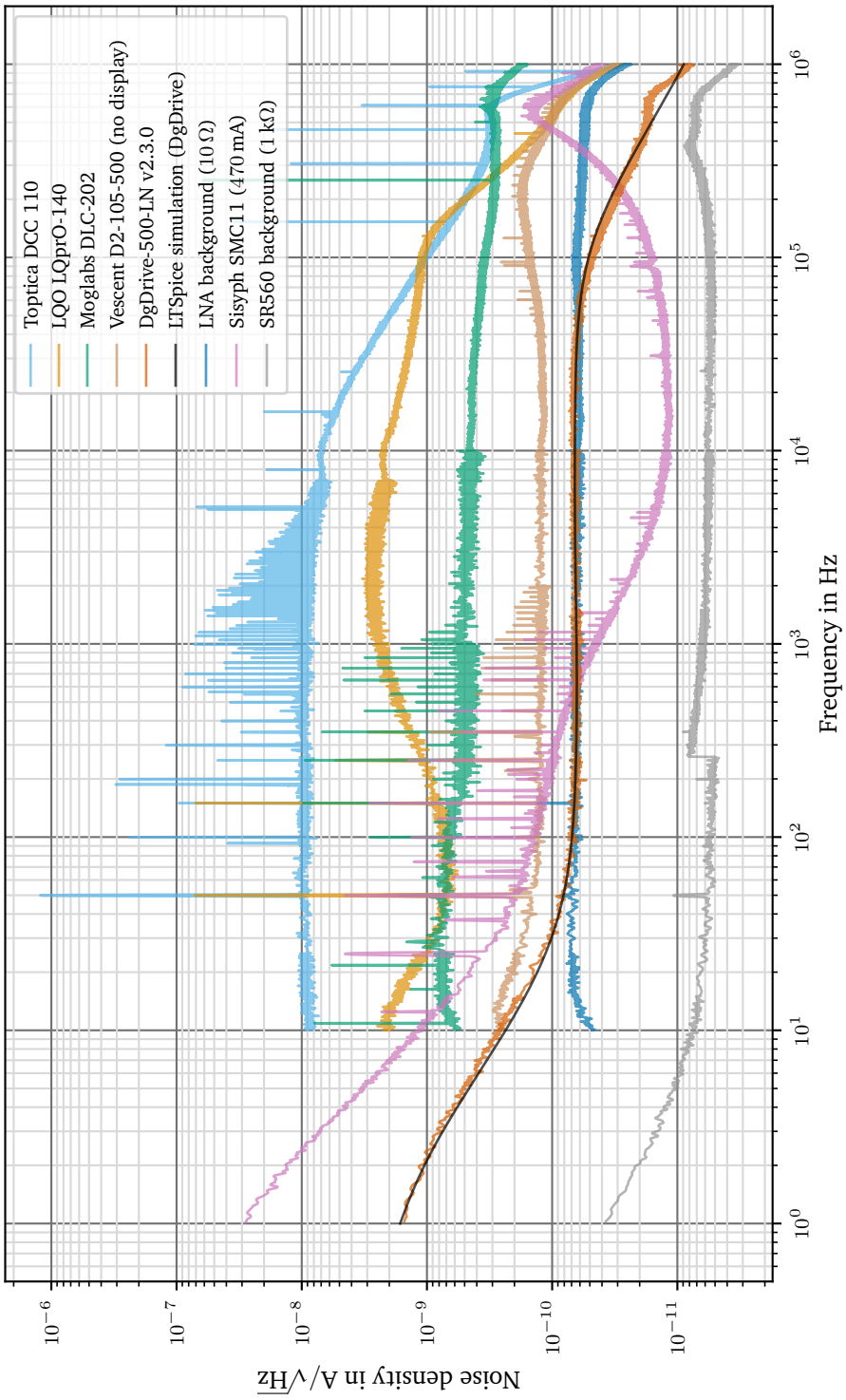

Figure 4.35.: Noise spectra of several current drivers tested. The `DgDrive-500-LN` and the `SMC11` were measured to $1\,\mathrm{Hz}$ using the `SR560` and a $1\,\mathrm{k\Omega}$ shunt resistor to improve the SNR. The amplifier noise floor was not subtracted form the measurements. The legend is ordered by the noise density in descending order.

adjusting internal trimpots. This was not done for the noise measurement because the origin of the peak is known, deliberately placed there and had no bearing on the measurement.

The Vescent `D2-105-500` delivered a performance close the LNA noise limit discussed above. With a measured noise of $120\,\mathrm{pA}/\sqrt{\mathrm{Hz}}$, the actual noise floor is closer to $100\,\mathrm{pA}/\sqrt{\mathrm{Hz}}$ when subtracting the amplifier noise, which is well below the conservatively specified $<200\,\mathrm{pA}/\sqrt{\mathrm{Hz}}$ [62]. The driver is susceptible to mains hum though, most likely coupled magnetically. The power supply that came with the driver, a Vescent `D2-005`, had a fairly short lead and used an E-core transformer inside, responsible for some magnetic leakage. The close proximity of the power supply in combination with the limited output impedance discussed in the previous section on page 142 leads to a strong coupling. Due to the $50\,\mathrm{Hz}$ noise, the driver is not capable of meeting the required $30\,\mathrm{nA_{rms}}$ noise figure (see specification 3.2). At frequencies below $10\,\mathrm{Hz}$ no measurement was possible because the cutoff frequency of the LNA is $10\,\mathrm{Hz}$. Using a larger resistor and the `SR560` was not feasible because the compliance voltage of the driver is limited to around $2.5\,\mathrm{V}$ and going above that, severe noise peaking was seen. Nonetheless, the noise corner frequency of the device at $80\,\mathrm{Hz}$ can be seen. This is due to the input current noise of the `AD797` op-amp used in the current source in combination with the setpoint filter as discussed in section 4.1.5. The flicker noise part is expected to start below this frequency. As a final note, all noise tests were conducted with the display board disconnected, as there was strong interference at $22.5\,\mathrm{kHz}$ and harmonics coming from this board. The issue was disclosed to Vescent in 2018-02 and reported fixed as of 2018-08 [206], but no retesting was done.

The Sisyph `SMC11` claims an even lower noise and indeed the noise floor reached $12\,\mathrm{pA}/\sqrt{\mathrm{Hz}}$ at $15\,\mathrm{kHz}$ but started starting rising again at $100\,\mathrm{kHz}$. The low noise figure seems to come from some very aggressive filtering of the current source using a very large inductor found on the PCB. In order to push the amplifier noise floor below that of the laser driver, the device was tested with shunt voltage of $5\,\mathrm{V}$ and a $1\,\mathrm{k\Omega}$ shunt running at $5\,\mathrm{mA}$ as discussed above. While this marks the upper end of the compliance voltage as per the datasheet, it was still within the limits and given the low current of $5\,\mathrm{mA}$ no issues should be expected. Nonetheless, significant peaking around $500\,\mathrm{kHz}$ and above is seen, obliterating the noise performance of the driver. Additionally an issue, likely with the power supply that came with the unit, can be observed in the noise spectrum. There is a significant amount of sub-harmonics below the $50\,\mathrm{Hz}$ mains frequency present, which point towards inductive saturation of the power supply transformer. Another problem can be noticed by looking at the low frequency performance. One would typically expect a flicker noise behaviour below the filter cutoff with the noise increasing at a rate of $20\,\mathrm{dB/decade}$ coming from the reference and the op-amps. When comparing the low frequency performance of the `DgDrive-500-LN` it can clearly be seen that noise rises more like $30\,\mathrm{dB/decade}$ pointing towards a mix of random walk and drift as discussed in section 3.6. This will be picked up in the next section when discussing the stability of the driver.

The last device to be discussed is the `DgDrive-500-LN` (serial number: #14), which is a low-noise $500\,\mathrm{mA}$ version. The noise measurement was again conducted using a $1\,\mathrm{k\Omega}$ shunt resistor with a compliance voltage of $5\,\mathrm{V}$ running at $5\,\mathrm{mA}$. The driver has a flat noise floor of $65\,\mathrm{pA}/\sqrt{\mathrm{Hz}}$ up to around $100\,\mathrm{kHz}$ where it appears to drop off. This is due to the reduced output impedance as shown in figure 4.31 on page 142. The output impedance at $100\,\mathrm{kHz}$ is only $5\,\mathrm{k\Omega}$ and therefore a considerable influence of the $1\,\mathrm{k\Omega}$ shunt resistor, which forms a voltage divider can be seen. Towards the low frequency end, the noise rises with the expected $20\,\mathrm{dB/decade}$. The flicker noise is mostly coming from the `AD797` op-amp input current noise as discussed in section 4.1.5. There is no additional noise coming from the mains or power supply and the noise spectrum is completely free of additional peaks. Electrical coupling from mains is suppressed by the filtered supply and magnetic coupling into the cable is efficiently suppressed using a twisted

pair (DVI) cable along with the very high output impedance effectively preventing radiated noise from entering the cable. The performance of the the input filter can be seen again in figure 4.36, which shows the DgDrive-500-LN in comparison to another DgDrive-500-LN being powered by a R&S HMP4040 switch-mode supply. This power supply has substantial noise at the switching frequency of 130 kHz and its harmonics, which was confirmed by the author in a separate measurement not shown here, but an example of the noise spectrum can be found in [25].

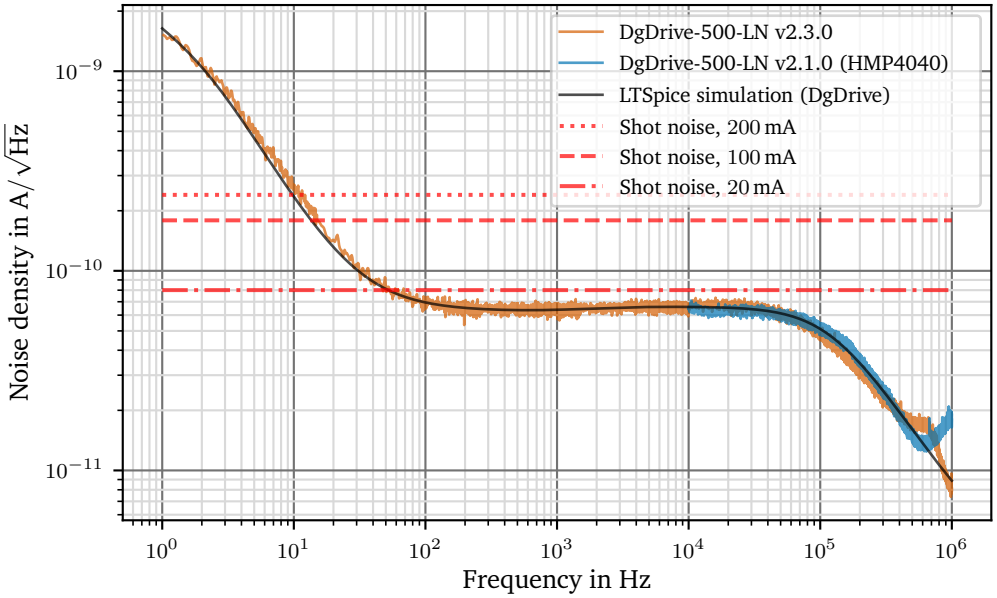

Figure 4.36.: Current noise of two DgDrive-500-LN operating at 5 mA and measured using a 1 kΩ shunt resistor. One is powered by a R&S HMP4040 switch-mode supply, the other by a linear supply. There is no excess noise measurable at the switching frequency of 130 kHz.

The noise floor of the two drivers is identical and only the high frequency behaviour is slightly different. This is due to a missing USB isolator between the RSA306 spectrum analyser and the computer, which is required at this noise level to prevent ground loops. The simulation results, which contain an accurate noise model of the Zener diode and the DAC, shown as a solid black line, are in very good agreement with the measurements. The noise model was built by the author from noise measurements of the LM399 and the AD5781. At low currents below 10 % I_{max} like in figure 4.36, most of the noise comes from the reference filter and the input current noise of the AD797. At currents above 10 % of the maximum output, the LM399 becomes the major contributor of noise below 1 Hz. This can only be improved by using a lower noise reference like the ADI ADR1399 in future revisions, which is currently subject to testing.

Figure 4.36 also includes the shot noise limit

$$S_{shot} = \sqrt{2eI} \tag{4.13}$$

for different laser diode injection currents. The shot noise limit translates into an amplitude noise limit at the quantum level for, e.g. optically pumped lasers. The drive current noise of a current source as described in this work can be well below the shot noise limit because their

noise is ultimately determined by the Johnson–Nyquist current noise of the resistor as given by equation 3.99 on page 84. Given a high impedance current source such as the DgDrive, the laser light can be amplitude squeezed below the shot noise limit as demonstrated by Machida et al. [145]. While this property was not confirmed in a measurement because there is currently no application for amplitude squeezed light in the group, it can be estimated that the laser driver is sufficiently low noise to produce squeezed light. For this estimation a Thorlabs L785H1 [118] laser diode is used as an example. The free-running laser diode is specified for an output power of $200\,\mathrm{mW}$ at $785\,\mathrm{nm}$ and $220\,\mathrm{mA}$ of current. This leads to a current of

$$I_{laser}(P_{out} = 200\,\mathrm{mW}) = P_{out} \cdot \frac{\lambda}{hc} \cdot \frac{1}{6.242 \times 10^{18}\,\mathrm{C}} \approx 127\,\mathrm{mA} \tag{4.14}$$

involved in the lasing process. The free-running laser diode may therefore display amplitude squeezed light because the $500\,\mathrm{mA}$ driver is able beat the shot noise limit at $20\,\mathrm{mA}$ of drive current as can be seen in figure 4.36. For an ECDL with that same laser diode, the requirement are stricter because the efficiency is lower. Typically ECDLs built in the group are characterised with $80\,\mathrm{mW}$ at $780\,\mathrm{nm}$ and $190\,\mathrm{mA}$ [176]. Applying equation 4.14 with output power $P_{out} = 80\,\mathrm{mW}$ leads to a current of $50\,\mathrm{mA}$ involved in lasing, which is still above the noise limit of the driver. Unfortunately, the matter is not that simple as an additional source of noise stemming from the feedback of the laser diode, called longitudinal-mode-partition noise [102, 115], degrades the squeezing. Given the low output current noise of the laser driver, further investigations into this matter are warranted in the future because amplitude squeezed light can offer interesting possibilities. Squeezed light can considerably increase the detection sensitivity beyond the standard quantum limit in applications where amplitude changes are observed, like Michelson interferometers [155] or the detection of small amplitude modulations [250].

A final aspect that must be mentioned is the behaviour of this type of current source with different load voltages. As discussed in section 3.8.5, the MOSFET must be biased into saturation for optimal performance. Failing to do so, will create strong noise peaking due to the reduction of the loop-gain, and hence the transconductance, of the precision current source. Since the design of the digital current driver is different and the issue less pronounced, as can be seen from the noise measurement with a load voltage of $5\,\mathrm{V}$ in figure 4.36, the Vescent D2-105-500 is used here as an example instead. For this measurement a $10\,\Omega$ shunt resistor was used and the current was gradually increased, thus increasing the load voltage, which at the same time decreases the drain-to-source voltage V_{DS} of the MOSFET. This behaviour effectively defines a maximum usable compliance voltage, where the device is still within its noise specifications. This is unfortunately only a soft limit as the driver will still function beyond this limit and give no indication of the diminished performance. There is no possibility to sense the load voltage on the driver side with any of the commercial drivers tested. The DgDrive, on the other hand, reads out the load voltage digitally and allows accesses via an integrated analog output to monitor the voltage.

Figure 4.37 shows the consequence decreasing the drain-to-source voltage V_{DS} from $9.8\,\mathrm{V}$ to $0.5\,\mathrm{V}$. There are two apparent effects. The first is an increase in the noise floor of the driver. The origin of this is not the driver, but rather the amplifier. As discussed above, the noise of the amplifier increases with decreasing battery voltage and those measurements were all recorded with the same set of batteries over the course of several hours. The noise floor below $200\,\mathrm{pA}/\sqrt{\mathrm{Hz}}$ therefore seems to increase between the measurements. This can be safely ignored and is not part of the discussion. The more interesting part is the noise at the high frequency end. With decreasing V_{DS} a pronounced noise peak starts building up due to the reduced transconductance of the MOSFET as discussed in section 3.8.4 and also observed by Seck et al.

[196]. At $V_{DS} = 0.5\,\mathrm{V}$ the current source is past the maximum compliance voltage and it drops out of regulation causing a massive increase of noise over the whole spectrum bringing the driver well above its specification. The exact voltage of when this happens was not determined because as discussed in section 3.8.4 the limit is expected to vary between individual samples of the device, but those number allow to estimate the maximum compliance voltage. The Vescent `D2-105-500` uses a $11\,\mathrm{V}$ supply voltage, a $12\,\Omega$ sense resistor and adds about $1.3\,\Omega$ of resistance after the MOSFET coming from an inductor and a small damping resistor. Using these numbers and taking $1.7\,\mathrm{V}$ from figure 4.37 as the minium V_{DS}, the maximum compliance voltage at the specified output current of $500\,\mathrm{mA}$ can be estimated as

$$\begin{aligned} V_{comp} &= V_{sup} - V_{sense} - V_{DS} - V_{inductor} \\ &= 11\,\mathrm{V} - 500\,\mathrm{mA} \cdot 12\,\Omega - 1.7\,\mathrm{V} - 500\,\mathrm{mA} \cdot 1.3\,\Omega \\ &= 2.65\,\mathrm{V}\,. \end{aligned}$$

Do note that the $12\,\Omega$ sense resistor and the typical $7\,\mathrm{V}$ reference voltage indicates a maximum output current of $580\,\mathrm{mA}$ but the driver is only specified for $500\,\mathrm{mA}$, so the latter value is used for the estimation. The maximum compliance voltage of $2.65\,\mathrm{V}$ limits the use of this driver to NIR laser diodes when operating at full output current. Alternatively limiting the current to $100\,\mathrm{mA}$ allows to meet the requirement of $8\,\mathrm{V}$ for blue laser diodes as defined in specification 3.2 at the expense of the higher current noise of a $500\,\mathrm{mA}$ driver in comparison to a $100\,\mathrm{mA}$ driver.

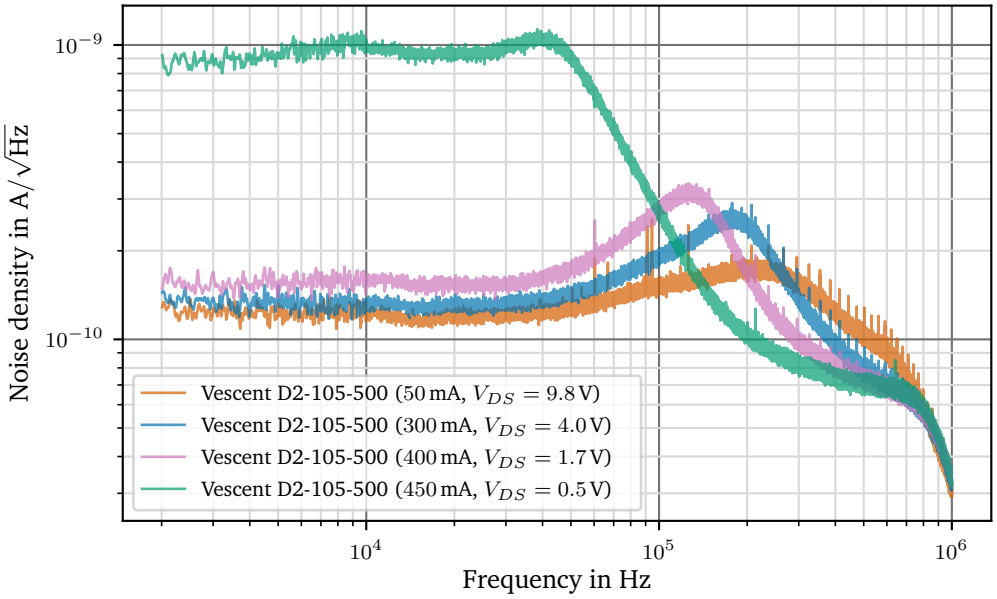

Figure 4.37.: Increasing current noise peaking as the load voltage is increased up to a total failure of regulation when V_{DS} has dropped to $0.5\,\mathrm{V}$. Measured using a $10\,\Omega$ shunt resistor.

To summarize the results of this section, it was shown that the unique architecture of the `DgDrive` combined with the ultra low noise performance ensures a predictable low noise performance of the current driver even under full load and high compliance voltage requirements. Other commercial current drivers tested had, in part, a noise floor that was orders of magnitude

higher, stability problems and severe compliance voltage issues at higher output currents. Additionally due to the excellent filtering and very high output impedance, noise in the current source output is effectively suppressed and was not measurable and well below the noise floor of the device. This was demonstrated for both $50\,\mathrm{Hz}$ mains hum and noise from a switch-mode power supply used to power the driver. The current noise is so low that the `DgDrive-500-LN` beats the shot-noise limit at currents above $20\,\mathrm{mA}$. The `DgDrive-500-LN` and the Sisyph `SMC11` are the only laser drivers to have less than $30\,\mathrm{nA_{rms}}$ noise over a bandwidth of $100\,\mathrm{kHz}$. The Sisyph `SMC11` unfortunately demonstrates strong noise peaking at $500\,\mathrm{kHz}$ that brings the driver well above the noise figure of the `DgDrive-500-LN` making the `DgDrive` the overall lowest noise laser driver available.

Figure 4.35 on page 150 along with table 4.12 can be used to judge the noise performance of the current state of the art systems commercially available. This allows intercomparison using a common basis.

Laser driver	Current noise, $10\,\mathrm{Hz}$ to $100\,\mathrm{kHz}$	Current noise, $10\,\mathrm{Hz}$ to $1\,\mathrm{MHz}$
Toptica `DCC 110`	$1.67\,\mu\mathrm{A_{rms}}$	$1.74\,\mu\mathrm{A_{rms}}$
LQO `LQprO`	$471\,\mathrm{nA_{rms}}$	$555\,\mathrm{nA_{rms}}$
Moglabs `DLC-102`	$128\,\mathrm{nA_{rms}}$	$521\,\mathrm{nA_{rms}}$
Vescent `D2-105`	$42.0\,\mathrm{nA_{rms}}$	$114\,\mathrm{nA_{rms}}$
Sisyph `SMC11`	$8.57\,\mathrm{nA_{rms}}$	$76.9\,\mathrm{nA_{rms}}$
`DgDrive-500-LN`	$19.1\,\mathrm{nA_{rms}}$	$27.7\,\mathrm{nA_{rms}}$

Table 4.12.: Integrated current noise for different bandwidths of the lasers drivers compared in figure 4.35. The table is ordered by the noise figure integrated over $10\,\mathrm{Hz}$ to $1\,\mathrm{MHz}$ in descending order.

Device Properties 4.4: DgDrive current noise performance

- Current noise density $<70\,\mathrm{pA}/\sqrt{\mathrm{Hz}}$ above $100\,\mathrm{Hz}$
- Current noise density $\leq 1.6\,\mathrm{nA}/\sqrt{\mathrm{Hz}}$ at $1\,\mathrm{Hz}$ for $I_{out} <= 0.1 I_{max}$
- Current noise density $\leq 10\,\mathrm{nA}/\sqrt{\mathrm{Hz}}$ at $1\,\mathrm{Hz}$ for $I_{out} = I_{max}$
- Current noise of $19.1\,\mathrm{nA_{rms}}$ in $10\,\mathrm{Hz}$ to $100\,\mathrm{kHz}$ bandwidth
- Output noise is independent of the compliance voltage up to $10\,\mathrm{V}$
- The noise spectrum is devoid of external noise even when using a switch-mode power supply
- `DgDrive-500-LN` is below the shot noise for $I_{out} \geq 20\,\mathrm{mA}$

4.1.11. Test Results: Temperature Stability

As it was shown in section 3.2.1, the ambient temperature can vary by as much as $2\,\mathrm{K}$ in a typical temperature stabilized environment. The laser driver must therefore be tested in a representative temperature range. The racks typically have a temperature of around $26\,^{\circ}\mathrm{C}$ when actively cooled. The laser driver was tested in a custom thermal chamber and the ambient temperature was swept several time from 20 to $30\,^{\circ}\mathrm{C}$. During the test, the output current of the driver was measured using either a $10\,\Omega$ or a $100\,\Omega$ Vishay `VPR221Z` shunt resistor, depending on the output current setting of either $50\,\mathrm{mA}$ or $510\,\mathrm{mA}$. The voltage across the resistor was measured using a Keysight `3458A`. The shunt was mounted in an aluminium housing and its temperature was monitored using a Keithley `DMM6500` and a PT100 glued to the shunt.

Repeating the test both for a low output current and additionally for the maximum output allows to discriminate between the temperature coefficient (tempco) resulting from offset drifts and voltage reference drifts because at low output values the effect of the reference voltage is scaled down. In case of the `DgDrive-500-LN` at an output current of $50\,\mathrm{mA}$ the scaling factor is $\frac{50\,\mathrm{mA}}{I_{max}} = \frac{50}{510}$, making the reference drift contribution almost negligible. In this case the op-amp offset drifts and other drifts from effects like thermal EMF dominate the temperature coefficient while effects that are proportional to the output are suppressed. At full output the voltage reference drift is fully added and also the drift of the sense resistor is more pronounced due to the higher temperature of the resistive element.

Another effect that can only be seen at full output is burst noise coming from the Zener diode used as a reference. This manifests as sudden jumps in the output current. The `DgDrive-500-LN` #14 tested uses one of the earlier revisions of the reference board that contains an affected Zener diode, which was discovered during those tests. This issue and its solution is discussed in more detail in the next section.

As it was discussed in section 4.1.5, great care was taken to reduce the offset related drift, which can be seen in figure 4.38. These efforts were rewarded with a very low temperature coefficient of $112\,\mathrm{nA/K} \equiv 0.22\,\mu\mathrm{A/(A\,K)}$ when running at $10\,\%$ output current. At a maximum current of $510\,\mathrm{mA}$ the drift of the sense resistor and the Zener diode add to the result and the temperature coefficient increases to $355\,\mathrm{nA/K} \equiv 0.70\,\mu\mathrm{A/(A\,K)}$. These results are typical values for this batch as all sense resistors are from the same batch, ordered directly from Vishay.

Other laser drivers were tested in a similar fashion if it was possible to fit them into the thermal chamber. Larger devices like the Moglabs `DLC-102` or the Vescent `D2-105` were placed in a cooling cabinet and once the current had stabilised, the door was opened to apply a step change of about $10\,\mathrm{K}$. The results are summarised in table 4.13.

Device	Tempco at $50\,\mathrm{mA}$	Tempco at full current
LQO `LQpr0`	$8.6\,\mu\mathrm{A/(A\,K)}$	–
Moglabs `D2-105`	$1.3\,\mu\mathrm{A/(A\,K)}$	–
Vescent `DLC-102`	$3.5\,\mu\mathrm{A/(A\,K)}$	–
`DgDrive-500-LN`	$0.22\,\mu\mathrm{A/(A\,K)}$	$0.70\,\mu\mathrm{A/(A\,K)}$

Table 4.13.: Tempco of several laser drivers tested. Scaled to full scale output.

The `SMC11` was also tested, but not found stable enough over time to make out a temperature coefficient against the drift and low frequency noise of the device. It is therefore not included in table 4.13. The low frequency noise encountered is shown in figure 4.40 and discussed in section 4.1.12.

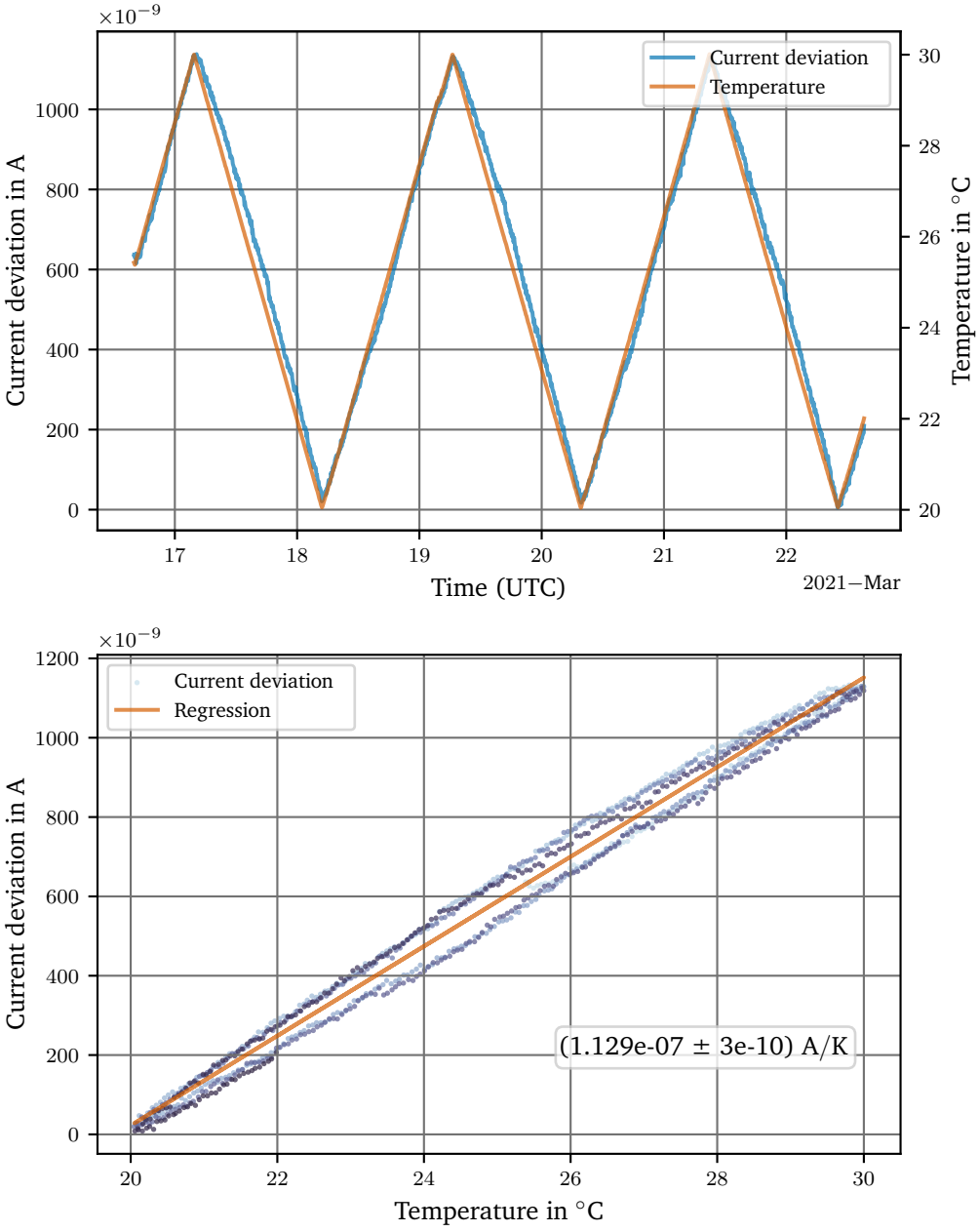

Figure 4.38.: Output current drift of a `DgDrive-500-LN` running at $50\,\mathrm{mA}$ over an ambient temperature range of 20 to $30\,^{\circ}\mathrm{C}$.

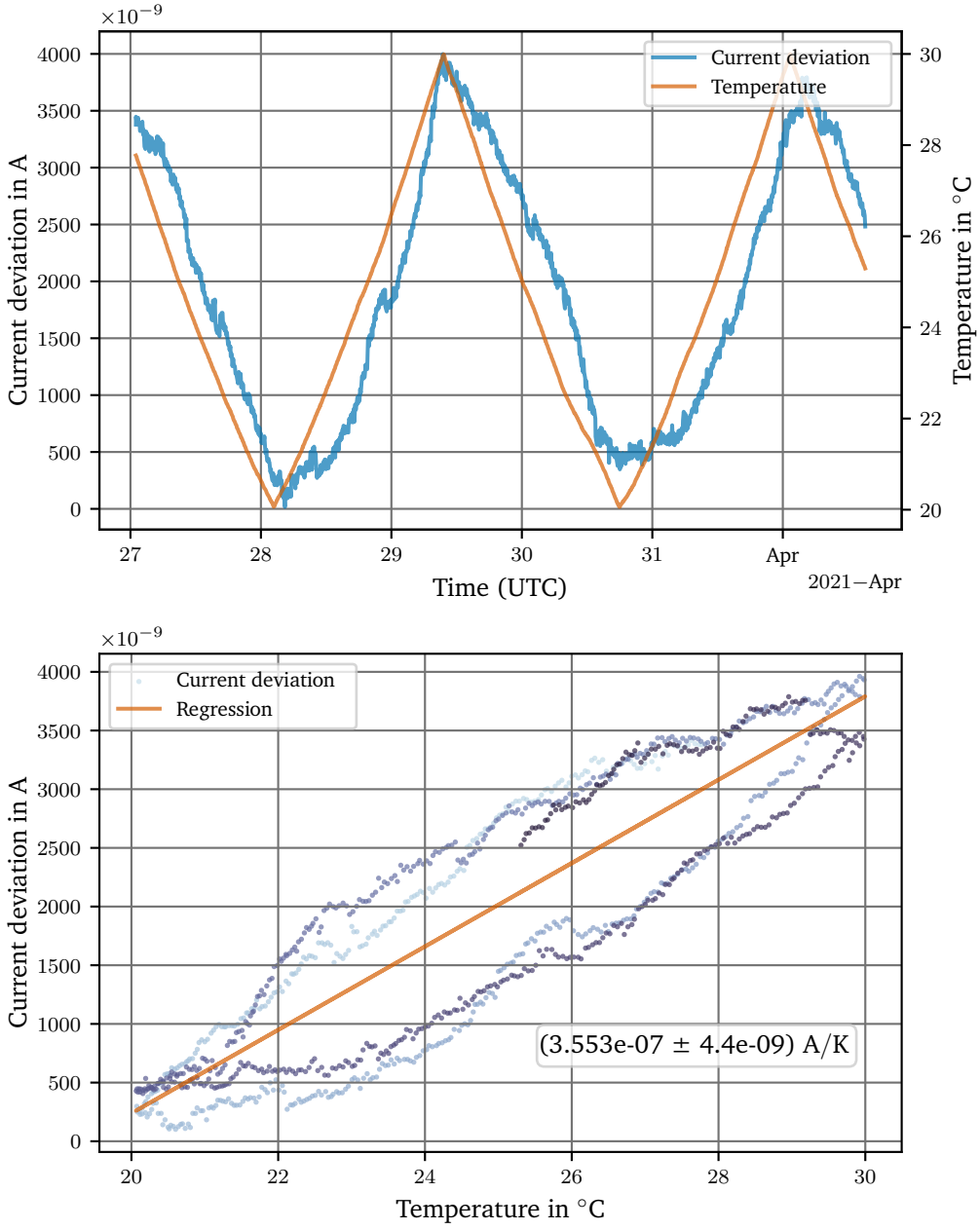

Figure 4.39.: Output current drift of a `DgDrive-500-LN` running at $510\,\mathrm{mA}$ over an ambient temperature range of 20 to $30\,^{\circ}\mathrm{C}$.

To conclude, the temperature coefficient of the DgDrive-500-LN was tested to be better than

$$0.2\,\mu A/K + 0.5\,\mu A/(A\,K) \cdot I_{out}\,. \tag{4.15}$$

This is well below the required target of $\leq 1\,\mu A/(A\,K)$ set in table 3.1. Since the tests typically take a week or more, only the most promising commercial drivers were tested. Unfortunately, no other driver was able to meet the target, although the Vescent `D2-105` came close with $1.3\,\mu A/(A\,K)$. The SISYPH `SMC11` could not be tested because it was not stable enough to allow any distinction between a temporal drift and a temperature coefficient. This topic will be discussed in the next section.

Device Properties 4.5: DgDrive temperature stability

- `DgDrive-500-LN`, $50\,mA$: $112\,nA/K \equiv 0.22\,\mu A/(A\,K)$
- `DgDrive-500-LN`, $510\,mA$: $355\,nA/K \equiv 0.70\,\mu A/(A\,K)$
- Combined temperature coefficient: $0.2\,\mu A/K + 0.5\,\mu A/(A\,K) \cdot I_{out}$

4.1.12. Test Results: Stability over Time

The stability measurements were conducted for $24\,h$ and the output current was recorded using a Keysight `34470A` DMM and a Vishay `VPR221Z` $10\,\Omega$ shunt resistor, which proved more stable than the internal shunt resistor of the `34470A`. The $10\,\Omega$ shunt voltage was recorded at the $1\,V$ range with 10 PLC and autozeroing enabled. Both the DMM and the laser driver were warmed up for $8\,h$ prior to the measurement. Ambient data of the lab, like temperature and humidity, was recorded using the LabKraken software (see section 4.2 for details of the software). The laser drivers themselves were not placed in a thermal chamber to reflect a typical use case. The lab temperature was kept within $\pm 0.5\,K$ though. All measurements were done at $50\,mA$ to align with the noise measurements in section 4.1.10. Do note, at such low currents the reference noise is strongly attenuated and therefore the burst noise of the commercial drivers cannot be judged from those measurements. This issue with the `LM399` was only discovered later and retesting of the commercial drivers was no longer possible. The burst noise issue is discussed in more detail in section 4.1.13.

All devices but one showed no obvious issues regarding the short-term stability. For reasons of brevity these measurements are not shown in detail here. The only device found unsuitable for the use in high precision spectroscopy was the Sisyph `SMC11` as it exhibited large drifts, which were in part due to the trimmer resistor used to set the output current. This was already seen in section 4.1.10 where the drift manifested itself as a large low frequency noise contribution. The effect in the time domain can be seen in figure 4.40, where the `SMC11` shows severe short-term drift issues with a varying output current of up to $1\,\mu A$ over the course of minutes. The drift after a setpoint change is not shown because the driver was warmed at the operating current before the measurement, as mentioned above, but a settling drift of up to $10\,\mu A$ were observed. This makes adjusting the driver difficult, especially if a lock to an atomic reference or a high finesse resonator is desired. Regarding the blue spectroscopy laser system for the ARTEMIS experiment with a stability margin of only few tens of µA as discussed in section 3.2.1, this behaviour renders the driver incompatible with the experimental setup. For comparison the output of the `DgDrive-500-LN` over the same time frame and transposed by $-2\,\mu A$ is shown

in figure 4.40 as well. This highlights the enormous low frequency noise component present in the Sisyph SMC11.

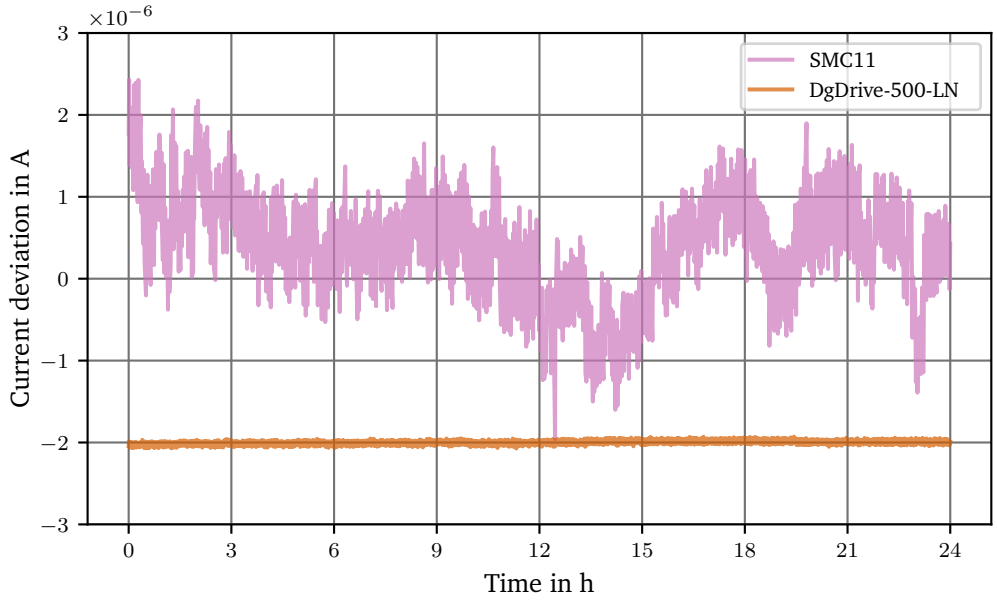

Figure 4.40.: Output current stability of the SMC11 at 50 mA over the course of 24 h. For reference the output of the DgDrive-500-LN is also shown.

The performance of the DgDrive-500-LN is again shown in figure 4.41 in full. No discernible drift over the 24 h period can be made out from figure 4.41 as the data is entirely obscured by the measurement uncertainty and noise of the 34470A DMM.

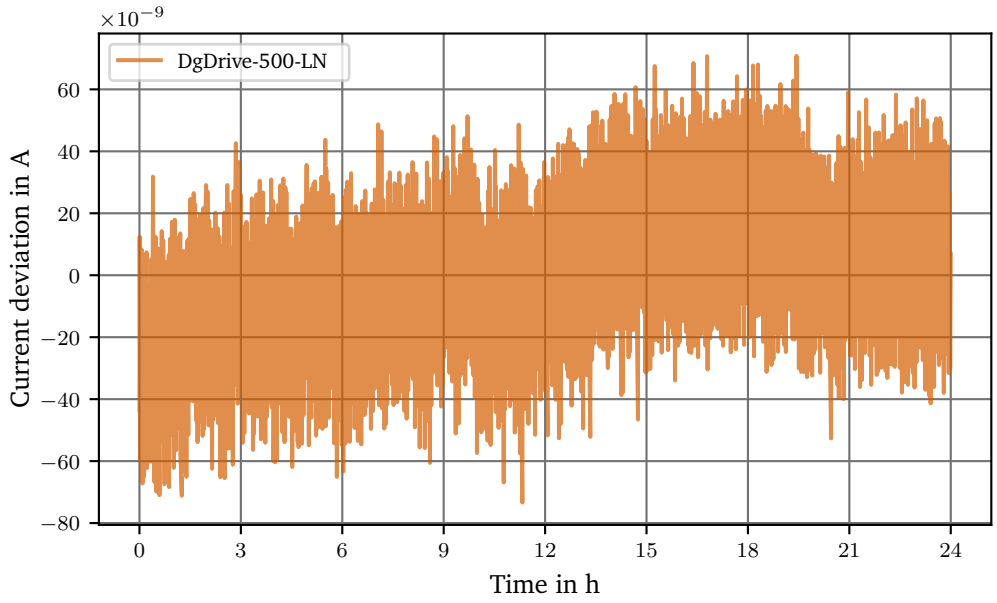

Figure 4.41.: Output current stability of the DgDrive-500-LN at 50 mA over the course of 24 h.

The 2-σ uncertainty of the `34470A` DMM [70] with these measurement settings is $10\,\mu A/A + 0.4\,\mu A = 0.9\,\mu A$, not including the shunt resistor, which renders a discussion about the apparent drift of $30\,nA$ seen in figure 4.41 questionable.

To get a more definitive answer on the actual drift, the measurement should be repeated with a lower noise and more stable multimeter like the `3458A` or, alternatively, a differential measurement between the shunt voltage and the Fluke `5440B` calibrator can be carried out. Nonetheless, an upper bound of less than $50\,nA/d$ can be given. Regarding the long-term drift, the annual calibration of the laser drivers currently in use can be evaluated. The first batch of laser drivers, which has been in use for more than one year was measured against a freshly calibrated `3458A` and a drift of $<(1 \pm 2)\,\mu A/A/a$ was found. This surpasses the requirements put up by the specification of $240\,\mu A/A/30d$ given in table 3.1 on page 19 by a far margin.

Device Properties 4.6: DgDrive stability over time

- Short-term drift: $<(0.1 \pm 2.0)\,\mu A/(A\,d)$
- Long-term drift: $<(1 \pm 2)\,\mu A/A/a$

4.1.13. Zener Diode Selection

As hinted in section 4.1.11, early temperature stability tests of the laser driver with an ADI `LM399` Zener diode as a voltage reference confirmed what the data sheet of the Zener diode [133] already suggest in the *Low Frequency Noise Voltage* plot. There are random bi-stable voltage step changes. This phenomenon is called burst noise or popcorn noise. The theoretical model to describe it is discussed in more detail in section 3.6.1 on page 48.

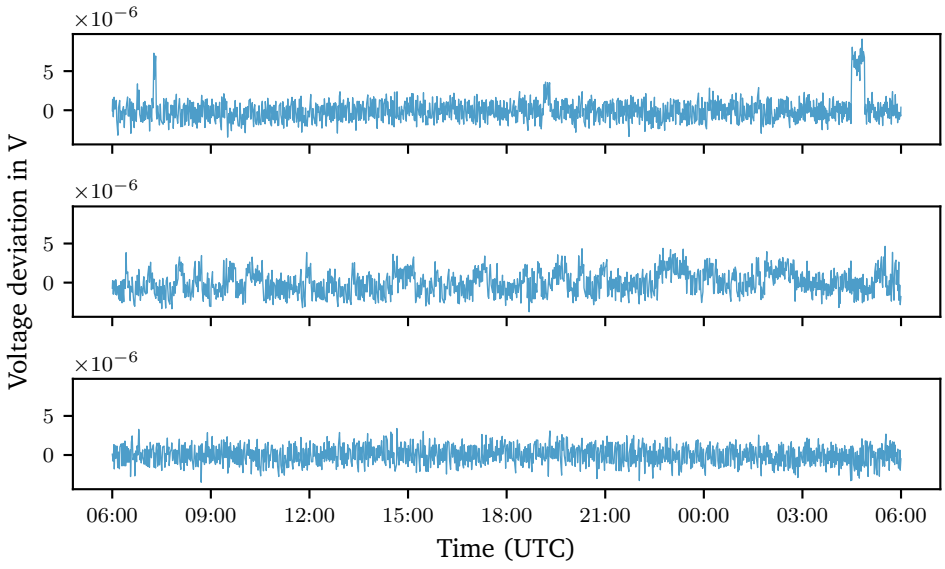

Figure 4.42.: Popcorn noise in different samples of the `LM399` over a $24\,h$ period as recorded by the scanner system using a Keithley `Model 2002` as discussed in this section.

Figure 4.42 shows two samples of the `LM399` that exhibit popcorn noise, while the last one does not.

The origins of popcorn noise in semiconductor devices are not yet fully understood, but some sources have been identified. Defects in the semiconductor crystal lattice and contamination of the semiconductor material have been linked to burst noise [111]. This problem has improved over the years as manufacturing processes and wafer quality has evolved. Unfortunately the LM399 is built around a process from 1991, as can be seen etched into the silicon die [110].

The popcorn noise caused by defects and contamination can be reduced by lowering the strain on the lattice and removing surface contaminants on the die. This can be achieved using a high-temperature burn-in process. Manufacturers like Fluke and Keysight use similar techniques in their products. Fluke, for example, uses a $60\,\mathrm{d}$ burn-in period for the Zener references used in their secondary voltage standards [181].

Fortunately, the LM399 is a heated reference, which heats itself to $90\,^{\circ}\mathrm{C}$ when turned on, so it is only required to install the Zener diodes in a simple test circuit to apply a burn-in procedure. The use of a separate test setup instead of the final circuit has both advantages and disadvantages. The disadvantage is that the Zener diode will be subjected to mechanical stress after burn-in when soldered into the final PCB. This stress will, of course, not be removed by the burn-in process but this mainly affects the voltage drift properties of the Zener diode and not the popcorn noise. The drift of the diode is only of secondary concern for the laser current driver as the output drift is mainly caused by the drift of the reference resistors, which is typically one order of magnitude higher than the drift of the Zener diode judging from the data sheet [133, 237].

The advantage of testing the Zener diodes separately, on the other hand, is that more diodes can be tested simultaneously using a compact test fixture. It is also simpler to remove and replace unsuitable Zener diodes from a test fixture because sockets instead of solder joints like in the final circuit can be used. Building such a burn-in test setup for multiple Zener diodes is detailed in the next sections.

4.1.14. Building a Test Setup for Zener Diodes

There are several ways to measure the popcorn noise of semiconductor devices. The most trivial one is to directly monitor the device in the time-domain. In this case, the Zener voltage can be measured with a long-scale multimeter. This requires a low noise DMM that can reliably distinguish between both voltage levels, which are about $4\,\mu\mathrm{V}$ apart.

A related option is to use a second reference whose voltage is close in value to the device under test (DUT). Measuring only the voltage difference between the two references, a lower resolution is required. Comparing the difference of two references using a millivolt meter is, for example, commonly applied for intercomparing primary voltage references. This method, however, increases the measurement noise by a factor of $\sqrt{2}$ assuming both references produce the same amount of uncorrelated noise. The noise of the LM399 measured with a $100\,\mathrm{PLC}$ integration time ($2\,\mathrm{s}$) is about $1.5\,\mu\mathrm{V_{pp}}$ as can be determined from the data in figure 4.42. Measuring the voltage difference between two references would then result in around $2.1\,\mu\mathrm{V}$ of noise. This makes distinguishing the two voltage levels possible, but challenging.

A third option is to use a high-pass filter and an amplifier. Additionally, the signal can be low-pass filtered to remove any excess high frequency noise. This approach also requires a lower resolution than directly measuring the Zener voltage because the signal-to-noise-ratio can be improved with the amplifier. It is therefore possible to use an off-the-shelf analog-to-digital converter (ADC). One such circuit, along with some examples, is demonstrated in [111, 112]. It must be noted, that due to the high-pass filtering, it not possible to evaluate voltage drifts of the Zener diode using this method.

The fourth and final option discussed here is to approach the problem in the frequency domain and requires a low-noise amplifier with a low frequency cutoff. As discussed in section 3.6.1, popcorn noise is found to have a frequency dependence of $1/f^2$. This property can be used to distinguish it from other random noise processes that show a frequency dependence of $1/f$. A good example of an op-amp that has excessive burst noise in comparison to a good sample is given in *The Art of Electronics* [96, p. 478]. Evaluating the frequency spectrum below $10\,\mathrm{Hz}$ allows to sort the references by their noise spectrum.

Considering these four options, one can see that going from the first to the last option, the test setup becomes simpler and the requirements for the data acquisition front end are more relaxed because either the common mode voltage is reduced or more filtering is applied. On the other hand, the interpretation of the measurement results becomes more challenging and requires more knowledge beforehand. For example, comparing the voltage difference between two references, a known good sample is required to reliably determine the presence of burst noise in the DUT. The other two options also require a baseline to compare samples to. At the start of the evaluation, most of the data available about the `LM399` came from the data sheet. Compiling a reference dataset with the performance of dozens of `LM399` was considered too expensive and time consuming. The only measurement schemes explored further is therefore the first option. The focus of the next sections lies on the selection of a scanner system and a digital long-scale multimeter to satisfy the requirements for testing multiple `LM399` Zener diodes simultaneously.

4.1.15. Choosing a Multimeter for Testing Zener Diodes

The DMM used plays an important role for the test setup as it mostly defines the signal to noise ratio and the measurement speed. In this section, some of the challenges that can be encountered when selecting a multimeter will be discussed. The expected amplitude of the popcorn noise produced by the `LM399` Zener diode is around $0.5\,\mu\mathrm{V/V}$ or $3.5\,\mu\mathrm{V}$ of the output voltage when considering the $7\,\mathrm{V}$ Zener voltage of the `LM399`. Those $7\,\mathrm{V}$ will typically be measured on the $10\,\mathrm{V}$ range of a DMM, which is not a trivial task, because a signal-to-noise-ratio of $0.35\,\mu\mathrm{V/V}$ or more than $130\,\mathrm{dB}$ is required. This calls for an instrument that not only has the required resolution, but also the stability over time and temperature to ensure the measurement will not be distorted by the DMM. A voltmeter with lower noise and a more stable reference than the DUT is therefore mandatory. This only leaves the class of very low noise 7.5 or 8.5 digit multimeters. These multimeters come with a different type of voltage reference, because the `LM399` is not suitable for such instruments due to its noise. The only Zener diodes that meet those requirements are the ADI `LTZ1000` [143], the Motorola `SZA263` (out of production) and the Linear Technology (LT) `LTFLU-1`, a proprietary design by Fluke and LT. The `LTZ1000`, for example, is specified for a typical noise of $1.2\,\mu\mathrm{V_{pp}}$ in a frequency range of $0.1\,\mathrm{Hz}$–$10\,\mathrm{Hz}$ [143] as opposed to $4\,\mu\mathrm{V_{pp}}$ of the `LM399`. Additionally, in comparison to the `LM399` those high performance Zener diodes do not suffer from popcorn noise issues to this extend.

Comparing only 7.5 and 8.5 digit voltmeters narrows down the choice of multimeters considerably. The market for high-end 8.5 digit DMMs is limited and every device on the market caters for a certain niche. It is therefore prudent to look at the individual specifications to choose the correct instrument for this purpose. Table 4.14 contains a list of popular 8.5 DMMs that were considered for this application. Several models included in the table are already discontinued but those DMMs can still be acquired on the second-hand market. While the author has not tested every multimeter in table 4.14, it is possible to judge most of them a priori by their

specifications. A quick overview will be given next to limit the options presented in table 4.14 to the most promising devices. In order to reach a high throughput of tested LM399 the DMM must deliver fast reading speeds, ideally multiple samples per second including autozeroing, combined with a low input noise to distinguish the burst noise voltage levels. This already rules out many DMMs in table 4.14.

Manufacturer	Model	Remarks
Advantest	R6581	Discontinued. Scanner cards available.
ADCMT	7481	In production.
Datron/Wavetek	1812	Discontinued. Wavetek was bought by Fluke.
Fluke	8508A	Discontinued. 20 V range. Slow.
Fluke	8588A	In production.
Keithley/Tektronix	2002	In production. Scanner card available. 20 V range.
Keysight	3458A	In Production.
Solartron	7081	Discontinued. Slow.
Transmille	8104	In Production. External scanner available. Slow.

Table 4.14.: Overview of 8.5 digit multimeters. The discontinued models listed were still available on the second-hand market at the time of writing.

The instruments considered unsuitable due to their conversion speed are the Solartron 7081 (also sold as a Guildline 9578), the Fluke 8508A, the Wavetek 1812 and the Transmille 8104. The Solartron 7081 takes 52 s for a measurement with 8.5 digits of resolution. Both the Fluke 8508A and the Wavetek 1812, which are very similar devices because Fluke bought Wavetek in 2000, are fairly slow, taking 25 s for a conversion at 8.5 digits. The 8104 takes 4 s for each conversion using its fastest setting [4], not including autozeroing. The ADCMT 7481 is made by the Japanese company ADC Corporation, which split off from Advantest in 2003. Both the Advantest R6581 and ADCMT 7481 are hard to come by in Europe as there are no official distributors available. These instruments were therefore not considered for this setup.

Having removed slow and unavailable instruments from the list leaves only a few devices for the test setup. The Fluke 8588A, the Keysight 3458A, and the Keithley Model 2002. The Fluke 8588A excels at stability and features a modern user interface whereas the Keysight 3458A is unbeaten in linearity and noise. A detailed comparison of those two meters can be found in the work of Lapuh et al. [123]. The Keithley Model 2002 focuses on its scanning capability. To narrow down the list even further, several 7.5 and 8.5 digit multimeters were tested. The results of those tests will be discussed here to give an impression of the performance of these devices. The tested multimeters are the Keysight 3458A, the Keithley Model 2002, a Keysight 34470A and a Keithley DMM6500. The 3458A was selected because of its low noise and the Model 2002 was chosen for its internal scanning unit. The 34470A was picked as a lower-end and cheaper alternative to see if such an instrument could be used as well. Finally the DMM6500 is on the list to give an impression of an instrument that uses an LM399 voltage reference instead of the superior LTZ1000 used in the other multimeters.

Two tests were carried out to assess both the ADC noise and the stability of the DMM. The noise is mostly determined by the front end amplifier and the ADC including the autozeroing algorithm as discussed in section 3.7. This test is implemented by taking measurements with a shorted input. The stability of a DMM, on the other hand, is determined by the reference voltage and the stability of the front end amplifier gain and can only be evaluated with a

known stable test signal. The second test was therefore run against a Fluke 5440B calibrator that supplied 10 V to all multimeters and readings were taken over the course of a week. This data was used to estimate the stability of the multimeters and to reveal any burst noise coming from the multimeter reference. The noise of a DMM at 10 V is typically not found in the datasheet and the performance is usually quoted for shorted inputs, which does not include the internal reference noise, in order to benchmark the ADC. The test was done at 10 V instead of the expected 7 V of the LM399, because 10 V is a more common value since primary voltage standards use this value. Using this voltage allows better intercomparison and promotes a broader application of the results. The calibrator has a specified output noise of <1.5 µV within a bandwidth of 0.1 Hz–10 Hz at 1 V and is stable to within 5 μV_{rms} over 30 d, a specification far superior to the LM399.

The test was conducted in a stable lab environment with a temperature deviation of at most $\Delta T = \pm 0.5$ K. All multimeters were connected to the same calibrator output. Although this might potentially cause interference between the multimeters due to the pump out current spikes caused by the switching intervals, no ill effects, like voltage offsets or increased noise, were observed during the tests. A more detailed discussion of the pump out current with a focus on the 3458A can be found in [183]. All instruments under test were connected using shielded cables, either Pomona 1167-60 or self-made cables with gold-plated copper spades crimped to twisted and shielded M27500A 18WJ4T24 PTFE insulated cables. The GUARD terminal of the calibrator was connected to the chassis GROUND at the calibrator and then connected to the cable shields. On the 3458A, the shield was connected to the GUARD terminal and the GUARD switch was set to open according to the manual [114]. For the other multimeters that do not have a GUARD terminal, the shield was left floating at the DMM side. Finally, the autocalibration routine of the Fluke 5440B calibrator, the 3458A and the 34470A was run prior to the measurement. The detailed settings used for the DMMs can be found in appendix A.1 on page 215, a summary is given in table 4.15 to show the important differences.

DMM	Integration time in PLC
HP 3458A	100
Keithley Model 2002	40
Keysight 34470A	100
Keithley DMM6500	90

Table 4.15.: ADC conversion speeds of the tested DMMs configured to give a total measurement time of 2 s. More details on the configuration can be found in appendix A.1 on page 215.

All DMMs were configured for the same total acquisition time of 2 s. Depending on the ADC conversion speed, this leads to different integration times that are given in power line cycles (PLC) at 50 Hz. The Keithley Model 2002 takes considerably longer for a measurement than the Keysight multimeters. The reason is the autozero function, which is shown in figure 3.27 on page 60. Recounting section 3.7, the Model 2002 does three steps when doing autozeroing as opposed to the two step autozeroing of the Keysight multimeters. It measures the signal, the zero point for an offset compensation and also the reference voltage to apply a gain correction. In comparison, the 3458A only corrects for the offset drift during the autozero cycle. A gain correction is only applied when using the autocalibration routine as was done at the start of the test. The autozero routine of the Model 2002 therefore takes longer but proves more stable

for long-term measurements.

A short 28 h excerpt of the measurement is shown in figure 4.43 because it captures the distinct properties of each multimeter very well and can be used for a qualitative discussion. More precise conclusions can only be drawn from the Allan deviation introduced in section 3.6.

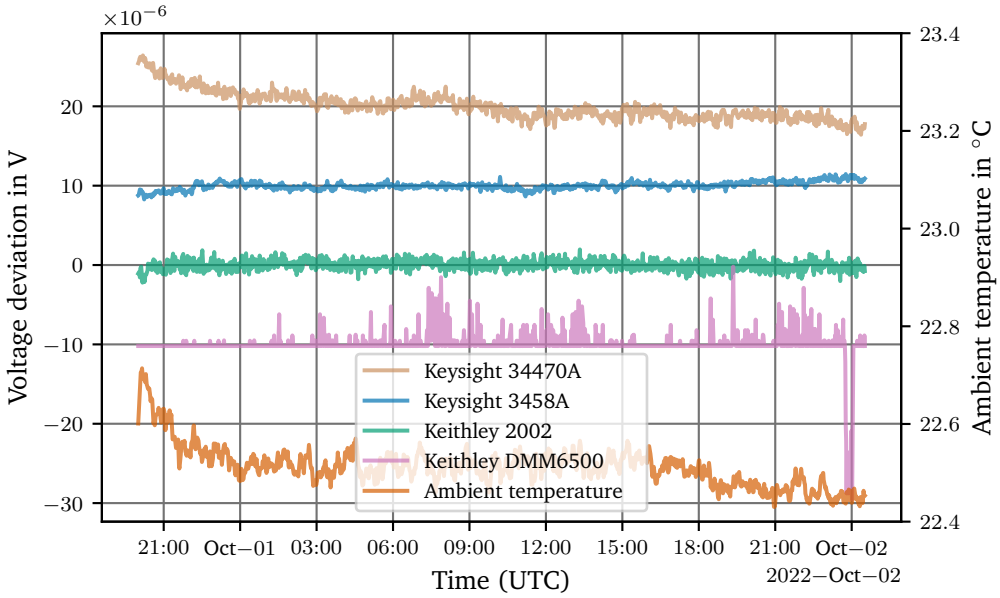

Figure 4.43.: Comparison of several DMMs measuring the 10 V output of a Fluke 5400B for 28 h. The traces are spaced 10 µV apart.

From the data shown in figure 4.43 several conclusions can already be drawn. Looking at the DMM6500, the 6.5 digit multimeter, two things that are immediately apparent are the limited resolution and towards the end of the measurement series there is an indisputable burst noise event. The latter aspect alone disqualifies the instrument for this task but nicely demonstrates the intricate matter of selecting the correct multimeter for the task. The magnitude of the burst noise event depends on the internal scaling of the reference voltage and in this case is very pronounced in comparison to the samples shown in figure 4.42 on page 161. The 34470A fared better in terms of resolution but there is either temperature instability or drift visible. Its short-term noise is slightly lower than the noise seen from the Model 2002. The Keithley Model 2002 demonstrates the most stable behaviour of all DMMs tested due to the more robust autozeroing. These first impressions can be quantified in numbers using the Allan deviation. The Allan deviation of the measurement series was calculated using the *AllanTools* Python library [238]. The algorithm chosen to estimate the Allan deviation was the Total deviation. This is a modified version of the Allan deviation estimator and extends the idea by appending the same dataset to the original record and thereby extracting more useful information from otherwise unused samples [97, 98]. This better suppresses end-of-data errors which are discussed in section 3.6. The 10 V dataset of the measurement against the calibrator is discussed first and shown in figure 4.44. This test can be used to estimate the long-term stability of the DMM, mostly affected by the ADC gain and the internal reference. The former is greatly affected by ambient temperature changes. Do note, that the measurement at 10 V instead of 7 V, which is the actual Zener voltage of the LM399 to be measured by the scanner

system, overestimates the noise figure of the Model 2002 due to the gain correction part of the autozero algorithm. The gain correction adds an additional scaled part of the ADC noise to the measurement as shown in section 3.7.2 on page 68. This noise contribution is only relevant at small values of τ, because the ADC noise contribution, which is mostly white after applying the autozeroing, quickly drops due to the averaging at longer ADC integration times as demonstrated in section 3.7.1.

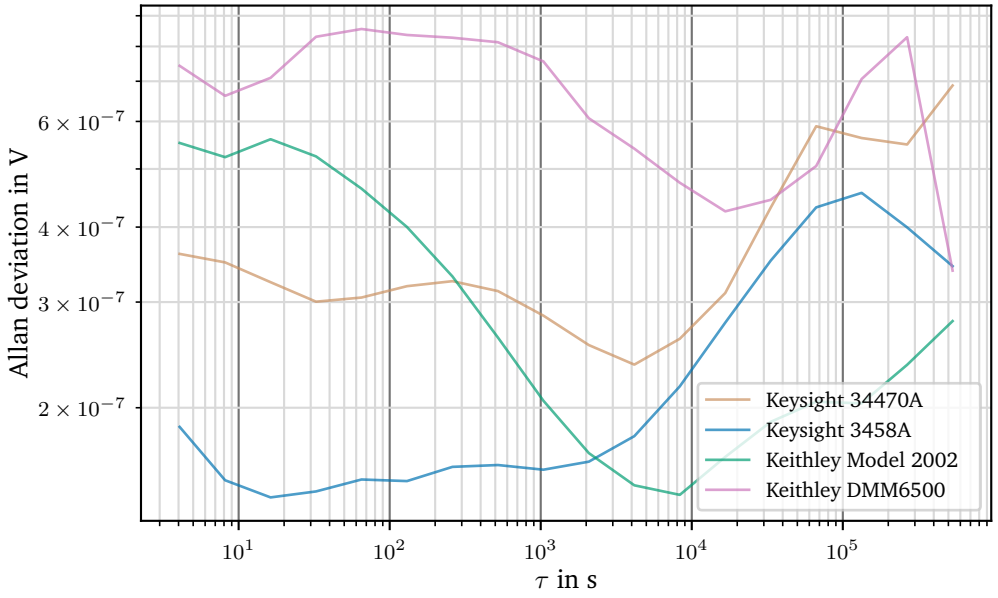

Figure 4.44.: Allan deviation of several DMMs measuring the $10\,\mathrm{V}$ output of a Fluke 5440B calibrator. The Allan deviation was estimated using the Total deviation.

The Allan deviation shown in figure 4.44 confirms what has already been found from figure 4.43. To put the numbers of figure 4.44 into perspective, the burst noise of the LM399 to be measured is expected to be around $3.5\,\mu\mathrm{V}$. The uncertainty of the measurement should be at least one order of magnitude lower to guarantee a good signal to noise ratio. Both the Keysight 34470A and the 3458A can deliver this performance at short integration times τ. The Allan deviation of all DMMs but the Model 2002 is similar in shape. Comparing with table 3.6 on page 46, the flat τ^0 part of the Allan deviation can be attributed to the flicker noise content caused by the DMM reference circuit and the front end gain as any offset drift is removed by the autozeroing. The Model 2002 starts at a higher noise floor with an Allan deviation of $5.5\,\mu\mathrm{V}$ and needs an integration time of $200\,\mathrm{s}$ to reach the desired $3.5\,\mu\mathrm{V}$ uncertainty. At longer integration times the superior stability of the Model 2002, due to the automatic gain correction, shows. At $2000\,\mathrm{s}$ ($0.5\,\mathrm{h}$) the noise performance is on par with the 3458A, which is renowned for its low noise ADC. At this time scale temperature effects play a dominant role which can be seen from the data of all other multimeters because the Allan deviation starts increasing at around $\tau = 2000\,\mathrm{s}$. Above $10^5\,\mathrm{s}$ ($24\,\mathrm{h}$) the plot shows the typical oscillations from the end-of-data errors as explained in section 3.6. The decreasing Allan deviation observed for some multimeters is a clear indicator.

Overall, the measurement shows that all DMMs but the 6.5 digit multimeter can be used for the scanner system although the higher noise of the Model 2002 makes detecting the burst noise more difficult on short time scales. Going to longer time scales the superior stability of

the `Model 2002` allows to clearly observe the initial drift of the Zener diodes which happens on timescales of a few days. The Allan deviation of the DMMs with shorted input reveals the performance of the ADC without the internal reference and gives even more insight into the instruments. This is shown in figure 4.45.

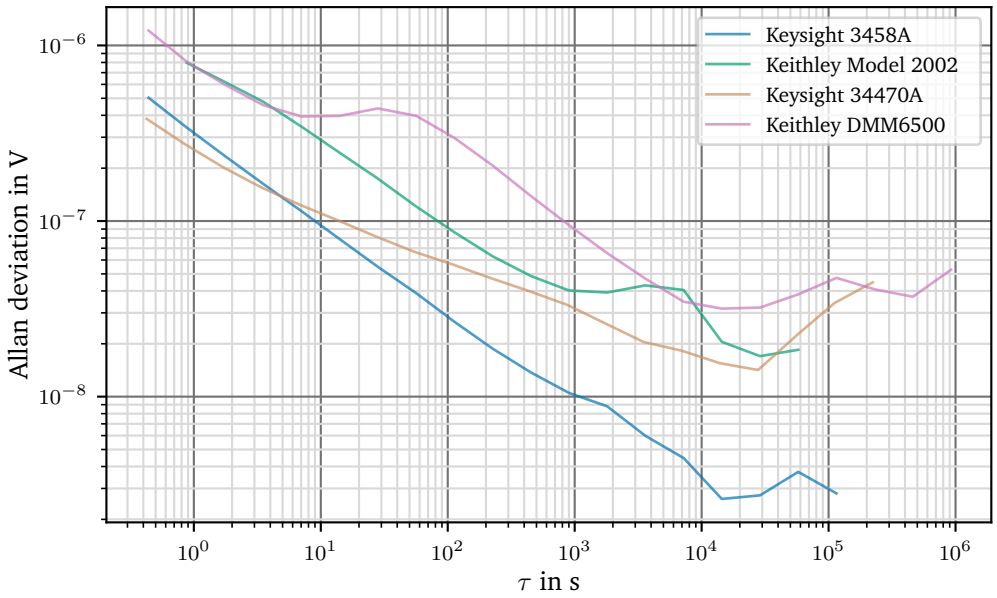

Figure 4.45.: Allan deviation of several DMMs with shorted inputs. The Allan deviation was estimated using the Total deviation.

Without the internal reference and the ADC front end drift the performance of the ADC can be evaluated and different noise types, according to table 3.6 on page 46, can be identified. The Allan deviation of the Keysight `3458A` is in good agreement with the simulated Allan deviation shown in figure 3.30 on page 62. Up to $\tau = 10^4\,\mathrm{s}$ a $\tau^{-\frac{1}{2}}$ dependence can be seen, indicating only white noise. The noise limit is around $2\,\mathrm{nV_{rms}}$ or $0.2\,\mathrm{nV_{rms}/V}$ which is the resolution limit of the ADC. The curve progression matches the theoretical limit and represents the high performance of the ADC implemented in the `3458A`.

The behaviour of the `Model 2002` is similar although there is a notable plateau between $\tau = 10^3\,\mathrm{s}$ and $\tau = 10^4\,\mathrm{s}$. This can be seen with all Keithley multimeters and is also present in the noise of the `DMM6500` albeit at a different integration time. The cause of this is likely to be found in the software of the multimeter. Keithley is using more parameters than just the offset voltage for the autozeroing algorithm. Due to the proprietary nature of the firmware an exact cause for the issue cannot be given. At longer intervals the curve seems to keep following a $\tau^{-\frac{1}{2}}$ dependency but due to end-of-data error this cannot be confirmed with low uncertainty. A longer measurement series would be required.

For the `34470A`, Keysight seems to also deviate from the classic autozeroing procedure. Although the ADC delivers very good noise performance at high frequencies and low τ. Going to higher τ, the instrument seem to follow a $\tau^{-\frac{1}{2}}$ dependency indicating some correlation between the samples, which should not be present after autozeroing. The nature of this effect is again hidden in the proprietary firmware. At long intervals this behaviour becomes a serious problem and therefore limits the use of the instrument to monitor long-term drifts over days

like the initial drift of the LM399 Zener diodes.

The Allan deviation shows that for a Zener diode test setup an 8.5 digit multimeter is recommended, yet a low noise DMM like the 34470A can be used, but only limited statements about the stability of the Zener diode can be made in this case due to the increased drift of the instrument. If cost is the driving factor of the setup such a multimeter can be considered, but an 8.5 digit instrument is recommended. A 6.5 digit multimeter was shown to be inadequate both from the perspective of the ADC performance and the burst noise of the internal voltage reference. The next section discusses the second part of the scanner system, namely the multiplexer used to test several Zener diodes simultaneously to increase the throughput of the DMM.

4.1.16. A Scanner System for Testing Zener Diodes

In order to test large amounts of Zener diodes, and considering the duration of the burn-in process, which can take anything between 100 to 1000 h, it is necessary to have an automated setup that can monitor multiple Zener diodes simultaneously. A minimum of at least 10 diodes should be tested at the same time. Such a setup consists of a digital multimeter as discussed in the last section, a scanner and test board that holds the Zener diodes and provides the necessary infrastructure for the diodes. Several commercial scanner options currently available were considered for this project and are shown in table 4.16.

	Keysight		Keithley			Fluke	Rigol
	DAQ973A	34980A	DAQ6510	2750	3706	2680	M300
DMM	6.5	6.5	6.5	6.5	7.5	18 bit	6.5
Channels	3x20	8x40	2x10	5x20	6x60	6x20	5x32
Solid-state	✓	✓	✓	✓	✓	✗	✗
Voltage	120 V	80 V	60 V	60 V	200 V	75 V	300 V
Scanner card	DAQM900A	34925A	7710	7710	3724	2680A-PAI	MC3132
USB	✓	✓	✓	✗	✓	✗	✓
Ethernet	✓	✓	✓	✗	✓	✓	✓
GPIB	✓	✓	✓	✓	✓	✗	✓

Table 4.16.: Overview of scanner mainframes commercially available in 2023. Features like integrated DMMs, the number of channels, the maximum voltage, solid-state relays and connectivity options are shown.

A recent trend to more compact devices has led major manufacturers to include multimeters in the scanner mainframe creating so called data acquisition units. Legacy devices, that only have switching capabilities are no longer available. For example Keithley replaced the small desktop switch mainframe Model 7001 with the DAQ6510 and Keysight is offering the DAQ973A, a scanning 6.5 digit DMM that accepts extension cards. Unfortunately, for this project, as discussed above, an integrated 6.5 digit multimeter does not add any value.

The scanner card used to multiplex the DMM does have to meet several specifications. The most important aspects are the number of channels and the lifetime of the relays. Other factors shown in figure 4.46, such as channel to channel isolation, the contact potential, resistance and

maximum voltage are not the limiting factors for this setup, because the voltage is low, there is no AC component involved and the the typical input impedance of high-end multimeters is far more than 100 GΩ [5, 127, 164, 183]. The lifetime of the scanner card can be greatly increased by using solid-state relays instead of mechanical relays. The number of actuations required for testing the expected 100 Zener diodes will be discussed in more detail below using a commercial scanner card as an example.

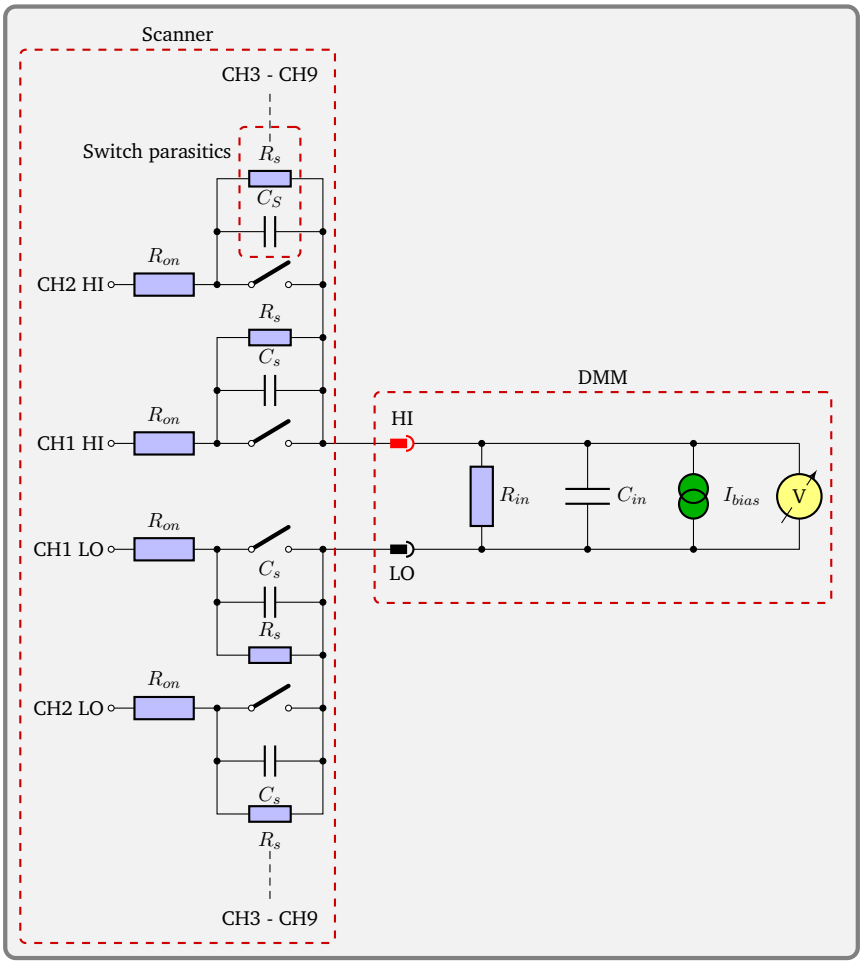

Figure 4.46.: Simplified schematic of the scanner front-end with parasitic elements.

Given the prospect that all scanner mainframes currently on the market include a multimeter that is not going to be used, but has to be paid for nonetheless, additional options were explored. The simplest solution found was to go with an 8.5 digit multimeter that already includes a scanner option like the Keithley `Model 2002` or buy a used Keithley `Model 7001` from a second-hand dealer to use with the `3458A`. The author tested both options and the simplicity and space saving of only having a single device to connect and program makes the integrated scanner card of the `Model 2002` very attractive.

For this work the Keithley (now Tektronix) `Model 2002` was chosen for three reasons. It is a very compact system requiring only a half-sized 2U rack in comparison to other 8.5 digit DMMs that are typically full-sized 2U rack devices. The other two advantages are the integrated scanner card slot that allows to fit a 10 channel scanner card and finally the 20 V measurement range. The latter is interesting for testing the final voltage reference boards, as these have a

15 V output.

The standard scanner card that comes with the Model 2002 is the Model 2000-SCAN card. These cards have a number of 2-pole relays mounted to them as shown in figure 4.46 which have an expected lifetime of 10^5 to 10^8 actuations. Considering 3 actuations per minute and a measurement interval of 1000 h per batch and 10 batches for a total of 100 Zener diodes results in 10^6 actuations. This could lead to premature failure of the test setup and unfortunately, there is no alternative scanner card available that has solid-state relays. To solve this issue, a solid-state scanner card replacement was developed by the author. This card fits into the standard slot and uses the same connector as the original card which is shown in figure 4.47. The replacement card is recognized as a Model 2000-SCAN card and can be used as a direct substitute.

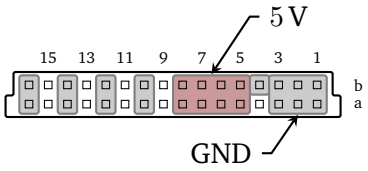

Figure 4.47.: The DIN 41612 32 pin extension connector used in several Keithley multimeters.

Pin	Function	Pin	Function
a1, b1	GND	a9, b9	$\overline{\text{NRST}}$
a2, b2	GND	a10, b10	GND
a3, b3	GND	a11, b11	STROBE/LATCH
a4	GND	a12, b12	GND
b4	ID, connect to 5 V or DATA	a13, b13	CLOCK
a5, b5	5 V supply	a14, b14	GND
a6, b6	5 V supply	a15, b15	DATA
a7, b7	5 V supply	a16, b16	GND
a8, b8	5 V supply		

Table 4.17.: Pin layout of the backplane connector, shown in figure 4.47 used for scanner cards by the Keithley Model 2002.

The replacement scanner card is based on an ICE40HX1K FPGA and its design files are available open-source at [34]. This scanner card can either be equipped with 10 channels or 20 channels. The Model 2002 only supports 10 channels, while newer Tektronix multimeters like the DMM6500 support up to 20 channels. The multimeter backplane connector is the same for both versions of the card, yet the communication protocol is different. Both protocols were implemented on the FPGA and are selectable by the user via a solder bridge during assembly of the PCB, but this solder bridge can also be changed later to convert a 20 channel card into a 10 channel card if the need arises. This is one of the reasons for using an FPGA instead of the simpler shift registers used by the original Model 2000-SCAN. An attempt was also made using a microcontroller, but the legacy protocol used by the Model 2002 does not work well with an 8 bit aligned microcontroller. There are other controllers apart from the scanner controller talking on the bus as well and both controllers have different packet sizes (and clock rates). The scanner card expects a 24 bit command from the DMM clocked in via the CLOCK and DATA

lines. Once the command is done, the STROBE pin is used to push the command to the relays via a shift register. The shift register makes sure that only the final 24 bit before the STROBE signal are registered as a command. Any data sent before those 24 bit gets dropped. As said above the other device on bus has a different, slower, clock rate and sometimes one or two bit are sent in between the 24 bit commands of the scanner card. This poses a problem for a typical microcontroller. Most microcontroller are byte aligned and any number of bits, that is not a multiple of 8, which is sent before the 24 bit command breaks the alignment. In addition, the high data rate of the scanner controller clocking at 2 MHz made sampling the signal in software impossible. An FPGA can easily mimic the shift register and also decode the more modern protocol of the `DMM6500`. More details on both protocols can be found with the design files of the scanner card at [34]. A picture of the finished board is shown in figure 4.48.

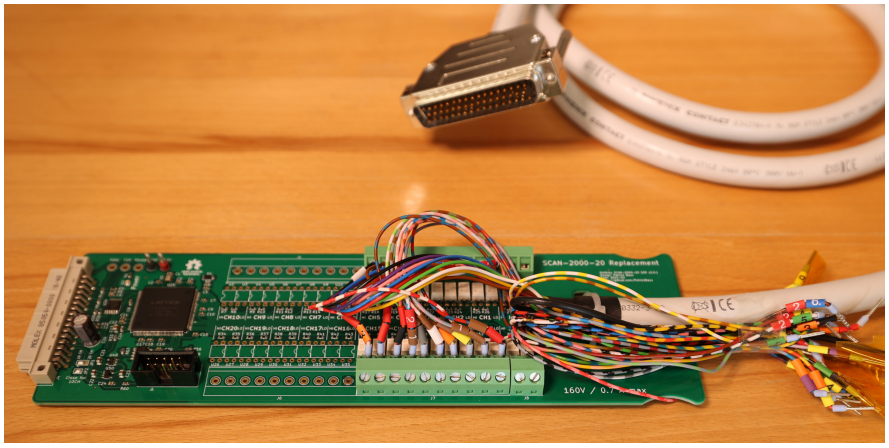

Figure 4.48.: A 10 channel solid-state scanner module developed for the Keithley `Model 2002` including the connector for the reference PCB.

With a scanner and multimeter selected, the focus now lies on the test fixture for the Zener diode. This test setup consists of a mounting PCB, that holds up to 20 Zener diodes [40]. It provides power regulation and a minimal circuit required to support each diode. This circuit is shown in figure 4.49.

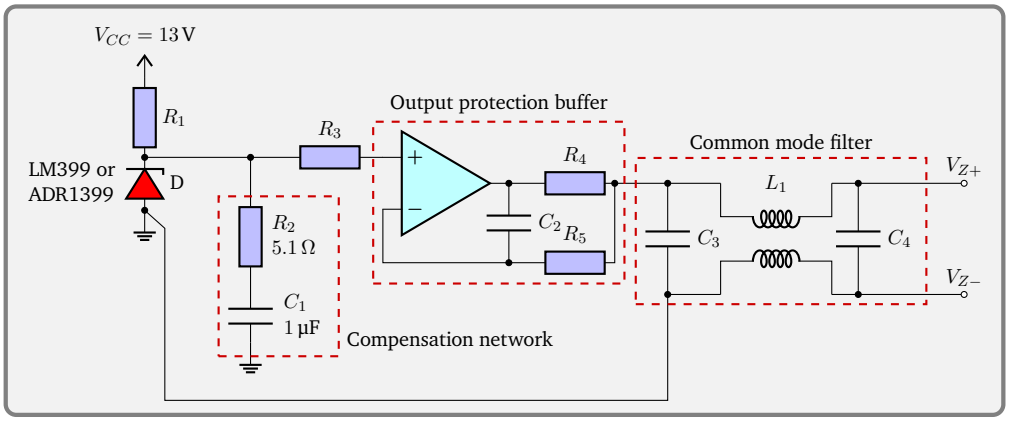

Figure 4.49.: Circuit used for the burn-in of `LM399` and `ADR1399` Zener diodes.

The compensation network is required when using the `ADR1399`, because of its very low dynamic impedance as recommended in the data sheet [15]. It is not strictly required for the

LM399, but fitted nonetheless, because there are no downsides to it. This makes the board compatible with both types of references. Each Zener diode output is protected using a buffer which provides isolation and short circuit protection. Finally there is a common mode filter at the output to suppress high frequency noise caused by ground loops.

Using this test setup, 102 LM399 Zener diodes were tested up to this date (2023-04). Of those 39 were found suitable for the DgDrive. This low yield of only 40 % is a matter of concern and has significantly delayed the development and production of the drivers. Using the automated test setup, the latter issue is manageable, but still slows down the production. Tests are currently conducted to replace the LM399 with the newer ADR1399 Zener diode, but unfortunately, it is still not available in quantities surpassing individual samples. Two of those samples were thoroughly tested and showed significantly better performance in terms of both lower white noise and reduced burst noise. Although these results are promising, more samples need to be tested to give a final verdict. Using the screened Zener diodes a first batch of 15 laser drivers was built and a second batch is in pre-production.

4.1.17. Summary

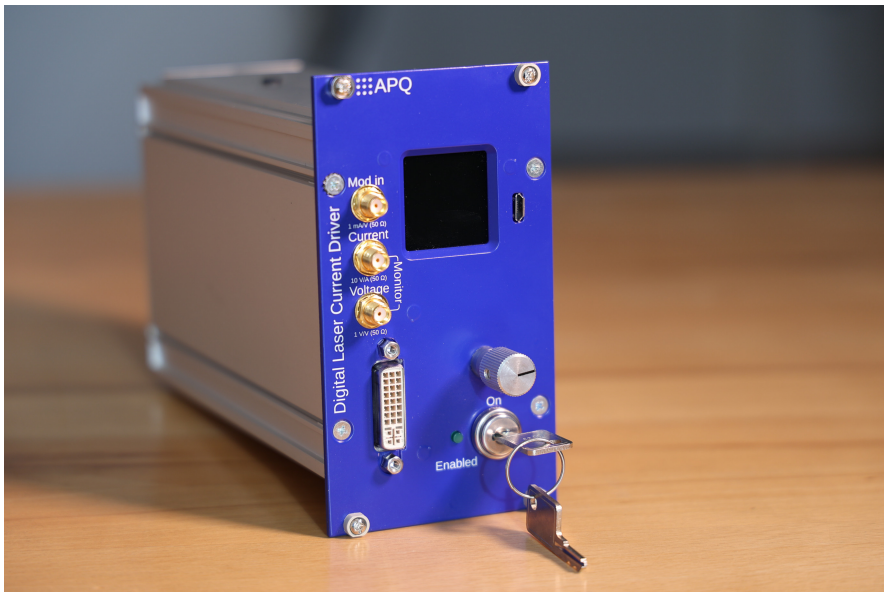

Figure 4.50.: Picture of the digital current driver DgDrive.

This section saw the evaluation of several commercial current driver representing the state of the art at the time of writing. These drivers were all found to be unsuitable to drive modern blue laser diodes like the Osram PL 450B [174] used in the ARTEMIS experiment for the 453 nm master laser. The most common problem identified was the limited compliance voltage especially with low-noise drivers like the Vescent D2-105 which can barely drive modern high power laser diodes like the Thorlabs L785H1 [118] that require a compliance voltage of more than 2.5 V at high currents. The only solution with such driver is to use a higher output current model and run it at a reduced current. This strategy negatively impact the noise figure as higher current models have a higher output noise. Additionally, none of the low noise drivers have a digital interface for remote control.

To address these problems, a new laser driver design is presented that not only surpasses all

commercial alternatives, both in performance and price, but also delivers the much needed digital interface to integrate into modern experimental setups. To address the compliance voltage issue which is an inherent problem in the original design by Libbrecht et al. [128] upon which all of the driver tested rely one, a novel current source configuration was developed that separates the current source from the load. This ensures low noise, a high compliance voltage and robust noise immunity.

The current driver performance was demonstrated in several of the previous sections and a summary of those finding can be found in the following table.

Device Properties 4.7: DgDrive device properties

- Maximum output current: $500\,\mathrm{mA}$ (p. 126)
- Temperature coefficient: $0.1\,\mu\mathrm{A/K} + 0.5\,\mu\mathrm{A/(A\,K)} \cdot I_{out}$ (p. 157)
- Stability: $<(1 \pm 2)\,\mu\mathrm{A/A/a}$ (p. 160)
- Noise: $<70\,\mathrm{pA}/\sqrt{\mathrm{Hz}}$ above $100\,\mathrm{Hz}$ (150)
- Below shot noise above $20\,\mathrm{mA}$ for the $500\,\mathrm{mA}$ version. (p. 152)
- Modulation bandwidth: $1\,\mathrm{MHz}$ (p. 131)
- Output impedance: $>1\,\mathrm{G\Omega}$ resulting in excellent noise immunity (p. 142)
- Digital control
- Python API for remote control

4.2. LabKraken

LabKraken allows real-time monitoring of experiments or environmental parameters. It was extensively used throughout this work to collect, for example, the measurement data produced by the Zener diode test setup described in section 4.1.16 and to give real-time feedback on the diode voltages. Other applications, among many other, are the monitoring of the laser output power for experiments or logging the ambient temperature, humidity, and air pressure.

As outlined in section 3.4, LabKraken was built using Python and the asyncio framework. It is running inside Docker containers for easier deployment and portability. The full source code can be found at [41]. It is programmed using a functional programming style and based on data streams to aggregate data from different sensors, which currently include

- Tinkerforge sensors
- GPIB devices via GPIB Ethernet adaptors
- LabNodes (see section 4.3)
- Ethernet capable SCPI devices

The collected data is sent to an MQ Telemetry Transport (MQTT) server, which decouples the data acquisition from the data storage back end. It also allows to aggregate the data of multiple LabKraken instances running in parallel. A simple flow diagram is shown in figure 4.51 to give an idea about the processing of the data.

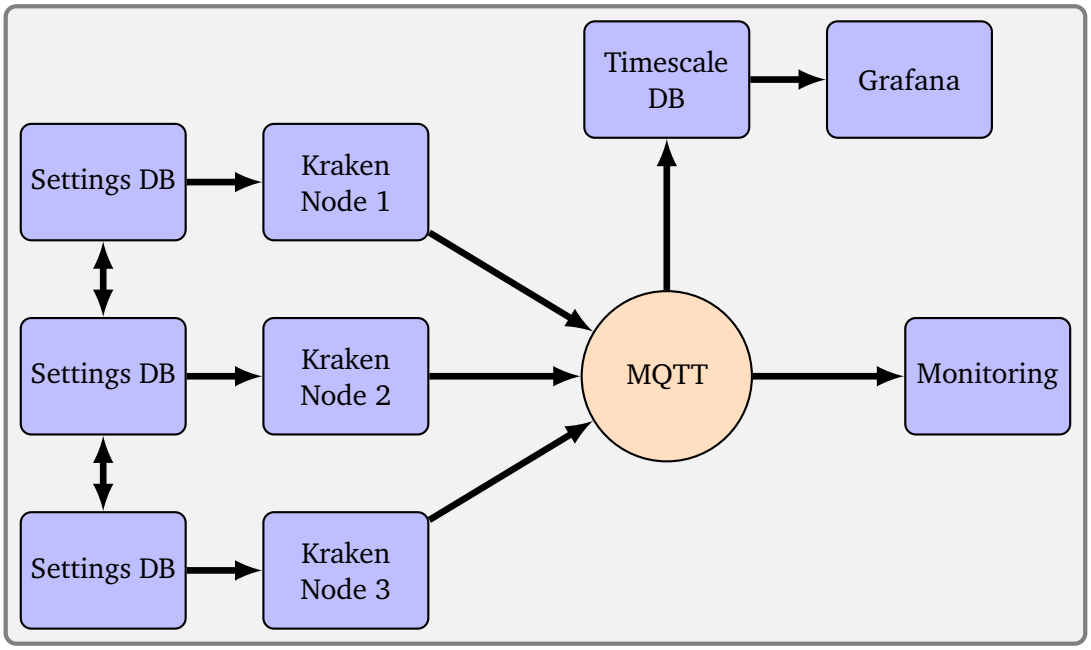

Figure 4.51.: Flow diagram showing the lab monitor system. The data is gathered by the LabKraken nodes, sent to the MQTT server, then stored in database and also used by a monitoring system.

Figure 4.51 shows multiple LabKraken nodes connected to the MQTT server. These nodes are independent data collectors, but also serve as backup for the other nodes. Sensors can be

dynamically moved between nodes, for example, to restart a server without data loss. Each LabKraken node is connected to a settings database with currently is a MongoDB cluster that synchronizes the settings for all LabKraken instances.

The MQTT server adds a layer of resilience to the system as it makes sure that the data get delivered to the clients using a quality-of-service protocol. This means that messages will be buffered and retained if a client disconnects. It also makes sure no duplicates are produced during an attempt to resend a message.

The data distributed by the MQTT broker can be monitored in real-time for debugging or monitoring purposes. It also stored in a TimescaleDB database which is a modified PostgreSQL database.

The data stored in the database is finally visualized using a Grafana back end and can be accessed by the end-user to monitor the experiment and the lab. Additionally, warnings are generated if certain measurands are no longer within their limits.

4.2.1. Performance

To give an idea of the workload that is currently being processed a few numbers can be given. As of 2023 more than 250 sensors across several labs and offices are being monitored. The typical monitoring interval is currently between $1\,\mathrm{s}$ and $60\,\mathrm{s}$. The database handles about 2×10^6 inserts/d and the MQTT server processes around 5×10^6 datagrams/d. Figure 4.52 shows the increasing data load created by adding new experiments and therefore more sensors over the recent years.

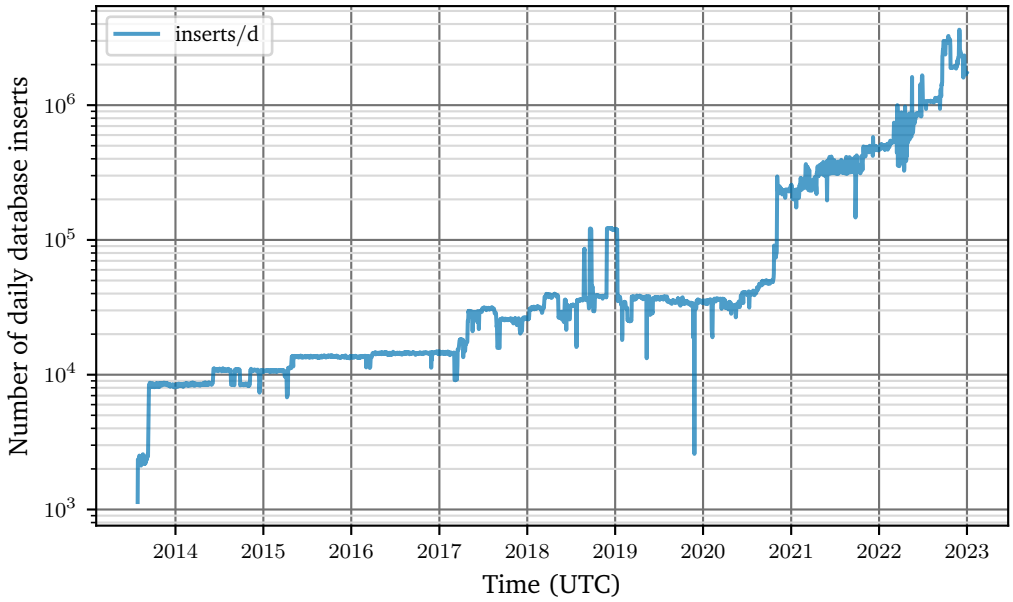

Figure 4.52.: Daily number of datasets collected by the Labkraken system over recent years.

The growth of the data intake was, in the past years, superexponential. To illustrate this, all the data collected in the first $7\,\mathrm{a}$ up to 2021 is the same amount as is being collected each month in 2023. There are multiple reasons for this growth rate. During the first years, only a very basic web interface was available to extract the data and without any real-time plotting

capabilities. This changed in 2020 with the introduction of the Grafana web interface and caused a spike of interest. Additionally new experiments are now equipped, by default, with temperature sensors and, for example, monitoring photodiodes that continuously stream data into the system. Currently the main database server is a 6$^{\text{th}}$ generation HP `ProLiant DL360` with two `Xeon L5630` processors and 48 GB of RAM. The LabKraken nodes run on different, less powerful, servers and even Raspberry Pis. The current bottleneck is the database server with its limited RAM and disk I/O performance. This system will be upgraded in the near future to meet the requirements for the coming years. It is expected that the data rate increases by another order of magnitude to around 500 datagrams/s on the MQTT server and about 200 inserts/s into the database.

4.2.2. Reliability

As explained in section 3.4, LabKraken is designed to be resilient and fault tolerant. This includes the ability to share the data acquisition between multiple instances of LabKraken. Theses instances are hosted in Docker containers on different servers. The use of Docker containers allows to easily build and test LabKraken and in case of problems roll back to a previous stable version.

Using multiple instances of LabKraken gives it the ability to move sensors from one instance to another to reboot a server for updates or other maintenance tasks. Even a full operating system migration was successfully conducted twice without service interruption. As of 2023 the uptime of the system is being monitored. To test the full data acquisition chain, from the transducer to the storage back end, a sensor that reports data at 1 s intervals is used. This timestamped data is binned into 1 min intervals and the number of bins that contain data is counted. This number is compared to the number of minutes that have actually passed in the interval of interest. The results of this evaluation are given in table 4.18.

	Minutes missed	Availability
2023-01	21	$99.95\,\%$
2023-02	7	$99.98\,\%$
2023-03	10	$99.98\,\%$
2023-04	22	$99.95\,\%$
2023-05	16	$99.96\,\%$
2023	76	$99.97\,\%$

Table 4.18.: Availability of the LabKraken system ordered by month and aggregated by year.

The downtime is mostly due to operator errors. Currently a proper configuration front end that could prevent misconfiguration is not implemented. The configuration is currently managed via the API of the LabKraken system and several Python scripts. Future software revisions will include a web front end for configuring LabKraken instead of directly manipulating the database. The mid-term goal for development in the coming years is a four 9s availability. This will likely require a few changes to the back end because the MQTT server is currently not redundant, a feature that is not supported by Eclipse Mosquitto broker in use.

4.2.3. Summary

A data aggregation daemon was presented that serves the need for a laboratory environment. Not only does it monitor environmental data, but also many devices found in scientific experiments are supported via the GPIB interface. Additionally the Tinkerforge ecosystem offers many solution for direct data capture through analog and digital input capture devices. The system currently manages about 60 datagrams/s with little load. It is expected to scale to 500 datagrams/s in the coming years without problems.

Device Properties 4.8: Labkraken properties

- Supports Tinkerforge sensors
- Supports GPIB devices via GPIB Ethernet adaptors
- Supports LabNodes (see section 4.3)
- Supports Ethernet capable SCPI devices
- Availability and uptime is $99.97\,\%$
- Currently manages more than 250 senors with 60 datagrams/s

4.3. Lab Temperature Controller

4.3.1. Controller Hardware

The lab temperature controller also called LabNode is an Ethernet connected PID controller, which is shown in figure 4.53.

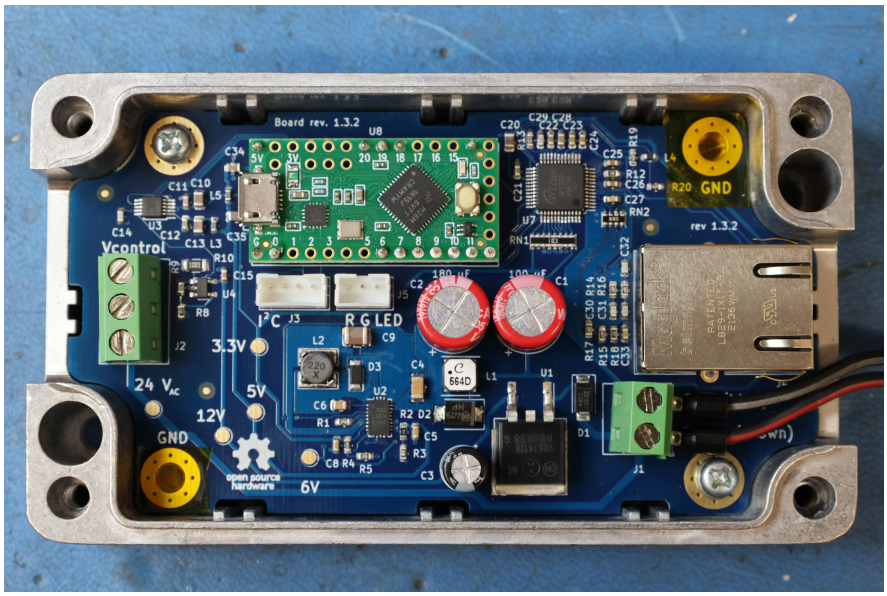

Figure 4.53.: Picture of a LabNode, an Ethernet connected PID controller using a `Teensy LC` microcontroller.

It was developed during the Bachelor's thesis of Liebmann [129] and is mainly used to connect to actuators like the Heimeier `EMO T` [76] which uses a $24\,V_{AC}$ supply and accepts a $10\,V$ input for the setpoint. The LabNode is far more versatile though and can be used for many other tasks as well.

The controller is based on the `Teensy LC` microcontroller, which has a 32 bit Cortex M0+ 48 MHz MCU. It can be controlled and configured via Ethernet using CBOR [46] encoded commands. The CBOR encoder is similar to a binary form of the poplar JSON [47] text format for data transfer. The CBOR encoder is available for many programming languages. Additionally, a Python implementation of the LabNode API is provided by the author [36], which can be easily installed via the PyPI repository using a single command. The LabNode features a highly optimized PID library [38], written, by the author, in C++ and assembly. The library was optimized for the Cortex M4 and performs even better on that platform. It makes use of the so called saturated math instructions, which is available as part of the DSP (Digital Signal Processing) extension of the M4. For implementation details see [38] and consult the source code documentation. Using the `Teensy LC`, a PID update rate of more than $100\,kHz$ was achieved, allowing the LabNode to be customized for more demanding tasks that require PID control. An external connection to the I²C bus of the MCU can be used to integrate custom sensors. Additional features can be implemented via the Arduino integrated development environment (IDE) which is geared toward beginners, which results in a lower barrier to entry for students to adapt the system to their needs.

The controller is capable to work with a broad range of actuators as is has a switchable gain

block at the output to accommodate the two most common input ranges of linear actuators of 0 to 5 V and 0 to 10 V. The 12 bit DAC is an ADI `AD5681R` [6] but for more demanding tasks a 16 bit version `AD5683R` can be installed as well with minimal software changes required. The full design files can be found at [35].

4.3.2. Controller Implementation

The lab temperature swings were already introduced in figure 3.3 on page 17 and it became obvious that given a 2 K temperature swing precision measurement requiring stability below 1 ppm are not possible. An example of a measurement within such an adverse environment is shown in figure 4.54.

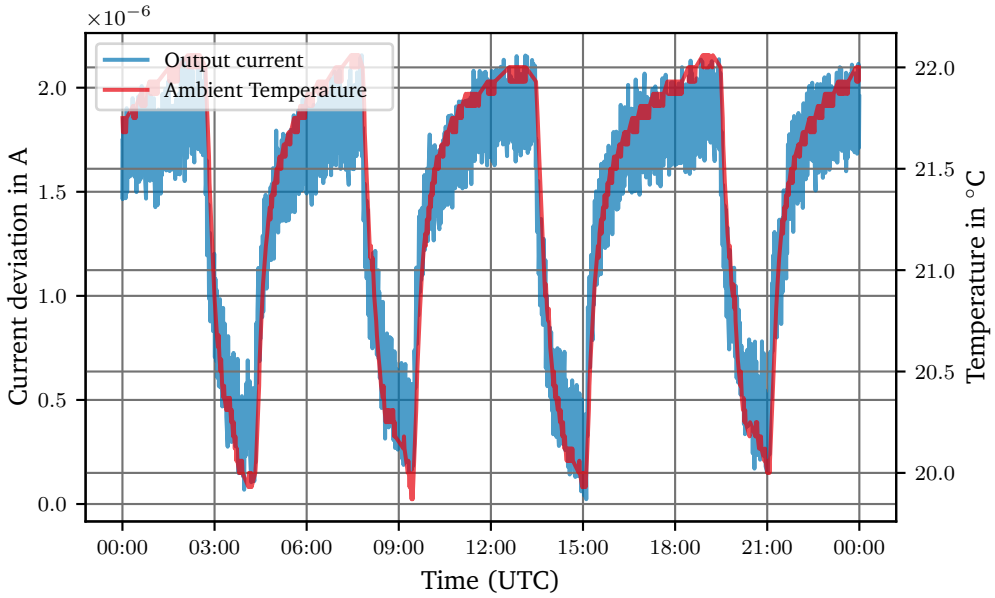

Figure 4.54.: Measuring a current of 50 mA using a Keysight `34470A` with changing ambient temperature. The current source is based on the design of Erickson et al. [77].

The device under test (DUT) for the measurement shown above was placed in a temperature controlled chamber and the Keysight `34470A`[3] was exposed to the lab environment. Admittedly, the example in figure 4.54 does not reflect the correct way to conduct a measurement with high stability requirements but serves as an excellent example to highlight the problem.

In order to resolve the situation, a LabNode was used to replace the commercial temperature controller of the air conditioner box. These boxes use an active radiator and are connected to the cooling water system of the building. The water flow can be regulated via an actuator to control the air temperature blown into the room. The lab, which is used as an example below has two such boxes and both are controlled by individual temperature controllers. To reduce the coupling between the two boxes it is desirable to keep the sensors close to the air conditioner unit. This also decreases the response time of the sensors and thereby increases the regulation bandwidth. On the other hand, only regulating the output temperature of the air conditioner unit will result in a temperature offset measured on the optical tables

[3] 100 mA range, 10 PLC, AZERO ON, $f_s = 0.5$ Hz

depending on the local heat load. This problem can be addressed using multiple sensors. One sensor that is close to output of the air conditioner and the other one at the location where the temperature is to be stabilized. This idea is hardly new and commonly used in industry [210]. Another intriguingly simple solution using two interleaved PID controllers was also presented by Znaimer et al. [254].

The bandwidth of the PID control loop required is not not very high and it was found that a controller update rate of 1 Hz was more than sufficient, even for sensors placed just below the air conditioner unit. This allows to connect the sensors via Ethernet instead of directly wiring them to the PID controller. Using Ethernet greatly simplifies the setup, because the infrastructure is already there. Additionally, when routing these sensor signals through a small computer, more elaborate control schemes like those presented by Znaimer et al. [254] can be implemented on the fly in software without modifying the LabNode controller firmware. This also simplifies testing and opens up more options regarding the sensor choice.

Such a control scheme is currently implemented and several sensors produced by Tinkerforge are distributed throughout the lab to give the desired feedback. A Docker container running on a server is processing these sensors and then hands a computed value to the LabNode controller. Should the server stop sending updates, a fail-safe engages and the controller will use a backup sensor to control the room temperature, albeit with a reduced bandwidth, because the sensor is located inside the controller box and not directed attached to the air conditioner.

To adjust the PID controller a model of the room was used as described in section 3.5.2 on page 34. The extraction of the model parameters is shown in the next section.

4.3.3. Controller Tuning

The FOPDT model was found to sufficiently describe the room under most circumstances and gave usable results for a PI controller. An exception to the rule is the case were the sensor is very close to the air conditioner. As an example this procedure is explained using the air conditioner of lab 011 that contains two such units. The model is created for the second air conditioner, located in back of lab. This is also the lab were the measurement shown in figure 4.54 was conducted. To fit the model to the data, timestamped values of the controller output and the room temperature are required. The LabKraken software shown in section 4.2 greatly simplifies this task as these values are routinely logged by LabKraken, so there is no special setup required. To extract the data later, either an SQL query can be used to have the Timescale database prepare a usable dataset or the Grafana web interface can be used to select the appropriate time frame. Appendix A.2 explains the required SQL queries and such a query was used to procure the data for the following example.

The procedure to extract the PID parameters is as follows

1. Place the sensors and log their output along with a timestamp.
2. Make sure the room temperature is stable.
3. Set the controller to manual mode, which freezes the output at the current output value.
4. Wait a few minutes to collect some data. This gives the fit a better starting point.
5. Apply a step pulse by increasing the output by 500 counts. Do make sure that this gives a reasonable (small-signal) response. Some rooms may require a smaller step like 100 counts.
6. Wait again until the temperature has settled to ensure a good fit to the measurement data.

7. Return the controller to automatic mode.

With the timestamped temperature and output values in hand, a fit to the model can be attempted. The type of model depends on the location of the sensor. Sensors located a few meters away from the air conditioner can be modeled, to a good degree, using a first order plus dead-time model. The result will then be a set of parameters for a PI controller as discussed in sections 3.5.2 and 3.5.3. Sensors located very close to the air conditioner or placed directly in the airflow require a different approach and can best be simulated with a second order model. The result will then be a set of PID controller parameters.

Figure 4.55 shows the fit to the internal backup sensor of the LabNode controller in the back of the lab. The controller is located about $1.5\,\mathrm{m}$ from the air conditioner and not directly placed in the airflow. Both the time delay until the cold air reaches the controller and the long decay time can be seen. The latter is due to the placement of the sensor inside the controller and is also the reason for the seemingly high temperature of more than $35\,^{\circ}\mathrm{C}$. The measurement typically takes about 3–4 h and the lab should best be undisturbed during this time. Fortunately, the controller is remote-controllable and can be programmed using the Python API introduced above to run the measurement sequence at night, for example. A documented Python example to set the controller output can be found with the source code of the library [36].

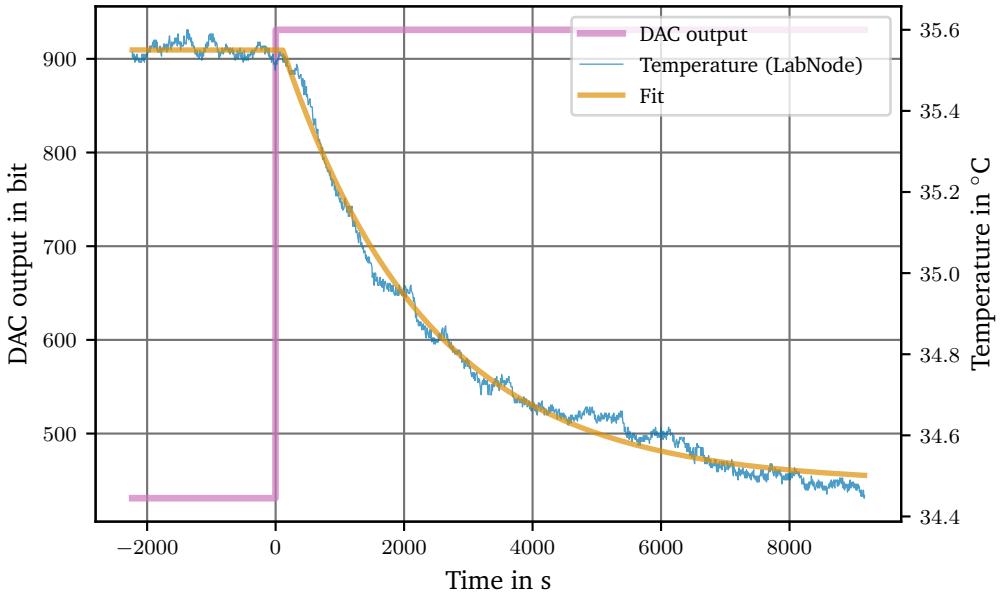

Figure 4.55.: Fitting a FOPDT model to the response of an output step of $500\,\mathrm{bit}$.

The fitting algorithm is implemented in Python and can be found along with the supplemental material [42] at data/fit_kraken.py. The fitting program tries to fit a FOPDT model to the data, then produces a plot like the one shown in figure 4.55 and returns the model parameters and finally calculates the PID parameters using several different tuning rules. The fit to the data presented above produced the following values for the FOPDT parameters:

$$K = (2.137 \pm 0.005)\,\mathrm{mK/bit} \qquad \tau = (2264 \pm 17)\,\mathrm{s} \qquad \theta = (113 \pm 8)\,\mathrm{s}$$

K is the normalised gain, τ the decay time, and θ the dead time or lag.

Tuning Rule	k_p	k_i
SIMC PI	$4688.57\,\mathrm{bit/K}$	$5.186\,\mathrm{bit\,s/K}$
AMIGO PI	$2927.71\,\mathrm{bit/K}$	$3.087\,\mathrm{bit\,s/K}$

Table 4.19.: PI tuning rules for lab 011 extracted from a fit to a FOPDT model.

As it was shown in section 3.5.4, the tuning rules that result in the smoothest response with very little overshoot in this application are the SIMC and the AMIGO rules. The results calculated using those rules are given below. They were derived according to table 3.5 on page 43.

For the backup sensor, the more conservative result is chosen as a starting point for tuning the controller. The reason is that the backup mode is supposed to 'just work' even under adverse conditions. The results obtained will likely need some more tuning to achieve optimal results. Retuning of the controller becomes necessary if extensive changes were made either to the heat load in the room or the air conditioning system. A well tuned system is shown in the next section.

4.3.4. Test Results: Temperature Stability

Having tuned the PID controllers the system was found to be stable even for fast changing loads, like high power devices being turned on, or sudden changes of the cooling water temperature. To demonstrate the performance, a typical week was chosen and the room temperature is shown in figure 4.56.

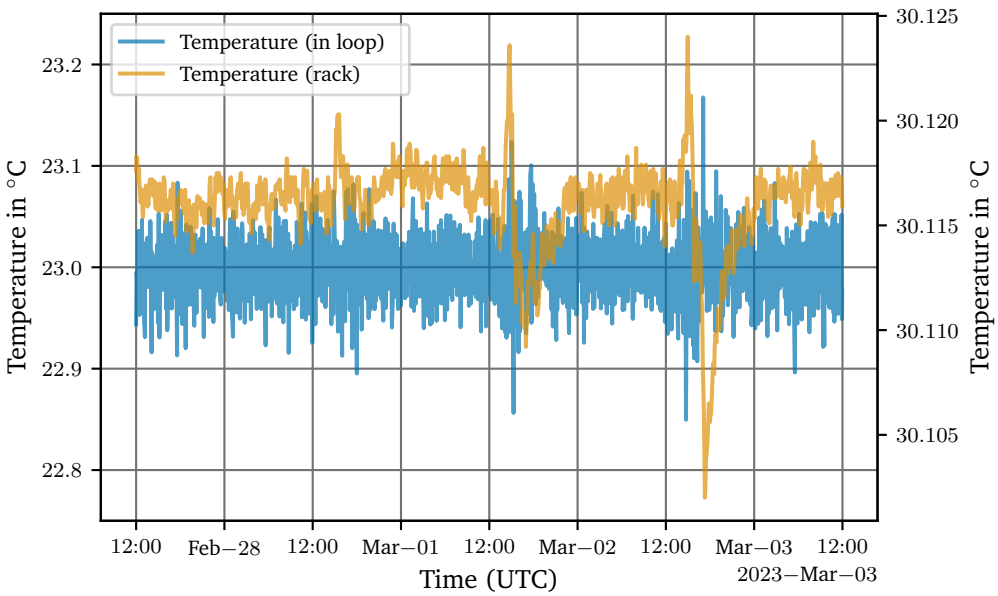

Figure 4.56.: Temperature measured by two sensors in the lab. The in-loop sensor is shown in blue. A second sensor located inside a rack nearby is shown in brown.

Figure 4.56 shows the temperature as measured by a sensor attached to the air conditioner

and a Fluke 5615-12-P PT100 sensor, which is placed inside the rack that monitors the Zener diode scanner setup described in section 4.1.16. The only deviations seen are caused by people working on the table right next to this rack. Typically the temperature is stable within $\pm 0.5\,\mathrm{K}$ over weeks, a significant improvement over the system previously installed.

It must also be mentioned that over the course of the last 6 years none of the 14 units currently in use has failed or shown issues. This highlights the build quality and reliability of the system. One of the key parameters for such an important aspect of the infrastructure.

4.3.5. Summary

An Ethernet connected PID controller called LabNode was presented. This controller can be programmed using the user-friendly Arduino IDE to make customisation available to a wide group of users. Additionally, the software provided can be controlled using a Python API via Ethernet. The PID controller software presented is a high performance solution handling an update rate of up to $100\,\mathrm{kHz}$.

Device Properties 4.9: LabNode properties

- Rugged, industrial PID controller
- Controllable via Ethernet and USB
- Sampling rate of up to $100\,\mathrm{kHz}$
- Programmable via the Arduino IDE
- Python API
- Application in temperature control. A room temperature stability of $\Delta T = \pm 0.5\,\mathrm{K}$ was demonstrated.

4.4. Digital Temperature Controller

A diode laser as implemented by the APQ group requires two temperature controllers. One is used to stabilise the external resonator and the other is used to control the temperature of the laser diode. For this purpose, a two-channel controller was conceived in this work and a prototype was tested. This section is split into two parts, just like temperature controller hardware. There is the analog front end that does the data acquisition and there is a power driver board that is responsible for driving two thermoelectric coolers (TEC). The analog front end was developed during the Master's thesis of Sattelmaier [191]. An in-depth characterisation can be found there. The most imported findings will also be reproduced here.

The second part deals with driver board. The driver board features two $12\,\mathrm{V}$, $5\,\mathrm{A}$ output drivers and also contains the microcontroller.

4.4.1. Analog Board

The analog front end is isolated on a separate board to reduce noise coming from the power supply which drives the TECs running several ampere. The front end consists of two channels that are identical. Each channel has a current source, a multiplexer (MUX) and an ADC, including a buffer. A simplified overview is given in figure 4.57.

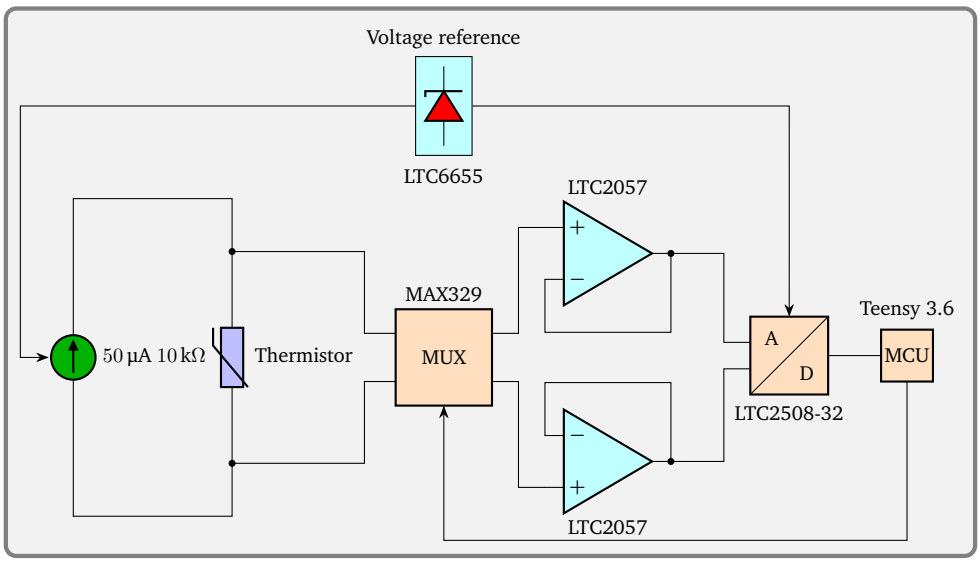

Figure 4.57.: Simplified schematic of the temperature controller front end. Shown is a single channel. Not included is an internal reference resistor that is accessible through the MUX for calibration purposes.

As can be seen in figure 4.57, the same reference voltage is used to create the thermistor sense current and the ADC reference. This has the advantage of cancelling out first order effects of the low frequency noise and drift of the reference, which allows a simpler reference circuit than the one shown in section 4.11 and used in the `DgDrive` laser current driver. The reference is an ADI `LTC6655-4.096` [141], a $4.096\,\mathrm{V}$ bandgap reference as opposed to the Zener diode used in the laser current driver design. These voltage references can operate with a lower supply voltage, but are less stable and nosier. The latter two properties are of little

concern as drift and noise mostly cancels out in this arrangement. The former property has the advantage of reducing the number of supply rails required for this design.

The voltage reference is buffered and split into two paths, one feeds into the ADC, a 32 bit ADI `LTC2508-32` [139] successive approximation (SAR) ADC. This ADC runs at 1 MHz, but does apply an internal filtering and decimation algorithm. Decimating the output is necessary, because the MCU, a `Teensy 3.6` with a 180 MHz Cortex M4 32-bit processor is not capable of transferring the 32 bit data value within the 650 ns as required by the `LTC2508-32` to cope with a 1 MHz data stream. Decimating the input allows to spread the readout over multiple acquisitions as detailed by Sattelmaier [191]. This has some drawbacks as discussed later though.

The other reference voltage path is going to the current sources. There, the reference voltage is again split into two paths again, one for each ADC channel, and fed into an ADI `AD5760` [7] 16 bit DAC with a very low temperature coefficient of $<0.05\,\mu V/V$. The DAC is used to adjust the output current, which is useful when using other temperature transducers than a $10\,k\Omega$ thermistor. The design of the current source is very similar to the design discussed in section 4.1.6 on page 122. This main current source (it actually is a sink) is a buffered Howland current source as shown in figure 3.54 on page 95 instead of the MOSFET based current source. The Howland current source is based on an ADI `LT1997-3` [137] difference amplifier as proposed in section 3.8.9. The reference resistor is a $100\,k\Omega$ Vishay `S102` [187] non-hermetic moulded precision resistor. The current is then fed into a CR-filter (do note the inverted order, because it is a current filter). The low output impedance of the filter requires a cascode with a an InterFET `SMP4338` JFET to restore the output impedance. After the cascode, the current is sourced from a virtual ground as shown in figure 4.19 on page 123. The current flow is in the opposite direction as in the laser current driver discussed in section 4.1.6 because the voltage across the thermistor must be of positive polarity to be read by the ADC.

The extremely high output impedance is required because it reduces the settling time of the current source and suppresses external noise sources. The former is important when considering the autozeroing routine. The acquisition procedure will be discussed next in more detail.

4.4.2. Data Acquisition

The thermistor to measure the temperature of the laser resonator and diode mount is an Amphenol `RL0503-5820-97-MS` [185] large bead thermistor. The large size of the thermistor results in a lower noise as compared to smaller thermistors like the TDK `B57550G103+` used in earlier laser resonator designs [186] of the APQ group. To reduce self-heating effects due to the sense current, a current of $50\,\mu A$ was chosen as opposed to the industry standard of $100\,\mu A$. This will produce a voltage of 500 mV across the thermistor at room temperature. Using the equation derived by Steinhart et al. [216], the temperature sensitivity of the thermistor can be estimated and is found to be $1.91\,\mu V/100\mu K$ at $23\,°C$ and $450\,nV/100\mu K$ at $60\,°C$. To reach the design goal of $100\,\mu K$ as stated in table 3.4 on page 24, small voltages need to be measured. This brings up several problems like low frequency noise from the amplifier and thermal EMF, which can introduce an offset voltage between two dissimilar metals of different temperature – an issue that arises at every connector and solder joint between the sensor and the analog front end. Copper oxide buildup on connectors can produce Peltier voltages as high as $1\,mV/K$ [96], orders of magnitude larger than the desired measurement resolution. Both the low frequency flicker noise and the random walk seen from thermal EMF can be treated as the same problem. The details and their nature were discussed in section 3.6.

To mitigate this low frequency noise autozeroing is required. As explained in section 3.7 autozeroing requires a second measurement of the zero value to subtract it from the measurement. This obviously slows down the measurement frequency by half. An alternative is to invert the polarity of the measurement, then average both as

$$\frac{V_{thermistor} + V_{off} - (-V_{thermistor} + V_{off})}{2} = V_{thermistor} \,. \tag{4.16}$$

$V_{thermistor}$ is the voltage across the thermistor and V_{off} the offset voltage introduced by the effects discussed above. Averaging two inverted measurements results in the desired thermistor voltage, but with the offset removed. This approach still bears the cost off bandwidth, but has no dead time. This is a considerable advantage as discussed in section 3.7.1 because it allows to increase the switching frequency until one ends up in the white noise region of the noise spectral density. The limits will be discussed later and the multiplexer is shown first. The design uses a low leakage ADI `MAX329` [153] dual four-channel multiplexer. This multiplexer is used to switch the current source between four configurations.

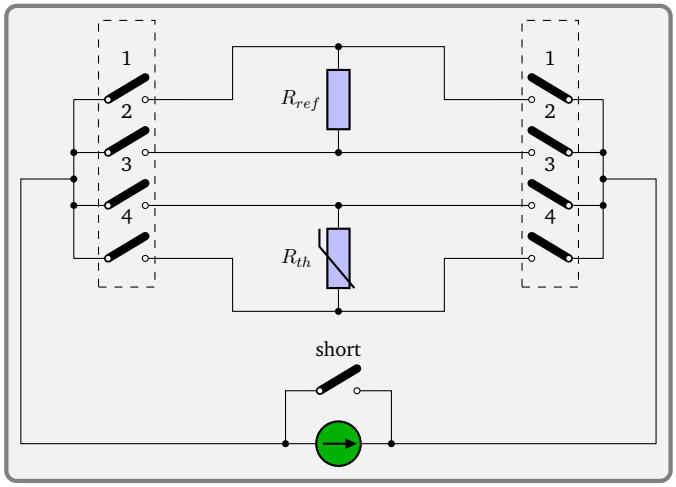

Figure 4.58.: Multiplexer of the analog front end to invert the current source and switch to a reference resistor used for calibration.

The multiplexer shown in figure 4.58 allows to invert the current source, but also to switch it to an internal reference resistor, a hermetic $10\,\mathrm{k\Omega}$ Vishay `VHP101` [234]. This resistor gives the analog front end a number of unique capabilities. The instrument cannot only autocalibrate its front end by checking against the known value of the reference resistor. It can also be used as a resistance bridge because both channels have access to this reference resistor. So by measuring a known resistor on channel 1 and an unknown resistor on channel 2, its ratio can be computed by comparing both channels with the reference resistor. This feature is not yet implemented in firmware, but can prove interesting for high precision resistance measurements. The shorting switch shown above the current source at the bottom of figure 4.58 is engaged before opening any of the multiplexer switches to ensure the current source does not increase the voltage to the maximum compliance voltage in an attempt to keep the current flowing.

Switching the polarity of the current source brings a number of challenges. First, the load is switched between a short and the $10\,\mathrm{k\Omega}$ within $1\,\mu\mathrm{s}$ [153] as this is the switching time of the `MAX329`. These fast switching times are desirable because in between the transition, the ADC cannot collect data samples. The current source must therefore follow these load changes

as fast as possible. This requires a very high dynamic output impedance as mentioned above. The second issue has to do with the cable. The cable has a capacitance and additionally the dielectric used as insulator displays dielectric absorption. The latter topic was already discussed in section 4.1.5 on page 117 in the context of capacitor leakage. The cable capacitance limits the maximum output impedance as shown in figure 4.31 on page 142. The resistance involved in this situation is one order of magnitude higher than the $1\,\mathrm{k\Omega}$ discussed in section 4.1.5, which makes the capacitive effect even more pronounced. Sattelmaier showed that using a $2\,\mathrm{m}$ twisted pair cable with a PVC insulator a decay time of $(0.1876 \pm 0.0794)\,\mathrm{s}$ could be observed. Given that the dielectric loss tangent of PCV is 2 orders of magnitude higher than that of PTFE [157] and the relative permittivity of PTFE ϵ_r is about $60\,\%$ that of PVC. PTFE cables were chosen to minimize the dead time. The cables used are 4-wire MIL-DTL-27500 `M27500A 18WJ4T24` cables. These cables did not cause any degradation of the measurement as opposed to several PVC insulated cables tested.

The inversion sequence of the autozeroing also affects the ADC filter. As mentioned above, the ADC has an internal filter and then decimates the result to reduce the amount of data that needs to processed by the microcontroller. The internal filter is, unfortunately, not aware of the switching and cannot apply equation 4.16. The filter therefore need be reset after each inversion. This forces the data acquisition to wait for the filter to settle again before processing new data. The internal filter needs 7 (decimated) samples to settle. The smallest downsampling factor, the $180\,\mathrm{MHz}$ `Teensy 3.6` could cope with, was 4096 which results in $244\,\mathrm{samples/s}$ with a bandwidth of $30\,\mathrm{Hz}$. The wait time of 7 samples introduces a dead time of $29\,\mathrm{ms}$. Figure 4.59 can be used to judge the impact of the slow data processing.

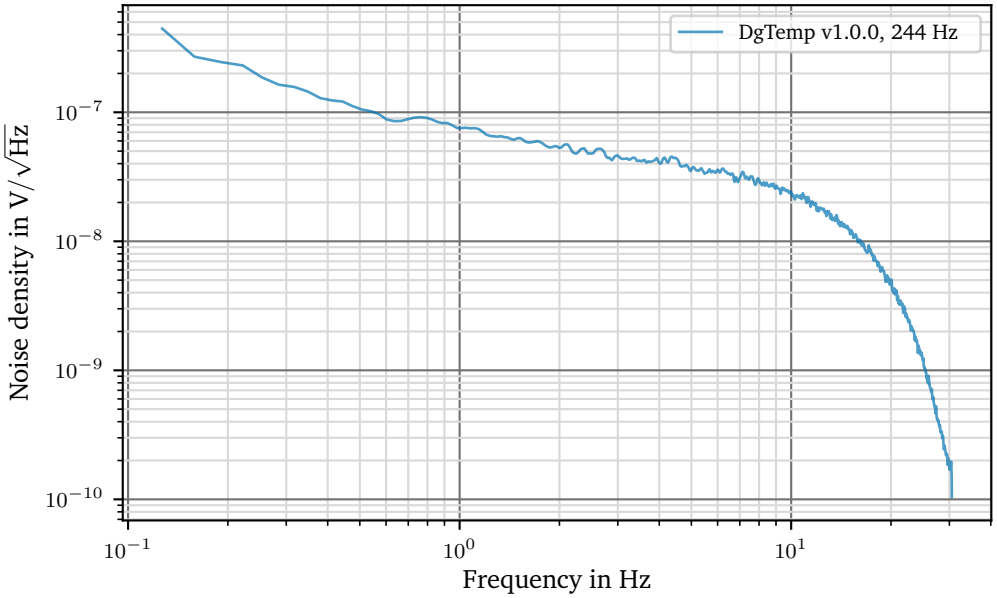

Figure 4.59.: Noise spectrum of the analog front end using an `LTC2508-32` with shorted inputs. The sampling frequency is $244\,\mathrm{Hz}$.

The most prominent feature of figure 4.59 is the bandwidth of $30\,\mathrm{Hz}$, which can be clearly identified. Although it is mostly shaped by the digital filter of the `LTC2508-32`, it can be seen that towards low frequencies, the noise floor takes the form of flicker noise from the ADC. The `LTC2057` used as a buffer has a noise floor of $10\,\mathrm{nV}/\sqrt{\mathrm{Hz}}$. Judging from the shape of the curve

in figure 4.59 it can be expected that towards higher frequencies, the noise should drop to that value. Unfortunately, this frequency range is out reach. To limit the impact of the digital filter on the measurement, the inversion frequency must be well within the filter bandwidth. The inversion was therefore chosen to be done every 512 samples, that is, with a frequency of about $2\,\mathrm{Hz}$ which is about a decade away from the filter cutoff.

4.4.3. Test Results: Linearity

Another important property of the analog front end is its linearity, not only for the application as a resistance bridge mentioned before, but also to ensure an accurate measurement of a calibrated temperature. This test was done by sweeping a Fluke `5440B` calibrator over the input range from 0 to $4.096\,\mathrm{V}$. A Keysight `3458A` with a specified linearity of $<0.1\,\mu\mathrm{V/V}$ was used to confirm the voltage. This lead to a parabolic calibration curve that was programmed into the microcontroller and was then corrected for in real-time. The integral non-linearity (INL) measurement is shown in figure 4.60.

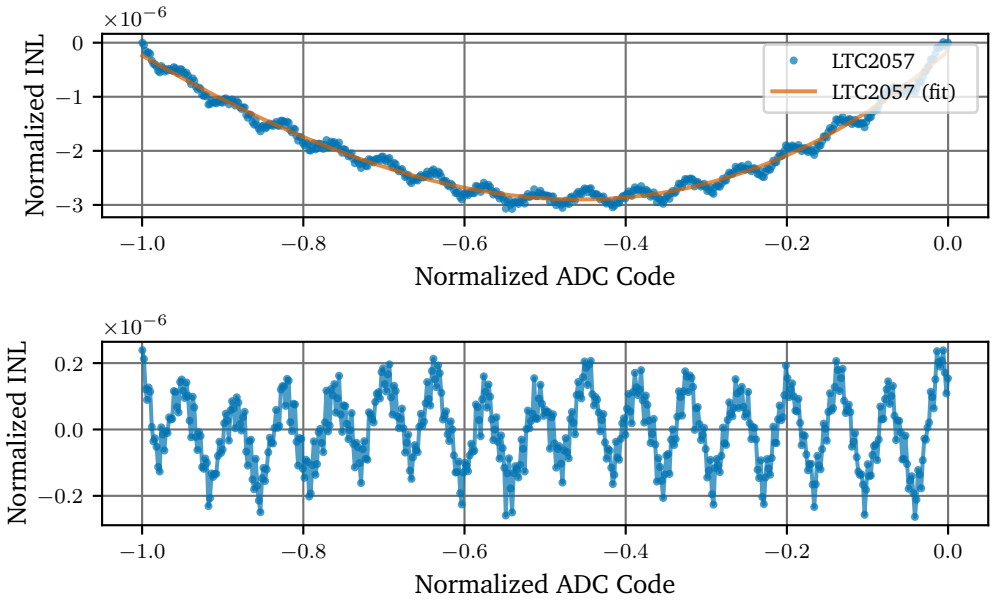

Figure 4.60.: INL of the analog front end with an `LTC2057` buffer. Top: uncorrected INL. Bottom: INL with the real-time correction applied.

Several other op-amps like the Texas Instruments `OPA827` and the ADI `ADA4625-1`, both JFET op-amps were also tested as an input buffer. While the `LTC2057` did not have the lowest INL of all devices tested, it had the most predictable INL. It was the only device producing a parabolic shape [191] which is easy to calibrate out. The other devices produced a non-symmetrical cubic shape likely due to the lower open-loop gain of the JFET op-amps. Another chopper op-amp, a TI `OPA189`, was tested, but was found not compatible with the $10\,\mathrm{k\Omega}$ input resistance of the thermistor. The switching current from by the autozeroing produced an offset voltage at the output of the op-amp of $2\,\mu\mathrm{V}$ when used with a $10\,\mathrm{k\Omega}$ input resistance. This offset additionally depended on the input impedance presented to the op-amp. The sinusoidal shape superimposed on the parabola is inherent to the architecture of the ADC and also shown in

the datasheet [139]. The parabola was stable over several weeks and tested multiple times, to ensure it can be calibrated out. The same parabola was also found with other temperature controller front end boards using the same topology. To rule out a drift with temperature, the INL was also tested at both $20\,°C$ and $30\,°C$ which also showed negligible difference.

4.4.4. Test Results: Temperature Stability

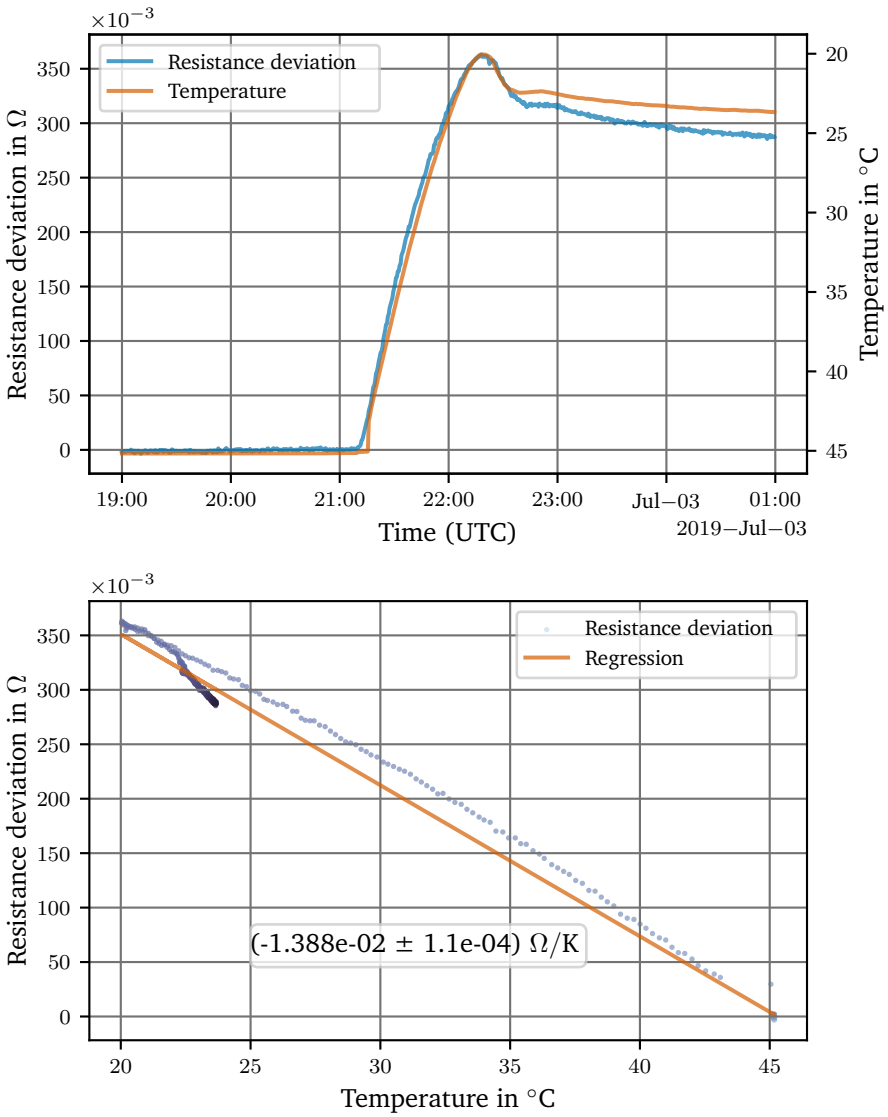

Figure 4.61.: Temperature coefficient of the temperature controller front end. Measured by stepping the ambient temperature by $22\,K$ while measuring a $10\,k\Omega$ reference resistor located outside the thermal chamber.

The temperature stability of the analog front end was also investigated. To give a realistic impression, a $10\,k\Omega$ reference resistor (ab-precision `RS2-10k`) was used to simulate a thermistor. The temperature controller was then placed inside a thermal chamber while measuring the

resistance of the reference resistor located outside of the chamber. The temperature was stepped from $23\,°C$ to $45\,°C$ ambient temperature. The results are shown in figure 4.61.

With the autozero function enabled a result of $(-13.9 \pm 0.1)\,m\Omega/K$ was measured, the equivalent of $-40\,\mu K/K$. Related to full scale input that is $-0.17\,ppm/K$, which can be attributed to the drift of the current source sense resistor. Form this result it can be inferred that the ambient temperature of the lab has little to no influence on the setpoint of the controller.

4.4.5. Test Results: Long-term stability

The final aspect tested was the long-term stability of the analog front end. For this test, the controller was left in the thermal chamber while CH1 was measuring the $10\,k\Omega$ `RS2-10k` reference resistor and CH2 was connected to the internal reference resistor. The thermal chamber did not contain a dry pouch, and the ambient humidity was therefore uncontrolled. This revealed a small dependence on said ambient humidity. The magnitude of the drift is similar for both channels and indicates that either the ADC gain or the sense resistor of the current source is affected by humidity. The most likely source is the $100\,k\Omega$ Vishay `S102` molded epoxy sense resistor. It is the only part that is not connected in a ratio configuration and therefore its drift is not attenuated in any way. The cause of the drift is the epoxy resin, which swells when exposed to humidity [105]. This puts pressure on the resistive element, which then changes its resistance.

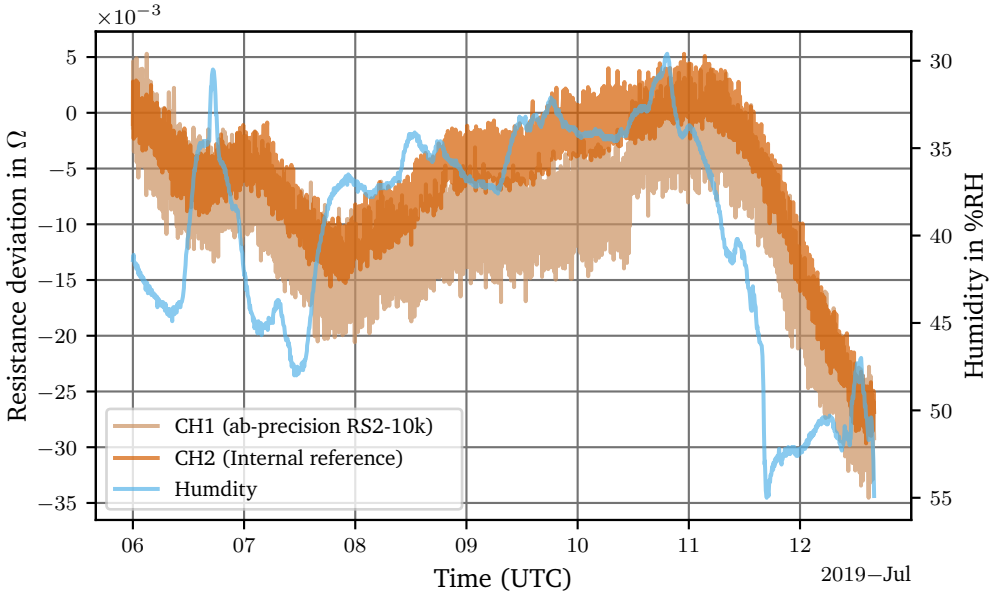

Figure 4.62.: Long-term comparison of the internal reference resistor against an external $10\,k\Omega$ reference.

This sensitivity can either be addressed in hardware by replacing the current source sense resistor with a hermetic version, or a software solution can be applied by activating the autocalibration routine in regular intervals. The device can then recalibrate itself using the internal hermetic reference resistor.

Nonetheless, the sensitivity to humidity is on the order of $80\,\mu K$ between $30\,\%RH$ and $60\,\%RH$, which is close to the full swing of the lab. The noise of the individual channels is $1.65\,m\Omega_{rms}$ for

the external channel and $0.89\,\mathrm{m\Omega_{rms}}$ for the internal channel, which is equivalent to $4.1\,\mathrm{\mu K_{rms}}$ and $2.2\,\mathrm{\mu K_{rms}}$ at $20\,^{\circ}\mathrm{C}$ respectively. This is all well below the requirements listed in table 3.4.

4.4.6. Output Driver

The output driver of the temperature controller is based on an ADI LT8714 bipolar DC/DC regulator that is designed for a maximum output of $\pm 12\,\mathrm{V}$ and $\pm 5\,\mathrm{A}$. Two of these controllers were integrated on a PCB. Using a DC/DC regulator instead of an H-bridge configuration has the advantage that the higher switching frequency of $300\,\mathrm{kHz}$ can be filtered more easily than a switching frequency on the order of a few kHz typically found in H-Bridge designs. The DC/DC regulator can be supplied with a input voltage of up to $20\,\mathrm{V}$ which reduces the required supply current accordingly. This allows to integrate more devices into a subrack powered by the same power supply. The output driver board also houses the microcontroller which is connected to the analog board via digital isolators to reduce the noise coupled into the analog side. Both boards were tested together and a laser resonator was temperature controlled for a test. This revealed a first problem. The laser resonators used in the APQ group are housed in an aluminium case that is not airtight. This allowed air drafts to considerably affect the resonator temperature. Even walking past the laser resonator caused temperature swings of $\pm 1.5\,\mathrm{mK}$ or more.

To address this issue, the laser was additionally shielded using a silicone sleeve that is put around the external laser resonator housing. The silicone sleeve was molded in house using a 3D printed replica of the laser resonator. The type of silicone used is an RTV2 platinum silicone with a shore hardness of $32\,\mathrm{ShoreA}$. This extra protection reduced the disturbances by half and the result is shown in figure 4.63

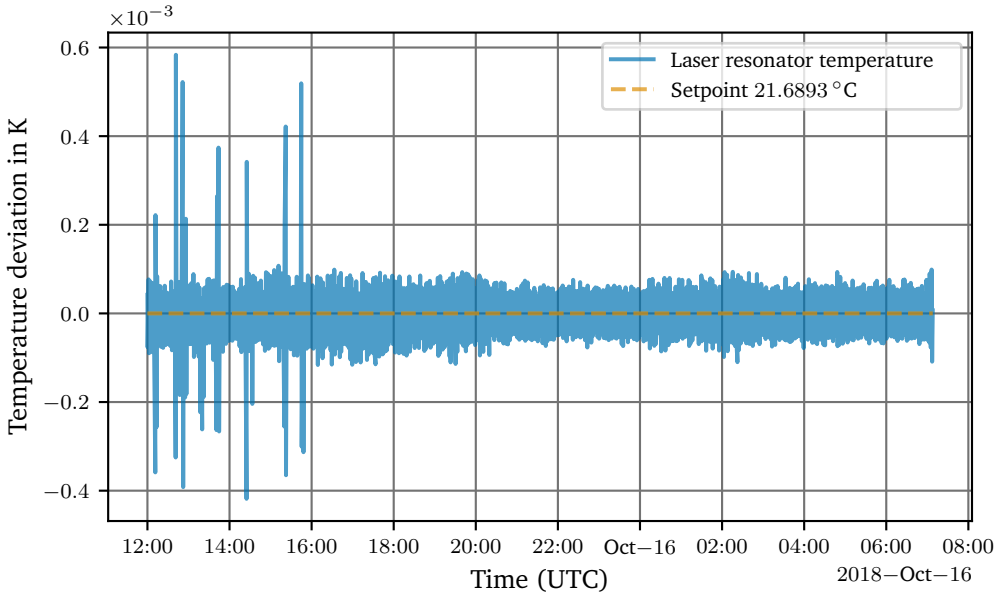

Figure 4.63.: Stability of a temperature controlled laser resonator. The disturbances are caused by air drafts that rapidly change the temperature of the outer aluminium housing.

The temperature controller typically keeps the resonator within $\pm 150\,\mathrm{\mu K}$ and the only

problem are the disturbances causes by drafts due to people working in the vicinity. To rule out the controller as the source of the problem, an aluminium block used as a test mass was placed inside a thermal chamber and a Keysight 3458A was used to read the voltage across the 10 kΩ thermistor also monitored by the temperature controller. The thermistor attached to the test mass was a calibrated Fluke 5611T-P 10 kΩ thermistor to rule out any problems like burst noise coming from the thermistor itself. Additionally, the temperature inside the chamber was swept from 20 °C to 15 °C to observe the temperature suppression of the controller.

The first observation made was that the disturbances observed in figure 4.63 were no longer present for as long as the internal fan was turned off and there was only natural convection present. As soon as the fan was turned on, the same noise as before could be observed. This gives a strong indication, that turbulent air is a major factor for the temperature noise seen in figure 4.63. The overall noise without the fan was also discovered to be lower than in figure 4.63. Whether this is due to the Fluke 5611T-P thermistor or the additional shielding of the thermal chamber was not investigated because both noise figures are well below the required 1 mK target.

Additionally, using the thermal chamber the gain of the controller was estimated. To do so, a 5 K temperature step was applied while the controller tried to keep the temperature stable. As can be seen an apparent error of about 100 µK remains. This allows to estimate the controller gain to be about 50×10^3 K/K. Do note, at this point there is an enormous uncertainty associated with this value because the voltage difference measured by the 3458A is only 2.5 µV. The measurement with the 3458A does not compensate for thermal EMF and 500 nV/K can easily be introduced by one or more metal-to-metal junctions between the sensor and the DMM. See [96] for a list of Peltier voltages created by different metals.

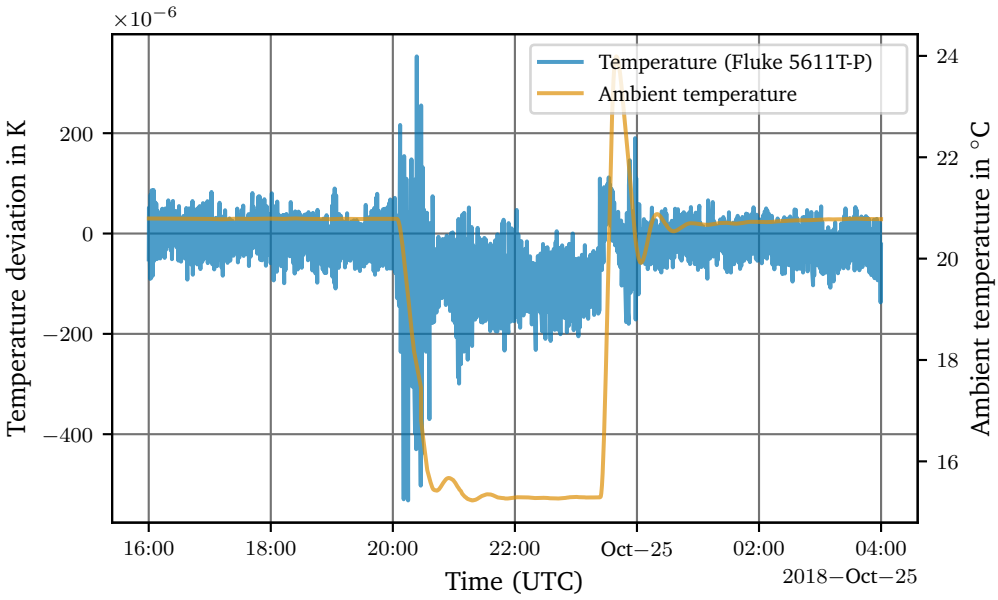

Figure 4.64.: Measurement of the gain of the PID controller. The voltage across the sense thermistor of the PID controller is measured by a Keysight 3458A and the temperature is stepped 5 K.

To further improve the stability of the laser resonators, the problem must be addressed in the future with an updated resonator design. For a high stability design it is imperative that

the resonator is, at least to some degree, air tight. An experimental version of such a laser was designed for the ARTEMIS experiment [151] and is currently part of the laser system. Using an airtight resonator also improves the noise immunity against acoustics as demonstrated by Cook et al. [54].

4.4.7. Summary

A high precision temperature controller with two $12\,\mathrm{V}$, $5\,\mathrm{A}$ channels was presented. An input noise of $1.65\,\mathrm{m\Omega_{rms}}$ at a sampling frequency of $\frac{1}{6}$ Hz resulting in a temperature noise of $4.1\,\mathrm{\mu K_{rms}}$ at $20\,^\circ\mathrm{C}$ was demonstrated. With a non-linearity of $<1\,\mathrm{\mu V/V}$ and an internal reference resistor, calibration of the instrument is as simple as having a resistor of a known value. It was shown that the system brings the current mechanical laser resonator design to its limits because air drafts can introduce considerable noise that cannot be suppressed due to the fast transients created. The performance of the laser system is therefore defined by the mechanical stability of the resonator. To improve the situation an airtight laser resonator is recommended and the benefits of such a construction are shown.

The temperature controller was also tested in a variety of environmental conditions and a suppression of ambient temperature fluctuations of 2×10^{-5} was derived from those tests albeit with considerable uncertainty due to the limited test setup. With a sensitivity of $4.1\,\mathrm{\mu K_{rms}}$ and a humidity drift of $2.8\,\mathrm{\mu K/\%RH}$ without autocalibration, the temperature controller is at the same level of accuracy as high stability thermistors that were shown to drift about $100\,\mathrm{\mu K/a}$ [73].

Device Properties 4.10: Temperature controller properties

- Two channels
- Supports $10\,\mathrm{k\Omega}$ thermistors
- Digital PID controller
- Autocalibration
- Output with $\pm 12\,\mathrm{V}$ and $\pm 5\,\mathrm{A}$
- Controllable temperature range 0 to $60\,^\circ\mathrm{C}$
- Measurement noise of $1.65\,\mathrm{m\Omega_{rms}}$
- Temperature noise of $4.1\,\mathrm{\mu K_{rms}}/18.5\,\mathrm{\mu K_{rms}}$ at $20\,^\circ\mathrm{C}/60\,^\circ\mathrm{C}$
- Linearity better than $\pm 0.5\,\mathrm{\mu\Omega/\Omega}$
- Stability over a week $<50\,\mathrm{m\Omega}$
- Temperature coefficient $<15\,\mathrm{m\Omega/(\Omega\,K)}$
- Ambient temperature suppression $20\,\mathrm{\mu K/K}$

4.5. Laser System

As discussed in section 3.1 the weak link of the laser system is the transfer resonator. In order address this problem the laser system was reworked and additionally a third laser was prepared for the upgraded system. The new system is shown in figure 4.65.

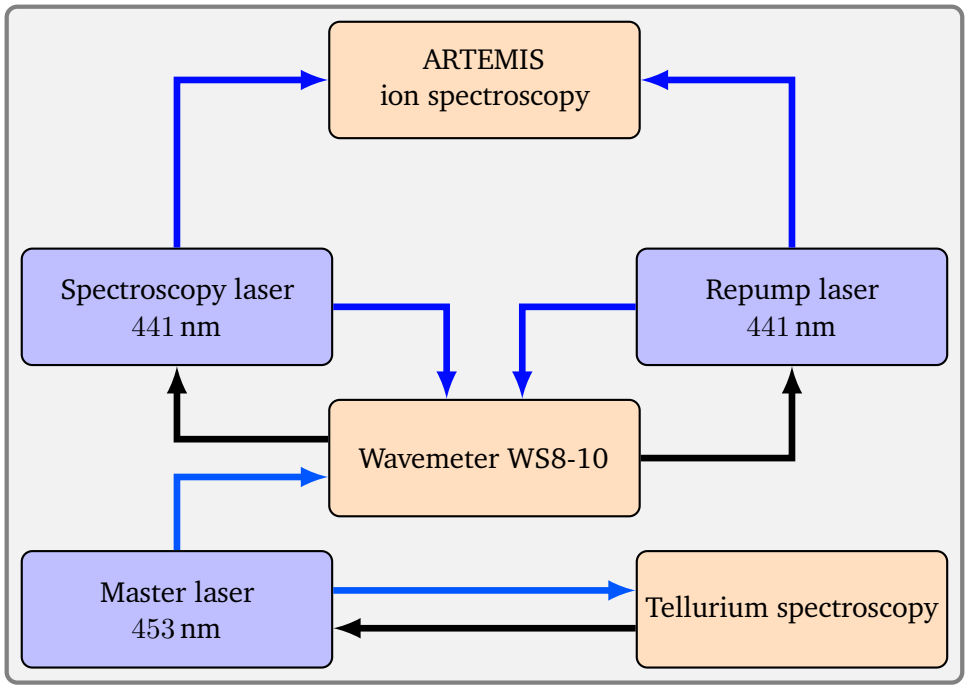

Figure 4.65.: Simplified setup of the laser system currently being set up for the ARTEMIS experiment. The wavemeter is undergoing commissioning to determine its stability. Blue arrows denote light paths. Black arrows are electronic control signals.

Having two lasers at 441 nm the laser-microwave double-resonance spectroscopy of highly charged Ar^{13+} can be attempted as discussed in section 3.1. One spectroscopy laser is a Toptica `DL 100 pro` which was also used in the old system and was already characterised by Martin [150]. The new laser is a Newport `Vantage TLB-7100` running at 441.15 nm. The third laser is taken from the old system as well and was characterised by Baus [31]. It is the master reference laser that is locked to the tellurium reference at 453 nm. This laser is used as the calibration reference for a HighFinesse `WS8-10` high precision wavemeter [248]. The wavemeter replaces the transfer resonator previously employed. This wavemeter features a 4-port optical switch to simultaneously measure the wavelength of up four lasers. Additionally, it comes with a PID controller for up to two lasers. The new locking scheme is much cleaner than the old system because the three lasers are now fiber-coupled to the transfer wavemeter. This ensure a higher reliability of the system as it is less susceptible to environmental factors like ambient temperature.

The Wavemeter is specified for an accuracy of 10 MHz which, on paper, is less than the accuracy of the legacy transfer resonator, which was estimated to be 2.2 MHz [150]. Preliminary tests conducted at 780 nm have shown that the wavemeter is far more stable than alleged by the datasheet. Since this accuracy defines later spectroscopy results, the wavemeter is currently

undergoing additional commissioning to determine the actual stability that can be expected given typical experimental parameters. The commissioning is a two step process and the wavemeter will be tested in two different wavelength regions. The aforementioned $780\,\mathrm{nm}$ and the $441\,\mathrm{nm}$ used by ARTEMIS experiment.

The APQ group maintains several laser systems at $780\,\mathrm{nm}$ that are locked to the rubidium $^{85}\mathrm{Rb}$ D_2 line. These system have been continuously monitored with the LabKraken system since 2022-06. A typical stability of the wavelength well below $100\,\mathrm{kHz}$ was observed by Preuschoff [176]. After recent upgrades to improve the stability of the laser power going into the spectroscopy, a stability of $<10\,\mathrm{kHz_{rms}}$ over more than two weeks can be reported as well. These two lasers and another laser at $795\,\mathrm{nm}$ locked to the $^{85}\mathrm{Rb}$ D_1 line will be used in the first step as these lasers have a known history and an upper bound for their stability can be easily given. The next step is a similar configuration using the ARTEMIS master laser locked to the tellurium transition at $452.756\,\mathrm{nm}$ [194]. The two lasers running at $441\,\mathrm{nm}$ will then be locked to the tellurium transition at $441.807\,\mathrm{nm}$, which can be found as line number 1855 in the tellurium atlas charted by Scholl et al. [194].

After the commissioning the new system is expected to reach a similar accuracy as the transfer resonator albeit being far easier to handle and being more versatile because the `WS8-10` is also intended to be used for the proposed spectroscopy of highly charged Krypton Kr^{17+} at $636.9\,\mathrm{nm}$ [93, 135], once the commissioning of ARTEMIS with Ar^{13+} is completed.

5. Discussion and Future Perspective

This work has pushed the boundaries of diode laser systems to a new level. Diode lasers built using the technology presented in this work will see their limits in the mechanical design rather than the control electronics. The design presented allows precision laser spectroscopy even in the presence of adverse environmental conditions that would otherwise pose serious challenges to the experimenter.

The development of such high precision devices as they are typically required for university labs has become more challenging over the recent years due to the decline in availability of many electronic parts. These shortages mostly affect microcontrollers and power electronics. It is the authors desire to make the instruments presented in this work available to the public via an open-source contribution of the design files and also to keep them available. This necessitates a few updates to the designs to make them more resilient to supply chain issues. The author proposes the following changes to the designs presented in this work.

The `DgDrive` laser current driver should be modified with the careful addition of an FPGA on the analog side to simplify the digital isolation between the front panel and the analog electronics. Recent developments have demonstrated that reducing the number of critical components like the digital isolators makes the construction more resilient to the varying supply and requires less requalification when replacing unavailable parts. The use of an FPGA can also simplify many of the logic elements on the board by bringing them into the FPGA core. Being able to change this logic software also improves the compatibility with future part changes. The FGPA also allows for smaller and simpler microcontroller, giving more options when adapting to supply changes. Another interesting new development that is currently pursued is the integration of the new ADI `ADR1399` reference Zener diode which has shown promising results regarding the burst noise issue as well as deliver a lower floor. Given those early results future batches of the current driver may not even need the additional screening process of the Zener diodes discussed in section 4.1.13. This would greatly simplify the manufacturing process in terms of hardware and time required.

Much of the same as said above can be said about the temperature controller. The supply situation is even more dire in this case, because many of the specialised parts come with tight specifications. For example the `LTC2508-32` ADC used in the analog front end is explicitly tailored to the microcontroller. Adding an FPGA front end for the ADCs can greatly simplify and even improve the performance of the system as it is right now. With the advent of new high performance ADCs in recent years an FPGA also gives the needed flexibility when choosing suitable substations if the need arises. The work on these changes was already started, but is not yet finalised.

Regarding the driver board of the temperature controller, the availability of the new ADI `LT8722` TEC driver is much anticipated because it integrates many of the components used on the driver board into a single chip allowing a simpler design, reducing the production cost and complexity. This presents a key feature to further the widespread adoption of the design.

These developments are independent of the benefits than can already be reaped from the designs currently available. The new laser system built for the ARTEMIS experiment is

expected to deliver the much desired stability for the spectroscopy of Ar^{13+}. Clearing the commissioning of the Penning trap is major step forward and and also opens up the road towards the spectroscopy of Bismuth ($^{209}Bi^{82+}$) as the new electronics can provide the needed stability for the seed laser at 976 nm. Parts of this system integrating the new electronic are currently being performance tested. Some of this work was already presented in [176].

Additionally, the new control electronics allows the use of a wide variety of modern laser diodes and opens up other experimental avenues like the spectroscopy of highly charged Krypton Kr^{17+} at 636.9 nm [93, 135].

A final aspect that has come up with the new electronics are the limits of the mechanical design of the laser resonators. While not surprising, the unsealed laser makes for a good barometer as shown in figure 5.1.

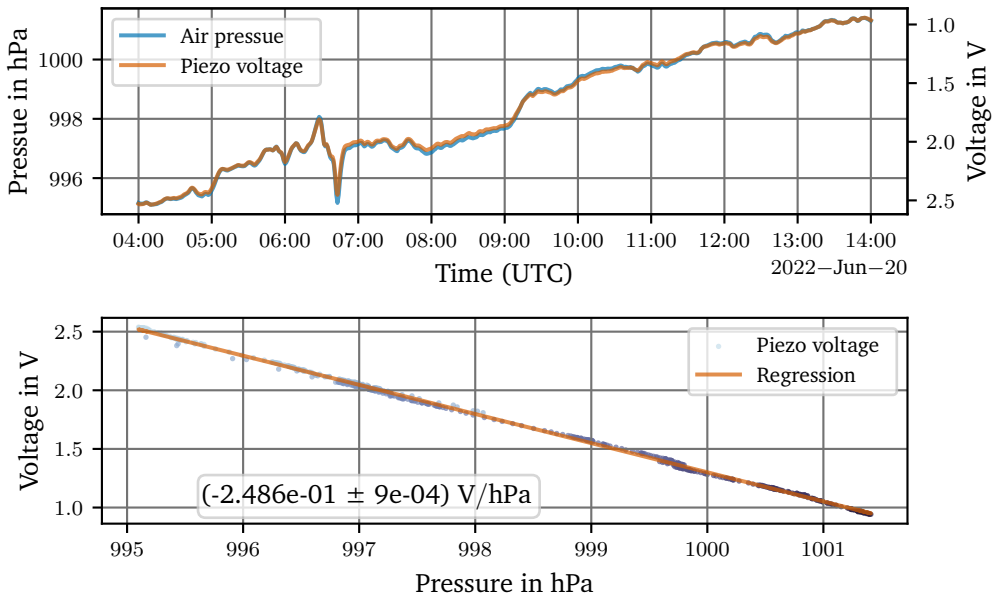

Figure 5.1.: A 780 nm laser locked to the rubidium ^{85}Rb D_2 line. The piezo mounted inside the resonator moves the back reflecting mirror to follow the air pressure and to keep the laser frequency locked to the rubidium transition. The piezo voltage closely follows the changes in air pressure.

An o-ring seal, like demonstrated by [54], can improve the stability of the diode lasers and ensure the performance of the system becomes insensitive to weather conditions. In addition, the ample use of epoxy resin inside the resonator causes a sensitivity to humidity as the epoxy resin swells when exposed to water [105]. Preuschoff [176] already presented major improvements by presenting a mechanical mount for the collimation lens, but both the back reflecting mirror and the lenses forming the *cat-eye* [28] are fastened using epoxy resin. The currently employed technique of using silica gel to maintain a constant humidity should be superseded by a more permanent solution. A sealed resonator can therefore add an import part to the day-to-day stability of the experiments.

References

[1] *300144Z (Z-Foil) - Vishay Foil Resistors*. Vishay Precision Group, Inc. Sept. 2013. URL: https://foilresistors.com/docs/63115/144z145z.pdf.

[2] *6630B Series Single-Output, 80-100 W GPIB Power Supplies*. Keysight Technologies. URL: https://www.keysight.com/de/de/assets/7018-03200/data-sheets/5990-9303.pdf.

[3] *7808A Datasheet - 50 Ohm Wireless Transmission Coax, RF 240, RG58X, 15 AWG Solid BC, Foil + 95% TC Braid, PE Jkt*. 0.438. Belden Inc. Sept. 2022. URL: https://catalog.belden.com/techdata/EN/7808A%5C_techdata.pdf.

[4] *8100 Series - 8104 Extended Specifications*. 1.1. Transmille Ltd. URL: https://www.transmille.com/file%5C_upload/8104-Extended-Specifications-V1-1.pdf.

[5] *8588A Reference Multimeter - Product Specifications*. rev. G. Fluke Corporation. Aug. 2022. URL: https://us.flukecal.com/literature/product-literature/specifications/8588a-product-specifications.

[6] *AD5681R Data Sheet - Tiny 16-/14-/12-Bit SPI nanoDAC+, with ±2 (16-Bit) LSB INL and 2 ppm/°C Reference*. D. Analog Devices Inc. Dec. 2016. URL: https://www.analog.com/media/en/technical-documentation/data-sheets/AD5683R_5682R_5681R_5683.pdf.

[7] *AD5760 Data Sheet - 0Ultra Stable, 16-Bit ±0.5 LSB INL, Voltage Output DAC*. F. Analog Devices Inc. Apr. 2018. URL: https://www.analog.com/media/en/technical-documentation/data-sheets/ltc6655-6655ln.pdf.

[8] *AD5781 Data Sheet - True 18-Bit, Voltage Output DAC*. E. Analog Devices Inc. Apr. 2018. URL: https://www.analog.com/media/en/technical-documentation/data-sheets/AD5781.pdf.

[9] *AD797 Data Sheet - Ultralow Distortion, Ultralow Noise Op Amp*. K. Analog Devices Inc. Mar. 2015. URL: https://www.analog.com/media/en/technical-documentation/data-sheets/AD797.pdf.

[10] *AD8672 Data Sheet - Precision, Very Low Noise, Low Input Bias Current Operational Amplifiers*. F. Analog Devices Inc. Mar. 2015. URL: https://www.analog.com/media/en/technical-documentation/data-sheets/AD8671_8672_8674.pdf.

[11] *AD8676 Data Sheet - Ultraprecision, 36 V, Dual Rail-to-Rail Output Op Amp*. C. Analog Devices Inc. Aug. 2011. URL: https://www.analog.com/media/en/technical-documentation/data-sheets/AD8676.pdf.

[12] *ADA4077-4 Data Sheet - Low Offset and Drift, High Precision Amplifiers*. F. Analog Devices Inc. Aug. 2022. URL: https://www.analog.com/media/en/technical-documentation/data-sheets/ada4077-1_4077-2_4077-4.pdf.

[13] *ADA4625-1 Data Sheet - Low Noise, Fast Settling Single Supply, RRO, JFET Op Amp*. 0th ed. Analog Devices Inc. Oct. 2017. URL: https://www.analog.com/media/en/technical-documentation/data-sheets/ADA4625-1.pdf.

[14] *ADL-78901TX Datasheet*. 0th ed. Arima Lasers Corporation.

[15] *ADR1399 Data Sheet - Oven-Compensated, Buried Zener, 7.05 V Voltage Reference*. A. Analog Devices Inc. Mar. 2022. URL: https://www.analog.com/media/en/technical-documentation/data-sheets/adr1399.pdf.

[16] I Akasaki et al. "Shortest wavelength semiconductor laser diode". In: *Electronics Letters* 32.12 (June 1996), pp. 1105–1106. DOI: 10.1049/el:19960743.

[17] Isamu Akasaki et al. "Stimulated Emission by Current Injection from an AlGaN/GaN/GaInN Quantum Well Device". In: *Japanese Journal of Applied Physics* 34.11B (Nov. 1995), p. L1517. DOI: 10.7567/JJAP.34.L1517.

[18] Sebastian Albrecht. "Ein Lasersystem zur Spektroskopie von hochgeladenen Ionen, Tellurmolekülen und Rubidium-Rydberg-Zuständen". PhD thesis. Darmstadt: Technische Universität Darmstadt, Aug. 2014. URL: http://tuprints.ulb.tu-darmstadt.de/3906/.

[19] David W. Allan. "Statistics of atomic frequency standards". In: *Proceedings of the IEEE* 54.2 (Feb. 1966), pp. 221–230. DOI: 10.1109/PROC.1966.4634.

[20] David W. Allan. "Should the classical variance be used as a basic measure in standards metrology?" In: *IEEE Transactions on Instrumentation and Measurement* IM-36.2 (June 1987), pp. 646–654. DOI: 10.1109/TIM.1987.6312761.

[21] Phillip E. Allen and Douglas R. Holberg. *CMOS Analog Circuit Design*. 3rd ed. Oxford University Press, USA, Aug. 2011, p. 784. DOI: 10.1016/0167-9260(88)90044-2.

[22] T. Aoyama et al. "Automated calculation scheme for αn contributions of QED to lepton g−2: Generating renormalized amplitudes for diagrams without lepton loops". In: *Nuclear Physics B* 740.1 (Apr. 2006), pp. 138–180. DOI: 10.1016/j.nuclphysb.2006.01.040.

[23] Tatsumi Aoyama, Toichiro Kinoshita, and Makiko Nio. "Theory of the Anomalous Magnetic Moment of the Electron". In: *Atoms* 7.1 (Feb. 2019). DOI: 10.3390/atoms7010028.

[24] Jürgen Appel, Andrew MacRae, and A I Lvovsky. "A versatile digital GHz phase lock for external cavity diode lasers". In: *Measurement Science and Technology* 20.5 (Apr. 2009). DOI: 10.1088/0957-0233/20/5/055302.

[25] C. Arnaboldi et al. "Very low noise AC/DC power supply systems for large detector arrays". In: *Review of Scientific Instruments* 86.12 (Dec. 2015), p. 124703. DOI: 10.1063/1.4936269.

[26] K.J. Åström and R.M. Murray. *Feedback Systems. An Introduction for Scientists and Engineers*. 2nd ed. Princeton University Press, July 2020. DOI: 10.2307/j.ctvcm4gdk. URL: https://fbswiki.org/wiki/index.php/Feedback_Systems:_An_Introduction_for_Scientists_and_Engineers.

[27] Karl Johan Åström and Tore Hägglund. *Advanced PID Control*. English. ISA - The Instrumentation, Systems and Automation Society, 2006.

[28] X. Baillard et al. "Interference-filter-stabilized external-cavity diode lasers". In: *Optics Communications* 266.2 (May 2006). DOI: 10.1016/j.optcom.2006.05.011.

[29] Roger Barlow. *Asymmetric Errors*. Jan. 2004. DOI: 10.48550/arXiv.physics/0401042. URL: https://www.slac.stanford.edu/econf/C030908/papers/WEMT002.pdf.

[30] James A. Barnes et al. “Characterization of Frequency Stability”. In: *IEEE Transactions on Instrumentation and Measurement* IM-20.2 (May 1971), pp. 105–120. DOI: 10.1109/TIM.1971.5570702.

[31] Patrick Baus. “Characterization of a Wide Tunable, Robust, Multi Application Diode Laser for Spectroscopy”. MA thesis. Technische Universität Darmstadt, 2014.

[32] Patrick Baus. *LM399 sub-ppm Reference Voltage*. Version 3.3.0. May 2021. URL: https://github.com/TU-Darmstadt-APQ/Voltage_reference.

[33] Patrick Baus. *TinkerforgeAsync*. Version 1.2.0. July 2021. URL: https://github.com/PatrickBaus/TinkerforgeAsync.

[34] Patrick Baus. *Keithley SCAN2000 SSR Replacement*. Version 2.0.1. Feb. 2022. URL: https://github.com/PatrickBaus/SCAN2000.

[35] Patrick Baus. *Labnode - A Laboratory Temperature Controller*. Version 1.4.1. Jan. 2022. URL: https://github.com/TU-Darmstadt-APQ/Labnode_PID.

[36] Patrick Baus. *LabNode Python API*. Version 0.16.1. Sept. 2022. URL: https://github.com/PatrickBaus/labnode_async.

[37] Patrick Baus. *Line Injector*. Version 1.0.1. July 2022. URL: https://github.com/PatrickBaus/line_injector.

[38] Patrick Baus. *PID-CPP*. Version 1.0.0. Apr. 2022. URL: https://github.com/PatrickBaus/PID-CPP.

[39] Patrick Baus. *19 Inch DIN 41612 Backplane*. Version 1.0.0. Mar. 2023. URL: https://github.com/TU-Darmstadt-APQ/DIN_41612_Backplane.

[40] Patrick Baus. *ADR399/LM399 Burnin Board*. Version 1.0.1. May 2023. URL: https://github.com/TU-Darmstadt-APQ/LM399_Burnin_Board.

[41] Patrick Baus. *Kraken Labdeamon*. Version 4.2.1. May 2023. URL: https://github.com/PatrickBaus/sensorDaemon.

[42] Patrick Baus. *Simulation Scripts for the PhD Thesis*. 2023. URL: https://github.com/PatrickBaus/phd_supplemental.

[43] Patrick Baus. *Ultrastable, ultra low noise digital laser current controller*. Version 2.3.0. Mar. 2023. URL: https://github.com/TU-Darmstadt-APQ/DgDrive.

[44] Nikolai Beev. “Measurement of Excess Noise in Thin Film and Metal Foil Resistor Networks”. In: *2022 IEEE International Instrumentation and Measurement Technology Conference (I2MTC)*. May 2022, pp. 1–6. DOI: 10.1109/I2MTC48687.2022.9806690.

[45] Alexander Bordodynov. *Bordodynov’s Electronics*. 2022. URL: http://bordodynov.ltwiki.org (visited on 12/06/2022).

[46] Carsten Bormann and Paul E. Hoffman. *Concise Binary Object Representation (CBOR)*. RFC 8949. Dec. 2020. DOI: 10.17487/RFC8949.

[47] Tim Bray. *The JavaScript Object Notation (JSON) Data Interchange Format*. RFC 8259. Dec. 2017. DOI: 10.17487/RFC8259.

[48] G. Breglio et al. “Electro-thermal instability in low voltage power MOS: Experimental characterization”. In: *11th International Symposium on Power Semiconductor Devices and ICs. ISPSD’99 Proceedings (Cat. No.99CH36312)*. May 1999, pp. 233–236. DOI: 10.1109/ISPSD.1999.764106.

[49] Colin D. Bruzewicz et al. “Trapped-ion quantum computing: Progress and challenges”. In: *Applied Physics Reviews* 6.2 (May 2019). DOI: 10.1063/1.5088164.

[50] *BUK7S1R5 Data Sheet - N-channel 40 V, 1.5 mΩ standard level MOSFET in LFPAK88*. Nexperia B.V. Aug. 2002. URL: https://assets.nexperia.com/documents/data-sheet/BUK7S1R5-40H.pdf.

[51] Michael S. Cafferty and Eric D. Thompson. “Stable current supply with protection circuits for a lead-salt laser diode”. In: *Review of Scientific Instruments* 60.9 (Sept. 1989), pp. 2896–2901. DOI: 10.1063/1.1140625.

[52] Ondřej Čertík et al. *SymPy*. 2023. URL: https://www.sympy.org/en/index.html (visited on 04/07/2023).

[53] Philip E. Ciddor and Reginald J. Hill. “Refractive index of air. 2. Group index”. In: *Appl. Opt.* 38.9 (Mar. 1999). DOI: 10.1364/AO.38.001663.

[54] Eryn C. Cook et al. “High passive-stability diode-laser design for use in atomic-physics experiments”. In: *Review of Scientific Instruments* 83.4 (Apr. 2012), p. 043101. DOI: 10.1063/1.3698003.

[55] K.B. Cook and A.J. Brodersen. “Physical origins of burst noise in transistors”. In: *Solid-State Electronics* 14.12 (Dec. 1971), pp. 1237–1242. DOI: 10.1016/0038-1101(71)90112-2.

[56] B. Cordell. *Designing Audio Power Amplifiers*. 2nd ed. Focal Press. Routledge, June 2019, p. 792.

[57] THAT Corporation. *SPICE Macro Models*. 2023. URL: https://thatcorp.com/wp-content/uploads/2020/11/THATMacroModels-Rev05.zip (visited on 05/02/2023).

[58] Robert B. Cowdell. “Unscrambling the Mysteries About Twisted Wire”. In: *1979 IEEE International Symposium on Electromagnetic Compatibility*. Oct. 1979, pp. 1–8. DOI: 10.1109/ISEMC.1979.7568810.

[59] *CP14-127-06-L1-W4.5 Data Sheet - Ceramic Plate Series Thermoelectric Coolere*. 0th ed. Laird Thermal Systems Inc. Jan. 2022. URL: https://lairdthermal.com/products/thermoelectric-cooler-modules/peltier-cp-series/CP14-127-06-L1-W4.5/pdf/.

[60] S. Cuk and R.D. Middlebrook. *Advances in Switched-mode Power Conversion: Modelling, analysis and measurement*. Bd. 1. TESLAco, 1981.

[61] S. Ćuk. *Power Electronics: Modeling, Analysis and Measurements*. Vol. 2. Power Electronics. CreateSpace Independent Publishing Platform, Dec. 2015. Chap. 10, p. 272.

[62] *D2-105 Laser Controller*. Vescent Photonics LLC. Nov. 2020. URL: https://vescent.com/amfile/file/download/file/30/product/56/.

[63] *DAC91001 Data Sheet - 18-Bit, Low-Noise, Ultra-Low Harmonic Distortion, FastSettling, High-Voltage Output, Digital-to-Analog Converter*. B. Texas Instruments Inc. June 2020. URL: https://www.ti.com/lit/ds/symlink/dac91001.pdf.

[64] *Data Sheet J2101A 10Hz-45MHz Injection Transformer*. 2.0. Picotest Corporation. Feb. 2011. URL: https://www.picotest.com/images/download/J2100A-J2101A%5C_Spec%5C_Sheet%5C_FinalV2%5C_Email-2.pdf.

[65] *Data Sheet VP0106 P-Channel Enhancement-Mode Vertical DMOS FET*. A. Microchip Technology Inc. Apr. 2022. URL: https://ww1.microchip.com/downloads/en/DeviceDoc/VP0106-P-Channel-Enhancement-Mode-Vertical-DMOS-FET-Data-Sheet-20006658A.pdf.

[66] Samuel T. Dawkins, John J. McFerran, and Andre N. Luiten. "Considerations on the measurement of the stability of oscillators with frequency counters". In: *IEEE Transactions on Ultrasonics, Ferroelectrics, and Frequency Control* 54.5 (May 2007), pp. 918–925. DOI: 10.1109/TUFFC.2007.337.

[67] General Electric Company. Semiconductor Products Dept. *GE Transistor Manual*. 7th ed. 1964.

[68] A. Van Der Ziel. "Thermal Noise in Field-Effect Transistors". In: *Proceedings of the IRE* 50.8 (Aug. 1962), pp. 1808–1812. DOI: 10.1109/JRPROC.1962.288221.

[69] Lane Desborough and Randy Miller. "Increasing Customer Value of Industrial Control Performance Monitoring — Honeywell's Experience". In: Jan. 2002. URL: https://folk.ntnu.no/skoge/prost/proceedings/cpc6-jan2002/desborough.pdf.

[70] *Digital Multimeters - 34460A, 34461A, 34465A (6½ digit), 34470A (7½ digit)*. Keysight Technologies. June 2022. URL: https://www.keysight.com/us/en/assets/7018-03846/data-sheets/5991-1983.pdf.

[71] Edsger W. Dijkstra. "Cooperating Sequential Processes". In: *The Origin of Concurrent Programming: From Semaphores to Remote Procedure Calls*. Ed. by Per Brinch Hansen. New York, NY: Springer New York, May 2002, pp. 65–138. DOI: 10.1007/978-1-4757-3472-0_2.

[72] *DMN6040SSD Data Sheet - Dual N-Channel Enhancement Mode MOSFET*. 5 - 2. Diodes Inc. Nov. 2016. URL: https://www.diodes.com/assets/Datasheets/DMN6040SSD.pdf.

[73] Jr. Dratler Jay. "A proportional thermostat with 10 microdegree stability". In: *Review of Scientific Instruments* 45.11 (Nov. 2003). DOI: 10.1063/1.1686523.

[74] P. Dutta and P. M. Horn. "Low-frequency fluctuations in solids: $\frac{1}{f}$ noise". In: *Rev. Mod. Phys.* 53 (3 July 1981), pp. 497–516. DOI: 10.1103/RevModPhys.53.497.

[75] Pieter Eendebak et al. *qtt*. 2022. URL: https://github.com/QuTech-Delft/qtt (visited on 11/03/2022).

[76] *EMO T - Stellantriebe, Thermischer Zweipunkt-Stellantrieb*. IMI Hydronic Engineering Deutschland GmbH. Aug. 2019. URL: https://assets.imi-hydronic.com/Documents/Catalogues/German%5C_Int/PDF%5C_low/EMO-T%5C_IN%5C_DE%5C_low.pdf.

[77] Christopher J. Erickson et al. "An ultrahigh stability, low-noise laser current driver with digital control". In: *Review of Scientific Instruments* 79.7 (July 2008), p. 073107. DOI: 10.1063/1.2953597.

[78] D. M. Fleetwood. "Origins of 1/f Noise in Electronic Materials and Devices: A Historical Perspective". In: *Noise in Nanoscale Semiconductor Devices*. Ed. by Tibor Grasser. Springer International Publishing, Apr. 2020, pp. 1–31. DOI: 10.1007/978-3-030-37500-3_1.

[79] D. M. Fleetwood, T. Postel, and N. Giordano. "Temperature dependence of the 1/f noise of carbon resistors". In: *Journal of Applied Physics* 56.11 (1984), pp. 3256–3260. DOI: 10.1063/1.333845.

[80] Nathan Flowers-Jacobs et al. *The NIST Johnson noise thermometry system for the determination of the Boltzmann constant*. en. Dec. 2017. DOI: 10.6028/jres.122.046. URL: https://tsapps.nist.gov/publication/get_pdf.cfm?pub_id=923576.

[81] James B. Forsythe. "Paralleling Of Power MOSFETs For Higher Power Output". In: Infineon (formerly International Rectifier). URL: https://www.infineon.com/dgdl/para.pdf?fileId=5546d462533600a401535744b4583f79.

[82] Sergio Franco. *Design with Operational Amplifiers and Analog Integrated Circuits*. 3rd ed. McGraw-Hill, Inc., Aug. 2001.

[83] R. W. Franklin. *Analysis of Solid Tantalum Capacitor Leakage Current*. Technical paper. AVX, 1996. URL: https://www.avx.com/docs/techinfo/1_Analysis.pdf.

[84] Richard Frey. *New 500V Linear MOSFETs for a 120 kW Active Load*. Application note. Advanced Power Technology, June 2000. URL: https://www.microsemi.com/sites/default/files/micnotes/APT0002.pdf.

[85] Thorsten Führer. "Modellierung und Anwendung eines neuartigen Verfahrens zur aktiven Regelung und Kontrolle von Wellenlänge und Linienbreite eines Diodenlasers mit externem Resonator". PhD thesis. Darmstadt: Institut für Angewandte Physik der Technischen Universität Darmstadt, July 2012. URL: http://tuprints.ulb.tu-darmstadt.de/3060/.

[86] Thorsten Führer. *Ultra-Low Noise Current Controller LQprO*. TU darmstadt, Institut für Angewandte Physik, Laser und Quantenoptik. URL: https://www.iap.tu-darmstadt.de/media/iap_lqo/forschung_lqo/laser_development_lqo/LQO_datasheet.pdf.

[87] *GH0781JA2C Data Sheet*. Sharp Fukuyama Laser Co., Ltd.

[88] Gino Giusi et al. "Full Model and Characterization of Noise in Operational Amplifier". In: *IEEE Transactions on Circuits and Systems I: Regular Papers* 56.1 (Jan. 2009), pp. 97–102. DOI: 10.1109/TCSI.2008.927011.

[89] *GORE Ethernet Cables (4 Pairs, Cat5e/6/6a)*. W. L. Gore & Associates Inc. 2021. URL: https://www.gore.com/system/files/2021-11/GORE-Ethernet-Cables-4-Pairs-Data-Sheet-050121.pdf.

[90] Charles A. Greenhall. "Removal of drift from frequency stability measurements". In: *Telecommunications and Data Acquisition Progress Report* (Nov. 1981).

[91] Charles A. Greenhall. "Spectral ambiguity of Allan variance". In: *IEEE Transactions on Instrumentation and Measurement* 47.3 (June 1998), pp. 623–627. DOI: 10.1109/19.744312.

[92] M Grubič and U Würz. "High-precision low-cost temperature controller". In: *Journal of Physics E: Scientific Instruments* 11.7 (July 1978). DOI: 10.1088/0022-3735/11/7/025.

[93] Nicholas D. Guise et al. "Measurement of the Kr xviii $3d\,^2D_{5/2}$ lifetime at low energy in a unitary Penning trap". In: *Phys. Rev. A* 89 (4 Apr. 2014). DOI: 10.1103/PhysRevA.89.040502.

[94] Stewart M. Hansen. "Precision current control for quantum cascade lasers as flight calibration sources". MA thesis. Utah State University, Jan. 2014. DOI: 10.26076/bb34-2427.

[95] Ian Hegglun. *PAK Project*. 2022. URL: https://paklaunchsite.jimdofree.com/spice-models/ (visited on 12/06/2022).

[96] Paul Horowitz and Winfield Hill. *The Art of Electronics*. 3rd ed. Cambridge: Cambridge University Press, Apr. 2015, p. 1220.

[97] D.A. Howe. “An extension of the Allan variance with increased confidence at long term”. In: *Proceedings of the 1995 IEEE International Frequency Control Symposium (49th Annual Symposium)*. May 1995, pp. 321–329. DOI: 10.1109/FREQ.1995.483917.

[98] D.A. Howe. “The total deviation approach to long-term characterization of frequency stability”. In: *IEEE Transactions on Ultrasonics, Ferroelectrics, and Frequency Control* 47.5 (Sept. 2000). DOI: 10.1109/58.869040.

[99] David Howe. “Interpreting Oscillatory Frequency Stability Plots”. en. In: 2002 IEEE Intl. Freq. Cont. Symp , New Orleans, LA, Jan. 2002. URL: https://tsapps.nist.gov/publication/get_pdf.cfm?pub_id=105279.

[100] J. D. Hunter. “Matplotlib: A 2D graphics environment”. In: *Computing in Science & Engineering* 9.3 (June 2007), pp. 90–95. DOI: 10.1109/MCSE.2007.55.

[101] *INA821, Low-Power, Precision Instrumentation Amplifier*. D. Texas Instruments Inc. June 2020. URL: https://www.ti.com/lit/ds/symlink/ina821.pdf.

[102] Shuichiro Inoue, Seema Lathi, and Yoshihisa Yamamoto. “Longitudinal-mode-partition noise and amplitude squeezing in semiconductor lasers”. In: *J. Opt. Soc. Am. B* 14.11 (Nov. 1997). DOI: 10.1364/JOSAB.14.002761.

[103] *Generic Standard on Printed Board Design*. Standard. Bannockburn, USA: IPC International Inc., Nov. 2012.

[104] *IRF9610*. C. Vishay Siliconix. Aug. 2021. URL: https://www.vishay.com/docs/91080/91080.pdf.

[105] K.M.B. Jansen et al. “Effect of temperature and humidity on moisture diffusion in an epoxy moulding compound material”. In: *Microelectronics Reliability* 107 (Apr. 2020), p. 113596. DOI: 10.1016/j.microrel.2020.113596.

[106] Holger John. “Entwicklung eines Systems zum Fangen und Kühlen von atomarem Quecksilber”. PhD thesis. Darmstadt: Technische Universität Darmstadt, Feb. 2019. URL: http://tuprints.ulb.tu-darmstadt.de/8381.

[107] J. B. Johnson. “Thermal Agitation of Electricity in Conductors”. In: *Physical Review* 32.1 (July 1928), pp. 97–109. DOI: 10.1103/PhysRev.32.97.

[108] Kenji Kajiyama and Hiroshi Kanbe. “Temperature dependence of avalanche breakdown voltage in Si p-n junctions”. In: *Journal of Applied Physics* 47.6 (Aug. 2008). DOI: 10.1063/1.322999.

[109] N.J. Kasdin and T. Walter. “Discrete simulation of power law noise (for oscillator stability evaluation)”. In: *Proceedings of the 1992 IEEE Frequency Control Symposium*. May 1992, pp. 274–283. DOI: 10.1109/FREQ.1992.270003.

[110] Richard Kaußler. *Richi´s Lab - Linear Technology LM399*. 2021. URL: https://www.richis-lab.de/REF02.htm (visited on 09/02/2022).

[111] Arthur Kay. *Analysis and Measurement of Intrinsic Noise in Op Amp Circuits, Part VIII: Popcorn Noise*. Technote VIII. Texas Instruments Incorporated, Feb. 2008.

[112] Arthur Kay. *Operational Amplifier Noise: Techniques and Tips for Analyzing and Reducing Noise*. Newnes, Jan. 2012, p. 248.

[113] Dan Kegel. *The C10K problem*. May 1999. URL: https://web.archive.org/web/19990508164301/http://www.kegel.com/c10k.html.

[114] *Keysight 3458A Multimeter - Calibration Manual*. Keysight Technologies. July 2022. URL: https://www.keysight.com/us/en/assets/9018-01342/service-manuals/9018-01342.pdf.

[115] J. Kim, S. Somani, and Y. Yamamoto. *Nonclassical Light from Semiconductor Lasers and LEDs*. Springer Series in Photonics. Springer Berlin Heidelberg, Aug. 2012, p. 258. DOI: 10.1007/978-3-642-56814-5.

[116] A. Knobloch, H. Garbe, and J.P. Karst. "Shielded or unshielded twisted-pair for high speed data transmission?" In: *1998 IEEE EMC Symposium. International Symposium on Electromagnetic Compatibility. Symposium Record (Cat. No.98CH36253)*. Vol. 1. Aug. 1998, pp. 112–117. DOI: 10.1109/ISEMC.1998.750069.

[117] Alicja Konczakowska and Bogdan M. Wilamowski. "Fundamentals of Industrial Electronics". In: ed. by Bogdan M. Wilamowski and J. David Irwin. Taylor & Francis, Mar. 2011. Chap. Noise in Semiconductor Devices, p. 737. DOI: 10.1201/9781315218441.

[118] *L785H1 Datasheet*. A. Thorlabs, Inc. Jan. 2019. URL: https://www.thorlabs.com/_sd.cfm?fileName=QTN035673-S01.pdf&partNumber=L785H1.

[119] A. Lapierre et al. "Relativistic Electron Correlation, Quantum Electrodynamics, and the Lifetime of the $1s^2 2s^2 2p\ ^2P^o_{3/2}$ Level in Boronlike Argon". In: *Phys. Rev. Lett.* 95 (18 Oct. 2005), p. 183001. DOI: 10.1103/PhysRevLett.95.183001.

[120] Rado Lapuh. *Sampling with 3458A, Understanding. Programming, Sampling and Signal Processing*. 1st ed. Ljubljana: Left Right d.o.o., 2018.

[121] Rado Lapuh. personal communication. Nov. 26, 2022.

[122] Rado Lapuh et al. "Keysight 3458A Noise Performance in DCV Sampling Mode". In: *IEEE Transactions on Instrumentation and Measurement* 66 (Apr. 2017). DOI: 10.1109/TIM.2017.2681238.

[123] Rado Lapuh et al. "Fluke 8588A and Keysight 3458A DMM Sampling Performance". In: (May 2022). DOI: 10.48550/arXiv.2205.11321.

[124] Neil T. Larsen. "50 Microdegree Temperature Controller". In: *Review of Scientific Instruments* 39.1 (Nov. 2003). DOI: 10.1063/1.1683078.

[125] Paul J. Leach, Rich Salz, and Michael H. Mealling. *A Universally Unique IDentifier (UUID) URN Namespace*. RFC 4122. July 2005. DOI: 10.17487/RFC4122.

[126] Ho Seong Lee, Sung Hoon Yang, and Nak Sam Chung. "Temperature controller using an error signal modulation". In: *Review of Scientific Instruments* 61.4 (Apr. 1990). DOI: 10.1063/1.1141183.

[127] Ivan Lenicek, Damir Ilic, and Roman Malaric. "Determination of High-Resolution Digital Voltmeter Input Parameters". In: *IEEE Transactions on Instrumentation and Measurement* 57.8 (May 2008), pp. 1685–1688. DOI: 10.1109/TIM.2008.923786.

[128] K. G. Libbrecht and J. L. Hall. "A low-noise high-speed diode laser current controller". In: *Review of Scientific Instruments* 64.8 (Mar. 1993). DOI: 10.1063/1.1143949.

[129] Tobias Liebmann. "Mikrocontrollergesteuerte Temperaturregelung". Bachelor's Thesis. Technische Universität Darmstadt, Nov. 2017.

[130] David von Lindenfels et al. “Bound electron g-factor measurement by double-resonance spectroscopy on a fine-structure transition”. In: *Canadian Journal of Physics* 89.1 (Dec. 2011). DOI: 10.1139/P10-071.

[131] David von Lindenfels et al. “Experimental access to higher-order Zeeman effects by precision spectroscopy of highly charged ions in a Penning trap”. In: *Phys. Rev. A* 87 (2 Feb. 2013). DOI: 10.1103/PhysRevA.87.023412.

[132] David von Lindenfels et al. “Half-open Penning trap with efficient light collection for precision laser spectroscopy of highly charged ions”. In: *Hyperfine interactions* (Nov. 2013), pp. 197–207. DOI: 10.1007/s10751-013-0961-z.

[133] *LM199/LM399, LM199A/LM399A Precision Reference*. C. Analog Devices Inc. Dec. 2014. URL: https://www.analog.com/media/en/technical-documentation/data-sheets/199399fc.pdf.

[134] *LM317 3-Terminal Adjustable Regulator*. Y. Texas Instruments Inc. Sept. 2016. URL: https://www.ti.com/lit/ds/symlink/lm317.pdf.

[135] J.R. Crespo López-Urrutia et al. “Visible spectrum of highly charged ions: The forbidden optical lines of Kr, Xe, and Ba ions in the Ar I to Kr I isoelectronic sequence”. In: *Canadian Journal of Physics* 80.12 (Dec. 2002). DOI: 10.1139/p02-080.

[136] *LT1028 Data Sheet - Ultralow Noise Precision High Speed Op Amps*. D. Analog Devices Inc. 2015. URL: https://www.analog.com/media/en/technical-documentation/data-sheets/1028fd.pdf.

[137] *LT1997-3 Data Sheet - Precision, Wide Voltage Range Gain Selectable Amplifier*. A. Analog Devices Inc. Apr. 2018. URL: https://www.analog.com/media/en/technical-documentation/data-sheets/lt1997-3.pdf.

[138] *LT5400 Data Sheet - Quad Matched Resistor Network*. C. Analog Devices Inc. Feb. 2015. URL: https://www.analog.com/media/en/technical-documentation/data-sheets/5400fc.pdf.

[139] *LTC2508-32 Data Sheet - 32-Bit Oversampling ADC with Configurable Digital Filter*. C. Analog Devices Inc. Apr. 2017. URL: https://www.mouser.de/datasheet/2/609/250832fc-3125031.pdf.

[140] *LTC4365 Data Sheet - Overvoltage, Undervoltage and Reverse Supply Protection Controller*. B. Analog Devices Inc. Sept. 2019. URL: https://www.analog.com/media/en/technical-documentation/data-sheets/LTC4365.pdf.

[141] *LTC6655 Data Sheet - 0.25ppm Noise, Low Drift Precision References*. J. Analog Devices Inc. Apr. 2021. URL: https://www.analog.com/media/en/technical-documentation/data-sheets/ltc6655-6655ln.pdf.

[142] MOG Laboratories Pty Ltd. *DLC Performance*. 2023. URL: https://www.moglabs.com/support/performance (visited on 04/30/2023).

[143] *LTZ1000/LTZ1000A Data Sheet - Ultra Precision Reference*. D. Analog Devices Inc. Apr. 2012. URL: https://www.analog.com/media/en/technical-documentation/data-sheets/LTZ1000.pdf.

[144] Kent Howard Lundberg. “Noise Sources in Bulk CMOS”. In: 2002. URL: http://web.mit.edu/klund/www/CMOSnoise.pdf.

[145] Susumu Machida and Yoshihisa Yamamoto. “Observation of amplitude squeezing from semiconductor lasers by balanced direct detectors with a delay line”. In: *Opt. Lett.* 14.19 (Oct. 1989). DOI: 10.1364/OL.14.001045.

[146] Stefan Machlup. “Noise in Semiconductors: Spectrum of a Two-Parameter Random Signal”. In: *Journal of Applied Physics* 25.3 (Mar. 1954), pp. 341–343. DOI: 10.1063/1.1721637.

[147] Volkhard Mäckel et al. “Laser spectroscopy of highly charged argon at the Heidelberg electron beam ion trap”. In: *Physica Scripta Volume T* T156 (Sept. 2013), pp. 4004–. DOI: 10.1088/0031-8949/2013/T156/014004.

[148] P. K. Madhavan Unni, M. K. Gunasekaran, and A. Kumar. “± 30 μK temperature controller from 25 to 103 °C: Study and analysis”. In: *Review of Scientific Instruments* 74.1 (Jan. 2003). DOI: 10.1063/1.1529299.

[149] Amin Mahnam, Hassan Yazdanian, and Mohsen Mosayebi Samani. “Comprehensive study of Howland circuit with non-ideal components to design high performance current pumps”. In: *Measurement* 82 (Mar. 2016). DOI: 10.1016/j.measurement.2015.12.044.

[150] Alexander Martin. “Laser Spectroscopic Investigation of Exotic States in Noble Gases”. PhD thesis. Technische Universität Darmstadt, Apr. 2017. URL: http://tuprints.ulb.tu-darmstadt.de/6666.

[151] Alexander Martin, Patrick Baus, and Gerhard Birkl. “External cavity diode laser setup with two interference filters”. In: *Applied Physics B* 122.12 (Dec. 2016). DOI: 10.1007/s00340-016-6575-9.

[152] Herbert Paul Maruska and Walden Clark Rhines. “A modern perspective on the history of semiconductor nitride blue light sources”. In: *Solid-State Electronics* 111 (Sept. 2015), pp. 32–41. DOI: 10.1016/j.sse.2015.04.010.

[153] *MAX329 Data Sheet - Ultra-Low Leakage Monolithic CMOS Analog Multiplexers*. 3rd ed. Analog Devices Inc. Feb. 2011. URL: https://www.analog.com/media/en/technical-documentation/data-sheets/max328-max329.pdf.

[154] A.S. McCormack and K.R. Godfrey. “Rule-based autotuning based on frequency domain identification”. In: *IEEE Transactions on Control Systems Technology* 6.1 (Jan. 1998), pp. 43–61. DOI: 10.1109/87.654876.

[155] L. McCuller et al. “LIGO’s quantum response to squeezed states”. In: *Phys. Rev. D* 104 (6 Sept. 2021). DOI: 10.1103/PhysRevD.104.062006.

[156] *Measuring* $2\,\mathrm{nV}/\sqrt{\mathrm{Hz}}$ *Noise and* $120\,\mathrm{dB}$ *Supply Rejection on Linear Regulators*. Application note. Analog Devices Inc. (formerly Linear Technology Corporation), Feb. 2016. URL: https://www.analog.com/media/en/technical-documentation/app-notes/an-159.pdf.

[157] John A. Mergos et al. “The effect of accelerated UV-ageing on the dielectric properties of PVC, PTFE and HDPE”. In: *2010 10th IEEE International Conference on Solid Dielectrics*. July 2010. DOI: 10.1109/ICSD.2010.5568019.

[158] *Method for Determining Drop Cable Braid Coverage*. Tech. rep. 51. American National Standard, July 2018. URL: https://www.scte.org/documents/653/ANSI_SCTE20512 02018.pdf.

[159] Vincent Michel. *aiostream*. Aug. 2022. URL: https://github.com/vxgmichel/aiostream (visited on 05/06/2023).

[160] Microsoft. *ReactiveX*. June 2011. URL: https://github.com/ReactiveX (visited on 07/14/2024).

[161] RD Middlebrook. "Design techniques for preventing input-filter oscillations in switched-mode regulators". In: *Proc. Powercon*. Vol. 5. May 1978, A3–1.

[162] Mike Engelhardt. *LTspice*. Version 17.1.5. Jan. 2023. URL: https://www.analog.com/en/design-center/design-tools-and-calculators/ltspice-simulator.html.

[163] Edoardo Milotti. "1/f noise: a pedagogical review". In: (Apr. 2002). DOI: 10.48550/arXiv.physics/0204033.

[164] *Model 2002 - Multimeter Specifications*. M. Keithley Instruments, Inc. Aug. 2022. URL: https://www.tek.com/en/documents/specification/model-2002-multimeter-specifications.

[165] *MORN Datasheet - Dual-In-Line Thin Film Resistor, Surface-Mount Network*. Vishay Intertechnology, Inc. Nov. 2015. URL: https://www.vishay.com/docs/60129/morn.pdf.

[166] Shuji Nakamura et al. "InGaN-Based Multi-Quantum-Well-Structure Laser Diodes". In: *Japanese Journal of Applied Physics* 35.1B (Jan. 1996). DOI: 10.1143/JJAP.35.L74.

[167] *OP07 Data Sheet - Ultralow Offset Voltage Operational Amplifier*. G. Analog Devices Inc. Oct. 2011. URL: https://www.analog.com/media/en/technical-documentation/data-sheets/OP07.pdf.

[168] *OPAx140 Datasheet, High-Precision, Low-Noise, Rail-to-Rail Output, 11-MHz, JFET Op Amps*. F. Texas Instruments Inc. Mar. 2023. URL: https://www.ti.com/lit/ds/symlink/opa2140.pdf.

[169] Henry W. Ott. *Electromagnetic Compatibility Engineering*. John Wiley & Sons, Ltd, Apr. 2009, p. 843. DOI: 10.1002/9780470508510.

[170] *Paralleling power MOSFETs in high power applications*. Application note. Nexperia B.V., Sept. 2021. URL: https://assets.nexperia.com/documents/application-note/AN50005.pdf.

[171] Robert A. Pease. *A Comprehensive Study of the Howland Current Pump*. Application note. National Semiconductor (now part of Texas Instruments), Jan. 2008. URL: https://www.ti.com/lit/an/snoa474a/snoa474a.pdf.

[172] B. Pellegrini et al. "$\frac{1}{f^\gamma}$ noise in thick-film resistors as an effect of tunnel and thermally activated emissions, from measures versus frequency and temperature". In: *Phys. Rev. B* 27 (2 Jan. 1983), pp. 1233–1243. DOI: 10.1103/PhysRevB.27.1233.

[173] David W. Pessen. "A new look at PID-controller tuning". In: *Journal of dynamic systems, measurement, and control* 116.3 (Sept. 1994), pp. 553–557. DOI: 10.1115/1.2899252.

[174] *PL 450B Data Sheet (PRELIMINARY)*. 1.2. OSRAM Opto Semiconductors GmbH. Aug. 2021. URL: https://dammedia.osram.info/media/resource/hires/osram-dam-6557694/PL%5C%20450B%5C_EN.pdf.

[175] W. H. Press. "Flicker noises in astronomy and elsewhere." In: *Comments on Astrophysics* 7.4 (Jan. 1978), pp. 103–119.

[176] Tilman Preuschoff. "Laser Spectroscopic Investigation of Exotic States in Noble Gases". PhD thesis. Technische Universität Darmstadt, Feb. 2023. DOI: 10.26083/tuprints-00023242.

[177] Tilman Preuschoff et al. “Wideband current modulation of diode lasers for frequency stabilization”. In: *Review of Scientific Instruments* 93.6 (June 2022). DOI: 10.1063/5.0093520.

[178] Jr. Puckett Jason Niles. “An Electrical and Statistical Study of Burst Noise”. PhD thesis. California Institute of Technology, 1971. DOI: 10.7907/D816-7C55.

[179] W. Quint et al. “Laser-microwave double-resonance technique for g-factor measurements in highly charged ions”. In: *Phys. Rev. A* 78 (3 Sept. 2008). DOI: 10.1103/PhysRevA.78.032517.

[180] *R&S RTH1004 Handheld Oscilloscope*. 27.00. Rohde & Schwarz GmbH & Co. KG. Feb. 2022. URL: https://scdn.rohde-schwarz.com/ur/pws/dl_downloads/dl_common_library/dl_brochures_and_datasheets/pdf_1/RTH_Scope_Rider_dat-sw_en_3607-0517-22_v2700.pdf.

[181] Paul Rako. *Voltage reference drift considerations*. Dec. 2010. URL: https://www.edn.com/voltage-reference-drift-considerations (visited on 09/02/2022).

[182] B. Razavi. *Design of Analog CMOS Integrated Circuits*. 2nd ed. McGraw-Hill higher education. Tata McGraw-Hill, Oct. 2017, p. 800.

[183] G. Rietveld. “Accurate determination of the input impedance of digital voltmeters”. In: *Science, Measurement and Technology, IEE Proceedings* - 151 (Oct. 2004), pp. 381–383. DOI: 10.1049/ip-smt:20040700.

[184] William Riley and David Howe. *Handbook of Frequency Stability Analysis*. July 2008. URL: https://tsapps.nist.gov/publication/get_pdf.cfm?pub_id=50505.

[185] *RL0503-5820-97-MS Data Sheet - NTC Type MS Thermometrics Epoxy-Coated Thermistor*. Analog Devices Inc. Mar. 2022. URL: https://www.amphenol-sensors.com/hubfs/AAS-920-574B-Thermometrics-NTC-Type-MS-032822-web.pdf.

[186] Ivan Ryger et al. “Noise characteristics of thermistors: Measurement methods and results of selected devices”. In: *Review of Scientific Instruments* 88.2 (Feb. 2017). 024707. DOI: 10.1063/1.4976029.

[187] *S Series - High Precision Foil Resistor*. Vishay Precision Group, Inc. Mar. 2015. URL: https://foilresistors.com/docs/63001/63001.pdf.

[188] *S9055 Series Data Sheet - Si PIN Photodiodes*. Hamamatsu Photonics K.K. Sept. 2017. URL: https://www.hamamatsu.com/content/dam/hamamatsu-photonics/sites/documents/99_SALES_LIBRARY/ssd/s9055_series_kpin1065e.pdf.

[189] Sebastian D. Saliba and Robert E. Scholten. “Linewidths below 100 kHz with external cavity diode lasers”. In: *Appl. Opt.* 48.36 (Dec. 2009), pp. 6961–6966. DOI: 10.1364/AO.48.006961.

[190] Dror Sarid and David S. Cannell. “A $\pm$15 microdegree temperature controller”. In: *Review of Scientific Instruments* 45.9 (Nov. 2003). DOI: 10.1063/1.1686815.

[191] Thomas Sattelmaier. “Development and characterization of a temperature controller with sub-millikelvin stability”. MA thesis. Technische Universität Darmstadt, Mar. 2019.

[192] Vikram Savani and Dr. Lawrence A. Johnson. *Achieving Millikelvin Temperature Stability*. Application note. ILX Lightwave, Aug. 2013. URL: https://www.newport.com/medias/sys_master/images/images/hfb/h4d/8797050372126/AN38-Achieving-Millikelvin-Temperature-Stability.pdf.

[193] Rudolf Schieder and Carsten Kramer. “Optimization of heterodyne observations using Allan variance measurements”. In: *A&A* 373.2 (May 2001), pp. 746–756. DOI: 10.1051/0004-6361:20010611.

[194] T. J. Scholl et al. “Absolute wave-number measurements in $^{130}Te_2$: reference lines spanning the 420.9-464.6 nm region”. In: *J. Opt. Soc. Am. B* 22.5 (May 2005). DOI: 10.1364/JOSAB.22.001128.

[195] D.E. Seborg et al. *Process Dynamics and Control*. 4th ed. John Wiley & Sons, Mar. 2016, p. 512. DOI: 10.1017/9781139565080.

[196] Christopher M. Seck et al. “Noise reduction of a Libbrecht–Hall style current driver”. In: *Review of Scientific Instruments* 87.6 (July 2016). DOI: 10.1063/1.4953330.

[197] *Secrets Of Rf Circuit Design, Third Edition*. 3rd ed. McGraw-Hill/TAB Electronics, Dec. 2000, p. 548.

[198] A.S. Sedra and K.C. Smith. *Microelectronic Circuits*. 8th ed. Oxford University Press, Nov. 2019, p. 1296.

[199] Frank Seifert. *Resistor Current Noise Measurements*. Tech. rep. LIGO- T0900200-v1. URL: https://dcc.ligo.org/public/0002/T0900200/001/current_noise.pdf.

[200] Vladimir M. Shabaev et al. “Stringent tests of QED using highly charged ions”. In: *Hyperfine Interactions* 239 (Nov. 2018). DOI: 10.1007/s10751-018-1537-8.

[201] D.H. Sheingold. “Impedance & admittance transformations using operational amplifiers”. In: *Lightning Empiricist* 12.1 (1964), pp. 1–8.

[202] D.H. Sheingold and Staff. *Analog-digital Conversion Handbook*. 3rd ed. Analog Devices technical handbooks. Prentice-Hall, July 1986, p. 672.

[203] W. Shockley. “The Theory of p-n Junctions in Semiconductors and p-n Junction Transistors”. In: *Bell System Technical Journal* 28.3 (July 1949), pp. 435–489. DOI: 10.1002/j.1538-7305.1949.tb03645.x.

[204] W. Shockley. “A Unipolar ”Field-Effect” Transistor”. In: *Proceedings of the IRE* 40.11 (Nov. 1952), pp. 1365–1376. DOI: 10.1109/JRPROC.1952.273964.

[205] *SHR Datasheet - Super High Resolution DVI and HDMI Copper Cables*. DVIGear. URL: https://files.dvigear.com/docs/DataSheets/SHR%5C_Series%5C_Cables%5C_Data.pdf.

[206] Markus Sieger. personal communication. MG Optical Solutions GmbH, Aug. 13, 2018.

[207] Guillermo J. Silva, Aniruddha Datta, and S.P. Bhattacharyya. “PI stabilization of first-order systems with time delay”. In: *Automatica* 37.12 (Dec. 2001), pp. 2025–2031. DOI: 10.1016/S0005-1098(01)00165-0.

[208] Guillermo J. Silva, Aniruddha Datta, and S.P. Bhattacharyya. *PID Controllers for Time-Delay Systems*. Control Engineering. Birkhäuser Boston, Dec. 2004. DOI: 10.1007/b138796.

[209] Sigurd Skogestad. “Simple analytic rules for model reduction and PID controller tuning”. In: *Journal of Process Control* 13.4 (June 2003), pp. 291–309. DOI: 10.1016/S0959-1524(02)00062-8.

[210] Sigurd Skogestad and Ian Postlethwaite. *Multivariable Feedback Control: Analysis and Design*. Hoboken, NJ, USA: John Wiley & Sons, Inc., 2005.

[211] *SMBJ-Q Transient Voltage Suppressor Diode Series*. Bourns, Inc. Oct. 2020. URL: https://www.bourns.com/docs/product-datasheets/smbj-q.pdf.

[212] W.M. Smith. "Worst case circuit analysis-an overview (electronic parts/circuits tolerance analysis)". In: *Proceedings of 1996 Annual Reliability and Maintainability Symposium*. Jan. 1996, pp. 326–334. DOI: 10.1109/RAMS.1996.500682.

[213] *SR560 Low-Noise Voltage Preamplifier*. c. Stanford Research Systems. July 2021. URL: https://www.thinksrs.com/downloads/pdfs/catalog/SR560c.pdf.

[214] P. T. Starkey et al. "A scripted control system for autonomous hardware-timed experiments". In: *Review of Scientific Instruments* 84.8 (Aug. 2013), p. 085111. DOI: 10.1063/1.4817213.

[215] Sveinn Steinarsson. "Downsampling Time Series for Visual Representation". MA thesis. May 2013. URL: http://hdl.handle.net/1946/15343.

[216] John S. Steinhart and Stanley R. Hart. "Calibration curves for thermistors". In: *Deep Sea Research and Oceanographic Abstracts* 15.4 (Aug. 1968). DOI: 10.1016/0011-7471(68)90057-0.

[217] Th. Stöhlker et al. "Quantum Electrodynamics in Extreme Fields: Precision Spectroscopy of High-Z H-like Systems". In: *Precision Physics of Simple Atoms and Molecules*. Ed. by Savely G. Karshenboim. Berlin, Heidelberg: Springer Berlin Heidelberg, Dec. 2007, pp. 157–163. DOI: 10.1007/978-3-540-75479-4_9.

[218] *Supra DVI-DVI Single Link Datasheet*. Jenving Technology AB. URL: http://www.jenving.com/products/view/dvi-dvi-single-link-1001100930.

[219] Joseph Szwarc. *Predicting Drift in Foil Resistors*. Tech. rep. 63171. Vishay Precision Group, Sept. 2012. URL: https://foilresistors.com/docs/63171/TN104.pdf.

[220] H. Talvitie et al. "Passive frequency and intensity stabilization of extended-cavity diode lasers". In: *Review of Scientific Instruments* 68.1 (Jan. 1997), pp. 1–7. DOI: 10.1063/1.1147810.

[221] Matthew S. Taubman. "Low-noise high-performance current controllers for quantum cascade lasers". In: *Review of Scientific Instruments* 82.6 (June 2011), p. 064704. DOI: 10.1063/1.3600602.

[222] Matthew S. Taubman et al. "Precision control of multiple quantum cascade lasers for calibration systems". In: *Review of Scientific Instruments* 85.1 (Jan. 2014), p. 014704. DOI: 10.1063/1.4861200.

[223] *Technical Data Sheet Bode 100*. 1.3. OMICRON electronics GmbH. Oct. 2021. URL: https://www.omicron-lab.com/fileadmin/assets/Bode%5C_100/Documents/Bode%5C_100%5C_R2%5C_Technical%5C_Data%5C_V1.3.pdf.

[224] S. Tedja, J. Van der Spiegel, and H.H. Williams. "Analytical and experimental studies of thermal noise in MOSFET's". In: *IEEE Transactions on Electron Devices* 41.11 (Nov. 1994), pp. 2069–2075. DOI: 10.1109/16.333824.

[225] H. R. Telle, D. Meschede, and T. W. Hänsch. "Realization of a new concept for visible frequency division: phase locking of harmonic and sum frequencies". In: *Opt. Lett.* 15.10 (May 1990). DOI: 10.1364/OL.15.000532.

[226] U. Tietze, C. Schenk, and E. Schmid. *Electronic Circuits. Handbook for Design and Application*. 2nd ed. Springer Berlin Heidelberg, Dec. 2015, p. 1543. DOI: 10.1007/978-3-540-78655-9.

[227] Daylin L. Troxel, Christopher J. Erickson, and Dallin S. Durfee. “Note: Updates to an ultra-low noise laser current driver”. In: *Review of Scientific Instruments* 82.9 (Sept. 2011), p. 096101. DOI: 10.1063/1.3630950.

[228] Aaron S. Tucker, Robert M. Fox, and Rosalind J. Sadleir. “Biocompatible, High Precision, Wideband, Improved Howland Current Source With Lead-Lag Compensation”. In: *IEEE Transactions on Biomedical Circuits and Systems* 7.1 (Feb. 2013). DOI: 10.1109/TBCAS.2012.2199114.

[229] Johannes Ullmann et al. “High precision hyperfine measurements in Bismuth challenge bound-state strong-field QED”. In: *Nature Communications* 8, 15484 (May 2017), p. 15484. DOI: 10.1038/ncomms15484.

[230] *Vacuum Housing 6010/6020 Datasheet*. Stable Laser Systems. Nov. 2015. URL: https://stablelasers.com/wp-content/uploads/2017/06/6010_20_R1.pdf.

[231] Carel M. Van Vliet and Peter H. Handel. “A new transform theorem for stochastic processes with special application to counting statistics”. In: *Physica A: Statistical Mechanics and its Applications* 113.1 (July 1982), pp. 261–276. DOI: 10.1016/0378-4371(82)90019-X.

[232] Vincent C. Vannicola. “Modelling and Properties of Modulated RF Signals Perturbed by Oscillator Phase Instabilities and Resulting Spectral Dispersion”. In: *IEEE Trans. Inf. Theory* 29 (July 1983), p. 631. DOI: 10.1109/TIT.1983.1056690.

[233] F Vernotte and E Lantz. “Metrology and 1/f noise: linear regressions and confidence intervals in flicker noise context”. In: *Metrologia* 52.2 (Feb. 2015). DOI: 10.1088/0026-1394/52/2/222.

[234] *VHP101 data sheet - Ultra-High Precision Hermetically Sealed Bulk Metal® Foil Resistor Ultra-High Precision Hermetically Sealed Bulk Metal® Foil Resisto*. Vishay Precision Group, Inc. Mar. 2021. URL: https://foilresistors.com/docs/63003/vhp100.pdf.

[235] R. Vilanova and A. Visioli, eds. *PID Control in the Third Millennium: Lessons Learned and New Approaches*. Advances in Industrial Control. Springer London, Feb. 2012. Chap. The SIMC Method for Smooth PID Controller Tuning. DOI: 10.1007/978-1-4471-2425-2_5.

[236] Richard Von Mises. *Über Aufteilungs-und Besetzungswahrscheinlichkeiten*. 1939.

[237] *VPR221Z (Z-Foil) - Vishay Foil Resistors*. Vishay Precision Group, Inc. Mar. 2010. URL: http://www.vishaypg.com/docs/63116/vpr221z.pdf.

[238] Anders E.E. Wallin. *AllanTools*. 2022. URL: https://github.com/aewallin/allantools (visited on 10/17/2022).

[239] G. Wei. “Flicker noise process analysis”. In: *1993 IEEE International Frequency Control Symposium*. June 1993, pp. 321–325. DOI: 10.1109/FREQ.1993.367412.

[240] P. Welch. “The use of fast Fourier transform for the estimation of power spectra: A method based on time averaging over short, modified periodograms”. In: *IEEE Transactions on Audio and Electroacoustics* 15.2 (June 1967), pp. 70–73. DOI: 10.1109/TAU.1967.1161901.

[241] *Werkstoffdatenblatt Aluminium: EN AW-7020*. Analog Devices Inc. June 2020. URL: https://batz-burgel.com/wp-content/uploads/data-de/BB_7020.pdf.

[242] Carl E. Wieman and Leo Hollberg. “Using diode lasers for atomic physics”. In: *Review of Scientific Instruments* 62.1 (Jan. 1991), pp. 1–20. DOI: 10.1063/1.1142305.

[243] M. Wiesel et al. “Optically transparent solid electrodes for precision Penning traps”. In: *Review of Scientific Instruments* 88.12 (Dec. 2017). DOI: 10.1063/1.5002180.

[244] Jim Williams. “Split a temperature degree to 10 µ°C”. In: *Electronic Design* 2.10 (May 1974).

[245] Peter Wilson. *The Circuit Designer’s Companion*. 4th ed. Elsevier/Newnes, July 2017, p. 496. DOI: 10.1016/B978-0-08-101764-7.02001-6.

[246] D FA Winters et al. “Laser spectroscopy of hyperfine structure in highly charged ions: a test of QED at high fields”. In: *Canadian Journal of Physics* 85.5 (May 2007). DOI: 10.1139/p07-023.

[247] John Wright. *Don’t Be Fooled by Voltage Reference Long-Term Drift and Hysteresis*. Tech. rep. Linear Technology Corp., Apr. 2000. URL: https://www.analog.com/media/en/reference-design-documentation/design-notes/dn229f.pdf.

[248] *WS8-10 Series Data Sheet*. HighFinesse GmbH. Mar. 2023. URL: https://www.highfinesse.com/en/wavelengthmeter/wavelengthmeter-further-information/technical-information-wavelengthmeter-ws8-10-series.pdf.

[249] R. Wynands, T. Mukai, and T. W. Hänsch. “Coherent bisection of optical frequency intervals as large as 530 THz”. In: *Opt. Lett.* 17.24 (Dec. 1992). DOI: 10.1364/OL.17.001749.

[250] Min Xiao, Ling-An Wu, and H. J. Kimble. “Detection of amplitude modulation with squeezed light for sensitivity beyond the shot-noise limit”. In: *Opt. Lett.* 13.6 (June 1988). DOI: 10.1364/OL.13.000476.

[251] Y. Yamamoto. *Fundamentals of Noise Processes*. 2017. Chap. 9. URL: https://www.nii.ac.jp/qis/first-quantum/e/forStudents/lecture/index.html.

[252] Felix Zandman and Joseph Szwarc. *Non-Linearity of Resistance/Temperature Characteristic: Its Influence on Performance of Precision Resistors*. Tech. rep. 60108. Vishay Intertechnology Inc., June 2009. URL: https://www.vishay.com/docs/60108/nonlinea.pdf.

[253] J. G. Ziegler and N. B. Nichols. “Optimum Settings for Automatic Controllers”. In: *Journal of Dynamic Systems, Measurement, and Control* 115.2B (June 1993), pp. 220–222. DOI: 10.1115/1.2899060.

[254] Leith Znaimer and John Bechhoefer. “Note: Split PID control—Two sensors can be better than one”. In: *Review of Scientific Instruments* 85.10 (Oct. 2014). 106105. DOI: 10.1063/1.4898197.

[255] H. Zumbahlen, ed. *Basic Linear Design*. Analog Devices Inc., 2007. URL: https://www.analog.com/en/education/education-library/linear-circuit-design-handbook.html.

[256] Hank Zumbahlen, ed. *Linear Circuit Design Handbook*. 1st ed. Elsevier/Newnes, 2008. DOI: 10.1016/B978-0-7506-8703-4.X0001-6.

A. Appendix

A.1. Multimeter Settings for the Comparison Test

The Multimeters were configured for maximum stability and similar conversion times using the following settings via SCPI. For better readability, all commands are shown unabridged.

HP 3458A

```
PRESET NORM;  # reset the device
TARM HOLD;  # stop readings
BEEP;
OFORMAT ASCII;  # return text
TRIG AUTO;  # trigger when ready
NRDGS 1,AUTO; # take 1 reading
DCV 10;
AZERO ON;  # enable autozero
NDIG 9;
NPLC 100;
FIXEDZ OFF;  # High input impedance
TARM AUTO;  # enable readings
```

Keithley Model 2002

```
*CLS;  # clear events and errors
*RST;  # reset all settings
*OPC?;  # wait until device is reset
:INITiate:CONTinuous OFF;  # disable continuous initiation
:ABORt;  # place K2002 in idle
:SYSTem:AZERo:STATe ON;  # enable autozero
:SYSTem:AZERo:TYPE SYNChronous;  # azero for every reading
:SYSTem:LSYNc:STATe ON;  # line sync
:SENSe:VOLTage:DC:RANGe:UPPer 20;
:SENSe:VOLTage:DC:DIGits 9;
:SENSe:VOLTage:DC:NPLCycles 10;
:SENSe:VOLTage:DC:AVERage:COUNt 4;  # the averaging length
:SENSe:VOLTage:DC:AVERage:TCONtrol REPeat;  # filter type
:SENSe:VOLTage:DC:AVERage:ADVanced:STATe OFF;
:SENSe:VOLTage:DC:AVERage:STATe ON;  # Enable averaging
:FORMat:DATA REAL,64;  # read data as doubles
:FORMat:ELEMents READing;  # only return the reading
:FORMat:EXPonent HPRecision;  # Scientific notation
:INITiate:CONTinuous ON;  # Enable continuous triggering
```

Keysight 34470A

```
:SYSTem:BEEP;
:ABORt;
*RST;
*CLS;
:CONFigure:VOLTage:DC;
:SENSe:VOLTage:RANGe 10;
:SENSe:VOLTage:ZERO:AUTO ON;  # enable autozero
:SENSe:VOLTage:NPLCycles 100;
:SENSe:VOLTage:IMPEdance:AUTO ON;  # High input impendance
:FORMat:DATA ASCii,9;  # return 9 digits ASCII
```

Keithley DMM6500

```
SYSTem:BEEPer 500, 0.2;
ABORt;
*RST;
*CLS;
:SENSe:FUNCtion:ON "VOLTage:DC";
:SENSe:VOLTage:DC:RANGe:UPPer 10;
:SENSe:VOLTage:DC:LINE:SYNC ON;
:SENSe:VOLTage:DC:AVERage:COUNt 9;  # the averaging length
:SENSe:VOLTage:DC:AVERage:TCONtrol REPeat;  # filter type
:SENSe:VOLTage:AZERo:STATe ON;  # enable autozero
:SENSe:VOLTage:DC:NPLCycles 10;
:SENSe:VOLTage:INPutimpedance AUTO;  # High input impedance
:SENSe:VOLTage:DC:AVERage:STATe ON;  # Enable averaging
:FORMat:DATA ASCii;  # read data as double instead of text
:FORMat:ASCii:PRECision 16;  # return 16 digits ASCII
:DISPlay:VOLTage:DC:DIGits 6;  # set the screen to 6 digits
```

A.2. Querying the TimescaleDB via SQL

This is an SQL query to extract binned data from the Timescale DB of two sensors in lab 011: 011_humidity and 011_temperature. The data returned is of the form date,humidity,temperature. The database groups the asynchronous data into bins of 6 h and averages the data inside those bins. The time frame is from 2022-01-01 until 2023-01-01. In addition, the Tinkerforge sensors that only send a new value, if there is an update, the last observation must be carried forward. This is done using the *locf()* function call in SQL query.

SQL query

```
SELECT
  time
  ,data_values [1] humidity  --1st value in the array
  ,data_values [2] temperature --2nd value
FROM (
  SELECT
    bucket as "time"
    ,array_agg("data") as data_values
  FROM (
    SELECT
      time_bucket('6h',"time") AS "bucket"
      ,sensor_id
      ,locf(avg(value)) AS "data"
    FROM sensor_data
      WHERE
      time BETWEEN
        '2022-01-01T00:00:00.00Z' AND '2023-01-01T00:00:00Z'
      AND sensor_id IN (
        SELECT id
        FROM sensors
        WHERE
          label = '011_humidity' OR
          label = '011_temperature' AND
          enabled
      )
    GROUP BY bucket, sensor_id
    ORDER BY bucket
  ) t1
  GROUP BY "bucket"
) t2
```

When attempting to derive PID parameter for the lab temperature controller, the controller output and the sensor output is needed. This query will compile the data in buckets of 2 s. Missing data from the Tinkerforge sensors, which will only update their output on a change, is interpolated by filling the gap with the previous value. The order of the array depends on the values of the sensor ids and needs to be adjusted accordingly for each query.

SQL query

```
SELECT
  timestamp as time,
  arr[2] as output,
  arr[1] as "temperature␣room",
  arr[3] as "temperature␣labnode"
FROM (
  SELECT
    timestamp,
    array_agg(value) arr
  FROM (
    SELECT
      time_bucket_gapfill('2.000s',"time") AS "timestamp",
      sensor_id,
      locf(avg(value)) as value
    FROM sensor_data
    WHERE
      "time" BETWEEN
        '2022-09-22T04:10:00Z' AND '2022-09-22T10:30:00Z'
      AND
      sensor_id IN (
        SELECT id FROM sensors
        WHERE
          label = '011_temperature_back' OR
          label = '011_temperature_labnode_back' OR
          label ='011_output_aircon_back'
      )
    GROUP BY timestamp,sensor_id
    ORDER BY timestamp,sensor_id
  ) t1
  GROUP BY timestamp
) t2
```

A.3. The Transconductance Amplifier with a MOSFET

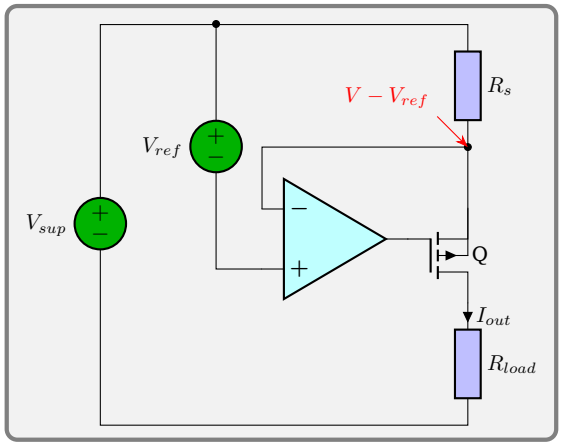

Figure A.1.: Transconductance amplifier with a p-channel MOSFET.

The amplifier shown in figure A.1 is a feedback transconductance amplifier as discussed in [198]. Its transfer function can be derived using the techniques presented in section 3.5.1. As a reminder, the general transfer function is defined as:

$$P(s) = \frac{I_{out}}{V_{ref}} \equiv A_f \,. \tag{A.1}$$

The closed-loop transfer function is sometimes also called gain-with-feedback A_f [198] or noise-gain.

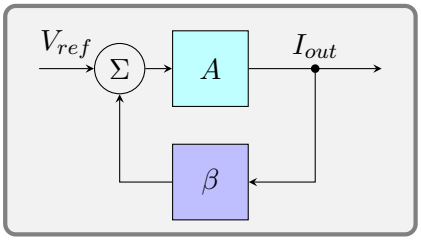

Figure A.2.: Block diagram of an amplifier with feedback β and gain A.

For the system shown in figure A.2, the closed-loop gain A_f can be written as

$$A_f = \frac{A}{1 + A\beta} \overset{A\to\infty}{=} \frac{1}{\beta} \,. \tag{A.2}$$

For the ideal transconductance amplifier with infinite open-loop gain A it follows that the gain is simply reduced by the feedback factor β. For the MOSFET source voltage shown in figure A.1, β can be easily determined by inspection. The ideal op-amp with infinite open-loop gain A_{ol} has the same voltage at the inverting and non-inverting input. This means that below R_s at the source node of the MOSFET, denoted in red, the voltage must be $V - V_{ref}$. This implies that the voltage V_{ref} is dropped across R_s, defining I_{out}. Using equation A.2, β can be calculated

$$A_f = \frac{I_{out}}{V_{ref}} = \frac{\frac{V_{ref}}{R_s}}{V_{ref}} = \frac{1}{R_s} \approx \frac{1}{\beta} \,. \tag{A.3}$$

Calculating the transconductance amplifier gain A requires a little more work and it is useful to switch to the small-signal model of the circuit. To build the small-signal model, a number of simplifications can be applied. In the same same way as it was done for the MOSFET with a source resistor in figure 3.44 on page 77. The AC component of V_{ref} can be set to zero because it is considered constant and so can the supply voltage V. The load is also considered constant and hence shorted to ground. In order to ground V_{ref}, the non-inverting input of the MOSFET must be disconnected, because there still is the voltage v_id connected to it. The model includes the differential input resistance R_{id} between the inverting and non-inverting input of the op-amp because for bipolar input op-amps, the differential input resistance can be as low as a few kΩ and must be considered. The common-mode input resistance of the op-amp inputs is typically several dozens of MΩ or higher and can be safely neglected. This leads to the small signal model shown in figure A.3. The MOSFET model is the Thévenin model introduced in figure 3.43 (b) on page 76. Do note that this model is for low frequencies only, as it neglects capacitive effects of the op-amp and MOSFET. Capacitors are treated as having infinite impedance in this model.

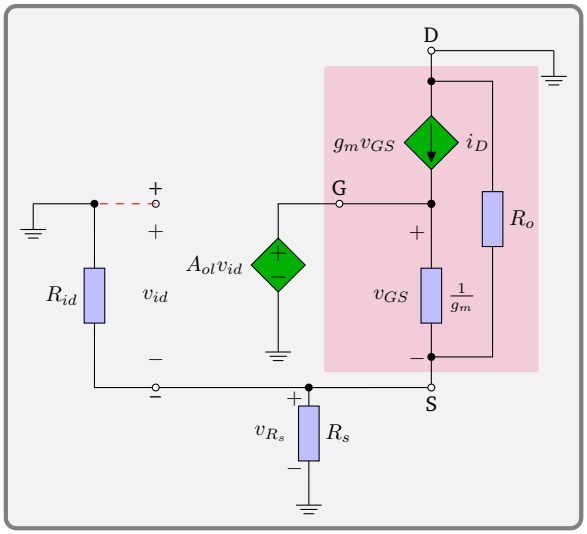

Figure A.3.: Small signal model for a transconductance amplifier with a MOSFET as shown in figure A.1

From the model in figure A.3, the following equations can be extracted in a similar fashion as it was done for the common-gate amplifier and equation 3.90 on page 77.

$$v_{GS} = A_{ol} v_{id} - V_{R_s} \tag{A.4}$$

$$V_{R_s} = i_D \left(R_o || R_s || R_{id}\right) = g_m v_{GS} \left(R_o || R_s || R_{id}\right) \tag{A.5}$$

$$\begin{aligned} A\beta = \frac{V_{R_s}}{V_{id}} &= \frac{g_m v_{GS} \left(R_o || R_s || R_{id}\right)}{\frac{1}{A_{ol}} \left(1 + g_m \left(R_o || R_s || R_{id}\right)\right) v_{GS}} \\ &= A_{ol} \frac{g_m \left(R_o || R_s || R_{id}\right)}{1 + g_m \left(R_o || R_s || R_{id}\right)} \end{aligned} \tag{A.6}$$

Dividing by R_s yields the open-loop gain of the transconductance amplifier, a quantity that is interesting for calculating the MOSFET noise contribution:

$$A = \frac{A_{ol}}{R_s} \frac{g_m \left(R_o || R_s || R_{id}\right)}{1 + g_m \left(R_o || R_s || R_{id}\right)} \tag{A.7}$$

This leads to the closed-loop transfer function

$$A_f = \frac{A_{ol}}{R_s} \frac{g_m \left(R_o||R_s||R_{id}\right)}{(A_{ol}+1) g_m \left(R_o||R_s||R_{id}\right) + 1}\,, \tag{A.8}$$

and finally the output impedance of the transconductance amplifier can be calculated using the output impedance of the common-gate amplifier 3.91 calculated on page 77.

$$\begin{aligned} R_{out} &= (1 + A\beta)\, R_{out,cg} \\ &= \left(1 + A_{ol} \frac{g_m \left(R_o||R_s||R_{id}\right)}{1 + g_m \left(R_o||R_s||R_{id}\right)}\right) \left(g_m R_s R_o + R_o + R_s\right) \\ &\overset{A_{ol} \gg 1}{\approx} A_{ol} \frac{g_m \left(R_o||R_s||R_{id}\right)}{1 + g_m \left(R_o||R_s||R_{id}\right)} \left(g_m R_s R_o + R_o + R_s\right)\,. \end{aligned} \tag{A.9}$$

Equation A.9 can be simplified for typical applications by approximating $g_m \left(R_o||R_s||R_{id}\right)$. Using the example parameters for the `IRF9610` in saturation, used previously on page 75, and additionally the ADI `AD797` [9] op-amp with the following parameters

$$\begin{aligned} &I_D = 250\,\mathrm{mA}\,, \lambda = 4\,\mathrm{mV}^{-1}\,, V_{DS} = 3.5\,\mathrm{V}\,, R_s = 30\,\Omega\,, \\ &R_{id} = 7.5\,\mathrm{k}\Omega\,, \kappa = 0.813\,\mathrm{A\,V}^{-2}\,, A_{ol} = 20\,\mathrm{V\,\mu V}^{-1} \end{aligned}$$

one finds

$$\begin{aligned} R_o &= \frac{I_D}{\frac{1}{\lambda} + V_{DS}} = 1014\,\Omega \\ g_m &= \sqrt{2\kappa I_D \left(1 + \lambda V_{DS}\right)} = 0.642\,\mathrm{S} \\ g_m \left(R_o||R_s||R_{id}\right) &\approx g_m R_s \approx 18.63 \\ \frac{g_m \left(R_o||R_s||R_{id}\right)}{1 + g_m \left(R_o||R_s||R_{id}\right)} &\approx 0.95 \end{aligned}$$

Using typical parameters, it can be seen that dropping the $\frac{g_m(R_o||R_s||R_{id})}{1+g_m(R_o||R_s||R_{id})}$ term will only lead to error of about $5\,\%$. Given the datasheet uncertainties for the MOSFET related parameters on the order of $50\,\%$–$100\,\%$, it can be safely neglected, leading to the following approximations

$$\begin{aligned} R_{out} &\approx A_{ol} \left(g_m R_o R_s + R_o + R_s\right) \\ A_f &\approx \frac{1}{R_s}\,. \end{aligned} \tag{A.10}$$

The approximation for the output impedance holds true when $g_m R_s \gg 1$, which typically is the case. While R_s might become small, this is compensated by an increase in g_m in this application because a smaller source resistor implies a higher output current, demanding a MOSFET with a higher transconductance. The product $g_m \cdot R_s$ therefore remains constant.

It can be said that the op-amp is simply amplifying the output impedance of the MOSFET along with the source resistor and the closed-loop gain is defined entirely by R_s, a very convenient property.

If the model is to be considered at frequencies $\omega > 0$, A_{ol} can be replaced by the first order approximation of the op-amp gain as

$$A_1(\omega) = \frac{A_{ol}}{\sqrt{1 + \left(\frac{\omega}{\omega_c}\right)^2}}\,, \tag{A.11}$$

which is valid for most compensated op-amps, which have a dominant pole at $\omega_c \approx 1\,\mathrm{Hz}$.

A.4. Simulating Current Source Properties in LTSpice

This section explains some more advanced concepts of LTSpice [162] to simulate device properties and circuit properties used when working with the current source presented in section 3.8.4. This section does not aim at explaining the basic functions of LTSpice, but rather some special functions. It is left to the interested reader to acquire those basic skills. The example presented here allows to generate the MOSFET *Typical Output Characteristics* plot found in datasheets, the transconductance of a MOSFET, and the (dynamic) output impedance of a current source. The typical output characteristics can be used to compare the model with the datasheet or with measurements taken. Comparing these model parameters with the datasheet can establish confidence that the simulation results can be transferred to a real circuit.

A.4.1. MOSFET Typical Output Characteristics

The output characteristic is a graph found in all MOSFET datasheets and is shown below in figure A.4.

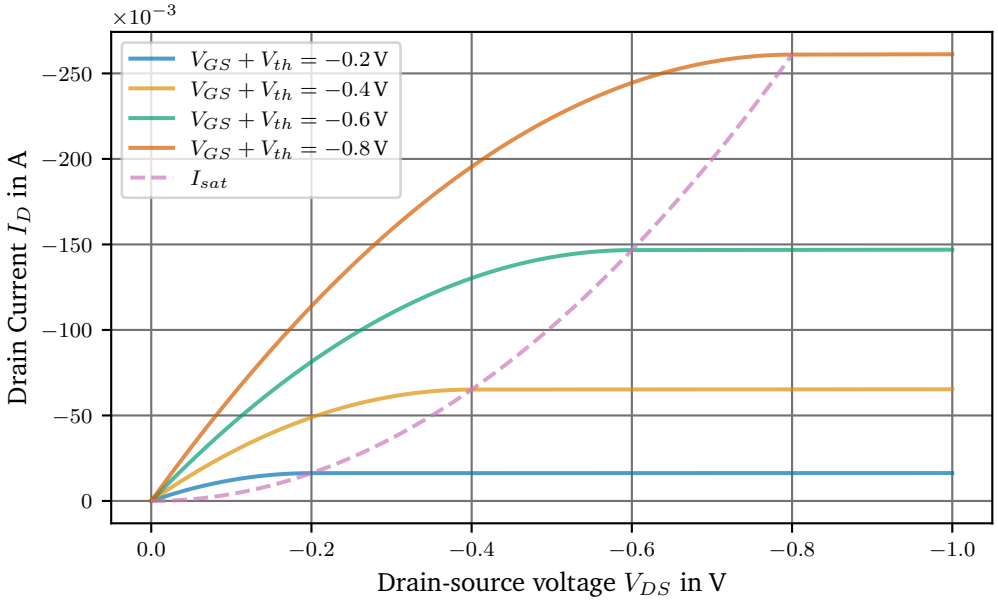

Figure A.4.: Simulated drain current over the drain-source voltage, also called output characteristics of a MOSFET.

Plotting this graph allows to compare the model to the datasheet or the measured values in order to tweak the model. To create this graph, the simulation file found in the folder source/spice/mosfet_gm-id.asc as part of this document can be used. The SPICE simulation for the output characteristics of the MOSFET simulates the following circuit shown in figure A.5 (a).

Do note that V_{DS} and V_{GS} are inverted and given as V_{SD} and V_{SG}. The reason is that the plotter in LTSpice works better with positive numbers to guess the correct scaling of the axis. Figure A.5 (b) shows the same circuit drawn in LTSpice. The MOSFET parameters are entered

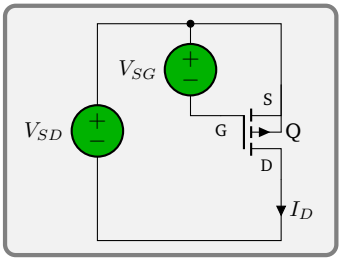

(a) P-channel MOSFET under test.

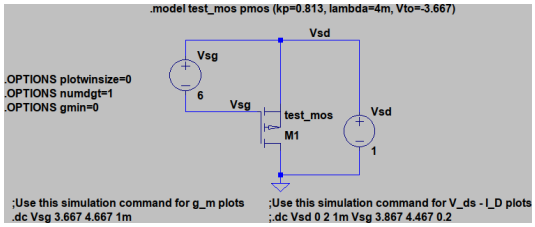

(b) LTSpice model.

Figure A.5.: P-channel MOSFET circuit and its LTSpice model.

using the **.model** syntax

.model test_mos pmos (kp=0.813, lambda=4m, Vto=−3.667)

with the parameters $\kappa = 0.813\,\mathrm{A\,V^{-2}}$, $\lambda = 4\,\mathrm{mV^{-1}}$ and $V_{th} = -3.667\,\mathrm{V}$. The options **plotwinsize** and **numdgt**, shown in figure A.5 (b), make sure that LTSpice does not compress the output data and increases the floating point precision. This is important because I_D spans a large range of values. Setting **gmin** to 0 prevents LTSpice from adding a small transconductance to every pn-junction, thus changing the MOSFET model. Finally, the most important command is the **.dc** command, which instructs LTSpice to step the voltage sources V_{SD} and V_{SG} to evaluate I_D over V_{SD}. The command

.dc Vsd 0 2 1m Vsg 3.867 4.467 0.2

steps the voltage source V_{SD} from 0–2 V in steps of 10 mV and for each step of V_{SD}, steps V_{SG} from 0.2–$0.8\,\mathrm{V} - \mathrm{V_{th}}$ in steps of 200 mV. Plotting

Id(M1)

results in the plot shown in figure A.4, which can be found in datasheets as the *Typical Output Characteristics* plot. To draw a line in the graph showing the point where the MOSFET enters the saturation region, denoted I_{sat} in figure A.4, as given by equation 3.79, add the following plot command to the graphing window and rescale the axis.

0.5∗0.813∗1A/1V∗∗2∗V(vsd)∗∗2

This command must be adjusted for the value of κ and do note that κ is entered with units of $\mathrm{A/V^2}$ to correctly display the output in A.

A.4.2. MOSFET Transconductance

Another interesting property to plot is the transconductance g_m of the MOSFET. Again, using the same model used previously in figure A.5 (b) and from equation 3.80 we known that g_m is defined as

$$g_m = \left.\frac{\partial I_D}{\partial V_{GS}}\right|_{V_{DS}=const}.$$

To derive g_m, we need to generate values of $I_D(V_{GS})$. This can again be done by stepping V_{GS}

.dc Vsg 3.667 4.667 1m

To produce a smooth plot, the steps size of V_{SG} was decreased to 1 mV. V_{DS} is constant in this plot and can be set using the voltage source V_{SD}. The MOSFET is intentionally biased into the saturation region at $V_{DS} = -1\,\text{V}$ as can be seen in figure A.4.

LTSpice is now able to numerically differentiate the data, which can be invoked by by plotting

```
−d(Id(M1))
```

The minus sign comes from the inverted $V_{SG} = -V_{GS}$. To plot g_m over I_D, the formula for g_m given above needs to entered manually into the *Expression Editor* by right clicking the expression label on top of the graph. Finally, the x-axis must be changed to $Id(M1)$, leading to the plot in figure A.6.

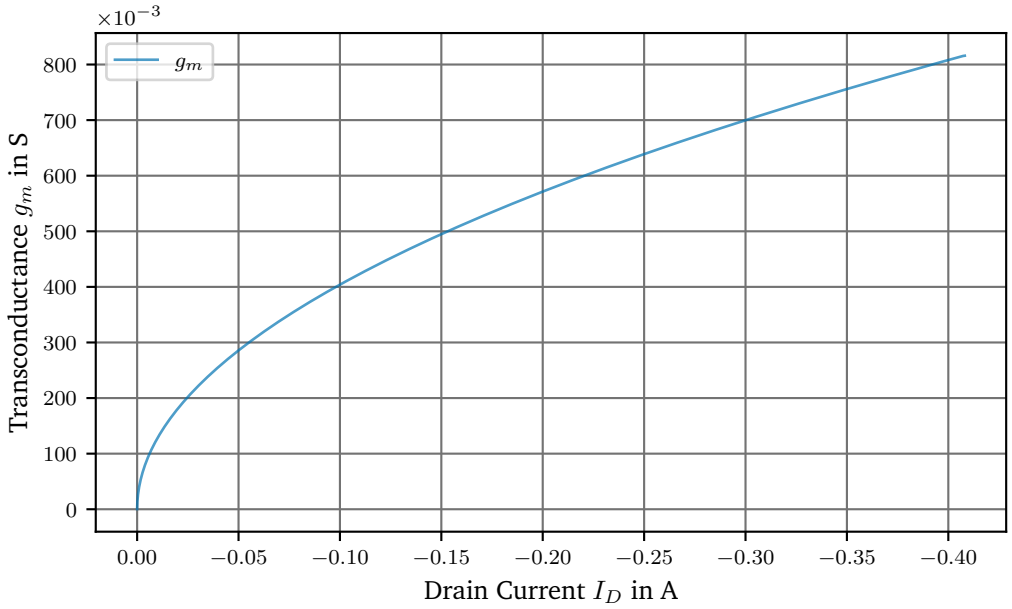

Figure A.6.: Simulated transconductance in saturation at $V_{DS} = -1\,\text{V}$.

As expected from equation 3.80, g_m is proportional to the square root of I_D when the MOSFET is in saturation.

As a sidenote, if the MOSFET model includes gate leakage, this leakage current may influence the calculation of g_m, especially at very low currents. In this case, it it better to plot the positive derivative of the source current $Is(M1)$, which does not include the leakage current.

```
d(Is(M1))
```

A.4.3. Output Impedance

This sections will explain how to calculate the dynamic output impedance using LTSpice. The example circuit used is the precision current source from section 3.8.4. The dynamic output impedance was defined in equation 3.83 as the inverse of the conductance leading to

$$R_{out} = \frac{1}{\frac{\partial I_D}{\partial V_{DS}}}\,.$$

Using the technique presented in the previous section, the obvious solution would be to again use the **.dc** sweep command and then numerically differentiate the result. Unfortunately this will lead to disappointing results, because the output impedance in question is very large and the limits of the numerical precision will be reached, nicely demonstrating the boundaries of numerical methods. LTSpice allows to increase the numeric precision to double floating point values using the option **numdgt**

.**options** numdgt=15

Unfortunately, this only forces LTSpice to internally use the double floating point number format, which does have a precision of 53 bit which means $\log_{10}\left(2^{53}\right) = 15.95$ decimals. So instead of using the large-signal model of the MOSFET, it becomes more convenient to evaluate the small-signal model

$$R_{out} = \frac{v_{load}}{i_D} = \frac{v_{DS}}{i_D}$$

at several different points of V_{DS}, thereby reconstructing the large-signal model from rasterized versions of the small-signal model. For the small-signal model, $v_{DS} = v_{load}$ because the supply voltage and the voltage across the sense resistor can be considered constant. Any change in the voltage across the load must therefore cause the opposite change in the source-drain voltage $v_{SD} = -v_{DS}$.

To run this simulation the small-signal simulation must be used and additionally some commands not available through the graphical user interface need to be entered by hand.

The LTSpice simulation is shown in figure A.7 and will now be explored.

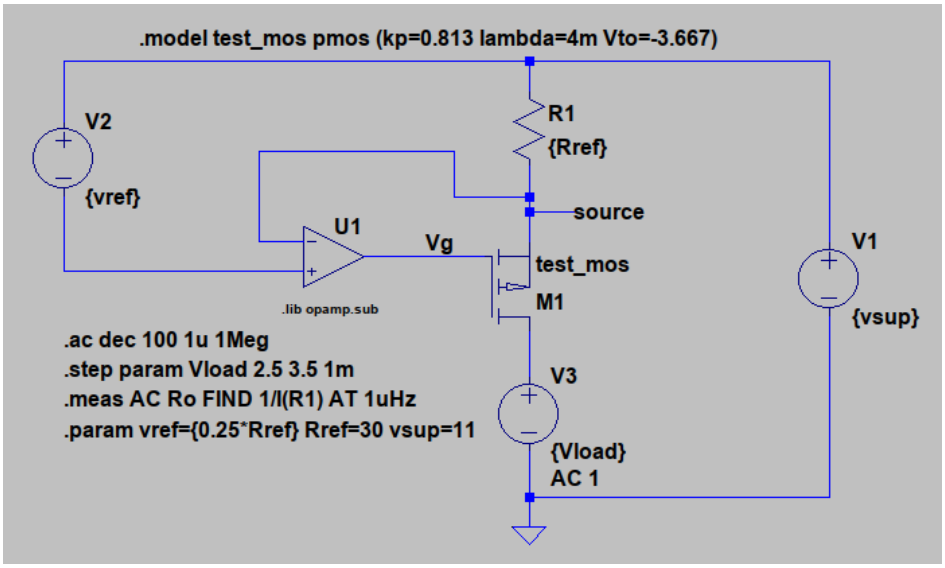

Figure A.7.: LTSpice model.

The simulation uses the same MOSFET model as above and adds an ideal op-amp to control the loop. The op-amp model has a open-loop gain of 2×10^6 and a gain-bandwidth product of 10 MHz as can be approximated from the the datasheet of the AD797 [9] and is also given in table 3.11. This leads to a 3 dB corner frequency of 5 Hz, which will be interesting later.

To access the small-signal model the **.ac** command is used because LTSpice uses the small-signal model to calculate the ac response of a circuit at a given working point. The command

.ac dec 100 1u 1Meg

calculates the ac response from $1\,\mu$Hz to $1\,$MHz with $100\,$points/decade. Additionally, as discussed, the load will be stepped by stepping the voltage source in the source leg of the MOSFET. We use a voltage source in this case instead of a resistor, because the AC impedance of a laser diode is typically very small. For the working point, it does not matter whether V_{load} is resistive or not. To step the voltage source, the command

.step param Vload 2.5 3.5 1m

is used to change V_{load} from 2.5–$3.5\,$V in steps of $1\,$mV, which is exactly the maximum V_{DS}, which is $V_{sup} - V_{ref} = 3.5\,$V. This is done to show the effect of the complete loss of regulation. The last thing to do, is to extract the desired output impedance from the many stepped small-signal simulations. This can be done using the **.meas** command telling LTSpice to save a single value at a certain frequency from each step.

.meas AC Ro FIND 1/I(R1) AT 1uHz

The **.meas** command shown will save the value of $\frac{1}{i_D} = \frac{1}{I(R1)}$ at $1\,\mu$Hz to the (error) log file whenever the **.ac** command is run. The value of v_{DS} was already set to $1\,V_{rms}$ in the LTSpice simulation as shown in figure A.7, thus $\frac{1\,V}{I(R1)} = R_{out}$. The current through the sense resistor instead of i_D was chosen because it is numerically more stable and since there is no gate current it is the same as i_D. The frequency were R_{out} is measured was chosen to be well below the corner frequency of the op-gain, which was calculated above to be $5\,$Hz. This gives the near DC output impedance of the current source.

To plot the values that are stored in the log file, click on *View* in the top menu, then *SPICE Error Log*. Now right-click on the error log and select *Plot stepp'ed .meas data*. This will open a new plot window showing the output impedance curve.

Those results are discussed in more detail in section 3.8.5.

A.5. MOSFET Noise Sources

This section gives the reader a quick overlook of the noise sources found in MOSFETs. A good overview of different types of noise in MOSFETs can also be found in [144] and goes beyond the scope presented here.

The MOSFET wideband noise can be attributed to thermal noise in the channel [68]. Der Ziel developed a model for the thermal noise in the saturation region of the MOSFET, while the classic Johnson–Nyquist noise [107] can be used for the ohmic region as it behaves like a voltage controlled resistor. This results in the noise density of

$$i_{n,thermal} = \begin{cases} \sqrt{4k_B T \frac{2}{3} g_m} & \text{saturation} \\ \sqrt{4k_B T g_{DS}} & \text{ohmic} \end{cases} \tag{A.12}$$

Using the example parameters from table 3.11, one finds

$$\begin{aligned} g_m &= \sqrt{2\kappa I_D \left(1 + \lambda V_{DS}\right)} = 0.642\,\text{S} \\ T &= 25\,^\circ\text{C} \\ i_{n,thermal} &\approx 83.9\,\text{pA}/\sqrt{\text{Hz}}\,, \end{aligned} \tag{A.13}$$

the equivalent noise of a resistor $R_D = \frac{3}{2g_m} = 2.3\,\Omega$.

A more detailed analysis, which also points out the limits of the model above can be found in [224].

Additionally the MOSFET also suffers from shot noise due to leakage through the gate, but this can be neglected because this leakage current is very small and even a relatively large current of $1\,\text{mA}$ only produces

$$i_{n,shot}^2 = \sqrt{2eI_D} \tag{A.14}$$

$$\approx 1.8\,\text{pA}/\sqrt{\text{Hz}}\,. \tag{A.15}$$

Shot noise becomes interesting when the MOSFET is used well below threshold or at higher frequencies because then the parasitic gate-drain capacitor C_{GD} will leak from the input to the output as can be seen in figure A.8. Figure A.8 shows the different parasitic capacitances of a MOSFET.

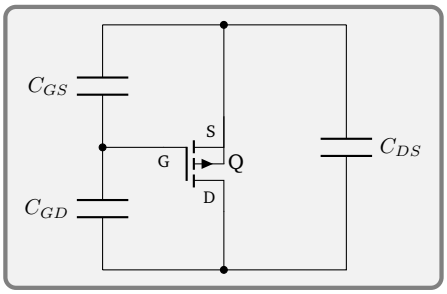

Figure A.8.: Parasitic capacitances of a MOSFET.

These capacitances can also be found in datasheets, although not directly, because they are

defined as

$$C_{iss} = C_{GD} + C_{GS} \quad \text{input capacitance} \tag{A.16}$$
$$C_{oss} = C_{DS} + C_{GD} \quad \text{output capacitance} \tag{A.17}$$
$$C_{rss} = C_{GD} \quad \text{reverse transfer capacitance}\,. \tag{A.18}$$

Regarding low frequencies, MOSFETs also show strong flicker noise. It is known from section 3.6.1, that the sources of flicker noise are not clearly understood, so there are several theories regarding flicker noise models for MOSFETs.

An an empirical model given by [144, 182] can be used to describe the flicker noise as

$$i_{n,flicker} = \sqrt{\frac{K_f I_D}{C_{ox} L^2} \frac{1}{f}}\,. \tag{A.19}$$

This model is presented here because it is both supported and easy to implement in LTSpice. While the parameter K_f is approximately $2 \times 10^{-10}\,\text{fC}^2/\mu\text{m}^2$ [144] for p-channel MOSFETs, the gate width and length W, L are device specific and unfortunately not given by the manufacturers. The typical corner frequency for MOSFETs, though, is between a few hundred kHz and a few dozen MHz depending on the size of the transistor. Larger transistors tend to show lower noise. Hence older processes are preferred in this regard. Given that the noise is uncorrelated, the total noise of the MOSFET in saturation can be written as

$$i_n = \sqrt{4 k_B T \frac{2}{3} g_m + \frac{K_f I_D}{C_{ox} L^2} \frac{1}{f}} \tag{A.20}$$

As a reminder, the MOSFET is a (transconductance) amplifier, that takes a voltage at the input and outputs a current. To make the noise figures comparable, the noise is divided by the gain g_m. This called the input referred noise. The input referred (voltage) noise e_n is given by:

$$e_{n,thermal} = \sqrt{4 k_B T \frac{2}{3 g_m}} \tag{A.21}$$
$$e_{n,flicker} \overset{3.81}{\approx} \sqrt{\frac{K_f}{2\kappa C_{ox} L^2} \frac{1}{f}} \tag{A.22}$$

We can see,that flicker noise is fully determined by the process parameters in this model.

A.6. Building an Injection Transformer

Typically devices in the lab at APQ are supplied with a positive and a negative voltage – usually $\pm 15\,\mathrm{V}$. This is readily achieved using two floating outputs of a power supply and connecting them in series, then tapping off the center as the common voltage around which the $\pm 15\,\mathrm{V}$ is centered.

When testing new devices like the current driver or temperature controller developed in this work, it is sometimes necessary to inject a disturbance into the power rails. This setup requires a positive and a negative line injector like the positive injector `PB02` presented in [37] and the negative Picotest `J2123A` line injector. When driving these injectors it is desirable to drive them both from a single output of a VNA. The Picotest `Bode 100` used for many low frequency applications does not have galvanically isolated inputs and outputs. Galvanic isolation can be achieved using a transformer to drive the injectors. Additionally using a transformer, it is easy to create two outputs, that are π rad out phase. Building one such transformer is explained in this section.

Before proceeding to the build instructions it is useful to have look at a model of the transformer with some parasitics to better understand the design decisions. A simple model is shown in figure A.9.

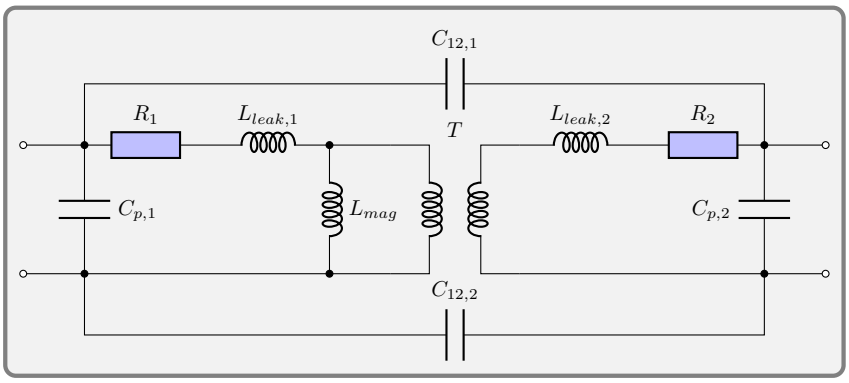

Figure A.9.: A simple model of a transformer, neglecting core losses and frequency and loading dependent effects.

The model only includes the major parasitic effects and their importance will now be discussed briefly. Starting with the resistance of the coil R_x, which should be well below $1\,\Omega$ and plays a rather small role, but will introduce some losses and dampen any resonances. The magnetizing inductance L_{mag} represents the energy that is stored in the core. In this model it is the flux that travels inside the core. Using a material with higher permeability increases L_{mag}, which is better, but one must look out not to saturate the core. The leakage inductance L_{leak} is the part of the magnetic field that is lost where the field lines do not pass through the secondary winding. This should ideally be low and can be lowered by tightly winding the transformer. Tightly winding the transformer has the downside of increasing the isolation capacitance $C_{12} = C_{12,1} + C_{12,2}$. Having less leakage inductance improves the high frequency behaviour of the transformer though. Therefore, a tightly wound bifilar winding scheme is chosen. Finally, there is a coupling capacitance C_p between the two input (and output) nodes, which becomes problematic at higher frequencies, when the impedance of the transformer goes up, while the impedance of the C_p goes down.

To summarize, for a good injection transformer that has a flat transfer function out to high

frequencies, it is important to keep L_{mag} high by using a high permeability material like a nanocrystalline core and to keep L_{leak} low by tightly coupling the windings. These choices unfortunately make a bad isolation transformer as will be shown later based on the electrical parameters of the finished transformer.

It was already said, that a flat transfer function is desired, so the frequency range of interest must be defined. The `Bode 100` covers a frequency range from 1 Hz to 50 MHz. The whole range is a bit too much to ask for because the low frequency end requires a large core to cope with the increased flux. The many windings required will then cause problems at the high end due to L_{leak}, which then limits the high frequency response. This transformer aims for a good compromise to cover most of the range, while accepting a limited performance at the corners.

This concludes the discussion of the design choices as the intricate details of the parasitic effects of different types of transformers, their geometry and materials are not discussed here for simplicity. The interested reader may look up [197] for more details. This section is only intended to be a simple instruction manual to allow the reader to build an affordable alternative to fairly expensive commercial solutions with similar performance.

The materials required are:

- A box like the the Hammond `1590B`.
- A nanocrystalline ferrite core is preferred for example, a Vacuumschmelze `T60006-L2040-W452` or `T60006-L2040-W424`.
- 3 m of Cat5e Ethernet cable. Preferably FEP insulated like Belden `7928A`, but any other will also do.
- 2–3 isolated BNC connectors like the Amphenol `031-10-RFXG1`. You will need 3 connectors for the center tapped version and 2 for a 1:1 transformer.
- 1 Cinch Connectivity Solutions `111-2223-001` earthing connector.
- Drills in sizes 6 mm and 9.7 mm.
- Kapton tape

The author used a Vacuumschmelze `T60006-L2040-W452` because it was available at the time but the `T60006-L2040-W424` might be a better choice because of its higher inductance per turn (101 µH at 10 kHz vs. 12.2 µH at 10 kHz). The `T60006-L2040-W452` has a slightly smaller inner diameter (25 mm vs 32 mm), so less windings will fit onto the core, this may offset some of the higher inductance coefficient of the core, but fewer windings also reduce the inter-winding capacitance due to the shorter cable length.

The target is 46 turns of the twisted pair cable around the core for a `T60006-L2040-W452`. This should give a tight fit. When center tapping the transformer do make sure to accurately count and then exactly cut one wire in the center. Do not cut the wire in advance, because you will need to leave some overhead at the beginning to leave plenty of room to solder the cable to the BNC connectors.

When done winding the transformer, wrap it with Kapton tape to secure the windings. It is recommended to test it before final assembly. Carefully solder the BNC connectors to the ends and test it with a VNA. These connectors will later be removed again. Make sure to calibrate the VNA beforehand and when the transformer matches the requirements, it is time to mount it in the box.

The box requires one 6 mm hole for the earthing connector and 3 9.7 mm holes for the BNC connectors. The finished device is shown in figure A.10.

Figure A.10.: Photo of the finished injection transformer in its box. The black rubber is used to secure it in the box.

After final assembly, the injection transformer was tested using a Picotest `Bode 100` VNA and also compared against a commercial Picotest `J2101A` 1:1 transformer.

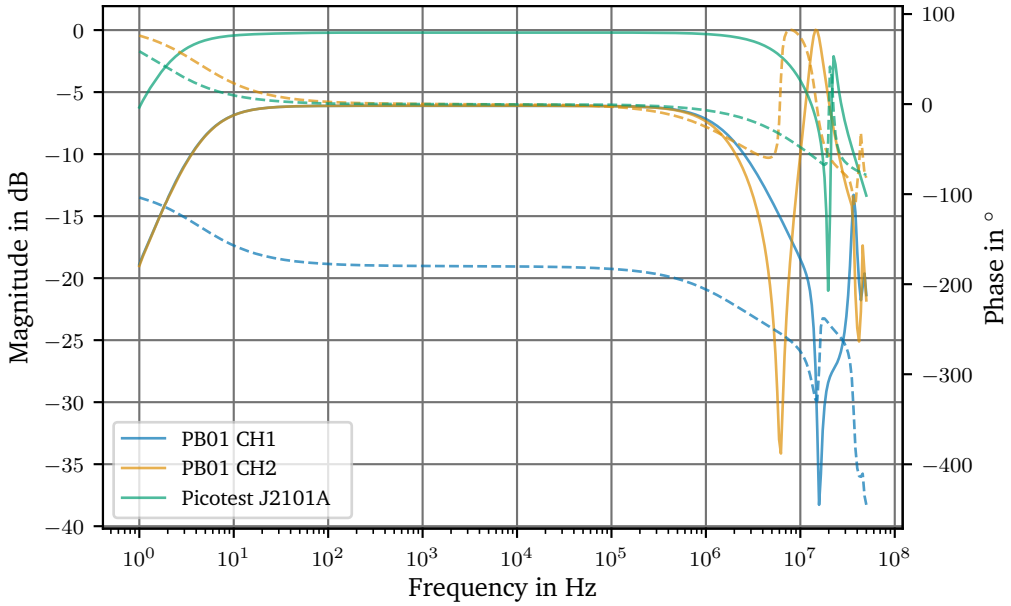

Figure A.11.: Bode plot of both channels of the injection transformer `PB01` and the Picotest `J2101A`. The solid lines are the magnitude, the dashed lines is the phase.

The VNA settings for the Bode plot were chosen to make sure that the core does not saturate, so the excitation voltage is very moderate. CH1 is used to monitor the primary side and CH2 monitors the secondary side. The most important VNA parameters can be summarized as

- Output $50\,\Omega$ $223.6\,\mathrm{mV_{rms}}$ ($0\,\mathrm{dBm}$)
- CH1 (measuring VNA output) set to $1\,\mathrm{M\Omega}$
- CH2 set to $50\,\Omega$
- Receiver bandwidth $1\,\mathrm{kHz}$

The choice of terminating the transformer output into $50\,\Omega$ is fairly arbitrary, but does have a bearing on the frequency response. It seems Picotest is terminating into $5\,\Omega$ and $50\,\Omega$ [64] in their setup. Using a high impedance termination on the secondary side leads to a self-resonance peak around $6\,\mathrm{MHz}$. The self resonance is caused by the inductance of the transformer together with the parallel capacitance of the winding. See below for the electrical parameters.

From the Bode plot shown in figure A.11 It can be seen that the transfer gain of the two outputs is identical within the limits of the measurement and is, as expected, at $-6\,\mathrm{dB}$. Do remember, that the `PB01` transformer has a 1:0.5 ratio, because it is bifilar wound and center-tapped. Additionally, CH1 is π rad out out phase. The reason is the center tapping, both output are referenced to the same ground in the middle, so one output must be out of phase with respect to the other.

The lower $-3\,\mathrm{dB}$ point is at around $4.5\,\mathrm{Hz}$ and the upper at $2\,\mathrm{MHz}$ and $1.7\,\mathrm{MHz}$ for CH1 and CH2 respectively. The Picotest `J2101A` has a $-3\,\mathrm{dB}$-bandwidth of $2\,\mathrm{Hz}$ to $8.4\,\mathrm{MHz}$, which is quite a bit better at the low end a fair bit worse at the high end. The claimed *usable Bandwidth* (whatever that is) is $10\,\mathrm{Hz}$ to $45\,\mathrm{MHz}$.

Lastly, some electrical properties of the injection transformers as measured using the `Bode 100` and confirmed using an LCR Research `LCR Pro1 Plus`.

Device	`PB01`	Picotest `J2101A`
Inductance @ $1\,\mathrm{kHz}$	$20.3\,\mathrm{mH}$	$68.8\,\mathrm{mH}$
Series resistance R_1	$540\,\mathrm{m\Omega}$	$470\,\mathrm{m\Omega}$
Isolation capacitance @ $10\,\mathrm{kHz}$ C_{12}	$95\,\mathrm{pF}$	$80\,\mathrm{pF}$
$-3\,\mathrm{dB}$-bandwidth	$4.5\,\mathrm{Hz}$ to $1.7\,\mathrm{MHz}$	$2\,\mathrm{Hz}$ to $8.4\,\mathrm{MHz}$

A final word regarding the isolation capacitance of the transformers. These two transformers are by no means isolation transformers, the isolation capacitance is far too high for this use-case. The reason for such a high capacitance is the type of wiring and winding chosen. For a better high frequency performance a twisted pair was chosen. Here, the wires are in very close contact to each other and there is no shield in between. The twisted pair was measured to have about $25\,\mathrm{pF/m}$ @ $10\,\mathrm{kHz}$ after removing the jacket, which resulted in much looser twists so the $95\,\mathrm{pF}$ seems to be a reasonable deviation from the expected $150\,\mathrm{pF}$ (Cat5e is supposed to have around $50\,\mathrm{pF/m}$).

A.7. The Howland Current Source

This section discusses the Howland current source and derives an equation for the output impedance with regard to several imperfections found in the non-ideal circuit. The discussion includes both the classic Howland current source (HCS) [201] and the *improved* Howland current source.

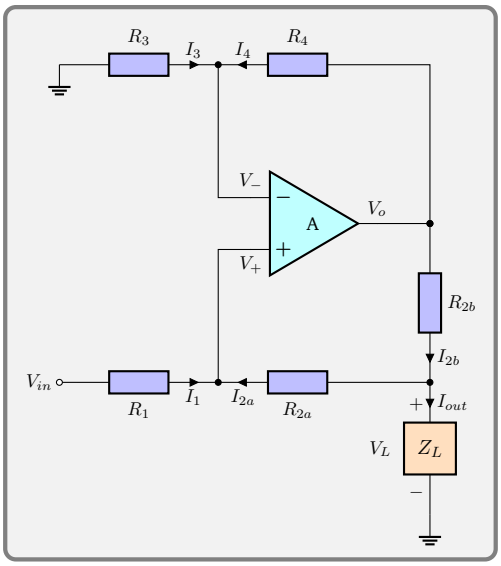

Figure A.12.: The Howland current source. Using $R_{2a} = 0\,\Omega$ is the classic version, while $R_{2a} \neq 0\,\Omega$ is the *improved* version.

First, an ideal circuit is discussed with perfectly matched resistors and an ideal op-amp, then the effects of an imperfect resistor matching and an non-ideal op-amp with finite gain are discussed, finally an equation including both effects is given. This model can then be used to create a list of requirements for the components. Other parasitic effects like stray capacitance or the input capacitance of the op-amp is neglected. This is valid for the low frequency range of interest. The op-amp is also assumed to be ideal with regard to the input bias current and voltage offset. While the input bias current depends on the type of op-amp, it is typically less than a few nA or even pA if a JFET op-amp is used. This is far less than the currents required for the applications in this work. The same argument applies to the offset voltage. The interested reader may look up some of those details in [149]. A discussion of the effect of the parasitic capacitance and its compensation can be found in [228], which demonstrates a Howland current source with a $-3\,\mathrm{dB}$ bandwidth of $450\,\mathrm{kHz}$ with an output impedance of more than $1\,\mathrm{M\Omega}$.

The calculations to derive the model were done using SymPy [52], a Python framework for symbolic calculation. The full source code can be found in data/simulations/howland_current_source.ipynb as part of the online supplemental material [42].

In order to calculate the output impedance, the voltage at the load is required, because the output impedance of the current source is

$$R_{out} = -\frac{\partial V_L}{\partial I_{out}} \tag{A.23}$$

The negative sign is due to the direction of the current I_{out}, which flows out of the output

node as shown in figure A.12, but the passive sign convention is that the current must flow into the device, hence a minus is applied, see for example [117]. V_L can be found using Kirchhoff's current law applied to the inverting input node, non-inverting input node and output node. The inverting node is the most simple one, so it is best to start there. Assuming, that no current is flowing into the op-amp pin it can be seen that

$$\begin{aligned} I_3 + I_4 &= 0 \\ \frac{-V_-}{R_3} + \frac{V_o - V_-}{R_4} &= 0 \\ \Rightarrow V_o &= V_- \left(1 + \frac{R_4}{R_3}\right) . \end{aligned} \tag{A.24}$$

The non-inverting node can be calculated as follows.

$$\begin{aligned} I_1 + I_{2a} &= 0 \\ \frac{V_{in} - V_+}{R_1} + \frac{V_L - V_+}{R_{2a}} &= 0 \\ \Rightarrow V_+ &= \frac{R_1 V_L - R_{2a} V_{in}}{R_1 - R_{2a}} . \end{aligned} \tag{A.25}$$

Finally, the output node is given as

$$\begin{aligned} I_{2b} - I_{2a} - I_{out} &= 0 \\ \frac{V_o - V_L}{R_{2b}} - \frac{V_+ - V_L}{R_{2a}} - I_{out} &= 0 . \end{aligned} \tag{A.26}$$

The missing piece of the puzzle is a relationship between V_+ and V_-. Since the feedback loop is closed the relationship below exists. It can be simplified by neglecting the offset voltage and assuming an infinitely high open-loop gain A_{ol}. The latter assumption will be treated separately later.

$$\begin{aligned} V_{out} &= A_{ol}(V_+ - V_-) \\ V_- &= V_+ - \frac{V_{out}}{A_{ol}} \approx V_+ \end{aligned} \tag{A.27}$$

Using equations A.24, A.25, A.26, and A.27, the load voltage V_L can now be calculated.

$$V_L = \frac{\left(R_1 R_{2b} R_3 + R_{2a} R_{2b} R_3\right) I_{out} - \left(\left(R_{2a} + R_{2b}\right) R_3 - R_{2a} R_4\right) V_{in}}{R_1 R_4 - \left(R_{2a} + R_{2b}\right) R_3} \tag{A.28}$$

Having the load voltage, the dynamic output impedance is

$$\begin{aligned} R_{out} = -\frac{\partial V_L}{\partial I_{out}} &= \frac{R_1 R_{2b} R_3 + R_{2a} R_{2b} R_3}{\left(R_{2a} + R_{2b}\right) R_3 - R_1 R_4} \\ &= \frac{R_{2b} + \frac{R_{2a} R_{2b}}{R_1}}{\frac{R_{2a}+R_{2b}}{R_1} - \frac{R_4}{R_3}} \end{aligned} \tag{A.29}$$

Looking at the denominator from equation A.29 it is clear, that the output impedance goes to infinity if

$$\frac{R_4}{R_3} = \frac{R_{2a} + R_{2b}}{R_1} . \tag{A.30}$$

It is also obvious that any deviation from the equality given in equation A.30 leads to a finite output impedance. This output impedance shall now be estimated. Similar to [82] an imbalance factor ϵ is introduced to describe the matching of the resistors.

$$\frac{R_4}{R_3} = \frac{R_{2a} + R_{2b}}{R_1}(1 - \epsilon) \tag{A.31}$$

Substituting equation A.31 into equation A.29 leads to the output impedance due to resistor mismatch

$$R_{out,m} = \frac{R_1 R_{2b} + (R_{2a} R_{2b})}{\epsilon(R_{2a} + R_{2b})} = \frac{(R_1 + R_{2a})\, R_{2b}}{R_{2a} + R_{2b}} \frac{1}{\epsilon} \tag{A.32}$$

To give a value for the mismatch factor ϵ the resistor tolerances must be considered. Typically when building a Howland current source, a resistor array is used, to ensure tight matching of the resistors to satisfy equation A.30, so it is safe to assume the tolerance T for all four or five resistors is the same. This tolerance is typically between $5\,\%$ and $0.01\,\%$ for the highest quality resistors. Further assuming $R_{2a} + R_{2b} = R_2$, $R = R_1 = R_2 = R_3 = R_4$ and a maximum mismatch due to the tolerance equation ϵ can be calculated from equation A.31.

$$\begin{aligned} \frac{R(1+T)}{R(1-T)} &= \frac{R(1-T)}{R(1+T)}(1-\epsilon) \\ \Rightarrow \epsilon &= \frac{4T}{(1-T)^2} \end{aligned} \tag{A.33}$$

For equal resistors values R, the output impedance due matching errors of those resistors degrades to

$$R_{out,m} = \left(\frac{R^2 - R_{2a}^2}{R}\right) \frac{(1-T)^2}{4T} \tag{A.34}$$

From equation A.34 the output impedance for the classic Howland current source with $R_{2a} = 0$ is easily found to be

$$R_{out,m,HCS} = R\frac{(1-T)^2}{4T} \approx \frac{R}{4T} \tag{A.35}$$

using the the Taylor expansion

$$\epsilon = \frac{4T}{(1-T)^2} = 4T + 4T^3 + \mathcal{O}(T^5)\,.$$

The improved Howland curret source is better treated with respect to R_{2b}, because R_{2b} defines the output current sensitivity with respect to V_{in}. Since R_{2b} defines the output current, the other resistor values can be chosen to be very large. The output impedance in case $R \gg R_{2b}$ can be calculated as

$$\begin{aligned} R_{out,m} &= \frac{R_{2b}\,(2R - R_{2b})}{R} \frac{(1-T)^2}{4T} \\ R_{out,m,iHCS} &= \lim_{R\to\infty} R_{out,m} = 2R_{2b}\frac{(1-T)^2}{4T} \approx \frac{R_{2b}}{2T} \end{aligned} \tag{A.36}$$

The result is that for $R \gg R_{2b}$, the output impedance of the improved Howland Current source is about twice as high as the basic Howland current source. The size of the resistors R

are only limited by the desired bandwidth, because circuit parasitics like the input capacitance of the op-amp must then be considered.

Resistor mismatch is not the only element that negatively affects the output impedance. Another limiting factor is the finite op-amp gain A, which, on top of that, also decreases with frequency. Not applying the approximation in equation A.27, yields a rather lengthy term for V_L

$$V_L = \frac{\begin{array}{r} AI_{out}R_1R_{2b}R_3 + AI_{out}R_{2a}R_{2b}R_3 - AR_{2a}R_3V_{in} - AR_{2a}R_4V_{in} \\ - AR_{2b}R_3V_{in} + I_{out}R_1R_{2b}R_3 + I_{out}R_1R_{2b}R_4 + I_{out}R_{2a}R_{2b}R_3 \\ + I_{out}R_{2a}R_{2b}R_4 - R_{2b}R_3V_{in} - R_{2b}R_4V_{in} \end{array}}{(A-1)R_1R_4 - (A+1)(R_{2a}+R_{2b})R_3 - R_1R_3 - (R_{2a}+R_{2b})R_4} \tag{A.37}$$

Again, differentiating to find the output impedance yields

$$R_{out} = \frac{\begin{array}{r} A_vR_1R_{2b}R_3 + A_vR_{2a}R_{2b}R_3 + R_1R_{2b}R_3 \\ + R_1R_{2b}R_4 + R_{2a}R_{2b}R_3 + R_{2a}R_{2b}R_4 \end{array}}{(A+1)(R_{2a}+R_{2b})R_3 - (A-1)R_1R_4 + R_1R_3 + (R_{2a}+R_{2b})R_4} \tag{A.38}$$

This time, assuming perfect matching of the resistors with $R_{2a}+R_{2b}=R_2$, $R=R_1=R_2=R_3=R_4$, R_{out} can be further simplified, yielding a term similar to equation A.34.

$$R_{out,A} = \left(\frac{R^2+R_{2a}^2}{R}\right)\frac{A+2}{4} \tag{A.39}$$

For a typical compensated op-amp, the frequency dependent gain was already introduced in equation A.11 as

$$A(\omega) = \frac{A_{ol}}{\sqrt{1+\left(\frac{\omega}{\omega_c}\right)^2}},$$

with the open-loop gain A_{ol} and corner frequency ω_c of the dominant pole at which the gain starts rolling off with an order of magnitude per order of magnitude in frequency ($20\,\mathrm{dB}$ per decade).

Comparing equations A.34 and A.39 it is clear, that the sensitivity of the output impedance to the resistor tolerances and the op-amp gain are of the same magnitude since $\frac{(1-T)^2}{4T} \approx \frac{1}{4T}$ for small T and $\frac{A+2}{4} \approx \frac{A}{4}$ for typical values of A. With regard to the resistor tolerances and the gain of op-amps, it is clear that at low frequencies, the contribution of precision op-amp with a gain $A \geq 10^6$ is insignificant, even when $0.01\,\%$ resistors are used. This makes trimming or selection of components inevitable if a high output impedance is required. Only at frequencies above $1\,\mathrm{kHz}$, when the op-amp gain has dropped to values comparable to $\frac{1}{\epsilon}$, the op-amp needs to be considered.

Finally, the same calculations can be done including both the finite gain and the resistor matching. These calculations are omitted here for brevity, but can be found in the Jupyter notebook mentioned above. The result is

$$R_{o,m,A} = \left(\frac{R^2-R_{2a}^2}{R}\right)\frac{(AR+R-\epsilon+1)}{A\,(R+\epsilon-1)+2R-2\epsilon+2}. \tag{A.40}$$

Another representation is also given by Mahnam et al. [149]. They decompose the output impedance into several components to build an equivalent circuit. This allows to treat the gain dependent part as a capacitance, hence the term output capacitance is sometimes used. The

formula given here is more suited for an analytical approach or for Monte Carlo simulations though.

Finally, the compliance voltage must be discussed. The output voltage of the op-amp can again be calculated using Kirchhoff's current law and the details are found in the Python notebook data/simulations/howland_current_source.ipynb as part of the online supplemental material [42]. The result is

$$V_o = \frac{2\left(RV_L + R_{2a}V_{in}\right)}{R + R_{2a}} \tag{A.41}$$

For the classic Howland current source ($R_a = 0$) one finds

$$V_{o,HCS} = 2V_L\,, \tag{A.42}$$

which is independent of the input voltage. It is largely independent of the resistors as well in case of a laser diode, because V_L is fairly constant with the output current. The improved Howland current source behaves differently and the op-amp output voltage for $R \gg R_{2b}$ becomes

$$V_{o,iHCS} = \lim_{R\to\infty} V_o = V_L + V_{in}\,. \tag{A.43}$$

In this case part of the load dependence is traded for an input voltage dependence. Whether that is an advantage depends on the application.

List of publications

Kanika, P.Baus, G.Birkl, Z.Guo, A.Khodaparast, J.Klimes, W.Quint, M. Shaaban, M.Vogel, *The ARTEMIS experiment for precision measurements of the electron gfactor in highly charged ions*, In HYPERFINE 2019 proceedings (2019).

A. Martin, P. Baus, and G. Birkl, *External cavity diode laser setup with two interference filters*. Applied Physics B **122.298** (Dec. 2016).

T. Preuschoff, P. Baus, M. Schlosser and G. Birkl, *Wideband current modulation of diode lasers for frequency stabilization*, Review of Scientific Instruments **93**, 063002 (2022).

Kanika, A. Krishnan, J. W. Klimes, B. Reich, K. Anjum, P. Baus, G. Birkl, W. Quint and M. Vogel, *Production of highly charged ions inside a cryogenic Penning trap by electron-impact ionisation*, submitted to Journal of Physics B (2023).

J. W. Klimes, Kanika, A. Krishnan, B. Reich, K. K. Anjum, P. Baus, G. Birkl, W. Quint, W. Schott, and M. Vogel, *Cryogenic vacuum valve with sub-second operation times*, submitted to Review of Scientific Instruments.

P. Baus and G. Birkl, *An Open-Source, Low Noise, High Stability Digital Laser Driver for the next Generation of Laser Diodes*, in preparation.